# Growth of anodic alumina nanopores and titania nanotubes and their applications

Bo Chen

Dissertation submitted to the faculty of the Virginia Polytechnic Institute and State University in partial fulfillment of the requirements for the degree of

Doctor of Philosophy
In
Materials Science and Engineering

Dr. Kathy Lu, Chair
Dr. Guo-Quan Lu
Dr. John Y. Walz
Dr. William T. Reynolds, Jr.

Dec 07, 2012
Blacksburg, VA

Keywords: alumina nanopores, $TiO_2$ nanotubes, focused ion beam, anodization, mechanism

# Growth of anodic alumina nanopores and titania nanotubes and their applications

Bo Chen

## Abstract

Anodic aluminum oxide (AAO) nanopores are excellent templates to fabricate different nanostructures. However, the pores are limited to a hexagonal arrangement with a domain size of a few micrometers. In this dissertation, focused ion beam (FIB) is used to create pre-patterned concaves to guide the anodization. Due to the advantage of FIB lithography, highly ordered AAO arrays with different arrangements, alternating diameters, and periodic pore densities are successfully achieved. Anodization window to fabricate ordered AAO is enlarged due to the FIB pre-pattern guidance. AAO has also been successfully used as a template to nanoimprint prepolymer to synthesize vertically aligned and high aspect ratio h-PDMS nanorod arrays with Moiré pattern arrangements.

The formation mechanism of anodic $TiO_2$ nanotubes is proposed in this dissertation. Moreover, FIB pre-pattern guided anodization is introduced to synthesize highly ordered $TiO_2$ nanotubes with different morphologies. The effects of inter-tube distance and arrangement to the structure of $TiO_2$ nanotubes are investigated. $TiO_2$ nanotubes with branched and bamboo-type structures are achieved by adjusting anodization voltage. The influence of patterned concave depth and surface curvature on the growth of $TiO_2$ nanotubes and AAO are studied. The efficiency of $TiO_2$ nanotubes in supercapacitors and photoelectrochemical water splitting are optimized by enlarging surface area and increasing electrical conductivity.

Focused ion beam can not only create concave arrays to guide the electrochemical anodization, but also be used for nanoscale sculpting and 3D analysis. When the $TiO_2$ nanotube surface is bombarded by FIB, there is a mass transfers due to ion-induced viscous flow and sputter milling, thus the $TiO_2$ nanotubes are selectively closed and opened. By combining FIB cutting and SEM imaging to create a series of 2D cross section SEM images, 3D reconstruction can be obtained by stacking SEM images together. This 3D reconstruction offers an opportunity to directly and quantitatively observe the pore evolution to understand the sintering process.

# Acknowledgements

First of all, I would like to express my great gratitude to my mother and all other family members. Without my mother's hard working and full support, I cannot have the opportunity to go to college, not to mention coming to the United States of America to purchase the Ph.D.

I would like to express my deep appreciation to my supervisor Dr. Kathy Lu. Dr. Lu has solid knowledge and great passion in science, I benefited and learned a lot from her guidance during my whole doctoral student career, such as plan the research, carry out multiple projects, write grant proposal, and always keep passion on research. I would also like to acknowledge my committee members: Dr. Guo-Quan Lu, Dr. William T. Reynolds, Jr., and Dr. John Y. Walz. They not only give me insightful comments on specific scientific problems, but also give me valuable suggestions on career plan.

I acknowledge the financial support from National Science Foundation under grant No. CMMI-0824741, No. CMMI-0969888, the Institute for Critical Technology and Applied Science of Virginia Tech, and Chinese Government Award for Outstanding Self-financed Students Abroad.

I would like give my thanks to Dr. Shashank Priya for the valuable guidance about writing grant proposal; to Dr. Junbo Hou and Jian Shi for the valuable discussion on supercapacitors and water splitting; to Dr. Pengtao Yue for helpful discussions on mechanism of soft lithography; to Dr. Amanda J. Morris and Andrew Haring for their kind help on photoelectrochemical measurement; to Dr. Alan Esker for the measurement on surface tension; to Dr. Dwight Viehland and Dr. Jiefang Li for equipment support on electrochemical anodization.

Assistance from John McIntosh, Stephen McCartney, Jay Tuggle, Dr. Mitsuhiro Murayama, and Navin J. Manjooran from the Nanoscale Characterization and Fabrication Laboratory of Virginia Tech is greatly acknowledged. I also want to thank Trevor Clark and Melisa Yashinski from Pennsylvania State University for the great help on FIB.

I appreciate the generous help from my colleagues: Dr. Tongan Jin, Dr. Wenle Li, Zhipeng Tian, Zhenbo Xia, Yongxuan Liang, Dr. Manoj Mahapatra, Devid Berry, Menghui Li, Yuan Zhou, Yuchang Wu, Dr. Yaodong Yang, Dr. Wenwei Ge, Zhiguang Wang, Dr. Jianjun Yao, Dr. Deepam Maurya, Dr. Su Chul Yang, Yu Zhao, Chenlin Zhao, Jeffrey Geldmeier, Kelly Ramsburg. I appreciate all the staffs and professors in MSE Department for their helps.

# Statement:

Most of the contents in this dissertation were published or will be published in scientific journals. In referencing this work, readers are asked to cite the journals.

Table of Contents

# List of Figures

# List of Tables

# Chapter 1. Introduction

## 1.1 Motivation and objectives

Anodic aluminum oxide (AAO) nanopore arrays, which can be synthesized by self-organized electrochemical anodization, have attracted intensive interest as a template for fabrication of low dimensional nanostructures, such as nanorods, nanowires, nanotubes, and nanodots. The main advantage of the AAO template is that the morphology of the nanopores (interpore distance, diameter, and length) can be easily controlled by the anodization condition. Moreover, novel AAO structures with branched nanopores and modulated diameters enrich the morphology of the AAO template. Anodic titanium oxide nanotube arrays, which can also be obtained by self-organized electrochemical anodization, have great application potentials in dye-sensitized solar cells and water photoelectrolysis due to the large specific surface area and the direct pathway for charge transport. Similar to the AAO, the morphology of the $TiO_2$ nanotubes can be adjusted by anodization condition.

However, self-organized AAO and $TiO_2$ nanotubes occur only for a small anodization window with limited ordered domain sizes at around just a few micrometers, and the arrangement is limited to hexagonal in ordered regions. Different pre-patterning techniques have been used to achieve highly ordered AAO template with large ordered domain sizes and provide controllable interpore distances. Up to now, most studies focus on uniform diameter and equal interpore distance porous anodic alumina patterns.

On one hand, even though several mechanisms have been proposed, the formation mechanism of anodic $TiO_2$ nanotubes is still uncertain, which hinders an effective approach to optimize $TiO_2$ nanotubular structures for specific applications. On the other hand, the pre-pattern guided anodization has never been investigated due to the fact that the large Young's modulus (116 GPa) of titanium; it is hard to create concave arrays on a titanium foil. It is unknown whether similar guided anodization approaches can be successfully applied to titanium anodization to obtain highly ordered $TiO_2$ nanotube arrays with different arrangements and diameters.

This dissertation aimed to fabricate highly ordered AAO and $TiO_2$ nanotubes with different arrangements, diameters, and pore densities by FIB pre-pattern guided anodization. This dissertation also aimed to investigate the formation mechanism of anodic $TiO_2$ nanotubes. The effect of patterned concave depth and surface curvature on $TiO_2$ nanotubes and AAO was investigated in this dissertation as well. The mechanism of FIB nanoscale sculpting and the application of FIB lithography in 3D microstructure reconstruction were also studied in this dissertation.

## 1.2 Contributions

In this dissertation, the focused ion beam lithography is applied to the electrochemical anodization. The advantage of focused ion beam lithography to create concave patterns with diverse structures is that it enables the fabrication of AAO arrays with different arrangements (such as hexagonal, square, rectangular, and graphite lattice structure), alternating diameters, and heterogeneous pore densities. These AAO arrays broaden the application of AAO and enable the manufacturing of nanomaterials with diverse structures.

For nanoimprint lithography, low surface energy of the template is the key for releasing the polymer nanorods from the AAO template. High aspect ratio h-PDMS nanorods with large Young's modulus are created. For soft lithographic micromolding, A mechanism to understand the effect of surface wetting properties on the fidelity of soft lithography is proposed, which is based on a combination of hydrostatic equilibrium maintained in the pores and the dynamic diffusion of trapped air through the nanoparticle suspensions. Soft lithographic micromolding offers a generic method to create patterns with different feature arrangements, feature sizes, and feature shapes.

For the first time, highly ordered concave arrays are pre-patterned on the electropolished Ti surface, which guides the anodization of Ti and leads to the development of nanotubes at pre-patterned locations. As a result, highly ordered $TiO_2$ nanotubes with different arrangements and intertube distances are successfully obtained. This dissertation investigates the effect of $OH^-$ concentration and $TiO_2$ nanotube structure evolution after the anodization, the phenomenon challenges the validity of all existing formation mechanisms of $TiO_2$ nanotubes. A new formation mechanism for anodic $TiO_2$ nanotubes is proposed, which facilitate the design of optimized $TiO_2$ nanotubular structures for specific applications.

The understandings of the effect of pre-patterned concave depth and surface curvature on electrochemical anodization demonstrate the significance of uniform concave depths and flat surface to highly ordered AAO and $TiO_2$ nanotubes. Moreover, the understanding of surface curvature effect on $TiO_2$ nanotubes is important for its application on non-planar substrate.

Based on the selective closing and re-opening of the $TiO_2$ nanotubes under FIB bombardment, mechanism of FIB nanoscale sculpting is proposed. The combination of this technique with electrodeposition can enable selective growth of different conductive materials into different regions of the $TiO_2$ nanotubes. The opening process under low energy ion beam sculpting will provide an approach to remove the barrier layer of freestanding $TiO_2$ nanotubes to obtain $TiO_2$ nanotubes with two open ends.

A new FIB cutting method is introduced, which involved a protruding tip with a thick platinum protective layer covering both the top and side surfaces, to overcome the drifting issue and waterfall artifact during FIB cutting, and improve the FIB cutting resolution to 10 nm. 3D reconstruction offers an opportunity to directly and quantitatively observe the pore and grain boundaries, which can have broad applications for structural analysis.

# Chapter 2. Background

## 2.1. Anodic aluminum oxide nanopores

### 2.1.1. The mechanism for the growth of AAO

Anodic aluminum oxide (AAO) nanopores formed by anodization of high purity Al in an appropriate acidic solution has been studied since 1953.[1] In the last two decades, due to its application as templates or host materials to synthesize different nanostructures, such as nanorods, nanowires, nanotubes, and nanodots, the researches about the mechanism for the formation of AAO and fabrication of highly ordered AAO membranes have attracted intensive interesting.

The most popular mechanism for the growth of self-organized alumina nanopores is based on mechanical stress. Jessensky et al.[2] found systematic dependence of the volume expansion of the aluminum into alumina during oxide formation on the anodizing voltage and corresponds current efficiency. Optimal conditions for the formation of self-organized alumina nanopores are accompanied by a moderate expansion of the aluminum, otherwise no ordered nanopore domains can be observed. Based on these observations, Jessensky et al. suggested the mechanical stress associated with the volume expansion was the cause of repulsive forces between neighboring pores during the oxidation process, and the mechanical stress was the driving force for the self-organized process. Later, Singh et al.[3] proposed the mechanical stress model, which considered significant elastic stress due to the oxide volume expansion as an indispensable factor for ordering of the pores, theoretical explain the formation of regular hexagonal arrangement of the alumina nanopore. However, the repulsion model still cannot explain many experimental observations, such as the generation of the initial nanopores, the formation of the hemispherical pore barrier layer at bottom, and the merging and furcation of the nanopores during growth.

Recently, Su et al.[4-6] proposed an equifield strength model based on equilibrium between the oxidation of metal by anions of $O^{2-}$ and $OH^-$ (mainly produced from dissociation of water) and the dissolution of oxides, and utilize this model to explain the alumina nanopore generation, self-adjustment of pore size and ordering, pore merging and splitting. During anodization, $Al^{3+}$ ions drift through the oxide layer and are ejected into the solution at the oxide/electrolyte interface; while oxygen containing ions ($O^{2-}/OH^-$) migrate from electrolyte through the oxide layer at the pore bottom. The overall dissolution reaction of $Al_2O_3$ is as follows:

$$Al_2O_3 + nH_2O \rightarrow 2Al^{3+} + (3 + n\text{-}x)O^{2-} + xOH^- + (2n\text{-}x)H^+ \quad (1\text{-}1)$$

where n is the ratio of the dissociation of water to the dissolution of $Al_2O_3$. The oxidization of Al at the oxide/metal interface is as follows:

$$2Al + 3O^{2-} \rightarrow Al_2O_3 + 6e^- \quad (1\text{-}2)$$

$$2Al + 3OH^- \rightarrow Al_2O_3 + 3H^+ + 6e^- \quad (1\text{-}3)$$

It is important to introduce the dissolution of aluminum oxide during anodization by acidic electrolyte to form nanoporous structure; otherwise a nonporous planar layer will form in a near-neutral electrolyte. For the near-neutral electrolyte, the dissolution of $Al_2O_3$ is very slow, and the thickness of the oxide layer will continuously increase following reactions (1-2) and (1-3). As a result, the electric field will continuously drop and finally too weak to drive the oxygen containing anions through the oxide barrier layer. Therefore, a nonporous planar layer will form at the aluminum surface (Figure 2-1a).

For acidic electrolyte, the dissolution of $Al_2O_3$ takes place at the oxide/electrolyte interface, which significantly decreases the oxide layer thickness. Although both the oxidation and dissolution rates are reduced as the electric field is decreased, the former is expected to reduce faster than the latter. This can be understood as follows. The inward oxygen ionic current j, which is related to the electric field E across the barrier layer, determines the oxidation rate:

$$j = j_0 \times e^{kE} \quad (1\text{-}4)$$

where $j_0$ and $k$ are material dependent constants. Therefore, the oxidation rate decreases exponentially with the electric field. However, the dissolution rate of $Al_2O_3$, which is affected by the electric field through polarization and impairment of the Al-O bond, decreases slowly as the electric field decreases. As a result, the dissolution rate of the oxide layer will increase slower than the oxidation rate. There always exists a critical thickness of the barrier layer ($d_B$) and corresponding electric field ($E_B$), at this steady state, the oxidation rate balance with the dissolution rate.

As shown in Figure 2-1b, some pits will grow at the surface of aluminum at the early stage of anodization due the defects such as impurities, dislocation, grain boundaries, or nonmetallic inclusions in the underlying metal cause a faster dissolution rate of oxide layer. When a pit form at the oxide surface, the oxide thickness at the pit center BB' is smaller than at the pit edge AA' and CC', which leads to the faster oxide dissolution rate the BB' and the pore grows at pit location. Due to the electric field tend to maintain uniform through the whole interface, and the oxide layer thickness at pore bottom tends to have the same oxide thickness (Figure 2-1c and 1d), and an ideal hemispherical pore bottom with uniform critical barrier layer thickness ($d_B$) would be obtained. Since the electric field along DD' and EE' at the wall is as same as that at the bottom, the oxide layer can move not only downwards but also sideways.

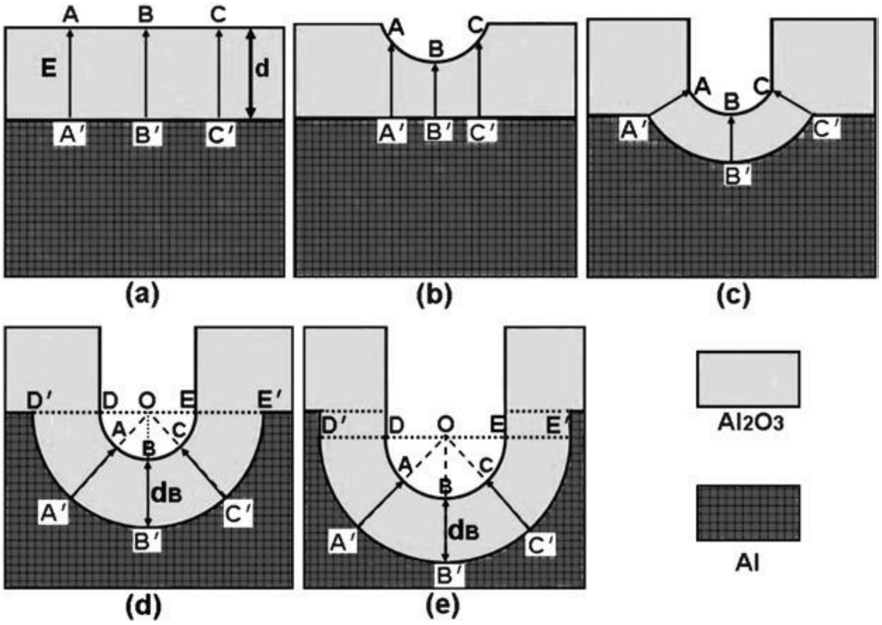

**Figure 2-1**: Schematic diagrams for the electric-field strength distribution on some typical barrier layers, (a) planar layer with a uniform thickness, (b) planar layer with a corrosive pit, (c) a corrosive pit at the electrolyte/oxide interface is replicated at the oxide/metal interface, (d) formation of the hemispherical pore base and (e) single pore formation.[6-7]

The free development of nanopore shown in Figure 2-1 only happens when the pores grow without the effect their neighbors. However, in the reality, the development of each pore is restricted by its neighboring nanopores due to the high pore density. When the two neighboring nanopores are completely separated with each other, the pores will free expand their outer wall until two walls merge with into a thicker combined wall $2d_B$. Due to both pore bottoms are perfectly hemispherical, the electric field at the joined position of the hemispheres (B) comes from both sides, which enhance oxidation rate at B. As a result, the joined position of neighboring barrier layers (B) will move down to a lower position (D) as shown in Figure 2-2b, which increase the oxide layer thickness at position D. Then, the dissolution rate at A and C will be relatively faster than the oxidation rate, and wall thickness between the neighboring nanopores will decrease from $2d_B$ to $2d_W$. The final shape of the nanopore bottom is not perfectly hemispherical, but has spherical angle 2θ smaller than 180º, which is confirmed by the SEM image of the nanopore bottom as shown in Figure 2-2d. And the oxidation rate still maintains the same at the whole oxide/metal interface. When the neighboring nanopores are close to each other (Figure 2-3a), the wall thickness between neighboring nanopores is small than $2d_W$. The electric field along BB' is equal to $E_B$, however, the electric field from B' to any the position range from A to B is smaller than $E_B$, because the oxide layer thickness there is larger than $d_B$. The smaller electric field leads to the relative smaller dissolution rate than the oxidization rate the positions range from A to B. As a result, the wall thickness will increases from d to $2d_W$.

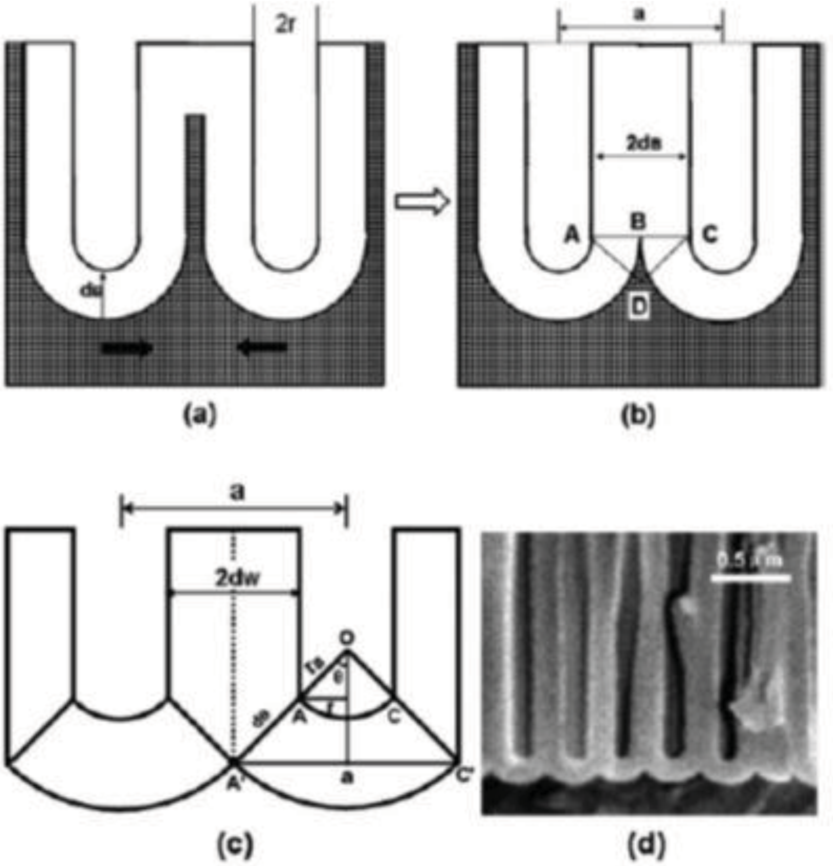

**Figure 2-2**: Schematic drawing showing that (a) two pores have a separation larger than $2d_B$, (b) the pores move towards each other to achieve a wall thickness of $2d_B$, (c) pores move closer with a balanced curvature of 2θ. (d) SEM image of pore bottom in an AAO. [6-7]

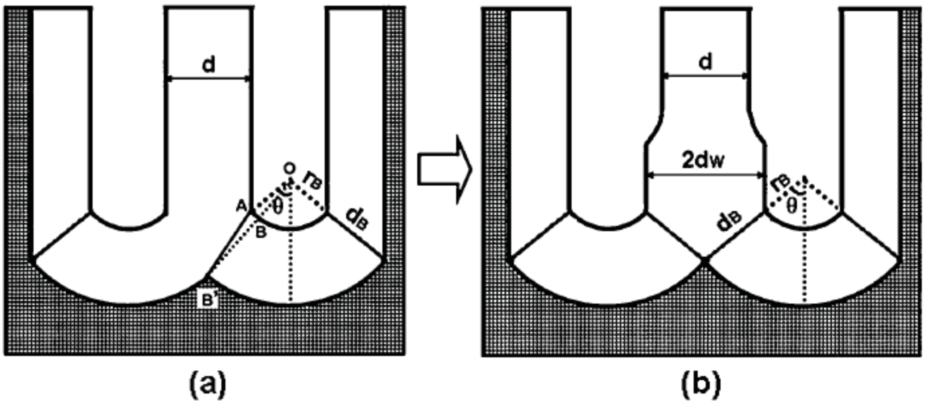

**Figure 2-3**. Schematic drawing of (a) two pores which are too close to each other and (b) their self-adjustment to increase the wall thickness.[5]

When the neighboring nanopores are too close to each other, all the nanopores tend to expand their diameters and confine the development of their neighbors. In this case, the wall thickness still tend to increase to the critical value $2d_W$, but the small interpore distance limit the wall thickness to reach that critical value. In this case, some of the nanopores will terminate the growth to release more space to the expansion of other nanopores. When the interpore distance is very large, even after the fully expansion of the nanopores there still have un-anodized metal left, as discussed above, the dissolution rate of oxide layer at the edge of pore bottom will be increased relative to the center of pore bottom. As a result, the nanopore can splitting into two or even more nanopores to maintain the oxidation rate at all oxide/metal interface are the same.

### 2.1.2. Anodization window and control the pore morphology

For the self-organized anodization condition, ordered alumina nanopore arrays normally were fabricated through anodization in sulfuric acid at 25 V,[8-9] oxalic acid at 40 V,[10-11] and phosphoric acid at 195 V[12-13] with the interpore distances of 63 nm, 100 nm, and 500 nm, respectively.

Nielsch et al.[14] found for the well-defined self-ordered porous alumina, $r/D_{inter}$ always the same for different anodization conditions, where r is radius of nanopore and $D_{inter}$ is interpore distance of neighboring nanopores. The porosity of a hexagonal nanopore array is given by

$$P = \frac{2\pi}{\sqrt{3}}\left(\frac{r}{D_{inter}}\right)^2 \qquad (1\text{-}5)$$

Since $r/D_{inter}$ is constant for self-ordered porous alumina, Nielsch et al.[14] proposed the well-known 10% porosity for the ordered self-organized alumina nanopore arrays independent of the specific anodization conditions.

It is well known that the interpore distance of alumina nanopores is linearly proportional to the applied potential U with a proportionality constant k≈2.5 nm/V: $d_{inter}=kU$, where under optimum conditions $d_{inter}=2d_B$, where $d_B$ is the thickness of the barrier. Therefore, the require applied potential for optimum self-ordering conditions can be wrote as:[14]

$$U=\sqrt{\frac{2\pi}{\sqrt{3P}}\frac{r}{k}} \qquad (1\text{-}6)$$

The diameter of the nanopore, 2r, is affected strongly by the dissolution rate of aluminum oxide layer, which is determined by the pH value in the electrolyte. The lower the pH, the smaller the applied potential threshold for the field-enhanced dissolution at pore bottom. Since $r/d_{inter}$ is constant for self-ordered porous alumina and $d_{inter}=kU$, the low pH value leads to small radius of nanopore and small interpore distance, and small applied voltage is needed for the optimum self-ordering conditions.

Hard anodization is a novel method developed recently to fabricate anodic alumina nanopore membranes with high growth rates by employing a high applied voltage and a high current density.[15-22] For example, hard anodization of alumina nanopores is carried out in oxalic acid at voltages of 100-150 V with current densities of 200-300 mA/cm$^2$, and the growth rate of nanopore film is ~50-70 μm/h. For the hard-anodization process, the interpore distance and pore size are found to be linearly proportional to the anodization voltage, but the porosity of self-ordered anodic alumina films is 3.3-3.4%,[15] which is deviate from the 10% rule.

Therefore, Su et al.[5-6] utilized the equifield strength model to explain the porosity by the relative dissociation rate of water to dissolution of $Al_2O_3$. Consider the hexagonally ordered pores, for the growth of ΔL length of nanopore at Δt, the whole pore bottom just moves down with the shape unchanged, the net change is the increase of ΔL pore wall. Assuming all the oxygen anions created from dissociation of water migrate to the oxide/electrolyte interface, and contribute to the oxidation of aluminum, the total moles ($N_0$) of these oxygen anions in the volume of the newly formed ΔL length of nanopore are:

$$N_0=\left(\frac{\sqrt{3}}{2}a^2-\pi\times r^2\right)\times\Delta L\times D_0 \qquad (1\text{-}7)$$

where a is the length of hexagonal outer shape, r is the diameter of nanopore, and $D_O$ is the density of oxygen anions in $Al_2O_3$. At the same time, oxygen anions are produced with the dissolution of $Al_2O_3$ by water at the oxide/electrolyte interface through reaction 1. The total molar number of aluminum dissolved within $\Delta t$ is $\pi r^2 \times \Delta L \times D_{Al}$, where $D_{Al}$ is the molar density of $Al^{3+}$ in $Al_2O_3$. According reaction 1, the total molar number of oxygen anions obtained by dissociation of water is $(\frac{n}{2})\pi r^2 \times \Delta L \times D_{Al}$, which should equal to the amount of oxygen increased in the alumina nanopore walls. Therefore,

$$N_0 = (\frac{\sqrt{3}}{2}a^2 - \pi \times r^2) \times \Delta L \times D_0 = (\frac{n}{2})\pi r^2 \times \Delta L \times D_{Al} \qquad (1\text{-}8)$$

Since $D_{Al}$:$D_O$=2:3, the porosity of alumina nanopores is

$$P = \frac{2\pi}{\sqrt{3}}(\frac{r}{a})^2 = \frac{2\pi}{\sqrt{3}} \times \frac{3\sqrt{3}}{2\pi(n+3)} = \frac{3}{n+3} \qquad (1\text{-}9)$$

From this relation of porosity with relative dissociation rate of water, Su et al. point out that the 10% rule has no special physical meaning, except that the porosity near 10% (when n=27) is not very sensitive to the variation of n. Moreover, with the increase of electric field and current density, the dissociation rate of water (n) will increase, and the porosity of alumina nanopore will decrease. Therefore, it should not be too surprising when Lee et al. applied high current density and applied voltage during hard anodization leads to very low porosity ~3.9%. From equation 9, this low porosity can be explained by increase the dissociation rate of water number n to 88.

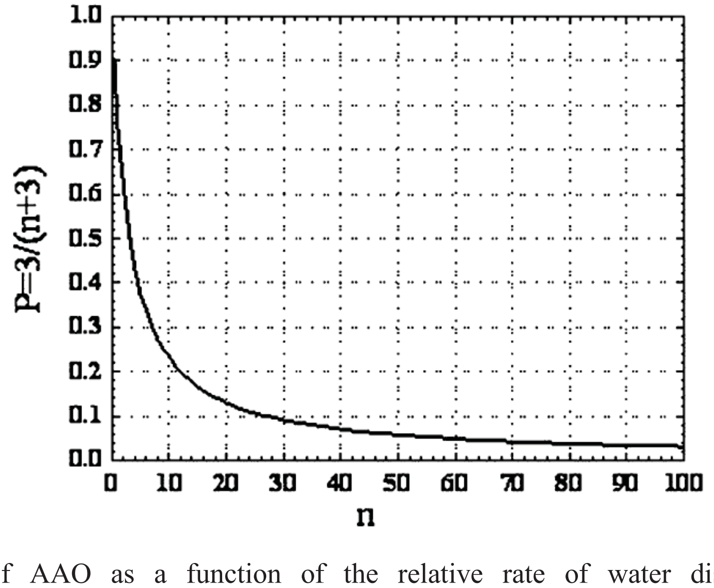

**Figure 2-4**. Porosity of AAO as a function of the relative rate of water dissociation at the oxide/electrolyte interface, n.[5]

### 2.1.3. Pre-pattern Guided anodization

Ordered self-organized porous alumina occurs only for a quite small anodization window with limited ordered domain sizes around just a few micrometers, and the interpore distances of the films are confined to several fixed values. To widen the applications of anodic porous alumina, different pretexturing techniques are used to fabricate an ideally nanochannel on AAO films with very large ordered domain sizes and provide controllable interpore distances. Using nanoimprint lithography (with SiC, $Si_3N_4$ or Ni mold),[23-27] focused-ion-beam (FIB) lithography,[28-32] and holographic lithography lithography[33] to create an highly ordered concaves pattern on the Al surface, and then those concaves in turn guide the subsequent anodization of Al to generate highly ordered AAO templates, which completely eliminate the presence of domain boundaries and obtain large orderly AAO area.

Combination of nanoimprint lithography or focused ion beam lithography with self-assembly anodization obtains alumina nanopore arrays having a hexagonal, triangular, or square arrangement. Nanoimprint lithography and focused ion beam lithography produce hexagonal pre-patterns to guide the growth of highly ordered hexagonal nanopore arrays. Porous anodic alumina with a square arrangement of square nanopore shape can be prepared by using a square array of indentations.[34-36] Similarly, porous anodic alumina nanopore with a graphite structure lattice of triangular pore shape also is synthesized by the guidance of graphite structure nanoimprinted concaves.[36]

Nanoimprinted concave pattern on the electropolished aluminum enlarge the anodizaiton condition for ordered alumina nanopore. In order to obey the 10% porosity rule,[14] self-assembly ordered nanopore arrays only synthesized under limited anodization condition, and the interpore distance is confined at several fixed values: 65, 100, 500 nm. However, under the guidance of imprinted nano-concave, the anodized nanopore remains the arrangement of pre-pattern with different interpore distance. Moreover, the interpore distance of the ordered alumina nanopore arrays can be reduced to $1/\sqrt{3}$ of the lattice constant of the master stamp, if anodized in particular applied potential to form a new pore at the centre of three pre-patterned concaves.[37-39] Ordered PAA with 115 nm interpore distance is obtained by anodizing a 200 nm periodic master pre-pattern at 46 V in oxalic acid. Similarly, an ordered 300 nm interpore distance nanopore arrangement is produced after the anodization of 500 nm interpore distance nano-imprinted concave pattern at 120 V in phosphoric acid.

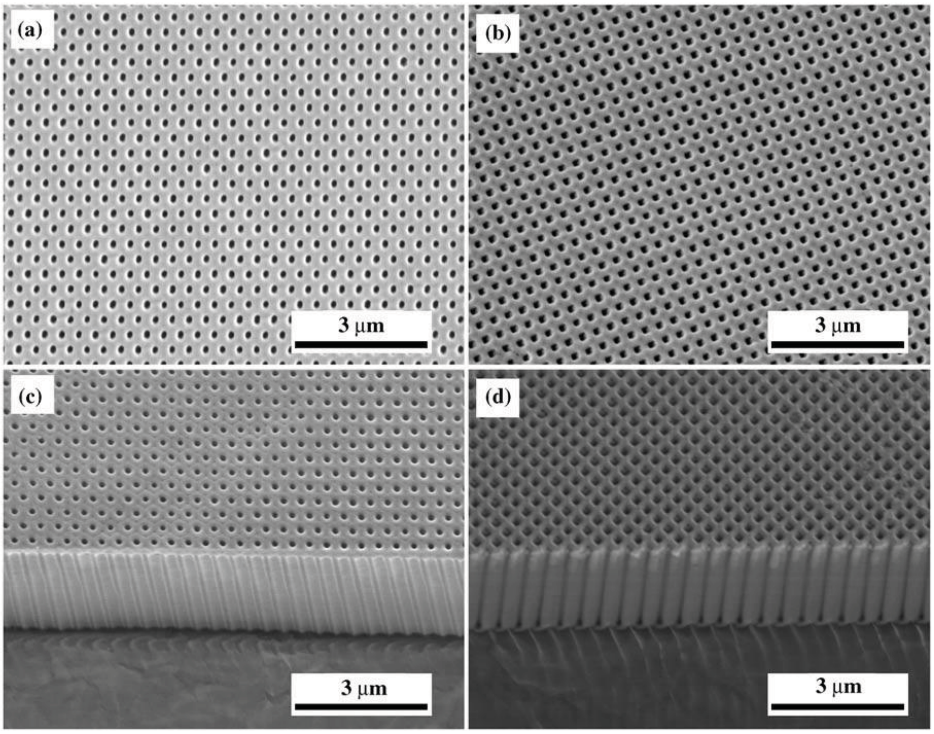

**Figure 2-5**. SEM images of long-range-ordered anodic alumina with a) hexagonal and b) square arrangements of nanopores. c,d) tilt views of the cross sections.[26]

### 2.1.4. AAO with branched structures and modulated internal diameters

Since branched nanopores grown in anodic alumina oxide membranes are promising candidates to synthesis novel nanowires and nanotube, considerable attention has been paid to the fabrication of branched nanopores. Y-branched AAO channels was first fabricated by reducing the anodic voltage by a factor of $1/\sqrt{2}$.[40] This is because that the interpore distance is proportional to the anodization voltage, thus suddenly decrease the applied voltage from 50 V to 35 V result in two small pores branched from the bottom of stem pore. Similarly, after primary stem pores were fabricated by a typical two-step anodization process, the anodization voltage was reduced by a factor of $1/\sqrt{n}$ can obtain create n-branched nanopores (notated as $1\prec n$, where "$\prec$"stands for the junction where the branching takes place, and n stands for the number of branches produced).[41-43] Moreover $1\prec n \prec m$ tree-like nanopore arrays can be obtained by further reducing the anodization voltage by a factor of $1\sqrt{m}$ to generate the third layer of branced pores at the bottom of second layer of branched pores.[41] However, in order to grow ordered the branched nanopores with hexagonal close-packed arrangement, n and m can only choose from 3, 4, and their common multiples and powers, such as 9, 12, and 16. Otherwise, disordered structures can still be generated by channel merging and splitting if prolong the anodization time.[42]

When the nanopores grow on the aluminum surface with concave structure, bifurcation of a single pore into two similar diameter new pores has been observed.[44-47] Due to the growth direction of nanopore perpendicular the concave surface, the space between neighbored nanopores increases. The pores must keep branching in order to maintain the same interpore distance. And the pore diameters stay almost constant because the anodization conditions have not been changed. This is different the above discussed branched nanopores due to the decreasing of applied voltage, which also decreases the interpore distances and the pore diameters.

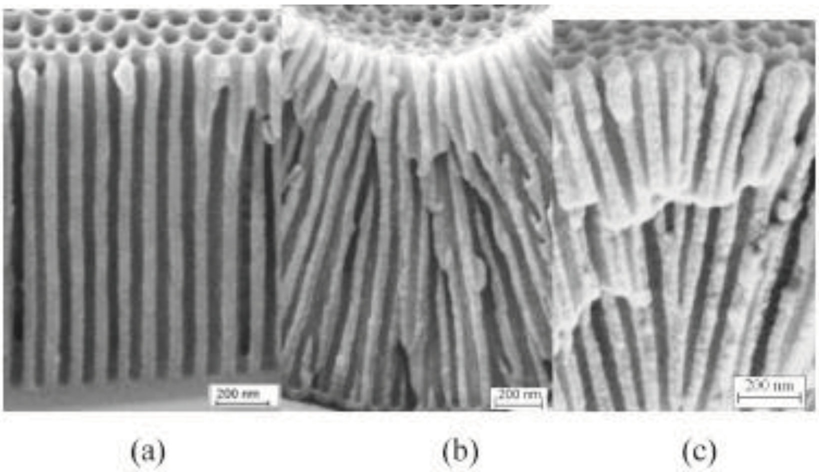

**Figure 2-6**. SEM image of alumina pore structures: (a) parallel pores on a planar surface; (b) diverging pores on a concave surface; (c) converging pores on a convex surface.[44]

The conventional mild anodization in oxalic acid is conducted at a low voltage (40 V) with a small current density (<5 mA/cm$^2$), and the film growth rate is only ~2 μm/h.[11-12] The combination of conventional mild anodization and hard anodization process at different electrolyte has been exploited to tailor the anodic alumina nanopores with modulated pore structures and periodically changed diameters (Figure 2-7).[15-18] Three-dimensional alumina nanopores with different pore periodicity and geometry are obtained by cyclic anodization through applying periodic oscillatory current density with different profiles, amplitudes, and periods to switch between mild anodization and hard anodization.[18]

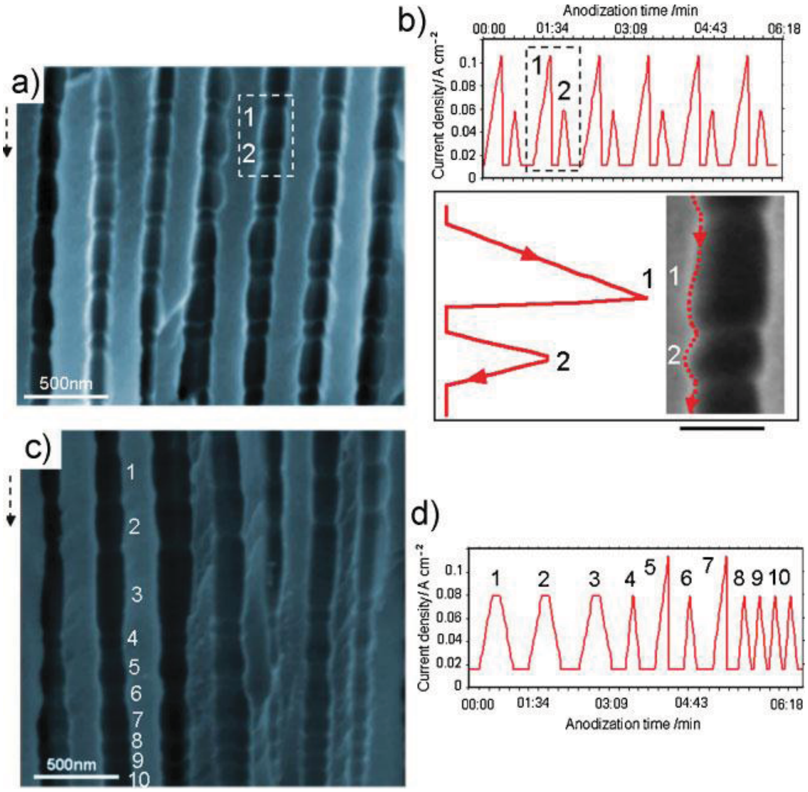

**Figure 2-7**. Fabrication of AAO with multi-modulated pores by cyclic anodization. a–b) SEM image of AAO with double-modulated pores fabricated by a current density profile consisting of two cycles. c–d) SEM images of AAO with multi-modulated pores fabricated using a complex current density profile consisting of 10 cycles with different shapes. [18]

### 2.1.5. Application of AAO

The most important application of AAO is serve as template to fabricate various nanostructures, such as nanodots,[48-49] nanowires,[50-54] and nanotubes.[55-58] The morphology of AAO, such as pore diameter, interpore distance and aspect ratio, can be easily adjusted by the anodization conditions, which facilitate the ability to control morphology of obtained nanostructures by AAO template.

Deposition of nanodot arrays with AAO template normally needs to transfer the AAO thin membrane to the substrate surface. For example, a 300 nm thick alumina nanopore membrane with 60 nm pore size havebeen used to deposit Fe nanodot arrays.[48] First the alumina nanopore membranes was transferred onto MgO substrate as shown in Figure 2-8b; then a 15 nm thick Fe layer was deposited by electron beam on the alumina nanopore membrane; subsequently, the alumina membrane was removed by 10% NaOH solution. This life-off process obtained Fe nanodot arrays with average diameter of 58 nm, which facilitate the research of magnetic characteristic at nanoscale. The main disadvantage of utilizing stiffness AAO membranes as mask to deposit nanodot arrays is large areas of the oxide shadow masks are not in contact with substrate. Voids will exist between the membrane and the substrate surface which leads to an inhomogeneous pattern transfer. Lee et al.[49] proposed that use electrochemical deposition to replicate the AAO master by the flexible Au nanotube membrane, and then utilize flexible Au nanotube membrane as mask to deposit nanodots. The outer diameter of nanotube membrane is determined by the channel diameter of the porous alumina template, and the internal diameter of nanotube is determined by electrodeposition time. Due to the nanotube architecture and a thin interconnections layer at bottom of Au nanotubes, the gold membranes are extremely flexible and can excellently contact with the substrate topography.

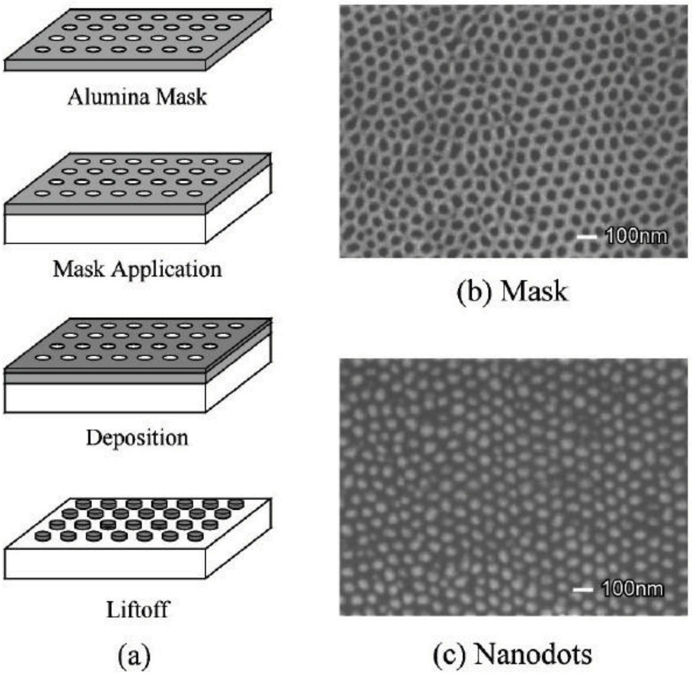

**Figure 2-8**: (a) Schematic of the porous alumina mask deposition technique; (b) top view of porous alumina membrane; (c) Fe nanodot array after the fabrication process.[48]

The most common method to fabricate the nanowire arrays by AAO template is electrodeposition.[50-52] First, free-standing AAO template with both end open is fabricated; then, one end of AAO template is physical deposited with conductive layer as electrode; eventually, the conductive nanowires are obtained by fully filling the AAO template through electrodeposition method. Moreover, the nanowires are grown inside a porous anodic aluminum oxide template by chemical vapor deposition assisted by an electrodeposited metal catalyst at one side of AAO membrane.[53-54]

Carbon nanotubes (CNTs) can be fabricated by applying porous anodic aluminum oxide as template.[55-58] CNTs were fabricated by flowing a mixture of acetylene (5%) and nitrogen (100 sccm) at 550 °C for 50 min. The carbon nanotubes grow at the wall of nanopore. The morphology of carbon nanotubes are determined by the AAO template, and thus were very homogeneous in diameter and length, well ordered, and almost perfectly aligned vertically with respect to the substrate. The field emission property of these ordered monodispersed carbon nanotube arrays shows current density higher than 1 $mA/cm^2$, which meets the requirement for flat panel displays.

Another method to fabricate nanotube arrays through nanoporous alumina template is introduce sol-gel into the nanopores and follow by dry process to form nanotube inside the alumina nanopore.[59] For example, highly ordered $TiO_2$ nanotubes were successfully fabricated by infiltrating the alumina nanopore with sol-gel mixture of $Ti(OC_3H_7)_4$ and ethanol in a 3:1 weight ratio, and then followed by drying the sol-gel at ambient environment with room temperature and approximately 54% relative humidity. Free-standing $TiO_2$ nanotubes eventual obtained by selective chemical etching alumina template in a solution of 3 M NaOH for 13 min.

## 2.2. Anodic $TiO_2$ nanotube arrays

### 2.2.1. Formation of anodic $TiO_2$ nanotubes and the mechanism

Up to now, there are several methods have been exploited to fabricate $TiO_2$ nanotubes, such as AAO template assisted methods (by electrodeposition,[60] sol-gel process,[59, 61] and atomic layer deposition methods[62-63]), hydrothermal method,[64] sol-gel techniques without templates,[65-66] and electrochemical anodization method. Among these methods the electrochemical anodization method is the most common and well developed method to fabricate $TiO_2$ nanotubes with self-organized structures with controlled diameter, interval distance, and length.

So far, self-organized anodic $TiO_2$ nanotubes have been obtained from four different generations of electrolytes. First generation is the dilute HF aqueous electrolyte.[67-69] For example, anodization of Ti foil in a two-electrode electrochemical cell with 0.5% HF aqueous solution at 20 V for 30 min leads to ordered $TiO_2$ nanotubes. However, the rapid rate of $TiO_2$ dissolution by the HF acid limits the maximum achievable nanotube length to ~0.5 µm. In order to reduce the rate of $TiO_2$ dissolution, the second generation electrolytes, buffered aqueous electrolytes (such as KF,[70] $NH_4F$,[71] or NaF[72] along with a buffer solution to control the pH) have explored to overcome that issue. As a result, the maximum length of $TiO_2$ nanotubes can increase to 5 µm. The pH value of the electrolyte greatly affects the rates of oxidation and chemical dissolution, when the pH varying from 1 to 4.5, the maximum nanotube length increases from 0.56 µm to 4.4 µm.[73] Nevertheless, the water content in the aqueous electrolytes still leads to rapid chemical dissolution of the formed $TiO_2$ nanotubes, which limits the formation of high aspect ratio nanotubes. Therefore, the third generation polar organic solvents such as formamide,[74] ethylene glycol,[75] and dimethyl sulfoxide[76] are used with a fluoride-containing species (such as $NH_4F$,[77] HF[76]) to minimum the water content in the electrolytes. With organic electrolytes, the length of $TiO_2$ nanotubes can be as long as several hundred of micrometers.[78-80] The maximum length of $TiO_2$ nanotube arrays reported is over 1000 µm by anodizing thick Ti foils at 60 V in 0.6 wt % $NH_4F$ and 3.5% water in ethylene glycol for 216 h.[81] The above three generations of electrolytes all contain fluoride to dissolve $TiO_2$ barrier layer by formation of water dissolvable $TiF_6^{2-}$ during anodization. The fourth generation of electrolyte is non-fluoride based electrolytes (such as HCl,[82] $HCl/H_2O_2$[83]), which might leads to different mechanisms for the formation of $TiO_2$ nanotubes.

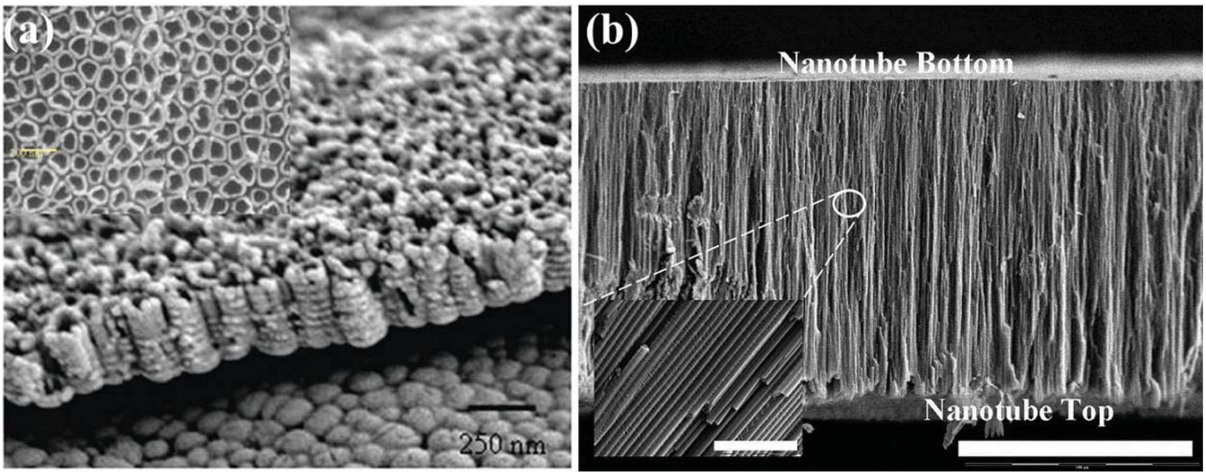

**Figure 2-9**. (a) Cross-sectional SEM image of a 500 nm long first generation nanotube array sample prepared by HF based electrolyte at 20 V. Inset shows top-view image.[68] (b) Cross-sectional SEM image of the freestanding $TiO_2$ nanotube membrane. A close-up of nanotubes marked in a circle is shown as an inset. The scale bars in the main image and inset are 100 and 2 μm, respectively.[79]

The development of the $TiO_2$ nanotubes should be similar as anodic aluminum oxide nanopore as discussed above. During the anodization, Ti is oxidized into $Ti^{4+}$ at the metal-oxide interface and migrates outwards under the applied electrical field. Meanwhile, $O^{2-}$ ions are incorporated in the oxide layer and migrate towards the metal–oxide interface. The $TiO_2$ layer forms due to the interaction of the $Ti^{4+}$ ions with the $O^{2-}$ ions in the electrolyte. The overall reactions for anodic oxidation of Ti can be expressed as:[84-85]

$$Ti + 2H_2O \rightarrow TiO_2 + 4H^+ + 4e^- \qquad (1\text{-}10)$$

At the same time, the $TiO_2$ barrier layer dissolves under the reaction:[85-86]

$$TiO_2 + 6F^- + 4H^+ \rightarrow TiF_6^{2-} + 2H_2O \qquad (1\text{-}11)$$

The two reactions reach a balance at steady state anodization. At the beginning of the anodization, the surface of Ti is covered entirely with a dense and uniform anodic $TiO_2$ layer, since active metal Ti is oxidized instantly at ambient condition. The large volume expansion from Ti to $TiO_2$ (~1.95) result into great compressive stress at the top $TiO_2$ layer, any defects such as impurities, dislocation, grain boundaries, nonmetallic inclusions, and the rough surface of the original oxide layer can lead to a pit growth as an initial step of pore growth. The distribution of the electrical field in the $TiO_2$ layer, however, is strongly correlated with the surface morphological fluctuations (more pronounced fluctuations lead to more localized electrical field). Due to the localized field-assisted dissolution of the oxide layer at the pit bottom, $TiO_2$ nanopores grow at the pit locations and reach a steady-state. During the anodization, the diameter and interpore distance of $TiO_2$ nanopores will self-organize to be proportional to the applied voltage: $D=2f_{growth}U$,[87-88] where $f_{growth}$ is the growth factor for anodic oxides, 2.5 $nm \cdot V^{-1}$ for $TiO_2$, and $U$ is the applied potential. When the interpore distance of the two neighboring nanopores is smaller than $D=2f_{growth}U$, the $TiO_2$ nanopores tend to expand the diameter and repel their neighbors, and the interpore distance will increase according to the equifield strength model. When interpore distance of the neighboring nanopores is larger than $D=2f_{growth}U$, and even when the nanopores are fully expanded, there are still un-anodized metallic Ti left between the nanopores, then a new nanopore will develop between them. As a result, the self-organized anodic titanium oxide will have nanopore close to each other with interpore distance around $D=2f_{growth}U$.

The mechanism for the formation of $TiO_2$ nanotubes is still unknown, and the driving force for the formation of nanotubular but not nanoporous anodic titanium oxide arrays still remains an unsolved problem. Up to now, there are four different models trying to explain the nanotubular structures. First, Su et al. proposed that oxides at the junction areas suffer a high degree of localized dielectric breakdown, which produces a large number of voids at the inter-pore areas and separates the neighboring $TiO_2$ nanotubes (Figure 2-10).[89] For the non-aqueous glycerol solution with very low water content, the small localized dielectric breakdown leads to the formation of anodic $TiO_2$ nanopores instead of nanotubes. Second, Grimes et al.[67, 90] proposed that the un-anodized metallic Ti between neighboring pores can undergo the same oxidation and field assist dissolution process, thus voids develop between the nanopores, and the growth of these voids lead to the formation of gaps between the $TiO_2$ nanotubes (Figure 2-11). However, it cannot explain why these voids leads to formation of gaps but not leads to the development of new nanopores. It also cannot explain why there will have un-anodized metallic Ti left between neighboring pores. Third, Schmuki et al.[88, 91-92] attributed the nanotube separation to the dissolution of the fluoride rich outer shell of nanotube walls (Figure 2-12). According to the TEM structure of $TiO_2$ nanotubes, the anodic $TiO_2$ nanotube has double layer structure of the tube wall. Schmuki et al. proposed the outer shell of the tube wall is fluoride rich layer. Due to small radius $F^-$ ions compare to $O^{2-}$ ions, the diffusion rate of $F^-$ ions is faster than $O^{2-}$ ions, a significant amount of $F^-$ ions is present at the tube outer wall boundaries, which facilitates the dissolution of the boundaries by forming water-soluble $TiF_6^{2-}$ complexes. The change from nanoporous to nanotubular $TiO_2$ structure is dependent on the solubility of the cell boundaries. However, the formation of anodic $TiO_2$ nanotubes in non-fluoride based electrolytes leads to the effect of fluoride rich outer shell into question. Fourth, Su et al.[4, 93-94] proposed that, during anodization, the Ti substrate are anodized both by $O^{2-}$ ions to form the $TiO_2$ inner shell and by $OH^-$ ions to form titanium hydroxide outer shell (Figure 2-13). The volume shrinkage due to the dehydration of the titanium hydroxide outer shell leads to the formation of gaps between the $TiO_2$ nanotubes. They proposed that the outer shell of the tube wall is the titanium hydroxide. Because the temperature-dependent Fourier transform infrared (FTIR) spectroscopy show the anodic $TiO_2$ nanotubes dried at 120°C have a peak at 1630 $cm^{-1}$ and a broad band between 3000 $cm^{-1}$ and 3700 $cm^{-1}$, respectively, which corresponding to the structural of $OH^-$. The peak intensities decease with the thermal treatment at 200°C and disappear after thermal treatment at 300°C. However, they cannot explain why the titanium hydroxide layer can form at the nanotube outer wall; and FTIR only prove the anodic $TiO_2$ nanotubes contain hydroxide structure, it cannot prove the hydroxide accumulates at the tube outer shell. Therefore, the reason for the formation of gaps between the $TiO_2$ nanotubes is still not resolved.

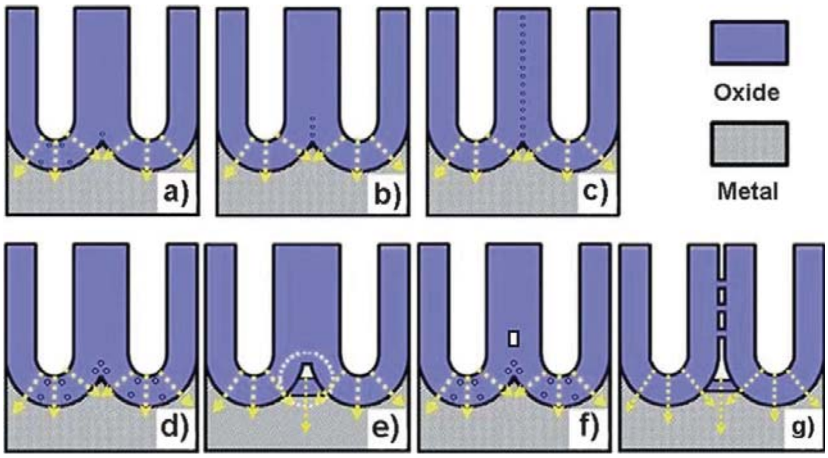

**Figure 2-10**. Schematic diagram illustrating the formation of nano-porous anodic oxides when the degree of localized dielectric breakdown is low (a–c), and the formation of nanotubular anodic oxides with ridges between neighbouring tubes when the degree of localized dielectric breakdown is high (d–g). The arrows indicate the potential inward moving directions of oxygen anions. [89]

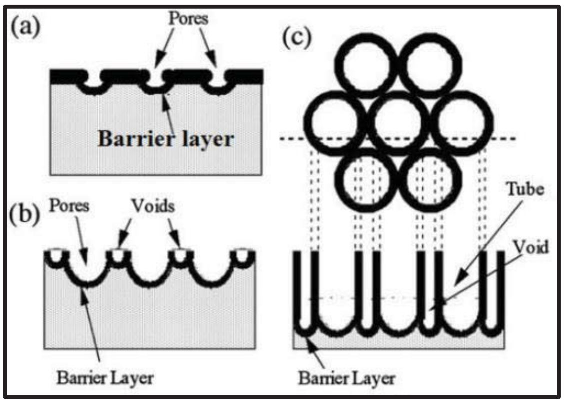

**Figure 2-11**. (a) Growth of pores, (b) metallic parts between pores undergo oxidation and field assisted dissolution, (c) fully developed nanotubes with a corresponding top view.[67, 90]

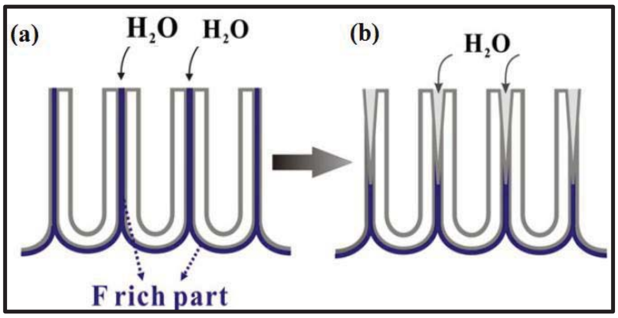

**Figure 2-12**. Schematic illustration of formation of nanotubes from a porous oxide layer by selective dissolution of fluoride rich layers at the cell boundaries of anodic porous layers.[91-92]

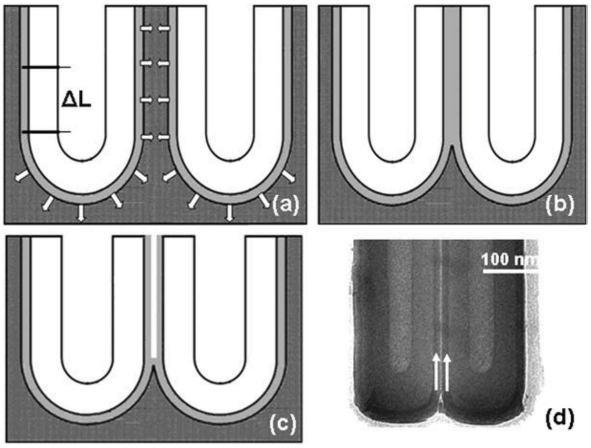

**Figure 2-13**. (a) Two adjacent nanotubes move closer to each other by expanding diameter. (b) The expansion stops when they touch each other. (c) Volume shrinkage due to dehydration process of titanium hydroxide at pore outer shell obtains nanotubes. (d) The corresponding TEM image of such twin nanotubes.[4, 93-94]

### 2.2.2. Parameters influence the structure of anodic $TiO_2$ nanotubes

The growth of the anodic $TiO_2$ nanotubes is based on the balance between the $TiO_2$ dissolution rate and $TiO_2$ oxidation rate. As a result, the parameters that can affect the $TiO_2$ dissolution rate or $TiO_2$ oxidation rate will influence the structures of the anodic $TiO_2$ nanotubes, such as pH value, applied voltage, conductivity of electrolyte, water content, temperature, and anodization time.

PH value of electrolyte affects both the behavior of the $TiO_2$ oxidation rate and chemical dissolution.[73,95] With the increase of pH the rate of chemical dissolution decreases. As a result, the $TiO_2$ oxidation rate is faster than dissolution rate, and longer nanotubes can be formed in higher pH solution. For example, when anodize Ti foils at 25 V in the electrolyte solutions containing 0.1 M KF and different PH value, with pH increasing from strong acidity (pH <1) to weak acidity (pH 4.5), nanotube length increased from 0.56 μm to 4.4 μm.[73]

The applied voltage influences the anodization rate, the $TiO_2$ nanotube diameter, and the nanotube length. During the anodization, the diameter of self-organize $TiO_2$ nanotubes is proportional to the applied voltage: $D=2f_{growth}U$. Therefore, the diameter will increase with the increase of applied voltage. When applied voltage increase, the enlarged electric field increases both the oxidation and dissolution rates, the former is expected to increase faster than the latter.[5] This can be understood as follows. The inward oxygen ionic current $j$, which is related to the electric field $E$ cross the barrier layer, determines the oxidation rate: $j = j_0 \times e^{kE}$,[5] where $j_0$ and $k$ are material dependent constants. Therefore, the oxidation rate increases exponentially with the electric field. However, the dissolution rate of $TiO_2$, which is affected by the electric field through polarization and impairment of the Ti-O bond, increase slowly as the electric field decreases. As a result, the increase of applied voltage leads to oxidation faster than dissolution rates, which leads to faster nanotube growth rate and longer nanotube length.

The low conductivity of the organic electrolytes leads to the IR-drop effects, and the effective applied voltages of the electrode is $U_{eff}=U_{applied}-IR$, where R is the resistivity of the electrolyte and I is the current.[91] As a result, even though the diameter of the nanotubes is still linearly controlled by the applied voltage, different electrolytes (such as aqueous and non-aqueous electrolytes) have different slope of voltage dependence as shown in Figure 2-14. During the anodization, the conductivity of the electrolyte changes, and thus the variations of the tube diameter are happened for longer anodization times.[96]

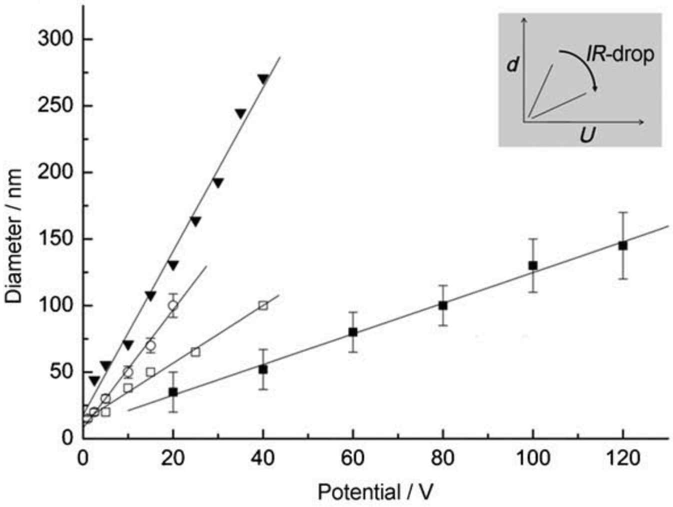

**Figure 2-14**. Voltage dependence of the tube diameter for different electrolytes: ○ water-based, ▼ glycerol/$H_2O$ 50:50, □ glycerol, ■ ethylene glycol.[91]

Water content in the electrolyte affects the nanotube growth rate and the chemical etching speed of the nanotubes, which influences the morphology of anodic $TiO_2$ nanotubes. The effect of water content is two-fold: it is required for the formation of oxide at tube bottom, but it also accelerates the dissolution of the nanotube layer. When Ti foil was anodized in anhydrous ethylene glycol with 0.2 wt% $NH_4F$ at 20 V, a minimum amount of 0.18 wt% water addition was required to form a well ordered $TiO_2$ nanotubular arrays.[97] When the water content is very low, the formation of ordered $TiO_2$ nanoporous structures can be observed.[98] For the glycerol electrolyte containing 0.2 M $NH_4F$ and differing water contents (1, 2.5, 5, 10, 25, and 50 vol%), the nanotubular structures can be formed. Moreover, with the increase of the water contents, the internal diameter, outer diameter, and barrier layer thickness are increased, while the length of the nanotubes is decreased.[88] The enlarged internal diameter and the reduced of the tube length are ascribed to the faster increase of dissolution rate when water content increases. When the water content increases, the conductivity of organic electrolyte increases, and this weakens the IR-drop effect on the electrolyte. As a result, the outer diameter and barrier layer thickness are increased due to the increased applied voltage on the oxide layer.

The temperature alters the ion diffusion rates during the anodization, and change the morphology of anodic $TiO_2$ nanotubes. $Ti^{4+}$ ions migrate from metal-oxide interface towards electrolyte, and $O^{2-}$ and $OH^-$ ions migrate from electrolyte-oxide interface towards the metal-oxide interface. The increase of temperature will facilitate the interaction of the $Ti^{4+}$ ions with the $O^{2-}$ ions and increase the oxidation rate. Moreover, the high temperature also increases the hydrolysis rate of water to increase the concentration of $O^{2-}$ and $OH^-$ ions. The dissolution rate of the $TiO_2$ oxide layer also is increased by the high temperature. As a result, the nanotube internal diameter and length will increase with the increase of temperature. But the interval distance maintain unchanged when temperature is varied. For example, when Ti was anodized in 0.5 wt% $NH_4F$ and 1 vol% HF ethylene glycol at 60 V for 1 h, the nanotube internal diameter and the nanotube length increased with the increase of the reaction temperature from -5 to 40 °C, from 37 to 138 nm, and from 0.92 to 7.28 μm.[95]

Anodization time also can influence the structure of the anodic $TiO_2$ nanotubes.[91, 95] The length of the nanotube increases with the anodization time. At the same time, the anodic current density decreases with the anodization time, because the local concentration of electrolyte at the tube bottom is decreased when the anodization time is prolonged. As a result, the increase rate of the nanotube length is reduced during the anodization. Moreover, the top layer of the as-formed $TiO_2$ nanotubes is chemically dissolved by the electrolyte during anodization. When the anodization rate is balanced with the chemically dissolution rate of nanotubes, the length of the $TiO_2$ nanotubes maintain the same even for longer anodization time. Due to the dissolution of the as-formed $TiO_2$ nanotube wall and decrease of anodization rate at bottom, during anodization the diameter of the nanotube at the top increase and the diameter of nanotube at bottom decrease, and the V-shape of internal nanotube diameter forms.[92, 99]

### 2.2.3. Ordered $TiO_2$ nanotubes and advanced geometries

For traditional one-step anodization in different electrolytes can only obtain disordered $TiO_2$ nanotube arrays. Similar to the anodic aluminum oxide, two-step anodization have been exploited to generate anodic $TiO_2$ nanotubes with ordered arrangement.[100-102] The long time first step anodization leads to self-organized $TiO_2$ nanotubes at the bottom of tube. After peeling off the $TiO_2$ nanotubes generated in first-step anodization, the well-ordered footprints of nanotubes serve as seeds to guide the growth of ordered $TiO_2$ nanotubes during second-step anodization, which carried out at the same conditions with same electrolyte and applied voltage as first anodization. The electropolishing before the anodization can further increase the order of the $TiO_2$ nanotube arrays.[43] Modified two-step anodization was also exploited to obtain more complicated structures. When the applied voltage in the second-step anodization was lower than in first-step anodization, lotus-root-shaped nanotubes with several smaller nanotubes contained in each footprints was obtained.[102]

Bamboo-like $TiO_2$ nanotubes can be obtained by voltage pulsing between two different levels. Alternating voltages in the same anodization electrolyte, with a sequence of high voltage (120 V for 1 min) and low voltage (40 V for 5 min), led to alternating growth of tubes and the formation of a compact layer.[103-104] When the applied voltage suddenly reduces into small value, the electric field will be dramatically decreased, and the growth of nanotube will stop. Instead, a compact layer will grow at the outer wall nanotubes. As a result, $TiO_2$ nanotubes with bamboo-like features were achieved. The spacing between the bamboo rings can be controlled by changing of the holding time at 120 V, such as the spacing was reduced from 200 nm to 70 nm by reducing the holding time at 120 V from 2 min to 30 s. The bamboo ring thickness can be adjusted by changing the holding time at 40 V.

When the anodization voltage was reduced from 120 V to 40 V and maintained at 40 V for a long period of time, the large truck nanotubes diverged into several small branched nanotubes.[47] However, the fabrication of hierarchically branched $TiO_2$ nanotubes with controlled branch numbers, nanotube diameters, and multiple layers have not been achieved. For anodic $TiO_2$ nanotubes, double-layer nanotube arrays with branched nanotubes growing underneath the truck nanotubes are obtained by anodization at the same applied voltage but in different electrolytes. For example, branched nanotubes were created by first anodization in a HF aqueous electrolyte, followed by anodization in a glycerol/$NH_4F$ mixture.[105] Due to the different IR-drop effects of aqueous and organic electrolytes, the effective voltages on the Ti foils change, which change the diameter of the anodized nanotubes. However, the diameters of the branched nanotubes and the number of branches were hard to control.

Double-walled $TiO_2$ nanotubes have been achieved by thermally annealing the as-anodized $TiO_2$ nanotube, whose oxide wall consists of two different regions: an outer fluoride-rich shell of the tube and the inner carbon-rich shell of the tube.[92] When annealing the samples up to 500°C with a heating rate of 1 °C/s, the inner shell and outer shell separate into two clearly visible layers due to the thermally decomposition of the carbon-rich layer into nanoparticulated inner tube wall. The outer shell remains compact, while the inner shell becomes porous. At the meantime, the nanotube is converted into a crystalline anatase structure during annealing. The structure of these double-walled $TiO_2$ nanotubes is dependence on the annealing conditions, espectively on the temperature ramping speed and holding time.

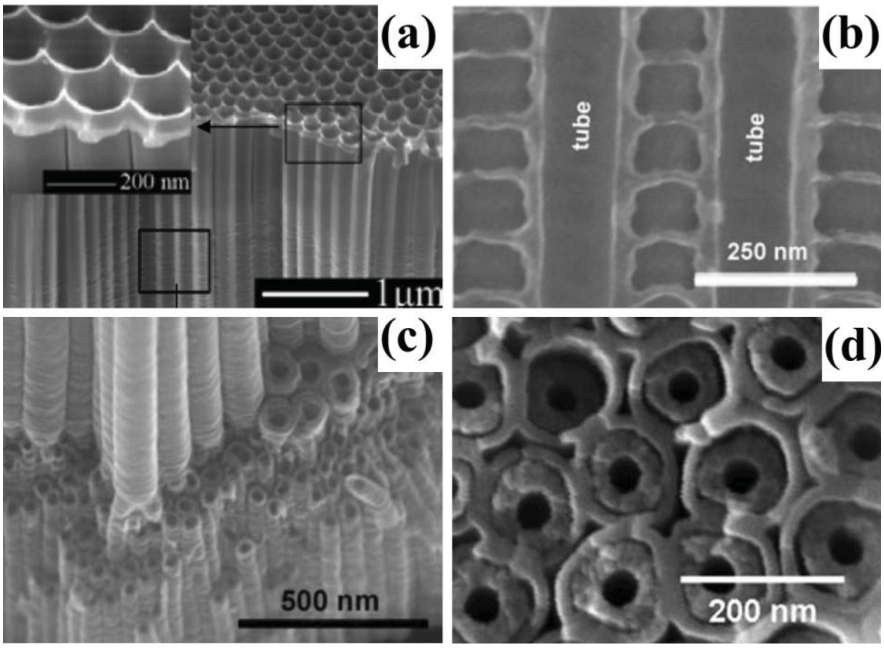

**Figure 2-15**. (a) $TiO_2$ nanotubes generated in the second-step anodization, the inset is the enlarged image.[45] (b) Bamboo-type tubes, grown under AV conditions, with a sequence of 1 min at 120 V and 5 min at 40 V. (c) Tilted cross section of a double layer formed by one AV step, first at 120 V (6 h) and then at 40 V (2 h).[47] (d) Double-walled $TiO_2$ nanotubes annealed to 500 °C with a heating rate of 1 °C/s.[92]

### 2.2.4. Annealing of $TiO_2$ nanotubes

The XRD measurement in Figure 2-16a shows the as-prepared $TiO_2$ nanotubes are amorphous, and the anodized sample only have peak for Ti substrate.[106-107] However, the annealing under oxidizing conditions in air or $O_2$ can convert the amorphous into anatase or rutile structures.[108] Detailed XRD investigations indicate that significant conversion of amorphous nanotubes into anatase begins at around 250 °C.[50] With the increase of temperature, the concentration of anatase structure increases. At annealing temperatures above 450 °C, the rutile phase starts to appear, and the rutile peak intensities are increased with further increase of annealing temperature, which indicates the enhance of the quantity of rutile crystallized structures. Interestingly, when the annealing time is prolong from 2.5 h to 20 h, the anatase intensity significantly increase even annealing at 250 °C, which can be used to convert the amorphous nanotubes into anatase just with low temperatures. And the rutile structures also appear when annealing at 350 °C for 20 h. Moreover, by annealing in $O_2$-containing atmospheres, a considerable new rutile layers underneath the nanotube bottoms are formed by direct oxidation of the titanium substrate. The thickness of this rutile layer increase with the annealing temperature. At 300-450 °C this rutile layer typically is 20-100 nm, while it can reach micrometers thickness at higher temperature.

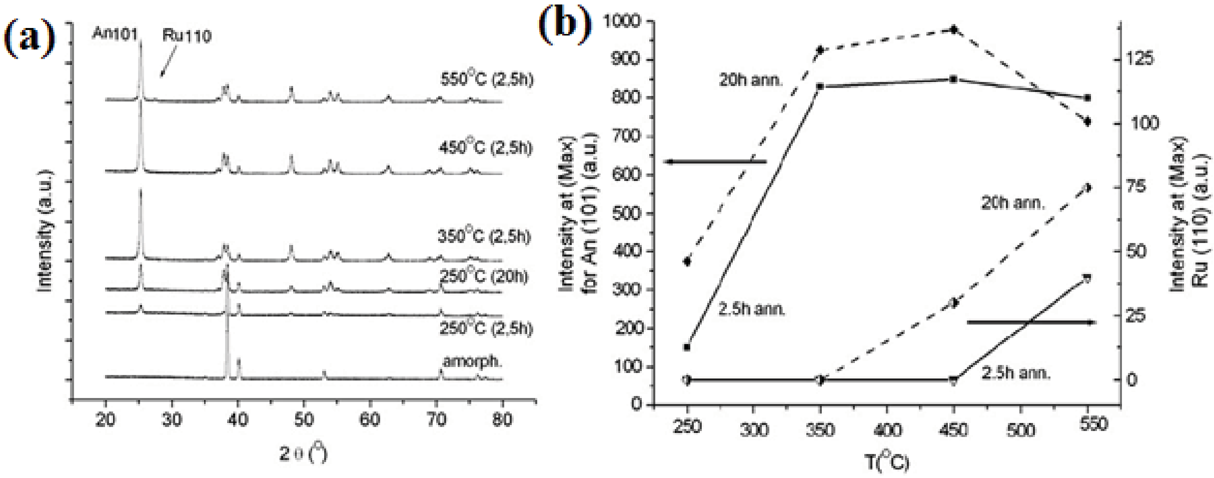

**Figure 2-16**. (a) XRD patterns of 7 μm long $TiO_2$ nanotubes annealed at different temperatures for 2.5 h annealing time. (b) Plot of the peak intensity for the anatase (1 0 1) and rutile (1 1 0) versus the temperature for 2.5 h and 20 h annealing.[107]

The thermal annealing treatment not only affects the crystal structure but also affects the conductivity of the $TiO_2$ nanotubes.[50] By variation of the thermal annealing conditions the conductivity of the $TiO_2$ nanotubes can be changed over several orders of magnitude. As shown in Figure 2-17, when temperature is low, resistance of the nanotube layers increases with the increase of annealing temperature, this can be attributed to the loss of incorporated water and fluoride. When the annealing temperature is higher than 250 °C, the resistance decreases rapidly due to the formation of crystal anatase structures. However, the conversion of $TiO_2$ nanotubes into low conductive rutile structures at high temperature increases the electrical resistance. And the formation of additional rutile layer by direct oxidation Ti metal further increase the resistance.

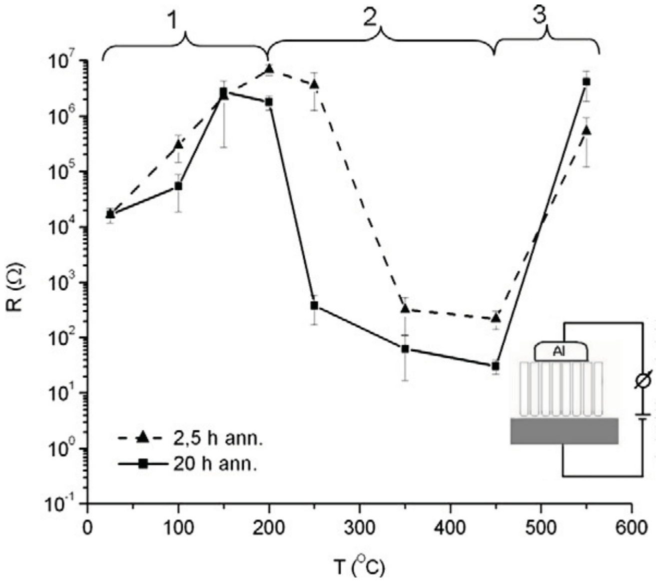

**Figure 2-17**. Electrical resistance as a function of annealing temperature for 7 μm long nanotubes for 2.5 h and 20 h annealing time. The inset shows the schametic of 2-point measurement.[107]

The nanotube morphology also strongly depends on the ramping rate, and single-walled, double-walled, or fused membrane structures can be obtained for the $TiO_2$ nanotubes anodized in ethylene glycol.[92] As mentioned above, when annealing the as-formed $TiO_2$ nanotubes at 500°C with a heating rate of 1 °C/s, the carbon-rich layer inner tube shell decomposited into nanoparticle layer, the double-walled tube obtained due to the separation of inner shell and outer shell. However, the annealing procedure with a heating rate of 25 °C/s leads to a single nanotube wall consist of crystallites with diameters in the range of 10–50 nm. Most remarkably, a more rapid heating rate of 50 °C/s result into to a complete fusion of $TiO_2$ nanotubes into a highly ordered porous membrane.

### 2.2.5. Filling and Decoration

For $TiO_2$ nanotubes, several methods for filling and decoration with different foreign materials (conductive metal, oxides, semcoductor) have been developed.

Similar to the anodic aluminum nanopores, the versatile method should be electrodeposition of foreign materials inside the $TiO_2$ nanotubes. However, the electrodeposition method is difficult to achieve for $TiO_2$ nanotubes, due to the $TiO_2$ is an n-type semiconductor and the surface and the bottom of the $TiO_2$ nanotubes are equally conductive. [109-112] During electrodeposition, the materials preferentially deposit at the entrance of the nanotubes, because this region is favored by diffusion. As a result, the deposition preferentially happens on top of the layers rather than at the bottom of the nanotubes, which leads to the clogging of the nanotubes before the insides can be completely filled. First method to overcome this issue is increase the conductivity of the tube bottom by the self-doping reduction of $Ti^{4+}$ to $Ti^{3+}$, and then electrodeposits conductive materials into the nanotubes.[109-110]

Second method to overcome the electrodeposition issue is using the dipping and deposition technique as shown in Figure 2-18.[111] The main reason of depositing materials at the entrance of the $TiO_2$ nanotubes is that diffusion makes deposition at the bottom of the nanotubes less favorable than deposition at the entrance of the nanotubes. As a result, a thick layer of deposited materials (such as CdTe in this case) cover on the top of nanotubes before significant portion of the internal area is covered. Therefore, Seabold et al. [111] utilize capillary forces to fill the pores of the $TiO_2$ tubes by dipping them in an electrolyte. The $TiO_2$ electrode is then transferred into a new inert supporting electrolyte without any deposition ions. Immediate electrodeposition after immersion the $TiO_2$ electrode into this electrolyte results in deposition of only occurs inside the nanotubes. The repeating time of this procedure can be used to control the thickness of materials deposited in the tubes.

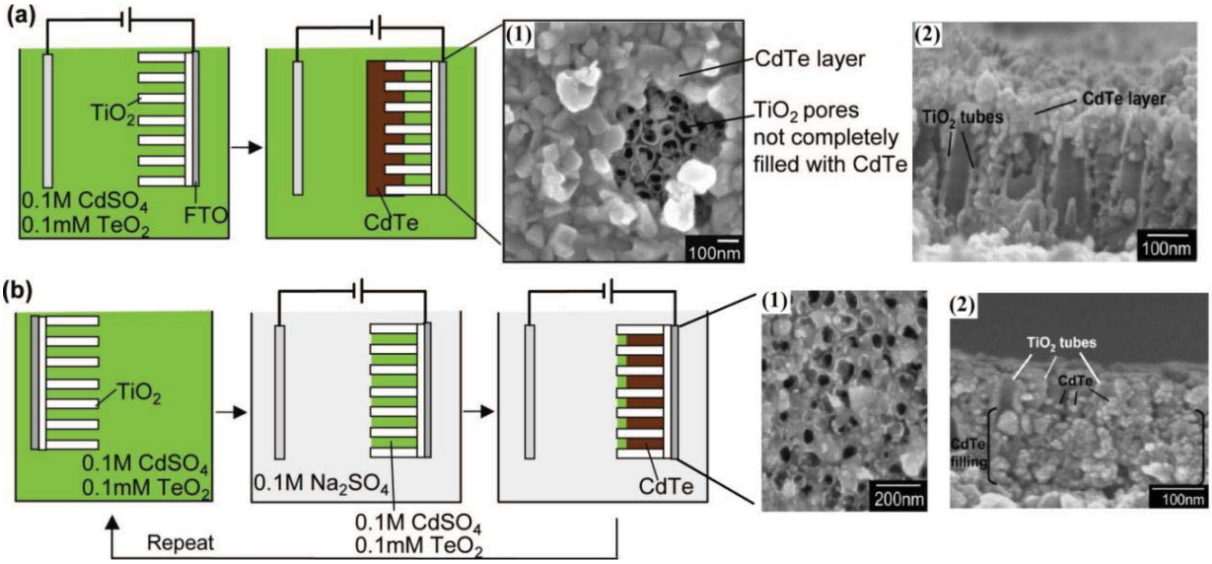

**Figure 2-18**. Illustration of (a) the regular electrodeposition method and (b) the newly developed dipping and deposition technique. Inset 1 and 2 is the top and side view SEM image of deposited materials, respectively.[111]

Third method is the using a potential cycling technique.[113] For example, electrodeposition of $MoO_3$ in the $TiO_2$ nanotube layers was carried out with a three electrode setup in 0.05M $(NH_4)_6Mo_7O_{24}$ via cycling from 0 to -0.7 V at a step rate of 0.02 V/s. It is very important to keep the potential at 0 V for 5 min to relax the electrolyte, and therefore the ion concentration inside the nanotube can increase to the same outside the nanotubes. As a result, the electrodepsition rates at the nanotube wall and bottom are always uniform, and homogenous $MoO_3$ coating can be achieved. Moreover, the coating thicknesses are controlled by the number of cycles and the thicknesses range from a few nanometers to complete filling of the nanotubes can be obtained.

Fourth approach is to obtain free-standing $TiO_2$ nanotubes with both-end open, then deposits electrode on one side by e-beam evaporation or coating Ag sol, and follows with electrodeposition conductive materials into the nanotubes. [114-117] For the free-standing $TiO_2$ nanotubes, several methods have been used to modify the barrier layer at the tube bottom, for example, chemically dissolving the barrier layer through immersing only the closed bottom side of the membrane into 5 wt% $NH_4F$-1M $H_2SO_4$ with the hold of a steel net;[114-115] exposing the wet nanotube membrane closed side to HF vapors;[116] covering the nanotube top by a protective layer and dissolving the barrier layer in a 0.5 wt% oxalic acid solution.[117]

In addition to the electrodeposition method, the hydrothermal method has been successful used to decorate $TiO_2$ nanotubes.[118-119] Ultrasonic pretreatment of $TiO_2$ nanotube with a nickel salt solution followed by hydrothermal process at 180 °C for 18 h in 0.1M $Ni(Ac)_2$ aqueous solution can introduce the NiO nanostructure inside the nanotubes.[118] On infiltrating $TiO_2$ nanotubes with $TiCl_4$ solution followed by hydrothermal synthesis, a uniform dense layer of 10 nm size $TiO_2$ nanoparticles were formed on the side walls of $TiO_2$ nanotubes.[11] This infiltration process can be repeated several times to achieve a thick nanoparticle layer on the N nanotube walls. As a result, compared with bare $TiO_2$ nanotubes, the surface area and dye loading can be significantly increased to improve the dye sensitized solar cell efficiency.

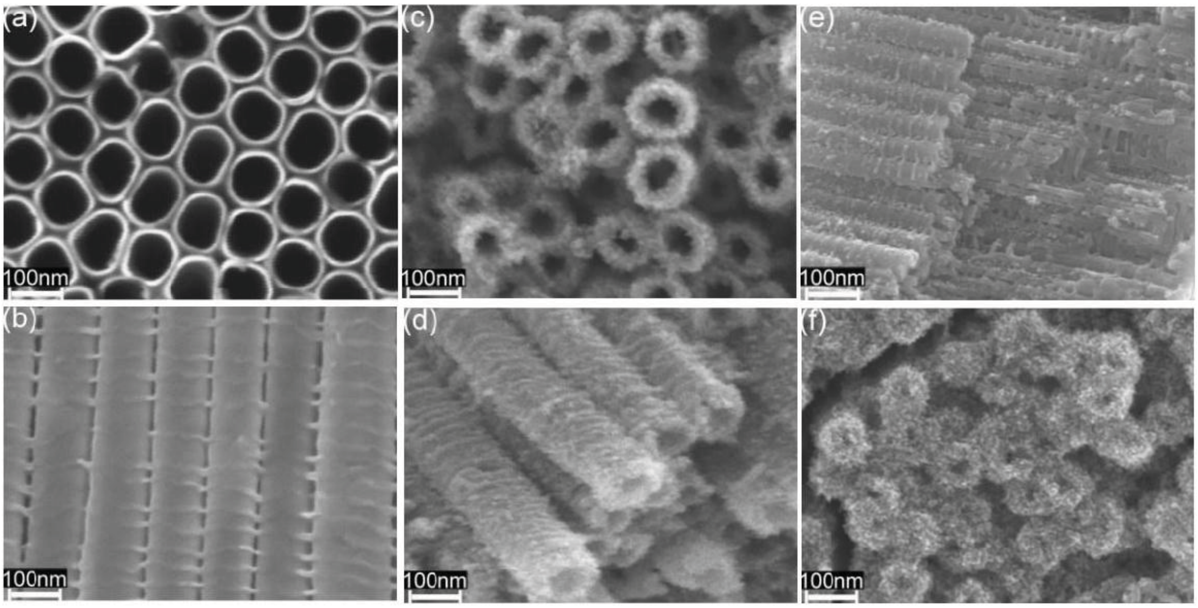

**Figure 2-19**. SEM images of $TiO_2$ nanotubes grown by electrochemical anodization: (a) top view and (b) side view. Nanoparticle and nanotubes mixed structure after one-cycle infiltration: (c) top view, (d) tilt view and (e) inside view of the split nanotubes; (f) Nanoparticle and nanotubes mixed structure after two-cycle infiltration.[119]

The close space sublimation technique has been investigated to deposit semiconductor into the $TiO_2$ nanotubes.[120] As shown in Figure 2-20a, the anodized $TiO_2$ nanotubes with the opening end facing down toward the CdS powder were placed in a semi-enclosed quartz tube, which located at the center of quartz tube furnace. The pressure was maintained at 500 Pa by vacuum pump. The temperature of the furnace was rapidly increased to 500 °C and held at 500 °C for 30 min, then was naturally cooled down to room temperature. CdS sublimated at 500 °C and decomposed to Cd vapor and $S_2$ vapor, which infiltrate into the $TiO_2$ nanotubes. When the temperature decreases, the vapor mixture undergoes a fast condensation reaction process and recombines to form crystalline CdS nanocrystalline inside the $TiO_2$ nanotubes. Figure 2-20c is the TEM image of the $TiO_2$ nanotubes after the deposition of CdS nanoparticles, and it clearly shows that 20 nm CdS nanoparticles have been deposited along the tube. The high resolution TEM image in left inset indicates the CdS nanoparticles are well-crystallized with 0.358 nm spacing.

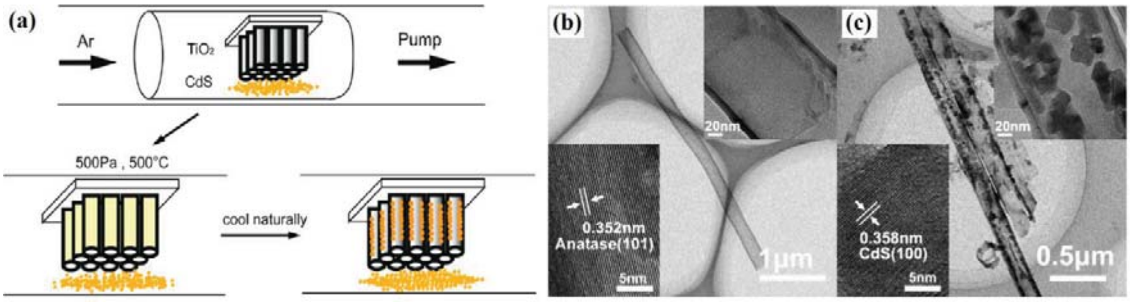

**Figure 2-20**. (a) Schematic of synthesis CdS nanoparticles inside $TiO_2$ nanotubes by close space sublimation technique. TEM image of $TiO_2$ nanotubes (b) before deposition and (c) after deposition of CdS nanoparticles.[120]

### 2.2.6. Application of $TiO_2$ nanotubes

#### 2.2.6.1 Conversion of $TiO_2$ nanotubes

In recent years, $TiO_2$ nanotubes have been successfully transformed into ferroelectric nanotube $MTiO_3$ (M=Sr, Ba, Pb) by hydrothermal treatment or annealing method (as shown in Figure 2-21). During the hydrothermal reaction, $TiO_2$ nanotubes serve as the Ti source, and the $M_3(NO_3)_2$ or $M(OH)_2$ serves as the M source.[121-126] Moreover, the TiO2 nanotube arrays serve as templates for their hydrothermal/annealing conversion to ferroelectric nanotube structures. For example, $BaTiO_3$ nanotubes can be obtained by hydrothermal treatment of the $TiO_2$ nanotubes in 0.05 M barium hydroxide solution at 150°C for 2 h.[123] The Ti-O bonds on the $TiO_2$ nanotubes are broken by hydrolytic attack to form soluble $[Ti(OH)_6]^{2-}$: $TiO_2 + 2OH^- + 2H_2O \rightarrow [Ti(OH)_6]^{2-}$, and $SrTiO_3$ is formed by the reaction: $Sr^{2+} + [Ti(OH)_6]^{2-} \rightarrow SrTiO_3 + 3H_2O$.[122, 125] $PbTiO_3$ nanotubes not only synthesized by hydrothermal treatment in 0.001 M lead acetate solution (Figure 2-21a), but also fabricated by annealing method. For the annealing method, Pb nanowires are first electrodeposited into the $TiO_2$ nanotubes and then the as-deposited samples are annealed in oxygen flow at 550°C for 2 h.[110] The reaction for formation of $PbTiO_3$ nanotubes is given as:

$$2TiO_2 + 2Pb + O_2 \rightarrow 2PbTiO_3 \qquad (1\text{-}12)$$

The structure of ferroelectric nanotubes will be determined by the structure of $TiO_2$ nanotubes, such as diameter, length, and interpore distance. These low dimension ferroelectric nanotube structures provide the opportunity to investigate the size influence on piezoelectric effect in nanoscale. The size constraint imposes additional stress on the nanotube that might influence the domain arrangement and piezoelectric effect.

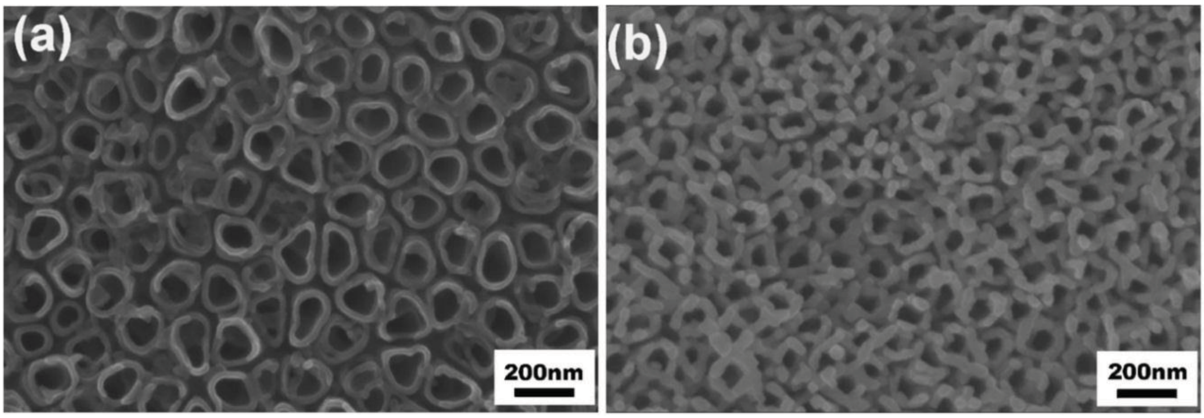

**Figure 2-21**. (a) SEM image of anodic $TiO_2$ nanotubes template grown at 20 V for 2 h. (b) SEM image of $PbTiO_3$ nanotube arrays obtained by hydrothermal method.[124]

### 2.2.6.2 Dye sensitized solar cells based on $TiO_2$ nanotubes

In 1991 Grazel and O'Reagan established a cheap and versatile dye sensitized solar cells (DSSC), which use $TiO_2$ nanoparticulates coated with dye as photon-absorber layer. The principle of DSSC involves a dye that absorbs light in the visible range and thereby excites electrons from the HOMO to the LUMO level, followed by a rapid injection of the excited electron into the conduction band of $TiO_2$. The electrons travel through the $TiO_2$ layer to the back contact; meanwhile, the oxidized dye on the surface is regenerated by an $I^-/I^{3-}$ electrolyte.

For the dye sensitized solar cells, $TiO_2$ nanotube arrays provide direct transport pathways and large internal surface area to improve the charge-collection efficiency by promoting electron transport and reducing recombination. Recombination rate of electron in nanotube films is 10 time slower than it in nanoparticulate layers.[127-128] The diffusion length of electron in nanoparticulate layers of DSSCs is around 0.9 μm,[129] while the diffusion length of nanotube layers is larger than 20 μm.[130] The enhanced optical absorption due to light-scattering effect and the transparent property of $TiO_2$ nanotube film further increase the dye sensitized solar cells efficiency. Therefore, the $TiO_2$ nanotube photoelectrodes are expected to significantly enhanced charge collection efficiency. The highest solar cell efficiencies today for pure $TiO_2$ nanotube systems reach approximately 4% while for some mixed systems, around 7% has been reported.

The crystal structures of the $TiO_2$ nanotubes influence the solar cell performance. Typically the anatase phase of titania has the most efficient for solar cell performance, while the present of rutile phase will decrease the energy conversion efficiency due to the low electron mobility in rutile compared with anatase. The efficiency of DSSCs increase with the increase of annealing temperature, due to the increase in crystal structure of anatase phase, which promote the connectivity between grains and improve in electron diffusion length and electron lifetimes. However, when annealing temperatures above 500 ℃ the efficiency decreases, due to the formation of high resistance rutile phase nanotube and a rutile layer underneath the nanotubes. Therefore, the optimum annealing temperature to obtain the highest energy conversion efficiency is around 400-450 ℃.

Aqueous HF based $TiO_2$ nanotubes normally have very low efficiency due to the highly irregular tube wall structure, which will greatly decrease the electron lifetime. For organic solvent based $TiO_2$ nanotubes, due to the increasing of the tube thickness and surface area, more dye can be adsorbed onto the nanotube wall surfaces, which increase in light harvesting efficiency. However, the electron diffusion length for the smooth $TiO_2$ nanotube is around 20 μm. By considering all the factors, 16–25 μm is found to be the optimum tube length for attaining the highest efficiency. The diameter of $TiO_2$ nanotubes also has significant effect on the solar cell performance. Smaller diameter indicate large surface area of tube wall, which increases the dye loading amount and increase the energy conversion efficiency.

Conventional dye-sensitized solar cells can efficiently harvest photons in the 350-650 nm spectral range, but the narrow window of absorption spectrum also greatly limits the solar cell efficiency. To improve the efficiency, the light absorption window must be extended into the near-infrared region of sunlight without compromise of performance in the visible region. Recently, Grimes et al.[131-133] utilized the Förster resonance energy transfer (FRET) to employ two organic dyes to enlarge the absorption range of window, which greatly enhance the dye-sensitized solar cells performance. FRET introduces the donor material and acceptor material to absorb blue/green and the red/near-infrared part of the spectrum, respectively. When the donor dye is excited by sunlight, due to the dipole-dipole interaction, it can fluoresce and return to the ground state by nonradiatively transferring the energy to nearby acceptor dye through exchange of a virtual photon. As a result, the donor returns to ground state, while the acceptor obtains its excitation. Therefore, through FRET the acceptor dye can also utilize the blue/green part of the spectrum which it would otherwise be insensitive. As long as the donor and acceptor is within the Förster radius (such as several nanometers) and donor fluorescence spectrum overlap strongly with the acceptor absorbance spectrum, the energy can efficiently transfer, which significantly avoid the direct contact of two organic dyes and the issue of relaxation for compatibility. Therefore, the FRET significant enhance the light harvesting and photocurrent generation of dye-sensitized solar cells.

### 2.2.6.3 Conversion of carbon dioxide to Hydrocarbon Fuels

Photocatalytic conversion of carbon dioxide and water vapor to hydrocarbons has been achieved by nitrogen-doped $TiO_2$ nanotube arrays with cocatalyst Pt and Cu nanoparticles on the nanotube array surface.[134-135] The conversion occurs by the following reaction:

$$CO_2 + 2H_2O \Leftrightarrow CH_4 + 2O_2 \qquad (1\text{-}13)$$

Hydrocarbon production rate of 111 ppm/cm$^2$/h is obtained under outdoor sunlight of 100 mW/cm$^2$, which is ~20 times greater than the previously reported values.[136-137]

In order to improve the yield rate of carbon dioxide conversion, it is important to use the following strategies. First, using high surface area $TiO_2$ nanotube arrays, and wall thickness should less than or in the range of the minority carrier diffusion length to enhance the transition of photogenerated charge carriers to the surface species. Second, modify the titania band gap to absorb and utilize the visible portion of the sunlight by nitrogen-doping. Nitrogen-doped $TiO_2$ was obtained in situ during anodization by $NH_4F$, and then annealed with limited oxygen flow at 460 or 600 °C for 3 h. The nitrogen-doped titania have the absorption edge at 540 nm, while the primitive 3.2 eV of anatase titania restricts excitation wavelengths to less than 400 nm. Third, distribute cocatalyst nanoparticles on the surface of nanotube array to adsorb the reactants and facilitate the redox process. Ultra-thin layers of cocatalyst Pt and Cu were deposited onto the crystalline $TiO_2$ nanotubes through DC sputtering. Without an appropriate cocatalyst, the photocatalytic conversion of carbon dioxide for $TiO_2$ nanotube arrays is very low. In the future, highly efficient photocatalytic $TiO_2$ nanotube arrays might enable the use of flow-through photocatalytic membranes, where $CO_2$ and water vapor enter one side of the nanotube array membrane with a fuel coming from the other side of membrane.

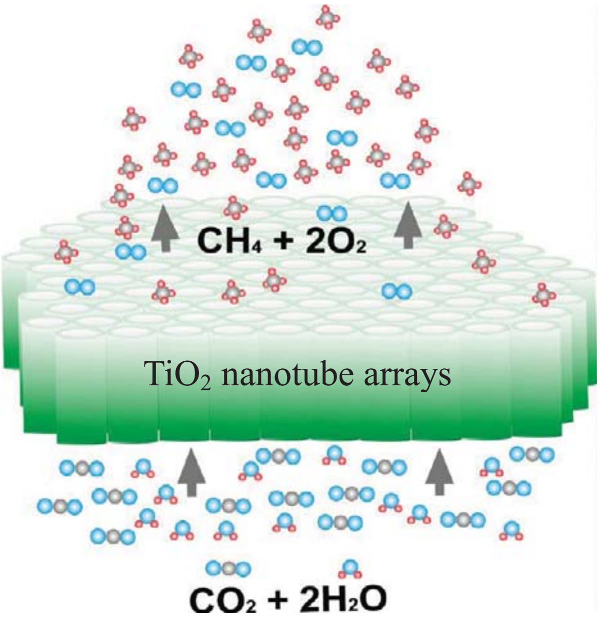

**Figure 2-22**. Schematic of flow-through photocatalytic membrane for $CO_2$ conversion.[134]

### 2.2.6.4 Photoelectrochemical water splitting

Since Fujishima and Honda[138] utilized $TiO_2$ semiconductor photoanode for solar water splitting, the direct photocatalytic decomposition of water into hydrogen fuel has attracted wide interest for near 40 years. The water splitting reaction includes several steps: (i) light absorption and charge separation; (ii) charge transfer; (iii) charge transport; (iv) surface chemical reactions. There are two critical requirement for the photocatalyst: (i) the band gap should allow for light absorption and electronic excitation, and the absorbed energy should large than 1.23 eV to split water; (ii) the conductive band-edge position should higher than $H_2/H_2O$ potential, and valence band-edge position should lower than $H_2O/O_2$ potential. As shown in Figure 2-23, titanium dioxide has a favorable band-edge positions and large band gap energy for water splitting.[139] Due to high surface-to-volume ratios and excellent charge transport, $TiO_2$ nanotube arrays can greatly enhance the light absorption and water splitting efficiency.[83, 140] However, the wide band gap (3.2 eV) of $TiO_2$ lead to the absorption only limit to UV region, which accounts for only a small fraction (≈5%) of the solar energy compared to visible light (45%). An enormous effort has been focused on enhancing the visible light absorption of $TiO_2$ nanotubes. Two versatile approaches are creation of impurity levels by doping deep into $TiO_2$ the band gap[141-143] and sensitization $TiO_2$ nanotubes with small band gap semiconductors.[144] On the other hand, it is equally important to enhance the electronic structure of $TiO_2$ to reduce the electron-hole recombination and facilitate the effective transportation of charge carriers.[145] In order to increase the photoelectrochemical water splitting efficiency, annealing treatment of amorphous anodic $TiO_2$ nanotubes is needed to increase the crystal structure of $TiO_2$ nanotubes.[83, 144]

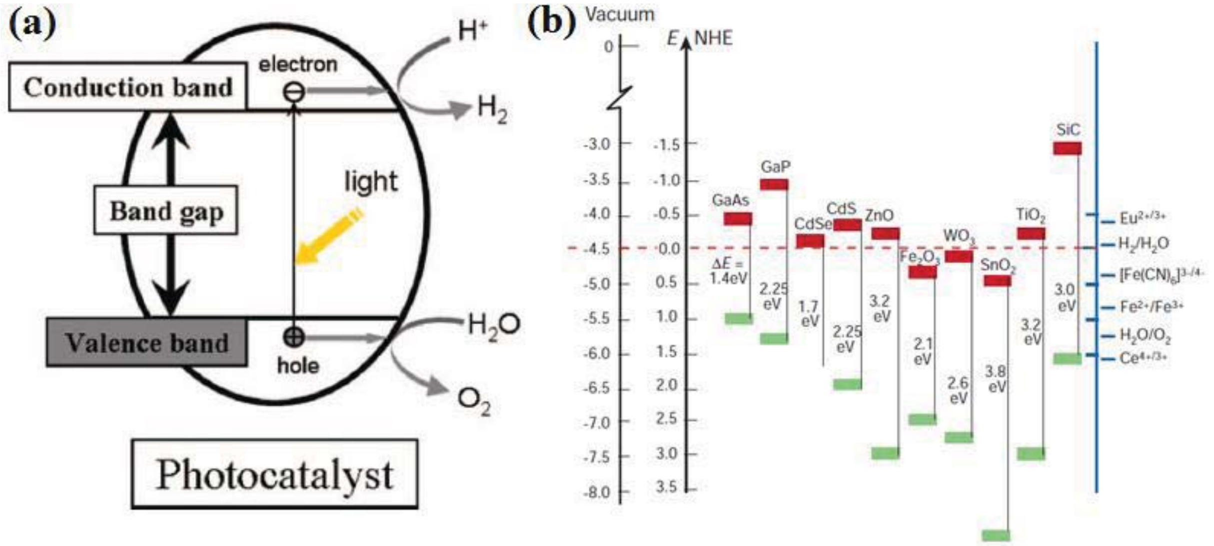

**Figure 2-23**: (a) Fundamental principle of photocatalytic water splitting for hydrogen generation.[146] (b) Band positions of several semiconductors in contact with aqueous electrolyte at pH 1. The lower edge of the conduction band (red colour) and upper edge of the valence band (green colour) are presented along with the band gap in electron volts. [139]

# Chapter 3. Fabrication of Anodic Alumina Oxide

## Abstract:

This chapter mainly focuses on applying the FIB lithography on guided anodization to achieve AAO arrays with different arrangements, pore diameters, and pore densities. First, FIB patterned concave arrays with hexagonal and square arrangements are created on electropolished Al surface to study whether FIB patterning can effectively guide the growth of AAO. By using a small FIB bombardment time, very shallow concaves can be created on Al surface, which opens the opportunity to study how deep the pre-patterned concave is needed for guided anodization. Under the pre-pattern guided anodization, AAO with different interpore distances can be achieved at the same anodization voltage, and AAO with the same interpore distance can be achieved at different anodization voltages. In the meantime, the interpore distance of the FIB patterns plays an important role in the guided anodization. Moreover, the ability of fabricating AAO with alternating-size and periodically nanopore densities are further investigated by the corresponding FIB patterns.

## 3.1. AAO arrays created by FIB pattern guided anodization

### 3.1.1. Introduction

Self-organized porous AAO arrays in hexagonal arrangement have attracted great interest due to its potential as a template for the fabrication of various low dimensional nanostructures.[50-58] However, self-organized porous alumina occurs only in a very small anodization window with ordered domain sizes around just a few microns.[8-13]

To increase the pore forming ability of AAO, different pre-texturing techniques, such as nanoimprint lithography,[23-27] holography lithography,[33] and FIB lithography,[28-32] are used to fabricate regular nanopore arrays with larger and more ordered domain sizes. However, the first two techniques have inherent limitations. During nanoimprint lithography, a pressure of 50-100 MPa is needed in order to transfer a pattern from a master mold to the Al surface. Since the technique is a contact method, any misalignment between the mold and the substrate can cause local pressure variation and residual stress and thus inhomogeneous pores or even defects. Although holographic lithography can pattern large areas, the resolution is restricted by the light wavelength and the grating precision. The pore size and the inter-pore distance are difficult to control.

Moreover, most studies have been directed towards uniformly ordered hexagonal porous anodic alumina patterns.[23-33] Gradient diameter or alternating diameter nanopore arrays with designed interpore distances have not been achieved yet. For nanoimprint lithography, large area master molds with hexagonal patterns of pyramids in uniform diameter and height have been fabricated,[23-27] but master molds with gradient or alternating diameter have not been possible yet. Focused ion beam lithography has the advantage of creating any nano-concave arrays with different arrangements and diameters. However, up to now, most studies focus on uniform diameter and equal interpore distance porous anodic alumina patterns, whether alternating size nanopore can be obtained by guided anodization are unknown.

In this study, FIB lithography is used to create different concave patterns with different arrangements and concave sizes. The effects of these concaves in guiding the growth of the nanopores in the subsequent anodization are analyzed. The formation mechanism of different nanopore patterns is discussed.

### 3.1.2. Experimental procedure

High purity aluminum foils (99.999%, Goodfellow Corporation, Oakdale, PA) with 8 mm×22 mm×0.3 mm size were used as the starting material. They were first smoothed by a Buehler specimen mounting press with 27.8 MPa pressure and then washed with ethanol and acetone. After that, they were annealed at 500°C for 2 hrs in high purity flowing Ar gas with 5°C/min heating and cooling rates to recrystallize the aluminum foils and remove mechanical stress.

For electropolishing, the annealed aluminum foils were degreased in ethanol and acetone for 5 min, respectively, followed by DI water rinsing after each step. The aluminum foils were then immersed in a 0.5 wt% NaOH solution for 10 min with ultrasound in order to remove the oxidized surface layer. After that, the aluminum foils were electropolished in a 1:4 mixture of perchloric acid (60%-62%): ethanol (95%) (volume ratio) under a constant voltage of 12 V at room temperature with 500 rpm stirring speed for 5 min.

A FIB microscope (Helios NanoLab 600 DualBeam, FEI Company, Hillsboro, OR) was employed to pre-pattern the Al surface before the anodization. The applied voltage was 30 keV.

The ion current was 28 pA. The ion beam scanned the pattern surface multiple times for each pore array. The beam dwell time at a specific location per scan was 3 μs. The total number of scans was set by trial and error based on the pattern quality. The FIB patterns and pore sizes were designed by the software Serif DrawPlus 4.0 (Serif, Nottingham, UK) using vector-enabled pixel images. Each pixel in the pore pattern designs was scaled to 1 nm in the actual FIB created patterns. There were only two contrasts in the pattern designs. The high contrast (white) part of the pixel images was designed to be removed and the low contrast (dark) part of the pixel images was designed to be retained. Different concave arrays were created by the FIB lithography.

The FIB patterned Al foils were anodized in 0.3 M phosphoric acid under 20 mA constant current at 0°C for 5 min. The voltage stabilized at ~140 V after a few seconds of anodization. Pore opening was carried out in 5 wt% phosphoric acid at 30°C for 10 min. The porous anodic alumina patterns were characterized by scanning electron microscopy (Quanta 600 FEG, FEI Company, Hillsboro, OR).

### 3.1.3. Results and discussion

#### 3.1.3.1 Highly ordered AAO by FIB pattern guided anodization

Figure 3-1a show the AFM image of the FIB created concave pattern with 65 nm diameter and 60 nm depth. The interpore distance is designed at 350 nm in order to match with the subsequent anodization process: $d_{inter}=k\times U=2.5\times 140=350\ nm$.[14] The concaves have homogeneous size, spherical shape, and hexagonal arrangement. After the anodization in 0.3 M oxalic acid at 140 V for 5 min, the FIB patterned concaves develop into hexagonally arranged spherical nanopores. The pore diameter is still around 110 nm and the interpore distance remains at 350 nm (Figure 3-1c). Even though one-step anodization in the oxalic acid cannot create hexagonal nanopore patterns, almost ideally ordered hexagonal nanopore patterns are made with the guidance of the FIB generated concaves on the Al surface. Figure 3-1c show the FIB created concave array with square arrangement and 350 nm interpore distance. After the anodization in 0.3 M phosphoric acid at 140 V, the anodized alumina nanopores all develop at FIB patterned locations, and the arrangement maintain square as the FIB concave arrays. Moreover, the outer wall of the nanopore has square shape.

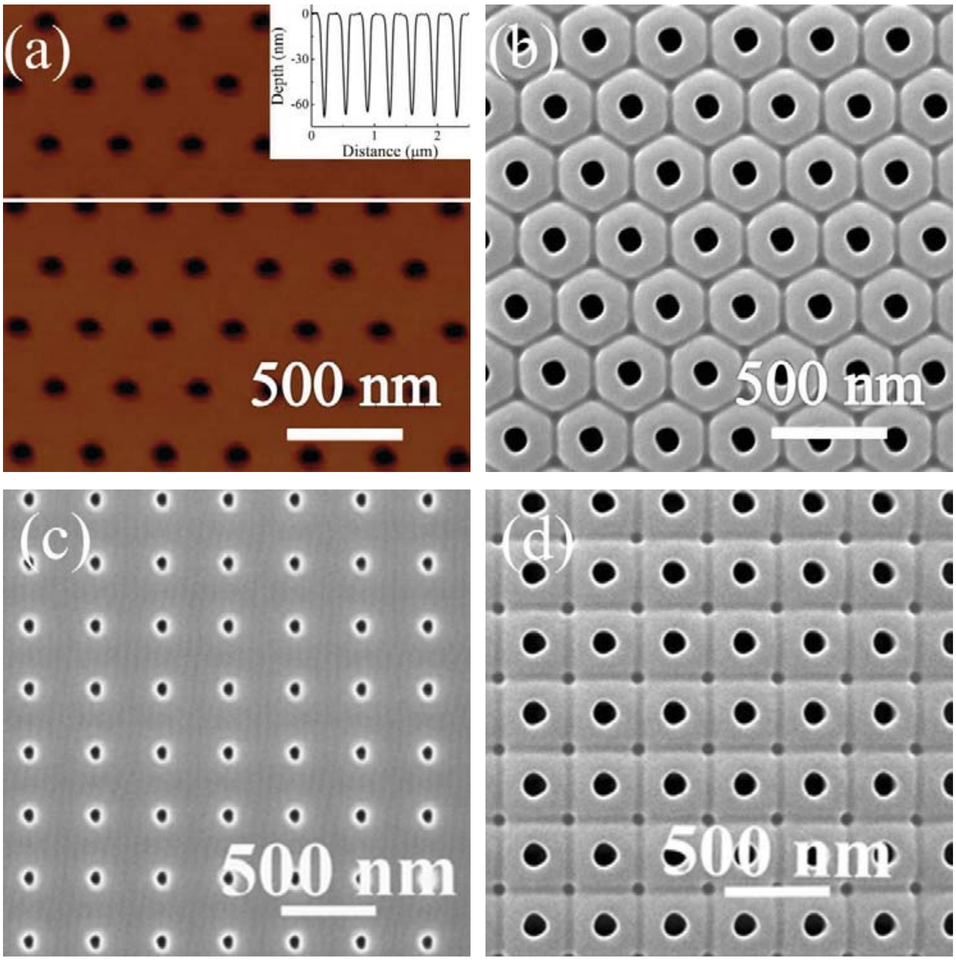

**Figure 3-1**. (a) AFM image of uniform hexagonal pattern created by FIB, and the inset is surface topology along the line in (a); (c) SEM image of FIB pattern with square arrangement; (b) and (d) are SEM images of the corresponding AAO after anodizing the patterns in (a) and (c), respectively.

To understand the FIB guided pore growth process, the anodization process from the electropolished Al surface can be considered first. For the conventional anodization, uniform oxidation takes place on the entire Al surface and the alumina thickness is determined by the applied electrical field. The mechanical stress associated with the volume expansion of aluminum during the alumina formation lead to the repulsive forces between neighboring pores during the anodization process. This repulsive force in turn acts as the driving force to form self-organized hexagonal pore arrays. At the same time, the electrical field drives ionic transport through the oxide barrier layer. Oxygen containing ions ($O^{-2}/OH^{-}$) migrate from the oxalic acid through the oxide layer to the Al; alumina dissolves into the oxalic acid electrolyte and induces pore formation. Without any pre-defined pattern, the pores formed can only self-organize if the electropolished surface is ideally smooth. If any defect is present, even with only a few nanometer depth, pores will preferentially form and grow in those locations. This is why it is challenging to form ordered self-organized pores by anodization alone, the anodization window is narrow, and the hexagonal patterns are often disrupted by defects and grain boundaries.

With the guidance of the FIB patterned concaves, pores preferentially grow at the concave locations because of the following reasons. First, the depth of the concaves exceeds the roughness variation of the Al surface. This leads to a higher electrical field at the oxide/electrolyte interface at the concave bottom. Second, the $Ga^+$ implantation during the FIB patterning creates more active surface around each concave and promotes faster alumina dissolution, which is partially reflected from the effect of $Ga^+$ irradiation on the volume expansion during the anodization.[147] An Al-Ga alloy gel has been shown to react with water and generate alumina.[147] During the FIB patterning, the $Ga^+$ ions penetrate 25 nm into Al and play an important role during the anodization.[148] Third, the Al layers around the FIB patterned concaves are likely amorphorized by the $Ga^+$ ion bombardment, which will facilitate the anodization.

#### 3.1.3.2 AAO with alternating diameter

The guiding effect of the alternating-sized concave patterns from the FIB pre-pattern guided anodization is also studied. FIB patterning has the advantage of designing any nano-concave arrays with different pore arrangement, pore diameter and interpore distance.

Figure 3-2a shows the alternating-sized concave pattern created by the FIB with 65 nm and 45 nm pore sizes and 200 nm interpore distance. After the anodization, alternating diameter pores grow and the interpore distance remains at 200 nm. The large pores have 105 nm diameter. The small pores are elongated in the direction perpendicular to the large pore connecting lines. The long axis of the small pores is 95 nm and the short axis is 50 nm (Figure 3-2b). The development of these pore sizes and shapes demonstrates unique opportunities in creating novel pore shapes and patterns by FIB guided anodization.

In Figure 3-2, the interpore distance of 200 nm is smaller than that of the self-organized anodization, 350 nm. The oxide walls of the nanopores developed from the large and small FIB patterned concaves meet and restrict the full growth of each other. Because of the larger diameter, more $Ga^+$ implantation, and aluminum amorphization, the nanopores developed from the FIB patterned large concaves grow faster and have thicker oxide walls. The development of the nanopores from the small concaves is confined in limited space. Alternating diameter nanopore arrangement is thus obtained. The large concaves have six small concaves in a symmetrical distribution as neighbors. The small concaves, however, have four small concaves and two large concaves in an asymmetrical distribution as neighbors. Because the oxide layers of the large pores grow much faster, the oxide layers of the small pores come in contact with those of the neighboring large pores first. The oxide layer growth in the direction of the large pore connecting line is restricted and thinner than that in the direction perpendicular to the large pore connecting line. Therefore, the small concaves grow into elliptical nanopores.

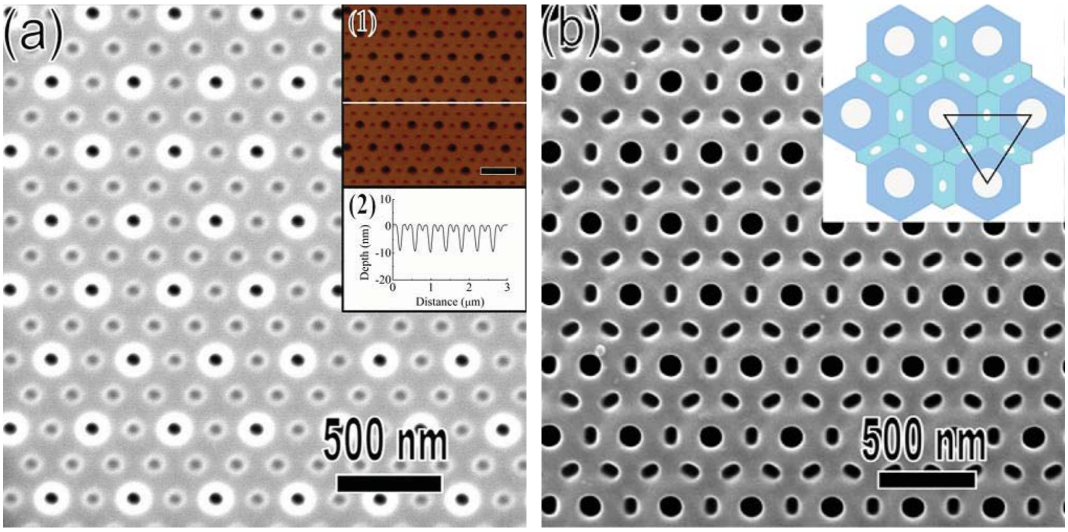

**Figure 3-2**. (a) Alternating FIB pattern with 200 nm interpore distance, the larger concave size is 65 nm and the smaller concave size is 45 nm, (b) after the anodization in 0.3 M phosphoric acid, the inset is the schematic of the pore shape and oxide wall shape development.

Figure 3-3a shows the alternating-sized nanopore array by the FIB patterning with three different pore diameters: 80 nm, 65 nm, and 45 nm, respectively. The interpore distance is again 200 nm. After the anodization, the pattern arrangement stays unchanged and the diameters of the nanopores grow to 105 nm, 90 nm, and 55 nm, respectively (Figure 3-3b). Alternating-sized nanopore arrangement with three different diameters is thus created. Similar to Figure 3-2, the shape of the small pores is not circular.

The pore development process in Figure 3-3 can again be understood based on the equifield strength controlled oxide layer growth model. During the anodization, the large concaves grow faster because of the more extensive FIB patterning (shown as white rings around the concaves in Figure 3-3a). Subsequently, large pores have thicker oxide layer and larger pore diameter (105 nm). Even though the FIB patterned concaves are larger than those large concaves in Figure 3-2, the anodized pore sizes are the same because of the larger size neighbors (65 nm) in Figure 3-3a. Because of the symmetrical distribution of the neighboring concaves, the large concaves grow into circular pores (pore 1 in Figure 3-3b inset). The medium-sized concaves also grow faster than the small concaves and thus have a higher tendency to maintain the original pore shape even though their surroundings are not symmetrical (pore 2 in Figure 3-3b inset, 90 nm). For the small concaves, the surrounding condition is a little complicated as shown in Figure 3-3b inset. The small pore "3" is surrounded by four small pores and two medium-sized pores and grows into an elliptical shape, 83 nm in the long axis and 51 nm in the short axis, and elongate in the direction without the confinement of the medium-sized pores. The small pore "4" is surrounded by two small pores and four medium-sized pores and also grows into an elliptical shape that elongates in the direction of the small pores. 86 nm in the long axis and 58 nm in the short axis, The small pore "5", restricted by two medium-sized pores "2" from the same side, grows into a cometary shape. Differently, the small pore "6" is surrounded by six small pores and has no medium or large pores to restrict its growth. Subsequently, it grows into a larger size (86 nm) than other small pores and the shape is circular.

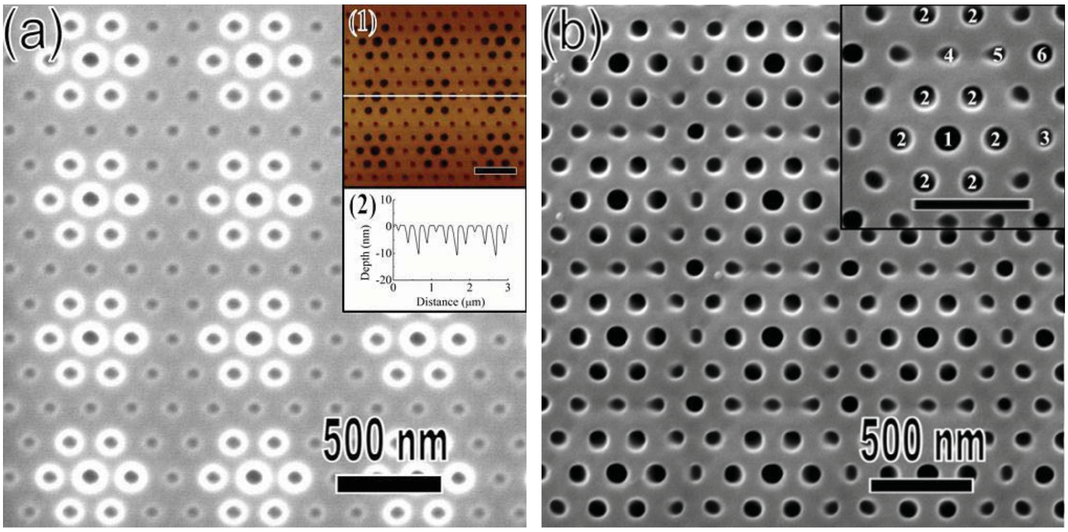

**Figure 3-3**. (a) Alternating FIB pattern with three different nanopore diameters: 80 nm, 65 nm, and 45 nm, the interpore distance is 200 nm. (b) Alternating FIB pattern after the anodization in 0.3 M phosphoric acid, the inset is the enlarged SEM image of (b) with different pores labeled.

The guiding function of gradient FIB concave patterns is also studied. Figure 3-4a shows the gradient diameter concave arrays produced by the FIB patterning with 200 nm interpore distance. The large concave size is 65 nm and the small concave size is 45 nm. After the anodization, the nanopores remain the hexagonal arrangement and the interpore distance stays at 200 nm. The anodized large and small concaves grow into circular pores with very similar diameters, 85 nm and 80 nm, respectively (Figure 3-4b). Similar to the pore "6" in Figure 3-3b, when a pore is symmetrically surrounded by six same diameter pores, it grows into a spherical shape and has the same oxide wall thickness. The diameter change can also be explained by the equifield strength model. The interpore distances for the large and small pores are the same. Both the large and small pores have the same oxide wall thickness as their neighbors. Since the thickness of the oxide barrier layer is determined by the anodization voltage, the oxide wall thicknesses of the large and small pores are similar. However, the small pores have a smaller size to start with. Subsequently, the anodized pores are slightly smaller than the large pores in the top region. The diameters of the nanopores along the boundary of the large and small pore regions are around 70 nm and the pore shape is elliptical. This is because the FIB patterned concaves along the boundary is surrounded by four small concaves and two large concaves and the oxide layer growth is restricted in the direction of the large pores.

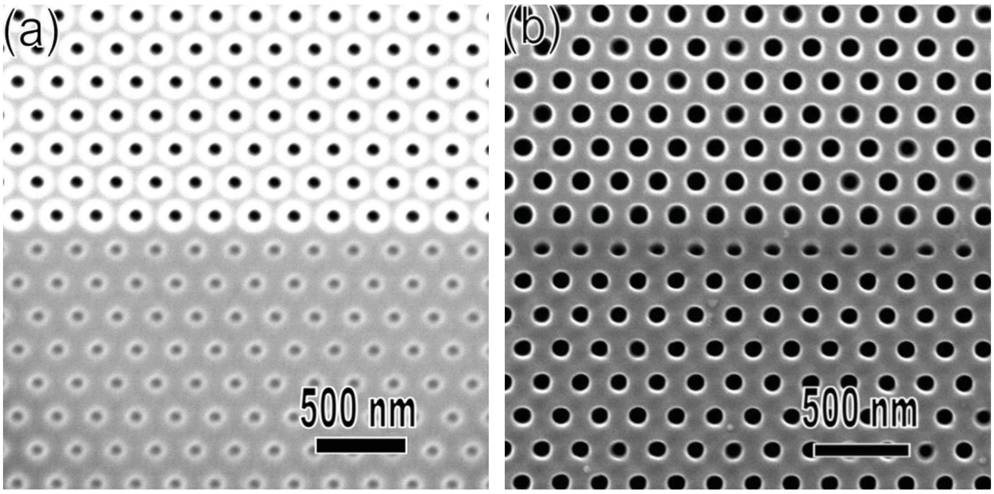

**Figure 3-4**. (a) Gradient concave pattern produced by FIB patterning with 200 nm interpore distance, the larger concave size is 65 nm and the smaller concave size is 45 nm. (b) SEM image of the FIB pattern after the anodization.

### 3.1.4. Summary

Highly ordered AAO arrays with both hexagonal and square arrangements have been successfully created by FIB pre-pattern guided anodization. Due to the preferential growth of nanopores at the FIB patterned locations, the anodized nanopore arrays have the same arrangement as the FIB pre-patterned concaves. With the guidance of the alternating-sized concaves, alternating diameter nanopore arrays with two or three different pore diameters are obtained. Due to limited space for the development of nanopores, after the anodization, the large concaves grow into large nanopores, while the small concaves grow into small nanopores.

## 3.2. Shallowest pre-pattern depth to guide the anodization

### 3.2.1. Introduction

In order to overcome limited ordered region of self-organized AAO, different pre-texturing techniques, such as FIB lithography and nano-indentation lithography with SiC or Ni nano-molds, have been used to produce hexagonal patterns to guide the growth of highly ordered AAO.[23-33] The depths of pre-patterned concave arrays by different pre-texturing techniques normally range from 5-50 nm.[23-33] Some studies indicate that the patterned concaves should be deeper than 5 nm in order to effectively guide the growth of the nanopores during the anodization.[30, 149-150] Otherwise, the Al foil surface roughness dominates the anodization behavior. However, how deep of pre-patterned concaves is needed for effectively guiding the growth of the nanopores during the anodization has nether been evaluated.

In this study, the Al foils are first electropolished to minimum the surface roughness, and then the concave arrays with shallow depth are created by FIB lithography with small ion beam current and short bombardment time. The effect of FIB pre-patterned concave depth to the guidance anodization is investigated.

### 3.2.2. Experimental procedure

The annealed Al foils was degreased in ethanol and acetone and then the oxidized surface layer was removed by immersed in a 0.5 wt% NaOH solution for 15 min. Subsequently, the aluminum foils were electropolished in a 1:4 mixture of perchloric acid/ethanol (1/4 volume ratio) under a constant voltage of 12 V at room temperature with 500 rpm stirring speed for 5 min. A dual beam focused $Ga^+$ ion bean microscope (FIB, FEI Helios 600 NanoLab, Hillsboro, OR) with 30 kV acceleration voltage, 9.7 pA current, and 1 μs dwell time was used to create shallow concaves on electropolished Al surface. It took 436 ms exposure time to create a 3 μm× 3 μm pattern with 125 nm interpore distance, as shown in Figure 3-1. The FIB patterned Al foils were anodized in 0.3 M oxalic acid at 50 V and 0°C for 30 min. Pore opening was carried out in 5 wt% phosphoric acid at 30°C. An atomic force microscope (Digital Instruments MultiMode SPM, Veeco Instruments Inc., Camarillo, CA) was used to measure the depth and diameter of the FIB patterned concaves.

### 3.2.3. Results and discussion

Figure 3-5a shows the AFM image of the electropolished Al surface. It is very smooth. No defects (dents or reliefs) or dust particles are observed. Also, the surface is free of the stripes or hexagonal concave patterns reported in other studies. The square root mean roughness for the sample surface is ~1 nm for a 1 μm$^2$ area (Figure 3-1b). Therefore, the main function of the electropolishing process is to provide a smooth Al surface for the subsequent anodization process. This smoothness/cleanness desirably offers the surface condition to study the FIB patterning effect on the pore pattern formation by the anodization.

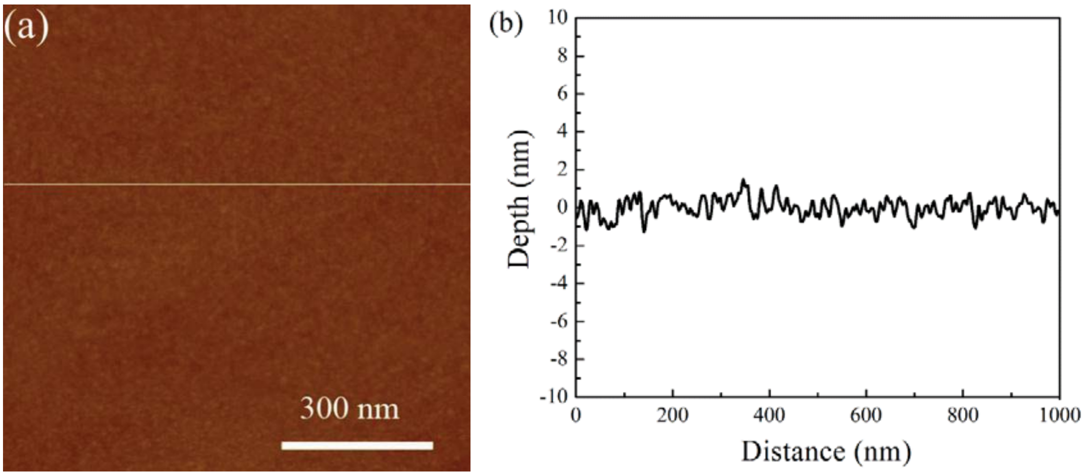

**Figure 3-5**. Electropolished Al foil surface: (a) AFM image, (b) surface topology along the line in (a).

Figure 3-6a shows the AFM image of the FIB patterned concaves, and the surface topology in Figure 3-6b demonstrates the depth of the concaves is only 1.5 nm, which is just a little larger than the surface roughness of electropolished Al foils. The diameter of the concaves is 30 nm, and the interpore distance is 125 nm. The FIB patterned concaves with such shallow depth can still effectively guide the growth of anodized nanopores, and leads to the highly ordered AAO arrays with hexagonal arrangement.

This high guiding effectiveness is attributed to the FIB patterned surface activity. For an electropolished aluminum surface, the anodized nanopore arrangement solely depends on the random fluctuation of surface potentials. This makes the anodized nanopore arrangement very sensitive to the anodization conditions and aluminum surface characteristics. The effective guidance of the 1.5 nm deep FIB patterned concaves indicates the importance of the Al surface properties before the anodization. For self-organized anodization, random depth concaves on the aluminum surface leads to random nanopore arrangement. For the FIB patterned surface, there are three factors from the FIB concaves that are conducive for the anodized pore pattern development. First, the electrical field at the oxide/electrolyte interface of the concave bottoms is higher because of the higher curvature, this accelerates the anodization rate at the concave bottoms. For the FIB patterned shallow concaves, the diameter is 30 nm and the depth is 1.5 nm, the curvature at the concave bottom is ~1/80 $nm^{-1}$, which is very large and leads to much higher electrical field, which can effectively enhance the oxidation rate by preferentially driving the oxygen anion dissolution. Moreover, the $Ga^+$ implantation during the FIB patterning and amorphorization at FIB patterned location further enhance the development of nanopores from the FIB patterned sites. These three factors in combination overshadow the effect of random surface potential fluctuation during the anodization and play a dominant role in guiding the anodized pore growth. Stable pores thus preferentially form at the FIB patterned sites.

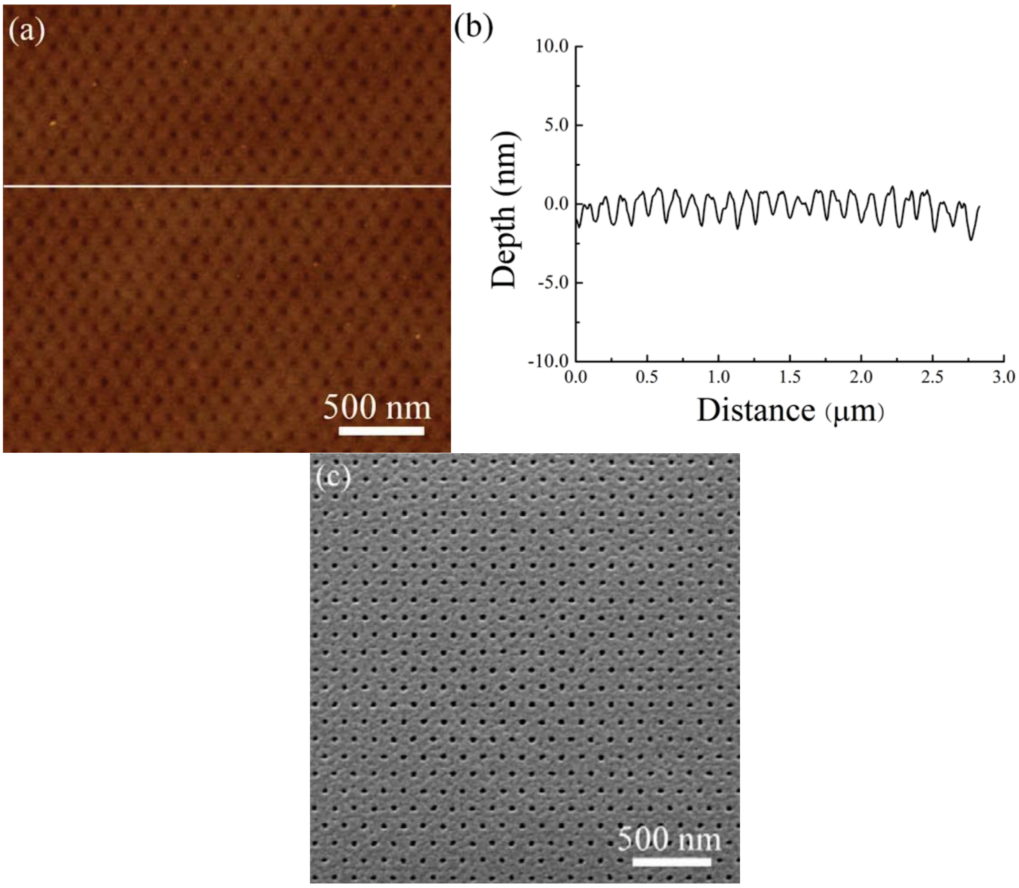

**Figure 3-6**. (a) AFM image of the FIB pattern obtained at 30 keV, 9.7 pA, and 436 ms exposure time, (b) the inset is the surface topology along the line in (a); (c) SEM image of the FIB pattern after the anodization in 0.3 M oxalic acid under 50 V and 0°C for 30 min.

For the nano-indentation with SiC or Ni mold, the guiding effect comes from the concave curvatures and the mechanical stress. During the nano-indentation with these master molds, a pressure of 50-100 MPa is needed in order to transfer an effective pattern to the Al surface, and the depth of the patterned concaves is generally 20-50 nm. If the pressure is too small, the size and depth of the concaves are often non-uniform; and disordered anodized nanopore arrangement is formed. Moreover, the patterned concaves lack the increased surface activity from ion implantation and aluminum amorphorization.

### 3.2.4. Summary

This study is focused on understanding the effect of the FIB pre-patterned concave depth on pore evolution during anodization. Ordered hexagonal nanopore arrays can be successfully fabricated under the guidance of FIB patterned concaves with 1.5 nm depth. This extends the smallest depth of patterned concaves needed for effective guidance of anodized nanopore growth to a much smaller value.

## 3.3. Enlarged anodization window under FIB guidance

### 3.3.1. Introduction

For conventional self-organized nanopore arrays can only be fabricated under very narrow anodization window and the interpore distance is confined to several fixed values. In general, AAO is fabricated through anodization in sulfuric acid at 25 V,[8-9] oxalic acid at 40 V,[10-11] and phosphoric acid at 195 V,[12-13] and the interpore distances are approximately 63 nm, 100 nm, and 500 nm, respectively. Based on the 10% porosity rule, the interpore distance ($d_{inter}$) is determined by applied voltage (U): $d_{inter}=kU$. [14] Whether different interpore distance can be obtained at same anodization condition or same interpore distance can be obtained at different applied potential under the pre-pattern guided anodization have seldom studied.

To examine whether of the FIB guided anodization can enlarge the anodization window, the anodization result of FIB pre-patterned concaves with different interpore distances at same applied voltage are examined; and the anodization result of same FIB pre-patterned concaves under different applied voltages are investigated.

### 3.3.2. Experimental procedure

After electropolishing, three hexagonal concave arrays were created on the same Al foil by FIB with same diameter (45 nm) but different interpore distances are created by $Ga^+$ ion beam with 30 kV and 28 pA: $d_{inter}$=350 nm (Figure 3-7a), $d_{inter}$=250 nm (Figure 3-7c), and $d_{inter}$=200 nm (Figure 3-7e). The FIB milling condition is 30 kV applied voltage and 28 pA current. Subsequently, the FIB patterned Al foil was anodized in 0.3 M phosphoric acid under 20 mA constant current at 0°C for 5 min. The voltage was ~140 V after a few seconds of anodization. Pore opening was carried out in 5 wt% phosphoric acid at 30°C for 10 min.

Some Al foils were patterned with hexagonal concave arrays, the interpore distance was 150 nm, and the diameter of the concaves was 45 nm. The FIB patterned Al foils were anodized in 0.3 M oxalic acid at 40~60 V and 0°C for 30 min, and in 0.05 M oxalic acid at 80 V and 0°C for 30 min. Pore opening was carried out in 5 wt% phosphoric acid at 30°C. The cross section of the anodized nanopores was obtained in the FIB microscope by using 0.28 pA current to cut the patterned AAO.

### 3.3.3. Results and discussion

As shown in Figure 3-7, after the anodization the FIB patterned concaves with different interval distance under 140 V, all of the anodized nanopore arrays maintain the original FIB patterned interpore distances while the pore diameters grow from 45 nm to 110 nm, 88 nm, and 80 nm, respectively. Ordered hexagonal nanopore patterns with 350 nm interpore distance as well as 250 nm and 200 nm interpore distances are obtained. Self-organized anodization at 140 V without the guidance of the FIB patterns only form disordered nanopores with the interpore distance at ~350 nm. This enlarged interpore distance range and the different anodized pore sites have not been explicitly addressed before and can be understood as follows.

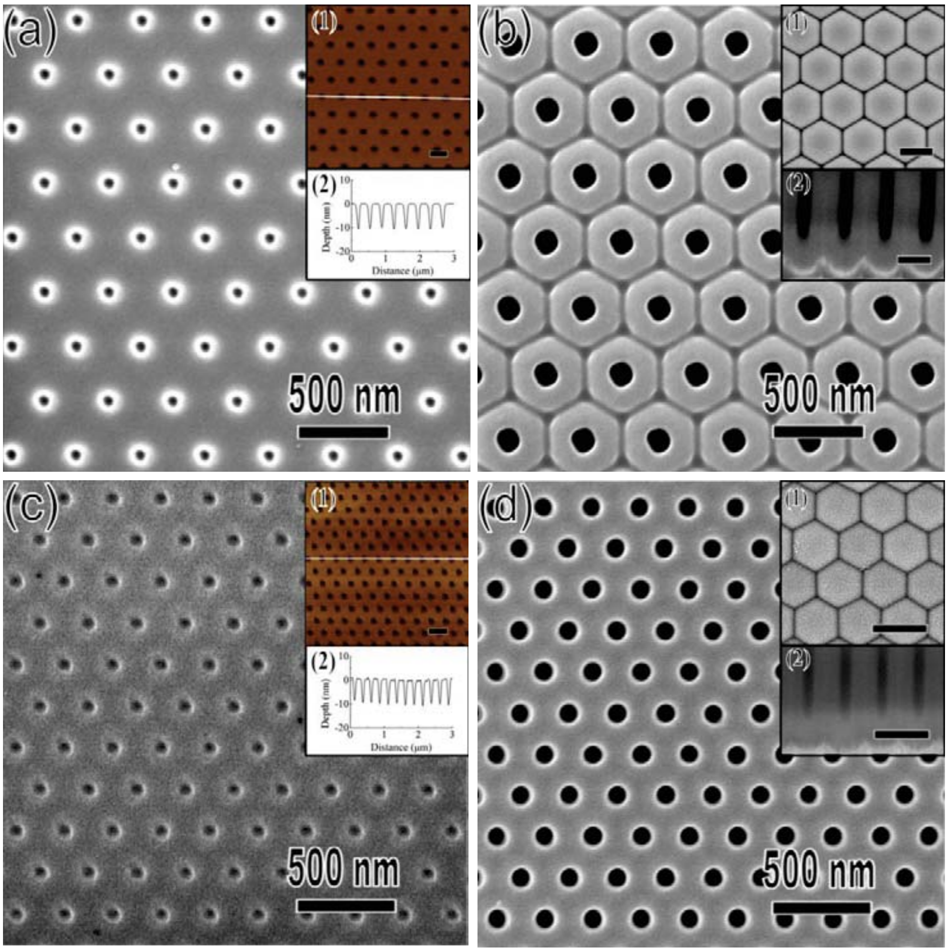

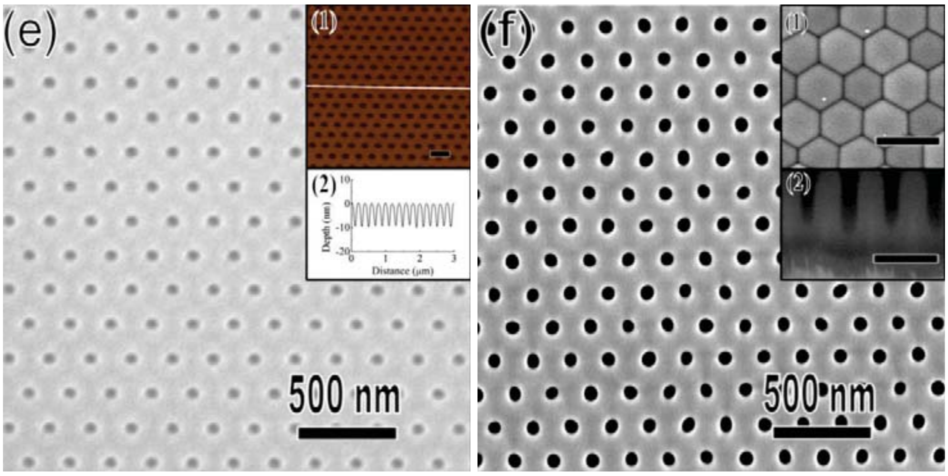

**Figure 3-7**. SEM images of FIB patterns ((a), (c), (e)) and the corresponding anodized nanopore patterns in 0.3 M phosphoric acid ((b),(d),(f)). The FIB patterns are designed with different interpore distances: (a) 350 nm, (c) 250 nm, (e) 200 nm.

For self-organized anodization, the electrical field balancing the aluminum oxidation rate and the oxide layer dissolution rate follows the following approximation:[5, 15] the barrier layer thickness $d_B \approx 1.3$ nm/V, the interpore distance $d_{inter} \approx 2.5$ nm/V, the pore diameter $D \approx 0.9$ nm/V, and the oxide pore wall thickness $d_w \approx 0.8$ nm/V. Under the guidance of the FIB patterning, the pattern with 350 nm interpore distance meets the linear proportional relationship with the applied voltage: $d_{inter} = 2.5$ nm/V × 140 V= 350 nm.[14] There is enough space between two pores for the oxide walls to fully expand before impinging each other. The oxide pore wall thickness is ~120 nm and can be observed clearly in Figure 3-7b, which also satisfies the relation $d_w \approx 0.8$ nm/V × 140 V= 112 nm.

As illustrated in Figure 3-8a, the oxide wall thickness between two neighboring nanopores is $2d_w$ and the barrier layer thickness $d_B = AA'$ is determined by the anodization voltage. The oxidation rate balances the dissolution rate at positions A and B. When the interpore distance is decreased ($d < 2d_w$), the oxide walls of two neighboring nanopores meet each other before they are fully developed according to the equifield strength model (such as in Figure 3-8b).[5-6] However, the FIB patterned concaves, $Ga^+$ implantation in aluminum, and aluminum amorphization during the FIB patterning are significant factors favoring nanopore growth at the FIB patterned sites. During the anodization, pores preferentially grow at the bottoms of the FIB patterned concaves. At the same time, the pores have a tendency to expand and the neighboring walls of these pores approach each other until two alumina layers merge. Since all the nanopores develop at the same rate, the neighboring pores restrain the change of the interpore distance. For the 250 nm interpore distance pattern, assuming the diameter of the nanopores stays the same as in Figure 3-8a, then the wall thickness should decrease to 120−(350−250)/2=70 nm and the thickness along BB′ is $d_B$. However, the thickness from B′ to any position in the range of A-B is larger than $d_B$ (Figure 3-8b), leading to a lower field strength. The field-assisted oxide dissolution rate in the area AB becomes slower than that at the position B and below. In order to balance the dissolution rate and the oxidation rate, the wall thickness between the pores increases by decreasing the nanopore diameters, as shown in Figure 3-8c. The cross section SEM image in the inset (2) of Figure 3-8b shows that when the interpore distance of the FIB patterned concaves decreases, the anodized nanopore arrays maintain the 250 nm interpore distance while the wall thickness increases to 82 nm and the diameter of the anodized nanopores decreases to 88 nm. The arc segment of the pore bottom also decreases and the barrier layer thickness stays at ~200 nm for the 250 nm interpore distance pattern as shown in the inset (2) of Figure 3-7d, just as expected in Figure 3-8c.

The same finding is true for even smaller interpore distance patterns. When the FIB patterned interpore distance further decreases to 200 nm, the diameter of the anodized nanopores is further reduced to 80 nm, the wall thickness increases from 82−(250− 200)/2=57 to 60 nm, and the barrier layer is still around 200 nm (as shown in inset (2) of Figure 3-7f). This explains why the anodized nanopore diameter from the 200 nm interpore distance FIB pattern (Figure 3-7f) is smaller than those from the 250 and 350 nm interpore distance FIB patterns (Figure 3-7b and 3-7d). When the interpore distance increases to larger than 350 nm, such as 425 nm, the space among the three neighboring pores is not large enough to develop a new pore; an ordered alumina nanopore array is still obtained with the guidance of the FIB pattern by increasing the pore diameter and decreasing the pore wall thickness.

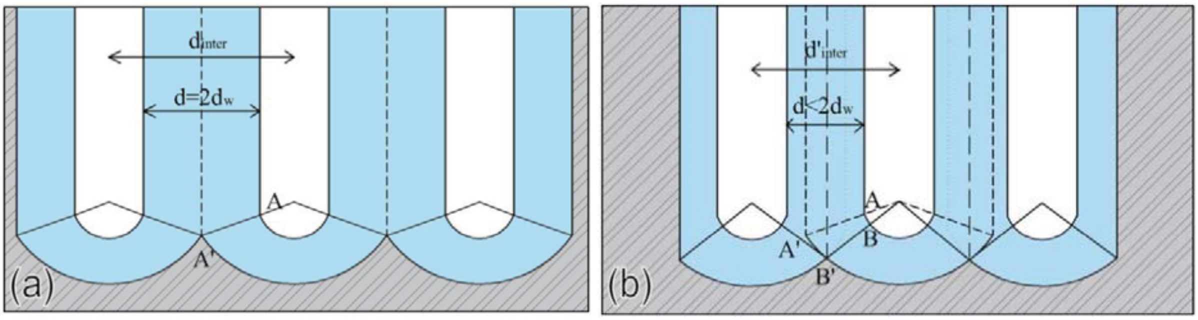

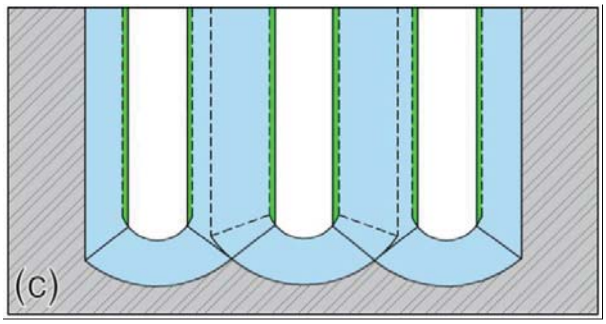

**Figure 3-8**. Schematic drawing of (a) large interpore distance; (b) decreased interpore distance; (c) decreased nanopore diameter.

On the other hand, the same FIB patterned hexagonal concave arrays with 150 nm interpore distance are anodized at different voltages: 40 V, 50V, 60 V, 80 V, 90 V, and 120 V. At 40-60 V the concentration of the oxalic acid electrolyte used is 0.3 M, and at 80-120 V the concentration of the oxalic acid electrolyte needs to decrease to 0.05 M. Otherwise, the anodization current would be too high and burning would occur on the aluminum surface.

The SEM images of the nanopores after the anodization are shown in Figure 3-9. At the conventional self-organized anodization condition, ordered hexagonal nanopore arrangement with 150 nm interpore distance can only be created at 60 V because the interpore distance is linearly proportional to the applied voltage with a constant of 2.5 nm·V$^{-1}$. With the FIB patterning, ordered nanopore patterns can be obtained from 50 V to 80 V anodization voltages (Figure 3-9). The patterned concaves, Ga$^{+}$ implanation, and aluminum amorphorization are significant favorable factors influencing nanopore growth at FIB patterned locations. This enlarged anodization window, which has not been explicitly addressed before, is directly related to the FIB patterning.

During the anodization, the thickness of the oxide layers depends on the applied voltage with a proportionality constant of ~1.25 nm·V$^{-1}$. Around each pore, an oxide layer (shown as gray color in the schematic inset 1 in Figure 3-9) with 1.25×U nm outer radius forms (U is the applied voltage), [5-6,14] which prevents the creation of new pores inside the boundary. When the applied voltage is 40 V ($< 60/\sqrt{2}= 42$V), the oxide layer has 50 nm outer radius around each pore (Figure 3-9a). The largest circle at the center of three neighboring pores is $R=150/\sqrt{3} - 50= 36$ nm (inset 1 of Figure 3-9a). Although it is a little smaller than 50 nm, some nanopores can split into two nanopores at the beginning of the anodization (as shown in circle of Figure 3-9a inset 2).

As a result, the arrangement is changed, and the interpore distance is decreased to 105 nm.

When the applied voltage is increased to 50 V ($> 60/\sqrt{2}= 42$V), the oxide layer has 62.5 nm radius, the largest circle at the center of three neighboring pores, $R=150/\sqrt{3}- 62.5= 24$ nm, is much smaller than 62.5 nm. Subsequently, there is not enough space left to form a new pore. As a result, the arrangement of the anodized nanopores maintains its hexagonal pattern, and the nanopores grow vertically.

When the applied voltage is 80 V ($<60\times\sqrt{2}= 85$V), the oxide layer has 100 nm radius, but the interpore distance of the FIB pattern is only 150 nm (Figure 3-9d). This means the oxide layers of two adjacent pores overlap with each other (inset 1 of Figure 3-9d). If there is no guiding effect from the FIB patterning, the self-organized anodization at 80 V would form nanopore array with 200 nm interpore distance. Under the guidance and confinement of the FIB pattern with 150 nm interpore distance, nanopores form at the locations of the FIB patterned concaves and the growth of the oxide layer stops when it encounters the neighboring oxide layers. Therefore, the anodized nanopores at 80 V also maintain the hexagonal arrangement, and the nanopores grow vertically.

However, when the applied voltage is further increased to 90 V ($>60\times\sqrt{2}= 85$V), the large overlap of the neighboring nanopore oxide layers leads to large compressive stress, and the depth of the nanopores maintains 150 nm interpore distance is only 1.75 μm. With further development, some nanopores terminate the growth (as shown in the circle of Figure 3-9e inset 2), and the interpore distance is increased to 230 nm. If the applied voltage is 120 V, the oxide layer has 150 nm radius, therefore, large compressive stress from the neighboring nanopores causes the termination of some nanopores occurs at 1.35 μm (as shown in the circle of Figure 3-9f inset 2), and the interpore distance is increased to 280 nm.

Clearly, the FIB patterning affects the anodized pore arrangement by influencing the oxide layer growth and enables an enlarged anodization voltage window. The FIB pre-pattern guided anodization not only obtain different interpore distance of alumina nanopore arrays at same anodization condition, but also enable to create same interpore distance at different applied potential.

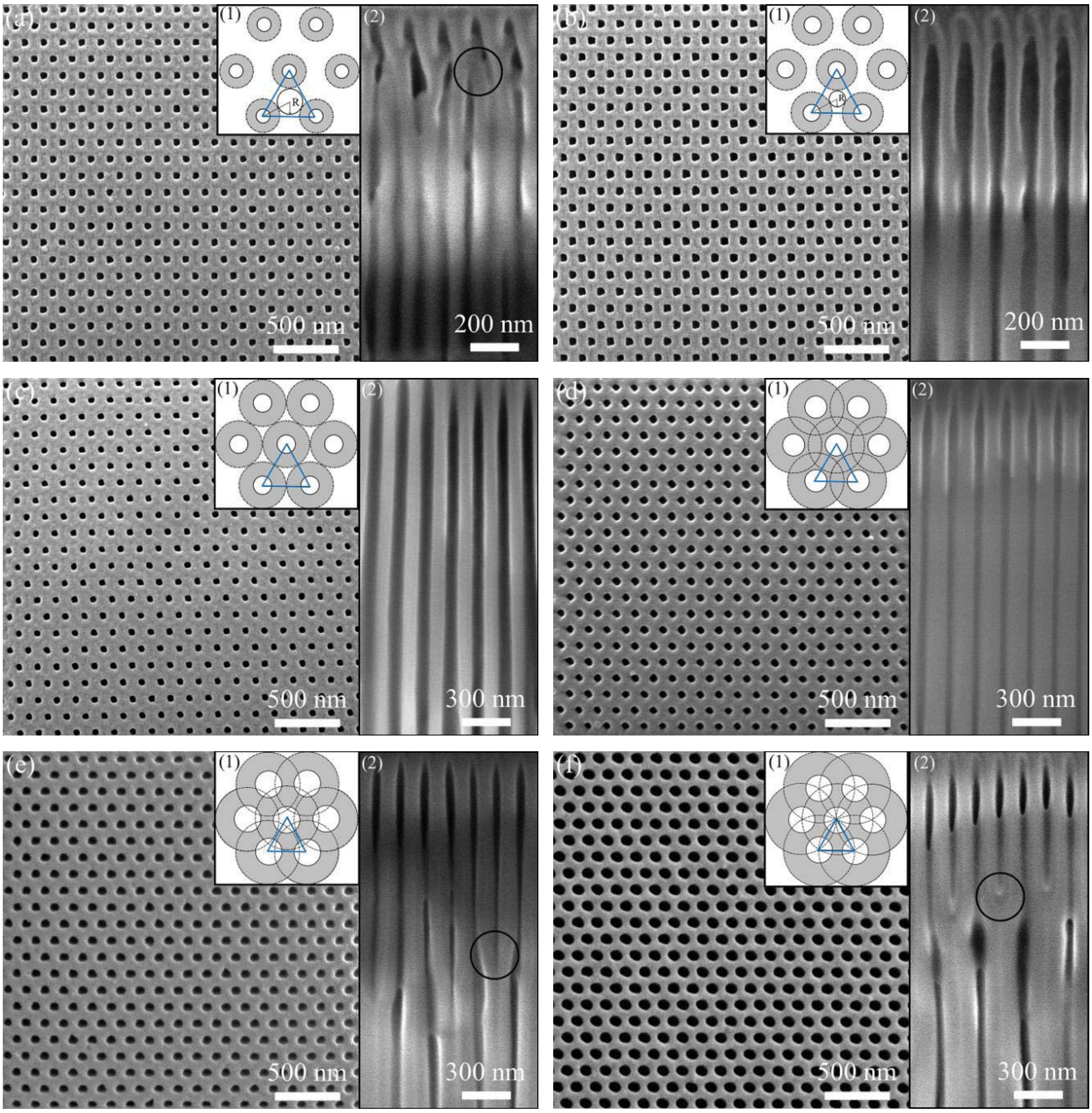

**Figure 3-9**. SEM images of anodized nanopore patterns with the same FIB pattern but different anodization condition. (a) 40 V, (b) 50 V, and (c) 60 V in 0.3 M oxalic acid at 0°C for 5 min. (d) 80 V, (e) 90 V and (f) 120 V in 0.05 M oxalic acid at 0°C for 5 min. Insets 1 in all images are the schematic drawing of the oxide outer layers of corresponding nanopores, and insets 2 in all images are the cross section images of corresponding nanopores at 52° tilt angle. The circles in the insets show the branch and termination of the nanopore.

### 3.3.4. Summary

With the guidance of the FIB patterned concaves, the interpore distance range for ordered porous anodic alumina enlarges. At 140 V in 0.3 M phosphoric acid, ordered hexagonal nanopore arrays with interpore distance from 200 nm to 350 nm can be fabricated. Moreover, hexagonal AAO arrays with 150 nm interpore distances have been obtained under the applied potential from 50 V to 80 V in oxalic acid. Therefore, FIB pre-pattern guided anodization greatly enlarges the anodization window to achieve ordered AAO arrays, which offers more capability to design the AAO template with different interval distance and arrangement.

## 3.4. Effect of FIB pattern interpore distance during guided anodization

### 3.4.1. Introduction

With the guidance of hexagonal pre-patterned concaves, all nanopores preferential develop at the concave sites. However, this effective guidance is based on the condition that the interpore distance for pre-patterned concaves match with the interpore distance of the self-organized AAO by the relation of: $d_{inter}=k\times U$.[14] It also has been reported that the interpore distance of ordered alumina nanopore arrays can be reduced to $1/\sqrt{3}$ of the lattice constant of the guiding patterns if the anodization window is such that a new pore forms at the centre of three patterned concaves.[37-39] Ordered porous anodic alumina with 115 nm interpore distance was obtained by anodizing a 200 nm interpore distance pattern at 46 V in oxalic acid.[38] Similarly, an ordered 300 nm interpore distance nanopore arrangement was produced after the anodization of a nano-indented concave pattern with 500 nm interpore distance at 120 V in phosphoric acid.[39] Therefore, the interpore distance plays an important role for the anodization result. In this section, I analyze the effect of $d_{inter}$ of pre-patterned concave arrays on AAO structure.

### 3.4.2. Experimental procedure

The Al foils are annealed in Ar atmosphere at 500ºC for 2 h, and then degreased in ethanol and acetone, followed by immersed in a 0.5 wt% NaOH solution to remove the oxide layer. Subsequently, the aluminum foils were electropolished in a 1:4 mixture of perchloric acid/ethanol (1/4 volume ratio) under a constant voltage of 12 V at room temperature with 500 rpm stirring speed for 5 min. The concave arrays with different arrangements and different interval distances were created by dual beam focused $Ga^+$ ion bean microscope (FIB, FEI Helios 600 NanoLab, Hillsboro, OR). The acceleration voltage was 30 kV, the current is 28 pA, and the beam dwell time at a specific location per scan was 3 μs. For the concaves with uniform diameter, the total FIB milling time at each concave is 25 ms. For the concave arrays with alternating diameter, the designed diameter of large concave was twice of small concaves, thus the total FIB milling time for small concave and large concave was 25 ms and 100 ms, respectively. The FIB patterned Al foils were anodized in 0.3 M phosphoric acid under 20 mA constant current at 0°C for 5 min. The voltage was ~140 V after a few seconds of anodization. Pore opening was carried out in 5 wt% phosphoric acid at 30°C for 10 min.

### 3.4.3. Results and discussion

Figure 3-10 shows the SEM images of the FIB patterns with different interpore distance after the anodization in 0.3 M phosphoric acid at 140 V for 5 min. As discussed in Figure 3-7, highly ordered AAO with interpore distance ranges from 200 nm to 350 nm can be obtained by FIB pre-pattern guided anodization. When interpore distance further increases to 400 nm, all nanopores still only grow at FIB patterned locations (Figure 3-10a). When the interpore distance increases to 500 nm, the nanopores develop at FIB patterned concaves have hexagonal outer shape (Figure 3-10c). However, new and small nanopores develop at the tri-junction center. When the interpore distance is further increased to 800 nm (Figure 3-10d), the nanopores initiate from the FIB patterned concave locations are fully expand the outer diameter into circle shape. And random nanopores develop between the neighboring nanopores, the small pore size and arrangement become irregular.

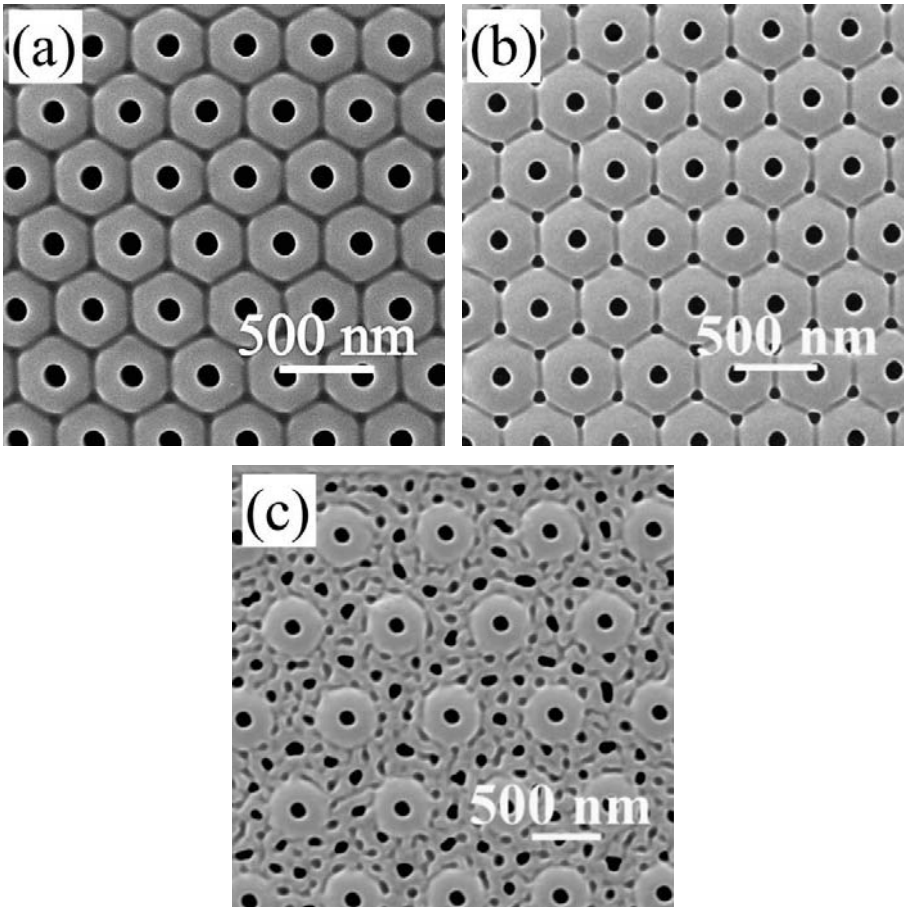

**Figure 3-10**. AAO arrays under the guidance of the hexagonal FIB patterns. The interpore distances are (a) 400 nm, (b) 500 nm, and (c) 800 nm.

The pore size and arrangement can also be directly affected by the interpore distance. As discussed in Figure 3-2, AAO with alternating-sized pores are created by the guidance of alternating-sized concave pattern with 65 nm and 45 nm pore sizes and 200 nm interpore distance. When the interval distance of same alternating-sized concave pattern is increased to 350 nm (Figure 3-11a), the diameters of the anodic nanopores developed from the large and small concaves are very close, around 105 nm. Ordered hexagonal nanopore arrays with uniform pore diameter have been fabricated. The main difference is the oxide wall thicknesses around the large and small concaves, with the large concaves showing thicker oxide walls. This is believed to result from the more extensive growth of the oxide walls for the large concaves before being restricted by their neighbors.

When the interpore distance of the FIB patterned concaves is increased to 500 nm (Figure 3-11c), the diameters of the anodized nanopores developed from the large and small concaves are close to each other, around 125 nm (Figure 3-11d). The oxide wall shapes for both pore sizes are regular hexagonal. Since the interpore distance is much larger than 350 nm, the value required for self-organized anodization in this study, the oxide walls of each FIB patterned pores fully grow before coming in contact with those of the neighboring pores during the anodization. The un-anodized space at the junctions of three neighboring pores increases as the interpore distance increases. When the interpore distance is 500 nm, the junction space is large enough to develop a new pore. Since the junction space of the three neighboring pores is limited and the new pores form later during the anodization, the new pores have a smaller diameter (~70 nm).

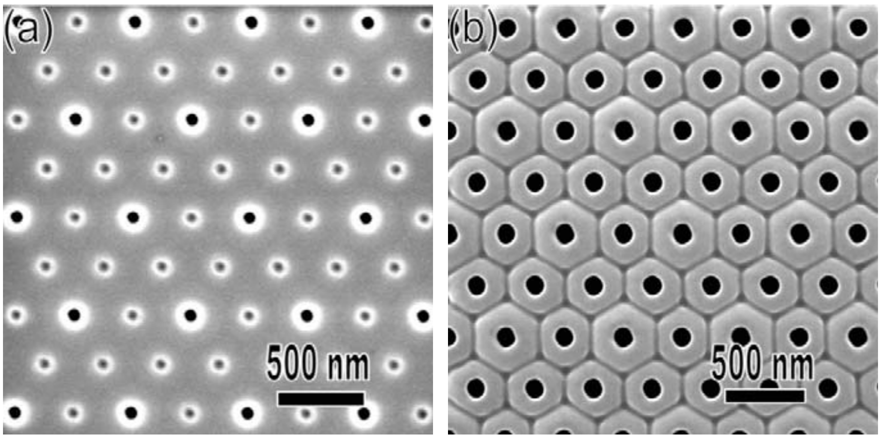

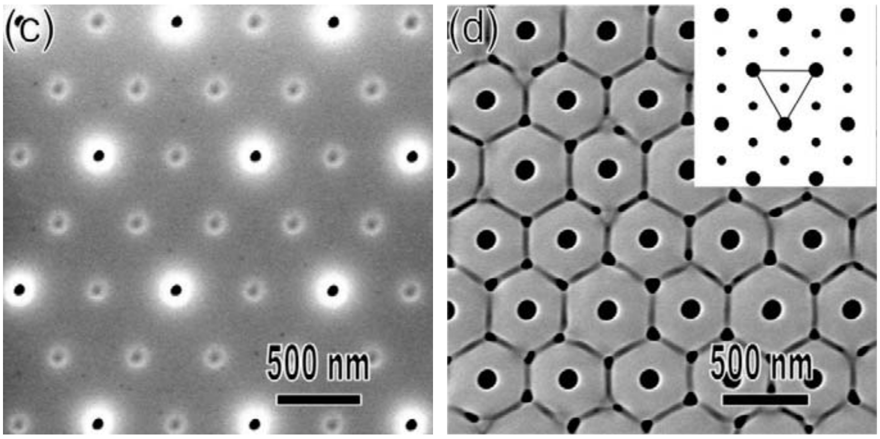

**Figure 3-11**. (a) FIB patterned alternating-sized concaves with 350 nm interpore distance, (b) FIB pattern (a) after the anodization, (c) FIB patterned alternating-sized concaves with 500 nm interpore distance, (d) FIB pattern (c) after the anodization.

Based on the above understanding, a variety of alternating diameter nanopore arrays with different arrangement of small and large pores can be obtained by designing different FIB concave patterns. Figure 3-12a shows the FIB patterned concaves with graphite lattice structure and the interpore distance is 250 nm. After the anodization, the anodized nanopores (large pores) remain the graphite lattice structure (Figure 3-12b). The shape of the anodized nanopores is not round but somewhat triangular because of the confinement from the three neighboring pores, as discussed in Figure 3-2b. Small and shallow pores form at the center of six neighboring large pores. In other words, the large pore locates at the center of triangle gravity of three small neighboring pores. When the interpore distance of the FIB patterned concaves is increased to 300 nm (Figure 3-12c), alternating diameter nanopore arrays are obtained (Figure 3-12d). Again, the large pore locates at the center of the triangle gravity of three small neighboring pores; the small pore locates at the center of the hexagonal gravity of six large neighboring pores. The shape of the oxide walls developed from the FIB patterned concaves is triangular. The diameters of the large pores and small pores are 120 nm and 60 nm, respectively. The 120 nm large pore diameter is very similar to that in Figure 3-11c, considering the large interpore spacing with the missing sites. Different from Figure 3-11b, the small pores are more developed in Figure 3-12d. This is because the large interpore distance in Figure 3-12d allows the small pores to grow more before being confined by the oxide walls from the large pores. Because of the larger influence of the better developed small pores, the large pores are also more round compared to those in Figure 3-

12b. Another difference is the more visible presence of the oxide wall boundaries shown in Figure 3-12d.

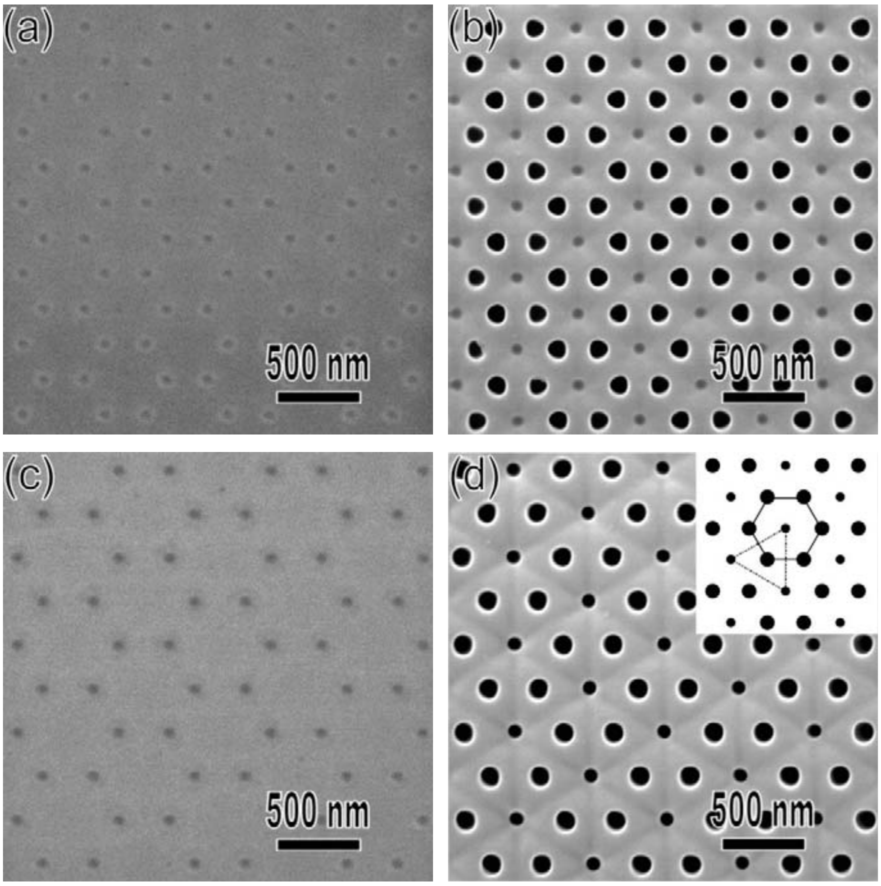

**Figure 3-12**. FIB patterned concaves with graphite lattice structure and the interpore distance is: (a) 250 nm, (c) 300 nm; (b) and (d) are the SEM images of the FIB patterns (a) and (c) after the anodization, respectively. The insert in (d) is the schematic of the alternating nanopore arrangement.

Different from all the hexagonal patterns discussed so far, Figure 3-13a shows the FIB patterned concaves in rectangular arrangement with the short and long interpore distances at 200 nm and $200\sqrt{3}$ nm, respectively. After the anodization, the nanopores remain in the rectangular arrangement (Figure 3-13b), which is fundamentally different from the familiar hexagonal arrangement. Due to the asymmetrical confinement of the neighboring pores, the shape of the nanopores is not round. Small and very shallow pores form at the center of four neighboring large pores. This is because the interpore distance is small, the oxide walls of each FIB patterned pores contact with those of the neighboring pores before full development, thus there is no space left to grow new pores. When the short and long interpore distances are increased to 300 nm and

$300\sqrt{3}$ nm, respectively (Figure 3-13c), new small pores form at the center of the large pores and a new alternating diameter nanopore hexagonal arrangement is obtained (Figure 3-13d). The small pore locates at the center of the rectangle gravity of the four large neighboring pores, and the large pore locates at the center of the rectangle gravity of the four small neighboring pores. The diameter of the large pore is 125 nm, and the diameter of the small pore is 80 nm. The 125 nm large pore diameter is similar to those in Figure 3-12d. The pores are round because of the symmetrical arrangement of their neighbors.

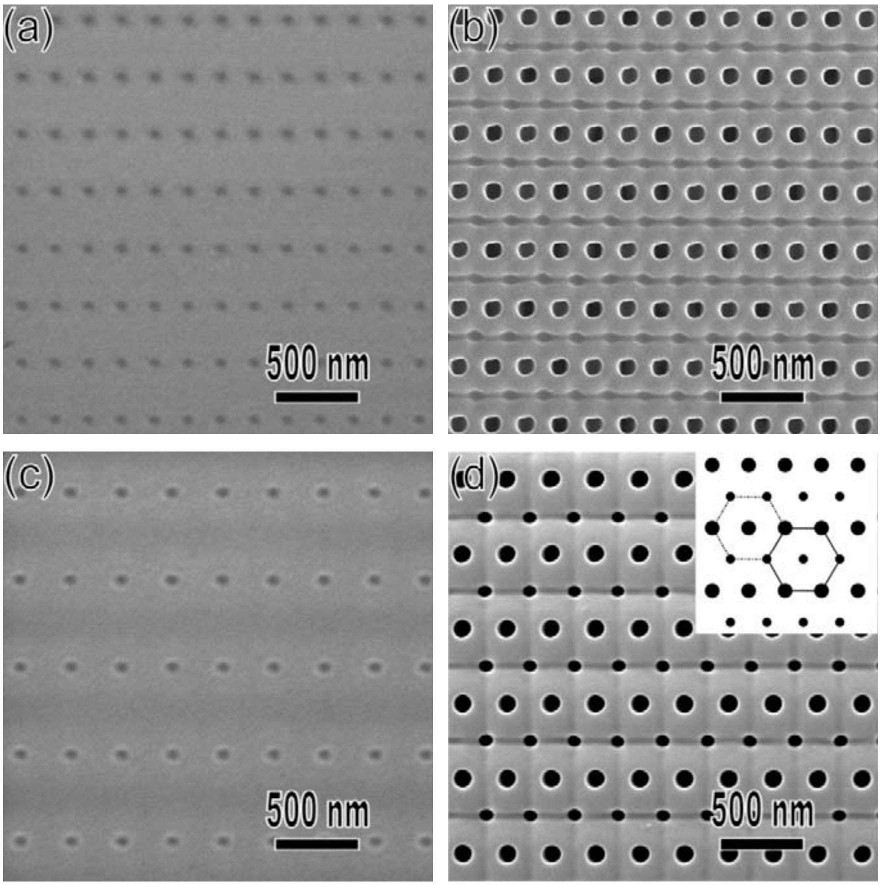

**Figure 3-13**. FIB patterned concaves in rectangular arrangement, the long interpore distance is $\sqrt{3}$ times of the short interpore distance, and the short interpore distance is: (a) 200 nm, (c) 300 nm; (b) and (d) are the SEM images of the FIB patterns in (a) and (c) after the anodization, respectively. The insert in (d) is the schematic of the alternating nanopore arrangement.

### 3.4.4. Summary

The interpore distance of FIB pre-patterned concaves influence the validity of guided anodization. When the interpore distance increases to 500 nm, there are new nanopores start to develop at the tri-junction center of hexagonal pattern. Moreover, the large interpore distance also sacrifices the successful guidance of alternating-sized concaves to produce alternating-sized AAO. Due to the large space for all concaves to grow, the nanopores develop from small concaves and large concaves have similar diameter. Small interpore distance restrict all nanopores follow the FIB patterned concaves even with graphite lattice structure or rectangular, while large interpore distance motivate new nanopores grow at the center of graphite lattice and rectangular patterns.

## 3.5. AAO with periodically pore density

### 3.5.1. Introduction

Most of the AAO research focuses on homogeneously distributed nanopore arrays; novel nanopore arrangements with periodically varying nanopore distribution have not been studied. The only exception is the fabrication of AAO with Moiré patterns by adjusting the rotation angle between two identical hexagonal nano-indented patterns.[151] Moiré patterns are composite patterns when repetitive structures are superposed on each other at certain rotation angles. The superposed Moiré pattern has alternating high and low area specific nanopore densities, although the original patterns are simple patterns with uniform feature arrangements. Although a Moiré pattern has various interpore distances, the whole pattern still has long-range periodicity. There are many different ways to generate Moiré patterns, for such as by overlapping two similar patterns with a rotation angle, or by using different initial patterns such as square or graphite lattice arrangements. Up to now, the fabrication of AAO with these Moiré patterns under guidance of FIB concave patterns has not been studied yet.

Several mathematical methods have been used to investigate the properties and periodicities of Moiré patterns.[152-154] The spectral approach based on the Fourier transform theory is the most commonly used method.[155-156] It has the benefit of analyzing the orientation and periodicity of Moiré patterns in both real and reciprocal spaces. The periodicity D of a Moiré pattern depends on the lattice constant of both the original patterns and the rotation angle. After applying Fourier transform to the reciprocal space, the fundamental frequency vector of a Moiré pattern in the reciprocal space is determined by the fundamental frequency vectors $\mathbf{f_1}$ and $\mathbf{f_2}$ from the first original pattern and $\mathbf{f_3}$ and $\mathbf{f_4}$ from the second original pattern: $\mathrm{f} = \mathrm{k_1 f_1} + \mathrm{k_2 f_2} + \mathrm{k_3 f_3} + \mathrm{k_4 f_4}$. The symmetry is the same in both real and reciprocal spaces, and the periodicity of the corresponding Moiré pattern in the direct space is given by D=1/f.

In this study, focused ion beam patterned concave arrays created by overlapping two periodic patterns show the exceptional ability of guiding the subsequent anodization and fabricating porous anodic aluminum oxide with Moiré patterns, which have a wide range of interpore distances and area specific pore densities. The periodicity of the Moiré patterns can be predicted by the interpore distance of the initial patterns and the rotation angle.

### 3.5.2. Experimental procedure

The annealed Al foils were electropolished in perchloric acid/ethanol electrolyte at 12 V with 500 rpm stirring speed for 5 min. Moiré patterns were created by overlapping two bitmap patterns with a rotation angle by overlapping two bitmap patterns with different interpore distances. Each bitmap size is 15 μm × 15 μm. The rotation angle is 5º, 10º, 22.6º, 36.9º, and 45º. The interpore distance of the concaves is 350 nm, 400 nm, and 500 nm. Moiré patterns were created by dual beam focused $Ga^+$ ion bean microscope (FIB, FEI Helios 600 NanoLab, Hillsboro, OR). The acceleration voltage was 30 kV, the current is 93 pA, and the beam dwell time at a specific location per scan was 3 μs. The FIB milling time at each concave is 1.5 ms, and the total FIB milling for Moiré pattern is around 1 min. The FIB patterned Al foils were anodized in 0.3 M phosphoric acid under 20 mA constant current at 0°C for 5 min. The voltage was ~140 V after a few seconds of anodization. Pore opening was carried out in 5 wt% phosphoric acid at 30°C for 10 min.

In order to observe the backside of the AAO, the un-anodized Al layer was removed in a saturated $CuCl_2$ solution (99+%, Acros Organics, Pittsburgh, PA). PDMS with 3 mm thickness was poured onto the porous AAO before the reaction with saturated $CuCl_2$ solution in order to handle the thin and fragile AAO membrane. The cross section of the anodized nanopores was obtained in the FIB microscope by using 0.28 pA current to cut the patterned AAO.

### 3.5.3. Results and discussion

Figure 3-14 shows the SEM images of the FIB patterned concave Moiré patterns and the corresponding anodized porous AAO. The FIB patterned concave Moiré patterns (shown in the insets 1 of Figure 3-14) are created by the superposition of two square concave patterns with identical interpore distance and a rotation angle α. The interpore distance of the square concave arrays is 350 nm, and the rotation angle is (a) 5°, (b) 10°, (c) 22.6°, and (d) 36.9°, respectively. The diameters of the FIB patterned concaves are 45 nm, and the depths of those concaves are 10 nm. After the anodization in 0.3 M phosphoric acid at 20 mA constant current for 2 min (the voltage at steady state is 140 V), the porous AAO with various Moiré patterns is created with the same arrangements as the FIB patterned concave arrays, and the periodicity of the Moiré patterns is: (a) 4.0 μm, (b) 2.0 μm (c) 1.24 μm, and (d) 0.78 μm, respectively. Moreover, all the Moiré patterns are still in 4-fold symmetry. The interpore distances within the Moiré patterns have different values, such as 350 nm in circle 1 and 250 nm in circle 2 for Figure 3-14a. For the self-organized porous AAO, the interpore distance is only dependent on the anodization voltage with a proportional constant of 2.5 nm/V, and it is difficult to obtain ordered arrays with different interpore distances. With the guidance of the FIB patterned concave arrays, ordered hexagonal AAO with different interpore distances is obtained at the same anodization condition. Similarly, the sophisticated Moiré patterns with various arrangements are fabricated here under the guidance of FIB patterned concave arrays.

The long-range periodicity of the Moiré patterns can be understood as follows by the Fourier transform theory in the reciprocal space.[155-156] For the Moiré patterns created by rotating two identical square patterns, $f_1=f_2=f_3=f_4=1/d$, $\mathbf{f_1}$ is perpendicular to $\mathbf{f_2}$, $\mathbf{f_3}$ is perpendicular to $\mathbf{f_4}$ (Figure 3-14 insets 2). The frequency in the reciprocal space is determined by the fundamental vectors $f_a = f_1$-$f_3$ and $\mathbf{f_b} = \mathbf{f_2} - \mathbf{f_4}$. Since $\mathbf{f_a}$ is perpendicular to $\mathbf{f_b}$ and $|\mathbf{f_a}|=|\mathbf{f_b}|$, the Moiré pattern has the long-range 4-fold symmetry, which has been observed in Figure 3-14. The periodicity of the Moiré pattern is:

$$D = \frac{d_1 d_2}{\sqrt{{d_1}^2+{d_2}^2-2d_1 d_2 \cos\alpha}} = \frac{d}{2\sin\left(\frac{\alpha}{2}\right)}. \qquad (1)$$

From this equation, the periodicities of the Moiré patterns in Figures 3-14a-d are calculated to be 4.01 μm, 2.01 μm, 0.89 μm, and 0.55 μm, respectively. The first two values are in good agreement with the measured Moiré pattern periodicities (4.0 μm and 2.0 μm, respectively).

If two identical square patterns are superimposed at a certain angle that $\alpha$ =arctan (m/n) and $m^2 + n^2 = k^2$, where m, n, k are integers, then the fundamental frequency of the Moiré pattern in the reciprocal space is equal to zero. The periodicity of these Moiré pattern can be derived from another arrangement of the same square pattern with new fundamental frequency vector $f' = f/\sqrt{k} = \frac{f}{\sqrt{m^2+n^2}}$. In this view, after rotating $\alpha$ degree, the two new square patterns just overlap with each other, the composited pattern has same fundamental frequency vector $f' = f/\sqrt{k}$. For example, when the rotation angle is 22.6° ($\alpha$ =arctan (5/12), $\mathbf{f} = \mathbf{f_1} - 5\mathbf{f_2} + \mathbf{f_3} + 5\mathbf{f_4} = \mathbf{0}$, see Figure 3-14c inset 2), the new lattice spacing of the square pattern in the reciprocal space is $f' = f/\sqrt{13}$, and the periodicity for this Moiré pattern is $D=\sqrt{13}d=\sqrt{13} \times 350$ nm = 1.262 μm, which is in good agreement with the measured value in Figure 3-14c (1.24 μm). Similarly, when the rotation angle is 36.9°($\alpha$ =arctan (3/4), $\mathbf{f} = \mathbf{f_1} + 2\mathbf{f_2} - 2\mathbf{f_3} - \mathbf{f_4} = \mathbf{0}$, see

Figure 3-14d inset 2), the new lattice of the square pattern is $f^{'} = f//\sqrt{5}$, as shown in the inset 3 in Figure 3-14d. As a result, the periodicity for this Moiré pattern is $D=\sqrt{5}d=\sqrt{5}\times 350\ \text{nm} = 0.783\ \mu\text{m}$, which is in good agreement with the measured value in Figure 3-14d (0.78 μm). The reciprocal pattern has square arrangement, thus the composited Moiré pattern has 4-fold symmetry.

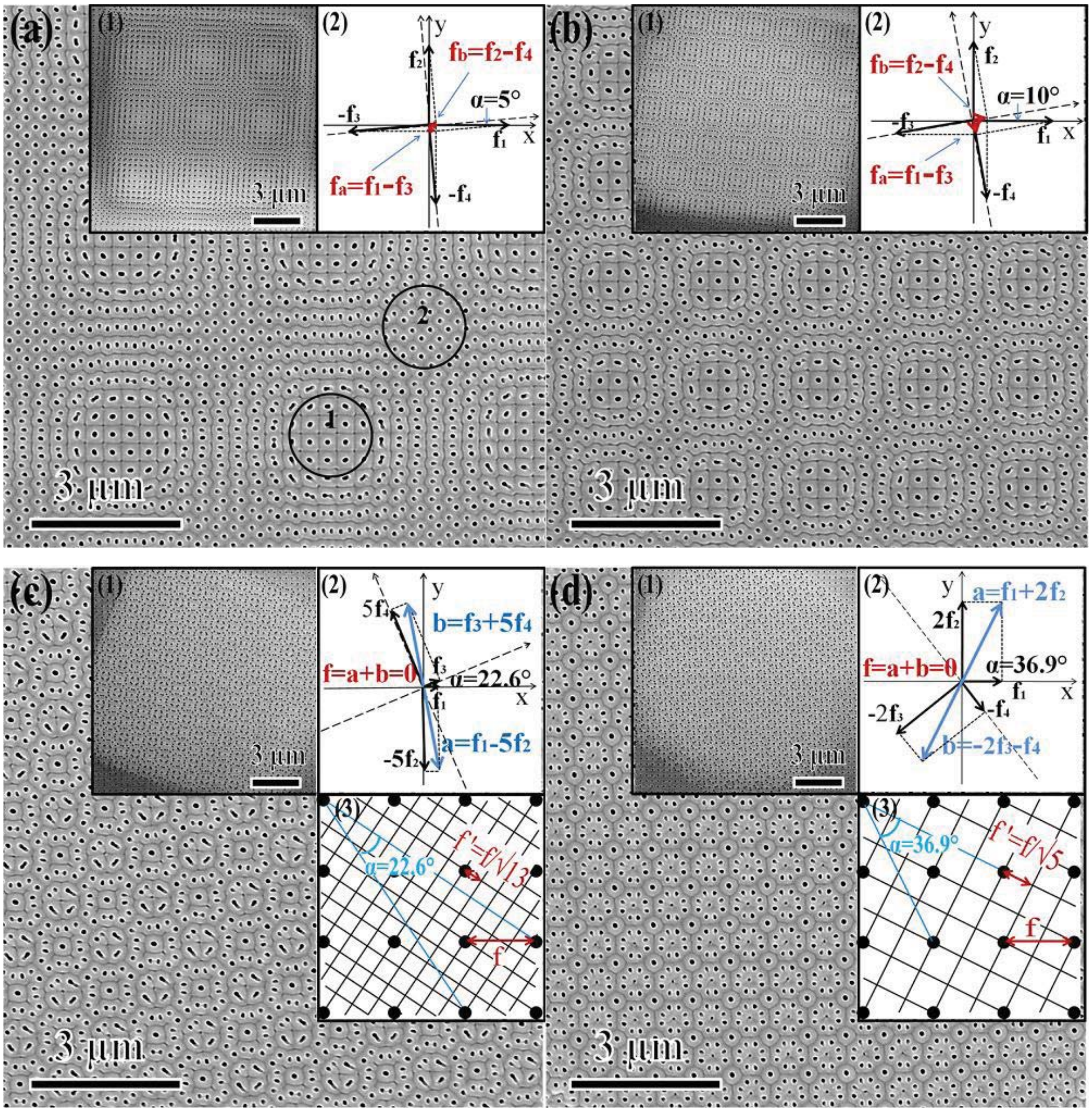

**Figure 3-14**. SEM images of porous AAO with Moiré patterns created from overlapping square patterns. The corresponding FIB patterned concave arrays are shown in the insets 1. The interpore distance of the square patterns is 350 nm, and the rotation angle between the square patterns is: (a) 5°, (b) 10°, (c) 22.6°, and (d) 36.9°, respectively. The insets 2 are the corresponding frequency vector diagram in the reciprocal

space. The insets 3 in (c) and (d) are the schematic of a square arrangement from a different view of the original square pattern. The scale bars in all insets are 5 µm.

After selectively removing the un-anodized aluminum with saturated $CuCl_2$ solution, Figure 3-15 shows the backside and cross section of the Moiré pattern from the square arrangements with 5° rotation angle as explained in Figure 3-14a. As discussed in Figure 3-14a, these Moiré patterns have different interpore distance, such as 350 nm in circle 1 and 250 nm in circle 2. The orientations of the square arrangements in circle 1 and circle 2 are different. After the anodization in 0.3 M phosphoric acid at 20 mA for 30 s, the thickness of the AAO is ~250 nm (the inset of Figure 3-15a), and the barrier layer clearly shows that both the square arrangement with 350 nm interpore distance (circle 1) and that with 250 nm interpore distance (circle 2) remain unchanged as in Figure 3-14a.

When the anodization time prolongs to 2 min, the thickness of the AAO increases to 1 µm (the inset of Figure 3-15b), and the periodic arrangement of the pores maintains the Moiré pattern. According to our previous work, ordered hexagonal porous AAO with 200 nm to 425 nm interpore distances can be fabricated under the guidance of FIB patterned concaves at the same anodization condition. Since the pores in the region near the circle 1 have very small interpore distance (175 nm as shown in Figure 3-15a), some pores terminate and change the arrangement into a square, just the same as in circle 1. Because most of the interpore distances range from 250 nm to 350 nm, these nanopores grow vertically and maintain the sophisticated Moiré pattern arrangement when the pore depth is around 1 µm. The flat surface of the AAO backside shows that all the nanopores have similar pore depth of ~1 µm.

When the anodization time further prolongs to 5 min, the depth of the nanopores increases to 2.5 µm (the inset of Figure 3-15c), and the arrangement in circle 2 changes. The initial Moiré pattern arrangement moves into square arrays with 350 nm interpore distance, separated by some less organized pores at the quadrate junctions. Therefore, the Moiré pattern disappears. However, the pattern transformation process is different from the stable growth the hexagonal nanopore arrays with 200-425 nm interpore distances. Unlike the symmetric hexagonal confinement of the neighboring pores, the asymmetric pore arrangement in the Moiré pattern leads to asymmetric mechanical stress after the anodization. Therefore, the nanopores within the Moiré pattern are unstable when the pores grow deep. However, the arrangement does not change into totally disordered. The square arrangement of the pores in circle 1 has the interesting effect of "aligning" the neighboring pores. As a result, the pores with interpore distance less than 350 nm tends to change the arrangement to the same as the pores in circle 1 with 350 interpore distance and square arrangement.

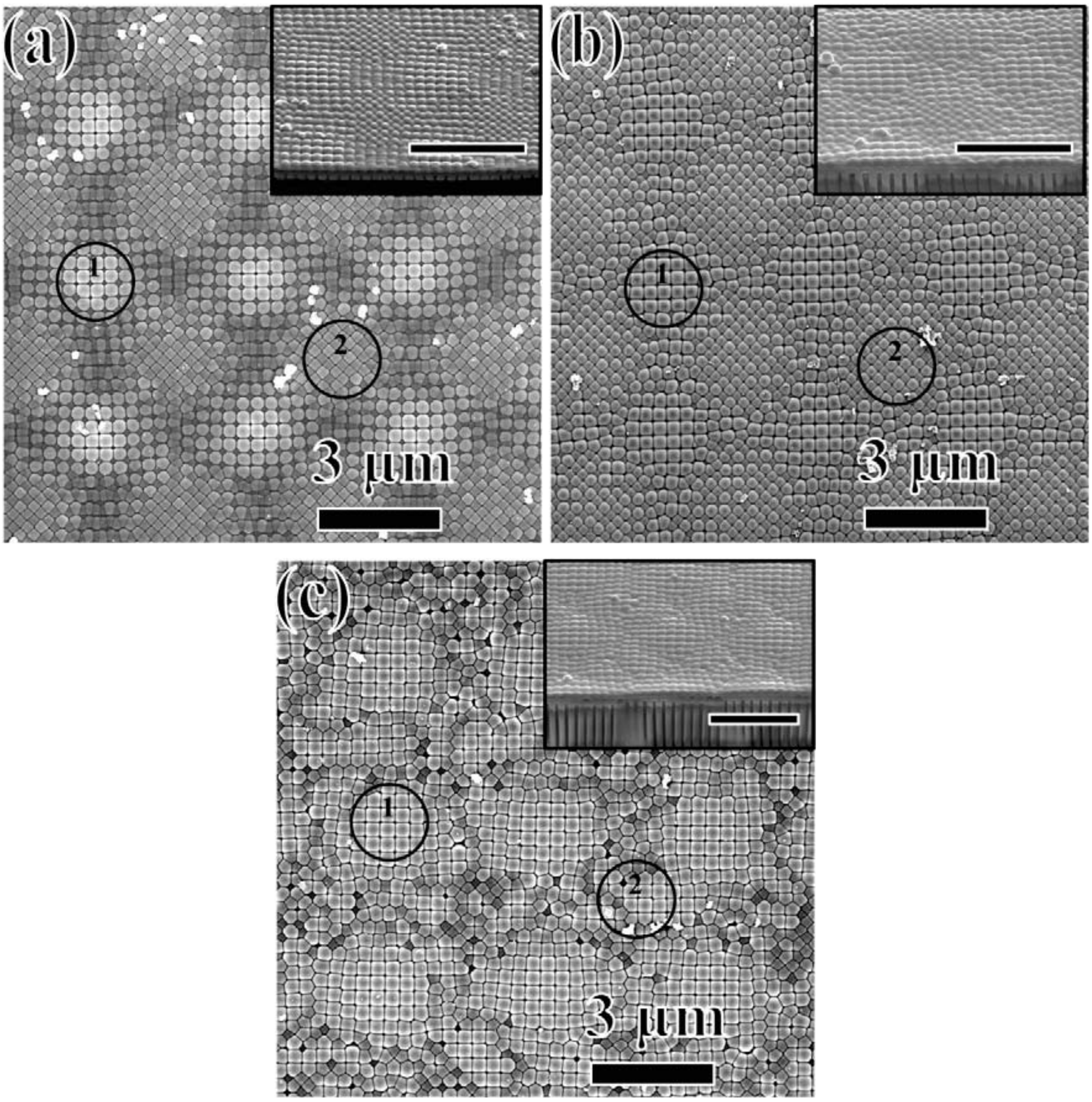

**Figure 3-15**. SEM images of backside and cross section of porous AAO with Moiré patterns created from square pattern concaves, the interpore distance of the square pattern is 350 nm, the rotation angle is 5°. The anodization time in 0.3 M phosphoric acid at 20 mA is: (a) 30 s, (b) 2 min, and (c) 5 min. The insets in the images are the tilted views of the cross section of the corresponding porous AAO at 52° angle. The scale bars in all insets are 3 μm.

Moiré patterns can also be created by the superposition of two square patterns with different interpore distances. The insets 1 in Figure 3-16 show the SEM images of the FIB patterned concave arrays with the superposition of two different square patterns. The interpore distances of the two square patterns are 400 nm and 500 nm, respectively, and the rotation angle is (a) $\alpha = 0°$, (b) $\alpha = 45°$. The diameters of the concaves are 45 nm and the depths of the concaves are 10 nm.[12] After the anodization in 0.3 M phosphoric acid at 20 mA constant current for 2 min (Figure 3-16), the porous AAO maintains the same Moiré pattern arrangements as the FIB patterned concave arrays, and the periodicity is (a) 1.94 µm and (b) 3.09 µm. The periodicity of the Moiré pattern in Figure 3-16a is in good agreement with the theoretical value $D = \frac{d_1 d_2}{\sqrt{d_1{}^2 + d_2{}^2 - 2d_1 d_2 \cos\alpha}} = \frac{d_1 d_2}{|d_1 - d_2|} = 2.00$ µm. The resulting Moiré pattern still has long range 4-fold symmetry. When the rotation angle is $45° > \sin^{-1}(d_1/2d_2) = 23.6°$, $|\mathbf{f_1} + \mathbf{f_3} - \mathbf{f_4}| < |\mathbf{f_1} - \mathbf{f_3}|$, the fundamental frequency vectors change to $\mathbf{f_a} = \mathbf{f_1} + \mathbf{f_3} - \mathbf{f_4}$ and $\mathbf{f_b} = \mathbf{f_2} - \mathbf{f_3} - \mathbf{f_4}$, where $\mathbf{f_a} \perp \mathbf{f_b}$ and $|\mathbf{f_a}| = |\mathbf{f_b}| = |\sqrt{2}/d_2 - 1/d_1|$ (as shown in the inset 2 of Figure 3-16b). The corresponding AAO Moiré pattern still has 4-fold symmetry and the periodicity is $D = \frac{1}{|\sqrt{2}/d_2 - 1/d_1|} = 3.04$ µm, in good agreement with the measured value of 3.09 µm.

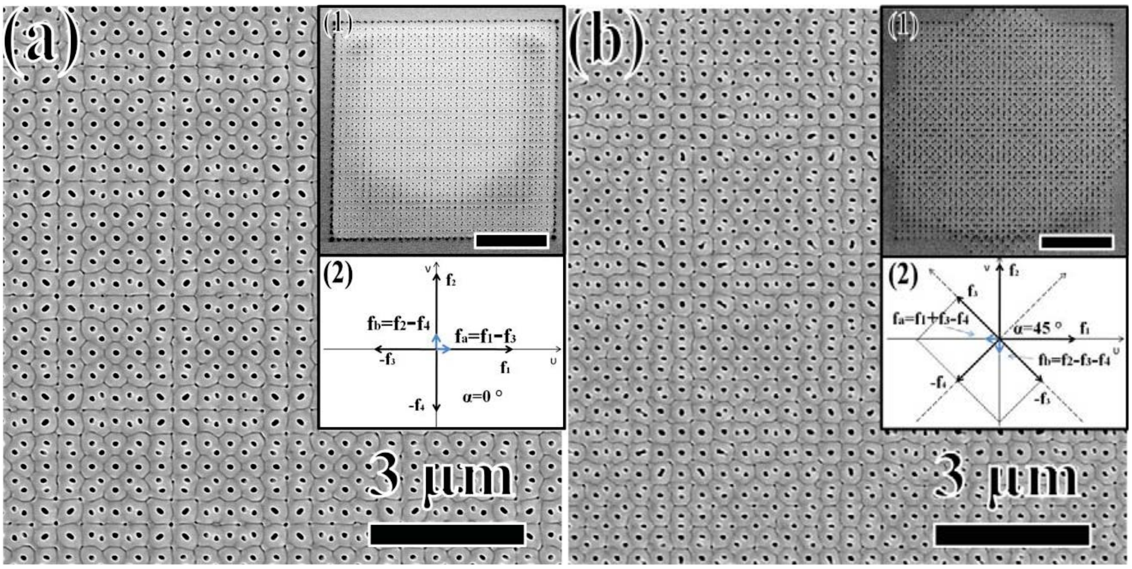

**Figure 3-16**. SEM images of porous AAO with Moiré patterns created from overlapping two square patterns with different interpore distances ($d_1$=400 nm and $d_2$=500 nm). The corresponding FIB patterned concave arrays are shown in the insets 1. The rotation angle is (a) $\alpha = 0°$, (b) $\alpha = 45°$. The insets 2 are the frequency vector diagram in the reciprocal space. The scale bars in all insets are 5 µm.

### 3.5.3. Summary

AAO with various Moiré patterns have been successfully fabricated by FIB guided anodization. The FIB patterned Moiré concave arrays are created by the superposition of two simple patterns with a rotation angle, such as hexagonal and square arrangements. Porous AAO Moiré patterns, with various interpore distances and alternating high and low nanopore area specific densities, are created and matched well with theoretical calculations. The maximum depth of the ordered nanopores for the AAO Moiré patterns is ~1 μm. With further growth of the nanopores, the Moiré pattern arrangement disappears.

# Chapter 4. Nanoimprint and Soft Lithographic Molding

## Abstract:

Nanoimprinting a prepolymer by AAO template has successfully synthesized vertically aligned and high aspect ratio h-PDMS nanorod arrays with Moiré pattern arrangements. Decreasing the surface energy of AAO template by using a proper demolding agent is critial to the release of the h-PDMS nanorods. Soft lithographic molding high solids loading ZnO nanoparticle suspension creates sub-micrometer rod arrays with an aspect ratio around 1. Ceramic micro-fabrication by soft lithography normally utilizes ceramic precursor solutions or sol-gel process. However, the low solids loading of the starting materials compromises the fidelity of soft lithography. In this study, well-dispersed, high solids loading ZnO nanoparticle suspensions are prepared by electrosterically stabilizing 20 nm ZnO nanoparticles. PDMS molds with different surface modifications are exploited to optimize the filling depth of the suspension into the mold cavities, producing ZnO sub-micrometer rods with the same dimensions as the mold features.

## 4.1. Fabricate polymer nanorods by nanoimprint with AAO template

### 4.1.1. Introduction

In recent years, polymeric nanorod arrays have attracted increasing attention due to the potential applications as superhydrophobic surfaces,[157] artificial adhesive structures,[158] and soft lithography molds.[159] Using porous AAO templates as molds to confine polymer melts and prepolymer solutions is a simple and versatile method to generate polymeric nanostructures.[160-162] As a rule, polymer melts and prepolymer solutions should have low surface energy and spread over the high surface energy alumina template pore walls and completely fill the nanopores.[163] When the temperature is cooled below the solidification temperature of the polymer, or when the prepolymer solution cross-links within the nanopores, polymeric nanorod arrays will form. However, synthesis of well-aligned and freestanding nanorods with small diameters and high aspect ratios is still difficult. Mechanically lifting off the polymeric nanorods from silanized porous templates is one method to overcome the aggregation of the polymeric nanorods.[164-165]

Using low surface energy organosilane to reduce the adhesion between the polymer nanorods and the pore walls can further help the release of the nanorods from a template.[166]

Poly(dimethylsiloxane) (PDMS) is highly UV-transparent and has low Young's modulus and surface energy, which allows it to be used as a soft lithographic molding material for conformal contact and easy release from the templates.[167-168] However, its low Young's modulus of ~1.5 MPa limits the ability of achieving sub-100 nm fidelity.[169-170] Hard poly(dimethylsiloxane) (h-PDMS), which has short cross-linker lengths and high Young's modulus of ~9 MPa, can overcome the low modulus problem and extend the resolution below 100 nm.[171] Although h-PDMS is brittle, composite molds can be made by using a thick backing layer of PDMS (~3 mm) to support a thin layer of h-PDMS (~30 μm).[172] For the h-PDMS replication of a silicon template with patterned nanoposts, the resolution is 80 nm. The bilayer composite mold further increases the resolution to 30 nm with phase-shifting photolithography.[173] However, for h-PDMS replication of anodized nanopores, h-PDMS nanorod bending, lateral collapse (adhesion between neighboring polymeric rods when they are close to each other), and ground collapse (collapse of nanorods under their own weight or suface adhesion force from the substrate) are serious problems, even for low aspect ratio nanorods.[174-177] In this study, highly ordered vertical h-PDMS rod arrays with small diameters and high aspect ratios are investigated by nanoimprint with AAO template.

### 4.1.2. Experimental procedure

Prior to filling h-PDMS into AAO template, a monolayer of 1H, 1H, 2H, 2H-perfluorodecyltrichlorosilane (97%, Sigma-Aldrich, St. Louis, MO) was self-assembled onto the AAO to yield a low energy surface to facilitate the detachment of the molded h-PDMS from the template. First, the porous anodic alumina was treated with aqueous hydrogen peroxide (30%, Acros Organics, Pittsburgh, PA) at 50°C for 2 h, rinsed with water, and dried in air. Then, the porous anodic alumina was placed in a petri dish with a few drops of 1H, 1H, 2H, 2H-perfluorodecyltrichlorosilane, followed by keeping it in an oven at 90°C for 3 h and then at 130°C for 3 h.

To prepare the h-PDMS nanorod arrays, 3.4 g of vinyl PDMS prepolymer (VDT-731, ABCR, Germany), 18 μl of Pt-containing catalyst (platinum-divinyltetramethyldisiloxane, SIP6831.2, ABCR, Germany), and one drop of modulator (2,4,6,8-tetramethyl-2,4,6,8-

tetravinylcyclotetrasiloxane, 87927, Sigma-Aldrich, St. Louis, MO) were mixed. Then 1 g of hydrosilane prepolymer (HMS-301, ABCR, Germany) was added into this mixture and gently mixed. Within 3 min, the h-PDMS precursor was spin-coated onto the porous anodic alumina template at 500 rpm for 5 s and then at 1500 rpm for 1 min. After being cured at 60℃ for 30 min, a degassed perpolymer layer (~3 mm) of Sylgard 184 PDMS was poured onto the h-PDMS layer and cured for 2 h at 60℃. The h-PDMS was carefully peeled off from the porous anodic alumina while still warm. The porous anodic alumina patterns and h-PDMS nanorod arrays were characterized by scanning electron microscopy (Quanta 600 FEG, FEI Company, Hillsboro, OR). The tilted views of the h-PDMS nanorods were obtained by the dual scanning electron microscope with 52° tilt angle.

### 4.1.3. Results and discussion

When the porous AAO Moiré patterns are used as molds for soft lithographic molding of polymer nanorod arrays, the rate of h-PDMS flow is determined by the surface tension, viscosity of the prepolymer, the size of the nanopores, and the depth of the nanopores. The time required for the h-PDMS to fill the anodic alumina nanopores can be estimated by:[178-179]

$$t = \frac{2\eta z^2}{R\gamma \cos\theta_c} \qquad (4\text{-}1)$$

where $t$ is the time, $\eta$ is the viscosity of the h-PDMS, $z$ is the depth of the nanopores to be filled, and $R$ is the hydraulic radius (the ratio between the volume of the liquid in the nanopore and the area of solid/liquid interface; $R$ is one-half of the nanopore radius), $\gamma$ is the surface tension at the polymer-air interface, $\theta_c$ is the contact angle between the h-PDMS and the anodic alumina nanopore mold. In a previous study,[180] it has been shown that the viscosity $\eta$ of the uncured h-PDMS prepolymer is 1 Pa·s, which is significantly lower than that of 3.74 Pa·s for the uncured Sylgard 184 and is more desired for the nanopore filling. In this study, the AAO nanopore depth is less than 1 μm. The diameter of the nanopores is around 80~120 nm. The surface tension $\gamma$ of h-PDMS is around 22-25 mN/m.[171, 181] The contact angle between the h-PDMS prepolymer and the porous anodic alumina is ~75°. Based on equation (12), complete filling of h-PDMS into the high surface energy AAO nanopores only takes ~18 ms. Spin coating the h-PDMS prepolymer at 500 rpm for 5 s and at 1500 rpm for 60 s is long enough for the h-PDMS to completely fill the nanopores. With 1H, 1H, 2H, 2H-perfluorodecyltrichlorosilane to minimize the adhesion between the pore walls and the nanorods formed inside the nanopores, the h-PDMS nanorod arrays can be easily peeled off from the AAO mold.

For polymeric nanorod arrays, the limitations for achieving high aspect ratio and stable arrays are mainly bending, ground collapse, and lateral collapse.[169, 182] When the diameter of the polymeric rods is micron-sized and well separated from each other, the gravity is the major force to induce bending and ground collapse.[183] When the diameter of the polymeric rods is reduced to sub-micron and nanometers, surface adhesion from the substrate is the main force to induce bending and ground collapse.[184] More importantly, when small diameter polymeric nanorods are close to each other, the adhesion of the neighboring nanorods, and thus lateral collapse, dominate over ground collapse and lead to lateral collapse.[185] For the h-PDMS nanorod arrays fabribcated from the AAO templates, the diameter is small and the density is high. Therefore, the limitation for the nanorod array stability is mainly from the lateral collapse and is determined by the critical aspect ratio:[182, 185]

$$\left(\frac{h}{d}\right)_c = \sqrt[3]{\frac{3^{3/4}\pi E w^{3/2}}{2^{1/4}32\gamma(1-\nu^2)^2 d^{1/2}}} \qquad (4\text{-}2)$$

where E is the Young's modulus of h-PDMS (~9 MPa), w is the lateral separation between adjacent h-PDMS nanorods, $\gamma$ is the surface tension of h-PDMS (22-25 mN/m), $\nu$ is the Poisson's ratio of h-PDMS, which is an insensitive facor in equation (4-2) and ranges from 0.3 to 0.5,[186] d is the diamter of the nanorods, and h is the height of the nanorods. If the aspect ratio exceeds the theretical critial value, the h-PDMS nanorod arrays would be unstable and lateral collapse would occur.

Figure 4-1 shows the h-PDMS nanorod arrays with Moiré pattern arrangements after being peeled off from the AAO molds. The h-PDMS nanorod arrays in Figure 4-1a have the same diameter and arrangement as the AAO nanopore Moiré patterns in Figure 3-14b. The AAO mold in Figure 4-1a is anodized for 1 min, and the depth of the AAO nanopores is 500 nm. The tilted SEM image in the insert of Figure 4-1a shows that all the h-PDMS nanorods are separated from each other and no lateral collapse occurs. All the h-PDMS nanorods have the same length of ~500 nm, which confirms the complete filling of h-PDMS into the AAO nanopores within the Moiré pattern. The h-PDMS nanorods in the low density region have 120 nm diameter and 230 nm inter-rod distance, and the aspect ratio is 4.2; the h-PDMS nanorods in the high density region have 80 nm diameter and 120 nm inter-rod distance, and the aspect ratio is 6.3. The predicted critical aspect ratio from equation (4-2) is, however, 1.7 and 1.9, respectively (as shown in Table 4-1). Even though the actual aspect ratio is larger than the theoretical critical value, the h-PDMS nanorods are still stable and maintain the vertical alignment. The main reason is believed to come from the low surface energy mold releasing agent used, which reduces the surface tension of the h-PDMS nanorods and increases the critical aspect ratio against the lateral collapse. When the depth of the AAO nanopores increases to 750 nm (anodized for 1.5 min, Figure 4-1b), the aspect ratio for the large diameter h-PDMS nanorods in the low density region increases to 6.3, and the h-PDMS nanorods are still stable and remain vertical alignment. For the thin h-PDMS nanorods in the high density region, the aspect ratio is 9.4, but bending and lateral collapse occur. When the h-PDMS nanorods are long, there also exist some missing nanorods in the pattern due to the breakage of the h-PDMS rods during the peeling off process.

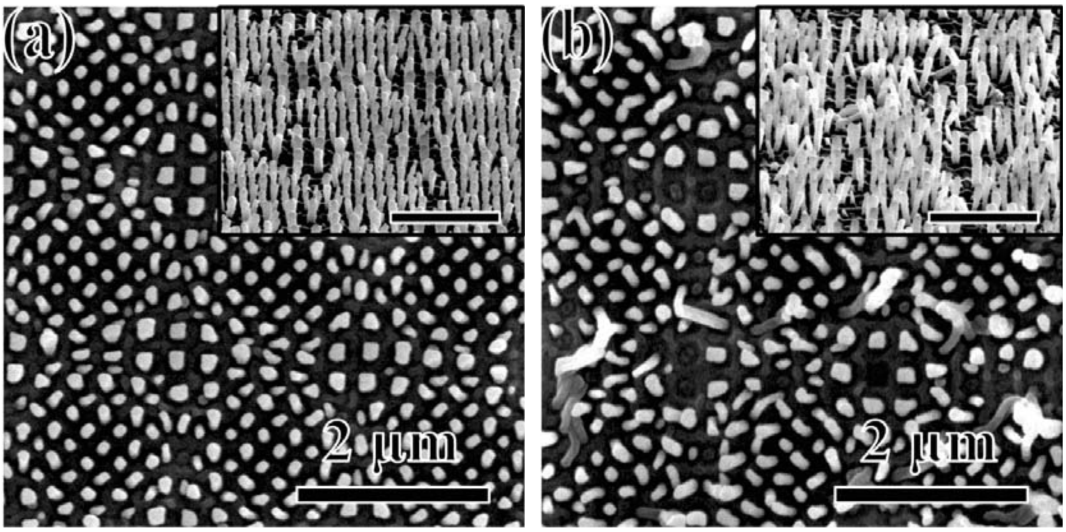

**Figure 4-1**. SEM images of h-PDMS nanorod arrays after demolding from porous anodic alumina template with square Moiré pattern, the interval distance is 350 nm, the rotation angle is 10°. (a) top view, the depth of the anodic alumina nanopore is 500 nm; (b) top view, the depth of the anodic alumina nanopore is 700 nm. The inserts are the tilt view of (a) and (b) under 52°. The scale bars in all inserts are 2 μm.

| h-PDMS rod dimensions | | | Aspect ratio | | Lateral collapse | | Demolding process | Reference |
|---|---|---|---|---|---|---|---|---|
| Diameter d (nm) | Height h (nm) | Spacing w (nm) | Calculated critical value | Experimental result | Predicted | Observed | | |
| 45 | 140 | 55 | 1.7 | 3.1 | Yes | Yes | Chemical etching | 174 |
| 50 | 350 | 100 | 2.3 | 7 | Yes | Yes | Peeling off without demolding agent | 175 |
| 50 | 900 | 100 | 2.3 | 18 | Yes | Yes | | |
| 200 | 318 | 200 | 2.8 | 1.6 | No | No | Peeling off with demolding agent | 176 |
| 200 | 747 | 200 | 2.8 | 3.7 | Yes | Yes | | |
| 810 | 2430 | 670 | 3.6 | 3 | No | No | Peeling off without demolding agent | 177 |
| 810 | 3400 | 670 | 3.6 | 4.2 | Yes | Yes | | |
| 920 | 1930 | 560 | 3.3 | 2.1 | No | No | | |
| 920 | 3860 | 560 | 3.3 | 4.2 | Yes | Yes | | |
| 80 | 500 | 120 | 1.7 | 6.3 | Yes | No | Peeling off with demolding agent | This study |
| 80 | 750 | 120 | 1.7 | 9.4 | Yes | Yes | | |
| 120 | 500 | 230 | 1.9 | 4.2 | Yes | No | | |
| 120 | 750 | 230 | 1.9 | 6.3 | Yes | No | | |

**Table 4-1**. Comparison of experimental results versus predicted stability against lateral collapse of h-PDMS rods arrays from different studies.

The current challenge for the polymeric nanorod arrays is achieving vertically aligned high aspect ratio rods. The dimensions, spacing, aspect ratio, stability, and demolding process for the synthesized h-PDMS nanorod arrays in the literature are list in Table 1. [174-175, 177, 187] In the other studies, the synthesized h-PDMS nanorod arrays with aspect ratio >1.7 show lateral collapse when the rod diameter is ≤ 200 nm. At ≥ 810 nm diameter, the critical aspect ratio increases to ~3.6. In either case, the aspect ratio for the rod arrays is limited to < 4. Low surface energy mold releasing agent has been used,[187] however, curved AAO surface creates a large shear force during the demolding process and the h-PDMS nanorods are not vertically aligned, which limits the highest achievable aspect ratio. Wet chemical etching method has been used to dissolve AAO and release h-PDMS nanorod arrays.[174] However, the capillary force during the drying process leads to the bending and lateral collapse of the h-PDMS nanorods arrays. In this study, the low surface energy mold releasing agent decreases the surface tension of the h-PDMS nanorods and the AAO surface is flat. Therefore, the high aspect ratio h-PDMS nanorod arrays are successfully fabricated (6.3 aspect ratio for the nanorods with 80 nm diameter).

### 4.1.4. Summary

The porous AAO is used as a template to fabricate h-PDMS nanorod arrays with the corresponding Moiré pattern. The self-assembled 1H, 1H, 2H, 2H-perfluorodecyltrichlorosilane serve as demolding agent to low the energy surface of AAO template, which facilitate the detachment of the molded h-PDMS from the template. Therefore, the h-PDMS nanorod arrays can be easily peeled off from the AAO mold. The diameter, density, and aspect ratio of the nanorods are determined by the dimension of porous AAO templates. Vertically aligned h-PDMS nanorods with aspect ratio 6.3 have been successfully obtained.

## 4.2. Synthesize of sub-micrometer rod by soft lithographic micromolding

### 4.2.1. Introduction

Soft lithography offers a novel and effective approach to create ceramic patterns with micro- to nano-structures.[188-200] Microelectromechanical systems (MEMS) based on ceramic materials have been successfully achieved by soft lithography.[192-195] Moreover, patterned sub-micrometer arrays of parallel lines and dots of different ceramic materials have been prepared by micromolding ceramic precursor solutions or sol-gels followed by annealing.[196-199] The width of the ceramic features ranges from 100 nm[198] to 600 nm[197], and the height from 25 nm[198] to 200 nm[197]. However, the solids loading of the ceramic precursor liquids has a significant effect on the aspect ratio of the ceramic features.[197-198] When the effective solids loading is low, even if the precursor liquid completely fills the patterns on the PDMS mold, shrinkage of the precursor liquid during solidification greatly reduces the height of ceramic features, which compromises the aspect ratio of the features. As a result, sub-micrometer ceramic patterns obtained using PDMS molds normally have an aspect ratio significantly smaller than 1. It is still a challenge to utilize the versatile and low-cost PDMS to fabricate sub-micrometer ceramic patterns with large aspect ratios while maintaining the fidelity of the patterns.

On one hand, the hydrophobic nature of PDMS greatly limits the ability of aqueous liquids to fill the patterns on the mold, which compromises the fidelity of soft lithographic micromolding. On the other hand, the soft lithographic technique causes air to be trapped inside the patterns on the PDMS mold. However, the hydrostatic equilibrium and dynamic process of trapped air has not been studied. The effect of air diffusion on the fidelity of soft lithographic micromolding is unknown. For the micromolding liquid, colloidal suspensions of nanoparticles are preferred in order to increase the solids loading of the filling liquids, desirably to as high as 40 vol%.[189-191, 201-204] Electrostatic stabilization by adjusting the surface charge of the nanoparticles and steric stabilization by adsorbing polymer dispersants on nanoparticle surfaces can be utilized to overcome nanoparticle agglomeration and high suspension viscosity.[202, 205-206] However, the ability of the nanoparticle suspension to push the fabrication scale into the sub-micrometer range needs to be further explored.

In this section, I focus on the fabrication of ceramic sub-micrometer arrays by micromolding nanoparticle suspensions using PDMS molds. The important parameters required to obtain high solids loading nanoparticle suspensions are studied. The effect of surface wetting on the filling depth of the suspension into the mold is examined, and its mechanism is discussed. The influence of solids loading on the fidelity of soft lithographic micromolding is analyzed.

### 4.2.2. Experimental Procedures

Commercial ZnO nanoparticles (Nanostructured & Amorphous Materials, Inc., Houston, TX) with a mean particle size of 20 nm and specific surface area of 50 m2/g were used. Suspensions of ZnO nanoparticles with different solids loadings (20 vol%, 30 vol%, and 40 vol%) were prepared by ball milling ZnO nanoparticles in water. Poly(acrylic acid) (PAA, Sigma-Aldrich, St. Louis, MO) with an average molecular weight of 2000 and 63 wt% concentration (in water) was used as a dispersant. ZnO nanoparticles were added into dilute ammonium hydroxide (with initial pH value at 11) in 1 g increments along with 3.0 wt% PAA dispersant (on ZnO basis); the suspension was ball milled for 20 min following each addition.

The zeta potential of the ZnO suspension was analyzed by dynamic light scattering (Zetasizer NanoZS, Malvern Instruments, Malvern, UK). The surface tension was measured by the Wilhelmy plate technique using a Cahn 2000 electrobalance with a filter paper plate at room temperature. The viscosity measurements of the suspensions were performed using a rheometer with cone-plate geometry (AR 2000, TA Instruments, New Castle, DE).

In order to prepare the PDMS molds, a silicon master with different features was first created using a dual beam focused Ga+ ion beam microscope (FIB, FEI Helios 600 Nano Lab, Hillsboro, OR) with 30 kV accelerating voltage and 0.28 nA beam current. Subsequently, PDMS prepolymer (Sylgard 184; Dow Corning, Midland, MI) with base and curing agents at 10:1 ratio was cast on the silicon wafer. The silicon wafer and PDMS prepolymer were placed in a vacuum chamber and subjected to a pressure of 10 mTorr for 30 min to remove air bubbles, then moved into an oven at 100ºC for 60 min to solidify the PDMS. The pristine PDMS mold was separated from the silicon wafer and coated with a 5 nm gold layer to change the surface wetting characteristics. The gold layer was coated by Cressington sputter coater 208HR with thickness controller MTM-20 to detect the thickness. For the hydrophilic PDMS mold, 3 wt% Triton X-100 (TX-100, C14H22O(C2H4O)n; Sigma-Aldrich, St. Louis, MO) was also added to the PDMS prepolymer to make it hydrophilic, which was then cast, degassed, solidified, and demolded in the same manner as the pristine PDMS.

The ZnO nanoparticle suspension was cast into the pristine PDMS molds, gold coated PDMS molds, and hydrophilic PDMS molds. The filled molds were put into a petri dish to dry under ambient conditions for 7 days. In order to maintain the humidity inside the petri dish during drying to avoid cracking, 1 ml of water was added to the petri dish. After the ZnO samples were dried, they were carefully separated from the PDMS molds.

The contact angle of ZnO nanoparticle suspension on different PDMS molds was measured by a contact angle analyzer (FTA 125, First Ten Angstroms, Portsmouth, VA). The structures of PDMS molds and ZnO samples were characterized by scanning electron microscopy (SEM, Quanta 600 FEG, FEI Company, Hillsboro, OR).

### 4.2.3. Results and discussion

#### 4.2.3.1 ZnO nanoparticle suspension

The TEM image of the commercial ZnO nanoparticles in Figure 4-2a shows the size of ZnO nanoparticles ranges from 15 nm to 26 nm, and the average particle size is around 20 nm. In order to obtain high solids loading ZnO nanoparticle suspensions, the ionic properties of the liquid and ionic polymer dispersant can be used simultaneously. Both electrical double-layer repulsion and steric forces are present to overcome the agglomeration of nanoparticles. Figure 4-2b shows the zeta potential of pure ZnO nanoparticle suspensions at different pH values, and the corresponding zeta potential of the suspensions with an additional 3 wt% PAA. When the pH value is above 9.0, the absolute value of zeta potential is greater than 25 mV, which facilitates the stability of the ZnO suspension. With the addition of 3 wt% PAA to the ZnO suspension, the absolute value of the zeta potential is increased over the entire pH range, which not only enhances the stability of the suspensions but also enlarges the pH window for stable suspensions.

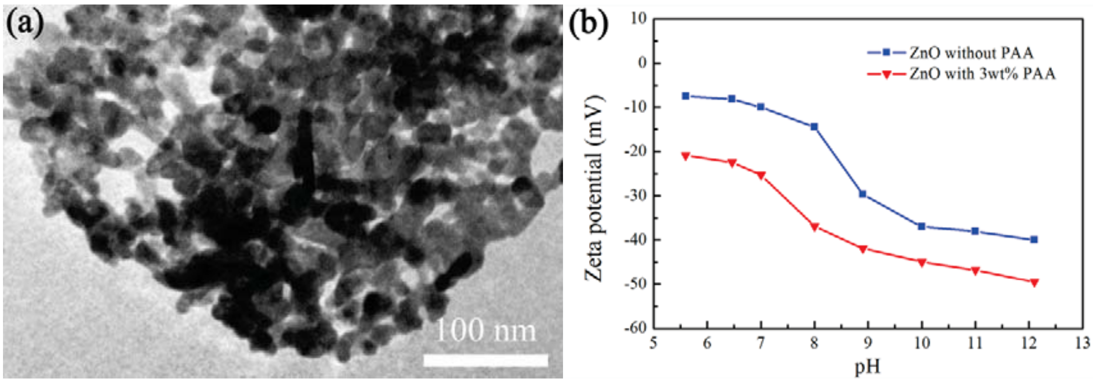

**Figure 4-2**. Zeta potential of ZnO nanoparticle suspensions with and without PAA as a dispersant.

Figure 4-3 shows the viscosity of ZnO nanoparticle suspensions with different amounts of dispersant and different solids loadings. Without any PAA as a dispersant, the viscosity of the suspension is high (from 85 Pa·s at 0.4 $s^{-1}$ shear rate to 0.12 Pa·s at 1000 $s^{-1}$ shear rate), and 10 vol% is the maximum solids loading for a flowable suspension. If more ZnO nanoparticles are added into the suspension, the suspension will rapidly lose fluidity, and the viscosity will increase significantly.

Desirably, the adsorbed dispersant layer plays an important role in creating steric repulsion between the ZnO nanoparticles, which increases the stability and decreases the viscosity of the suspension. Therefore, the viscosity of the 10 vol% nanoparticle suspension decreases significantly with increasing dispersant concentration and reaches a steady value after addition of 3 wt% PAA. The viscosity of the suspension with 3 wt% PAA is ~1/100 of that of the suspension without a dispersant. The small difference in the suspension viscosity at 3 wt% PAA and 4 wt% PAA indicates that the maximum adsorption of dispersant on the ZnO nanoparticle surfaces may have been achieved at 3 wt% PAA. Increasing the amount of PAA to 8 wt% leads to an increase in the suspension viscosity and the formation of bubbles during ball milling. Moreover, with the steric stabilization by 3 wt% PAA, the ZnO nanoparticle suspension can reach as high as 40 vol% solids loading while still retaining reasonable fluidity for soft lithographic micromolding, from 60 Pa·s at 0.4 $s^{-1}$ shear rate to 0.086 Pa·s at 1000 $s^{-1}$ shear rate, as shown in Figure 4-3.

Due to the acidity of the PAA, the addition of the dispersant will decrease the pH value of the ZnO nanoparticle suspension. To obtain a suitable final suspension pH value so that the absolute value of zeta potential is > 25 mV, the initial pH value of the aqueous solvent is set to 11, and the concentration of the PAA dispersant is fixed at 3 wt% based on ZnO weight. After dispersing the ZnO nanoparticles in the aqueous solvent, the resulting pH of the suspension with 20 vol%, 30 vol%, and 40 vol% solids loading is 8.9, 8.7, and 8.6, respectively. According to the zeta potential curve of the suspensions with the dispersant in Figure 4-2, all these pH values can lead to large zeta potential values (around -40 mV) and stable suspensions.

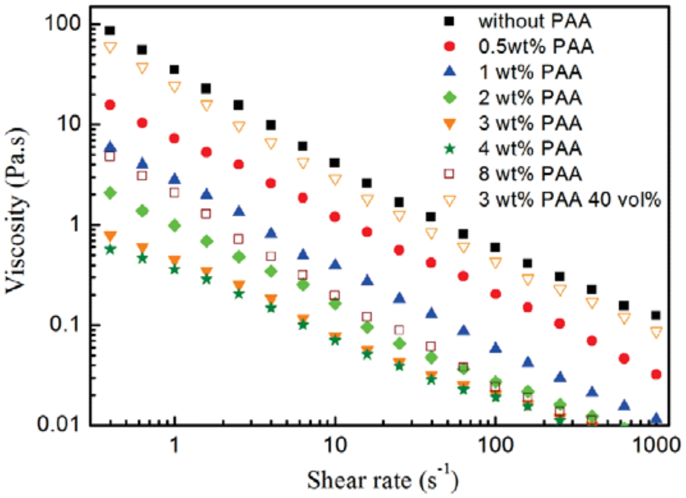

**Figure 4-3**. Viscosities of ZnO nanoparticle suspensions with different amounts of PAA dispersant. The solids loading of ZnO nanoparticles is 10 vol% unless otherwise noted.

#### 4.2.3.2 Soft lithographic micromolding

Figure 4-4a shows a typical tilt SEM image of the silicon master; the silicon rod arrays have a hexagonal arrangement with 750 nm diameter and 1:1 aspect ratio. Different types of PDMS molds (pristine PDMS, gold coated PDMS, and PDMS containing 3 wt% TX-100) prepared from the same silicon master have the same topography, as shown in the tilt SEM image of Figure 4-4b, which is the inverse of the silicon master: sub-micrometer pore arrays with hexagonal arrangement, 750 nm cavity diameter, and 750 nm cavity depth.

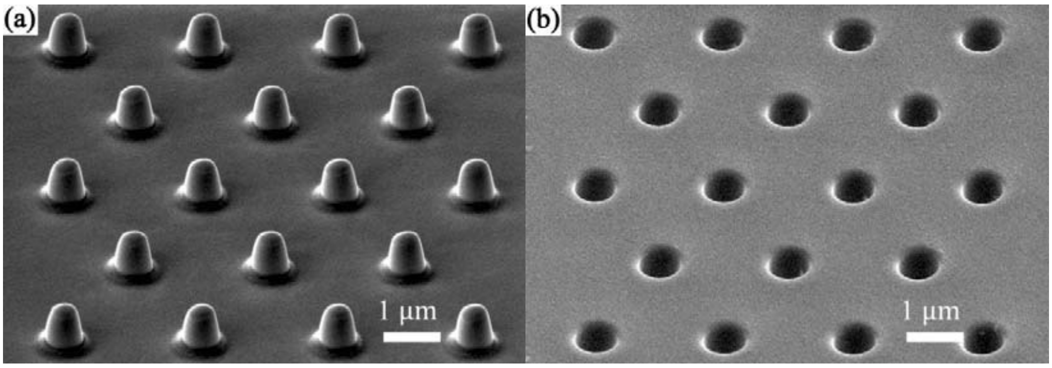

**Figure 4-4**. SEM image of (a) silicon master and (b) PDMS mold at 52° tilt angle.

However, different PDMS molds have distinct wetting properties. As shown in Figure 4-5, the contact angles of ZnO nanoparticle suspension with pristine PDMS, gold coated PDMS, and PDMS containing 3 wt% TX-100 are 104°, 88°, and 76°, respectively. As a result, casting the

ZnO nanoparticle suspension on different PDMS molds leads to different filling depths inside the pores. After drying, the ZnO rods obtained from the pristine PDMS and gold coated PDMS molds have very small heights: ~150 nm and ~90 nm, respectively; the aspect ratio of the ZnO rods in both cases is much smaller than 1. However, the ZnO rods prepared using the hydrophilic PDMS mold containing 3 wt% TX-100 have good fidelity and maintain the 1:1 aspect ratio (Figure 4-5e). The hydrophilic PDMS mold allows the ZnO nanoparticle suspension to fully fill the pores, while the large contact angles of the pristine PDMS and gold coated PDMS molds hinder the suspension from filling the pores, thus compromising the fidelity of the resulting rod arrays.

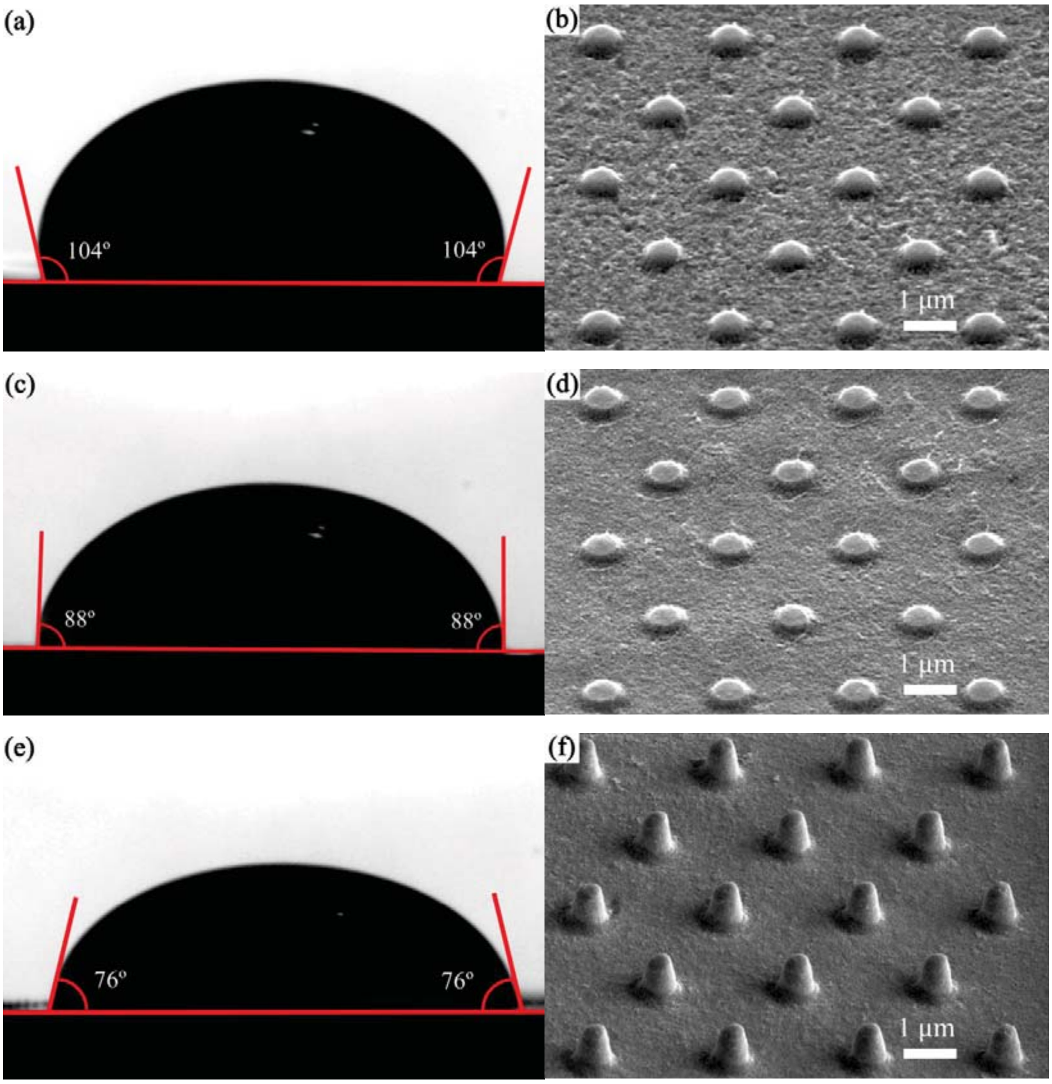

**Figure 4-5**. Contact angle of ZnO nanoparticle suspension on different molds: (a) pristine PDMS, (c) gold coated PDMS, and (e) hydrophilic PDMS containing 3 wt% TX-100; (b), (d) and (f) are 52° tilt SEM

images of the corresponding ZnO features after drying from the pristine, gold coated, and hydrophilic PDMS, respectively.

I propose that the mechanism for the effect of surface wetting properties on the fidelity of soft lithographic micromolding is based on a combination of the hydrostatic equilibrium maintained in the pores and the dynamic diffusion of trapped air through the ZnO nanoparticle suspensions.

For the pores on the PDMS mold with a diameter of 750 nm, the interface between the suspension and the mold forms a meniscus that is a portion of a sphere surface with radius $R=d/2\cos\theta$, where $d$ is the diameter of the pore and $\theta$ is the contact angle. The pressure difference across this surface is:

$$\Delta p = \frac{2\gamma}{R} = \frac{4\gamma\cos\theta}{d} \qquad (4\text{-}3)$$

where $\gamma$ is the surface tension of the suspension (59 mN/m). In order to maintain hydrostatic equilibrium, the induced capillary pressure is balanced by the liquid pressure from the ZnO suspension and the pressure from the compressed air trapped inside the pore. Therefore, the Young-Laplace equation can be written as:[207-208]

$$\Delta p = \frac{2\gamma}{R} = \frac{4\gamma\cos\theta}{d} = \frac{aP_0}{L-a} - \rho g h \qquad (4\text{-}4)$$

where $a$ is the filling depth of the suspension into the pore, $P_0$ is the atmospheric pressure ($1.01\times10^5$ Pa) , $L$ is the pore depth (750 nm) , $\rho$ is the suspension density (2.3 g/cm$^3$), and $h$ is the thickness of the suspension layer on the PDMS mold (2 mm). As a result, the filling depth of the suspension into the pore can be obtained:

$$a = \frac{L}{\dfrac{P_0 d}{4\gamma\cos\theta + \rho g h d} + 1} \qquad (4\text{-}5)$$

For the pristine PDMS, the 104º contact angle results in a calculated filling depth of a= –2.3 μm, which means the ZnO nanoparticle suspension cannot penetrate into the PMDS pore at all. However, as shown in Figure 4-6a, the negative Laplace pressure causes the meniscus formed at the suspension/air interface to have a convex shape; thus, the formed ZnO arrays still have a height of $a = R - R\sin\theta = \left|d/2\cos\theta\right|(1-\sin\theta) = 46$ nm (Figure 4-6a). According to equation (4-

5), the contact angle for the gold coated PDMS is 88º, which means that the suspension can fill 10% of the pore (75 nm), and the top surface of the ZnO pattern also conforms to the planar meniscus shape (Figure 4-6b). The predicted heights are slightly smaller than the experimental values (46 nm vs. 150 nm and 75 nm vs. 90 nm), which will be explained later. Nevertheless, in both cases the small aspect ratio and the shape of the ZnO rods are consistent with the experiment results shown in Figures 4-6b and 4-6d.

For the hydrophilic PDMS containing 3 wt% TX-100, according to equation (4-5), the 76º contact angle and positive Laplace pressure will cause the ZnO nanoparticle suspension to fill 335 nm (45%) into the pore with a concave meniscus shape, as shown in Figure 4-6c. This prediction contradicts the experimental results shown in Figure 4-5e, which show that the suspension fully fills the pores on the hydrophilic PDMS mold.

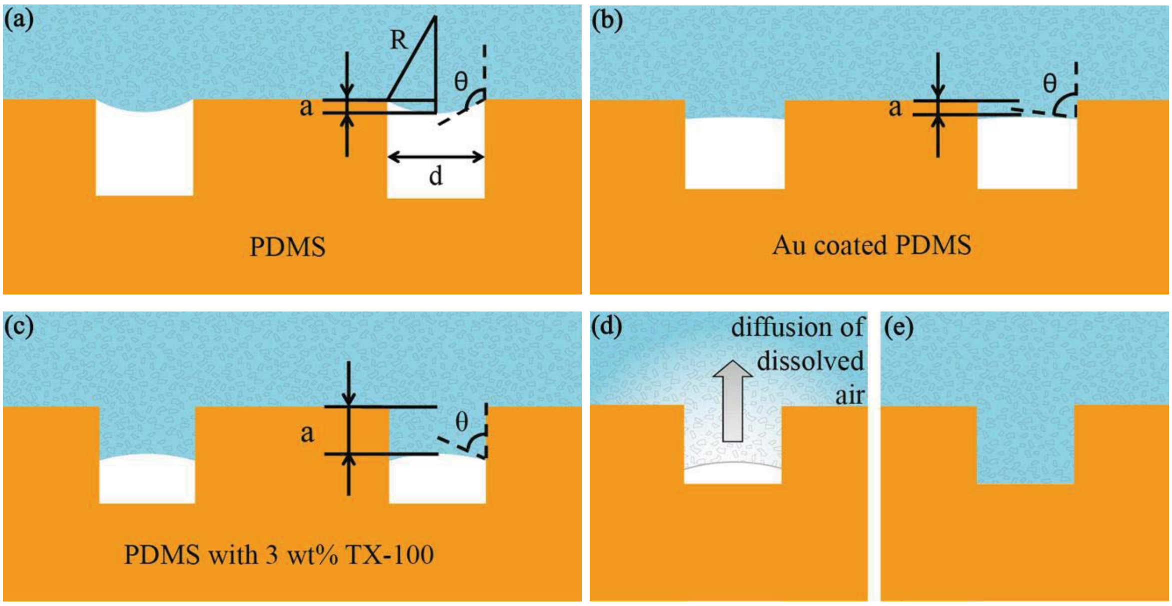

**Figure 4-6**. Schematics of the filling of ZnO nanoparticle suspensions into the pores on different molds: (a) pristine PDMS, (b) gold coated PDMS, and (c) hydrophilic PDMS containing 3 wt% TX-100; (d) diffusion of trapped air into the suspension on hydrophilic PDMS; (e) a pore on the hydrophilic PDMS mold fully filled with the suspension after the diffusion of trapped air.

In order to understand the filling of the pores on hydrophilic PDMS, the dynamic process within the ZnO nanoparticle suspension cast on the elastomeric mold needs to be considered. Even though the high density suspension is on top of the low density air, the small diameter of the pore causes the gravitational force to be much smaller than the capillary force; thus, the light air will not be pushed up by the heavy suspension as predicted by the Rayleigh–Taylor instability. Therefore, I focus on the dissolution and diffusion of trapped air through the ZnO nanoparticle suspension.

According to Henry's law, the dissolution of air in a liquid is directly proportional to the air pressure:

$$C = k_{H,CP} \times P \tag{4-6}$$

where $C$ is the concentration of dissolved air, $k_{H,CP}$ is the Henry's law constant, and $P$ is the pressure. Here, I can use Henry's law constant of air in water ($1.0\times10^{-3}$ mol/L/atm) to estimate the time scale for diffusion. Assuming that the trapped air behaves like an ideal gas, the pressure of trapped air is $P' = P_0 L/(L-a)$, where $P_0$ is the atmospheric pressure. The concentrations of dissolved air at the suspension/trapped air interface and at the suspension/atmosphere interface are $C_S = k_{H,CP} \times P_0 L/(L-a) = 1.74\times10^{-3}$ mol/L and $C_0 = k_{H,CP} \times P_0 = 1.0\times10^{-3}$ mol/L, respectively. As a result, the concentration of dissolved air at different pore heights and times can be calculated as:

$$C(x,t) = C_S + (C_S - C_0) erf(-\frac{x}{\sqrt{4Dt}}) \tag{4-7}$$

where $x$ is the distance to the suspension/trapped air interface, $D$ is the diffusion coefficient of air in the suspension, and $t$ is time. The diffusion coefficient of air in water is $2.0\times10^{-5}$ cm$^2$/s. According to Figure 4-3, the viscosity of 40 vol% ZnO nanoparticle suspension is ~10 Pa·s, which is about $10^4$ times of the viscosity of water (~1.0 mPa·s). Based on the Stokes-Einstein relation:

$$D = \frac{k_B T}{6\pi R_0 \eta} \tag{4-8}$$

where $\eta$ is the viscosity of the suspension and $R_0$ is the radius of air molecule, the diffusion coefficient of air in the ZnO nanoparticle suspension can be estimated to be around $2.0\times10^{-9}$ cm$^2$/s.

Due to the dissolution and diffusion of air, the volume of trapped air is decreased (Figure 4-6d). In the meantime, the capillary forces keep the trapped air compressed in order to maintain the hydrostatic equilibrium. Therefore, the suspension/trapped air interface will continually move downwards until all the trapped air diffuses away (Figure 4-6d). As a result, the suspension fully fills the pores on the hydrophilic PDMS (Figure 4-6e).

The flux of diffusion at the suspension/trapped air interface can be written as:

$$J(t) = -D\frac{dC(x,t)}{dt}\Big|_{x=0} \tag{4-9}$$

The mass transfer of air diffusing through the suspension/trapped air interface can be calculated as:

$$\Delta m(\tau) = \int_0^{\tau} J(t) \times \frac{\pi d^2}{4} dt \tag{4-10}$$

Therefore, it can be estimated that the time, $\tau$, to diffuse all of the trapped air in a pore with 750 nm diameter and 750 nm depth is only around 110 min. Since the suspension-filled patterns are allowed to dry for several days, this short diffusion time explains why the pores on the hydrophilic PDMS mold can be completely filled.

For the pristine PDMS and gold coated PDMS, the diffusion of trapped air still facilitates the filling of the pores with the suspension, which explains why the experimental values are larger than the theoretical values calculated based on equation (4-5). However, the increase in the pressure of the compressed air is limited for the pristine PDMS and gold coated PDMS according to equation (4-10), and more than 100 hours are required for the trapped air to completely diffuse out of these pores. Moreover, during this extended period of time, the drying process increases the viscosity of the suspension, which further slows down the diffusion of trapped air from the pores in the pristine PDMS and gold coated PDMS molds. As a result, the ZnO nanoparticle suspension maintains the shallow filling depth inside the pristine PDMS and gold coated PDMS molds, which limits the aspect ratio of the obtained ZnO rod arrays.

#### 4.2.3.3 Versatility of soft lithographic micromolding

FIB patterning enables this soft lithographic micromolding technology to create versatile ZnO rod features with controllable topographies. The advantage of the FIB lithography method is that various patterns with different arrangements, sizes, and shapes can be easily created on the silicon master by FIB bombardment. Besides the rod arrays with hexagonal arrangement and uniform size shown in Figure 4-4a, square arrangements of rods with different sizes and shapes have also been achieved, as shown in Figure 4-7a and Figure 4-7c. Under the guidance of the hydrophilic PDMS molds (with 3 wt% TX-100) obtained from these silicon masters, corresponding ZnO rod arrays with 200 nm, 400 nm, 750 nm, and 1 μm diameters are fabricated (Figure 4-7b), and ZnO rod arrays with circular, pentagonal, square, and triangular shapes are realized (Figure 4-7d).

When the diameter of the pores on the hydrophilic PDMS mold is decreased, it leads to increased capillary pressure and compressed air pressure, which facilitate the complete filling of the cavities on the mold. Theoretically, soft lithographic micromolding can successfully fill any cavities and create ZnO rods with very small dimensions. However, the diameter of the ZnO nanoparticles in the suspension limits the smallest possible dimensions of the ZnO rods. The diameter of 200 nm ZnO rods is only 10 times that of the ZnO nanoparticles (20 nm); if the diameter of the rods is further decreased, even fewer ZnO nanoparticles can fill in the pore, making it difficult to form an intact rod. Therefore, nanoparticles with an even smaller size are needed in order to obtain extra-fine ZnO nanorods.

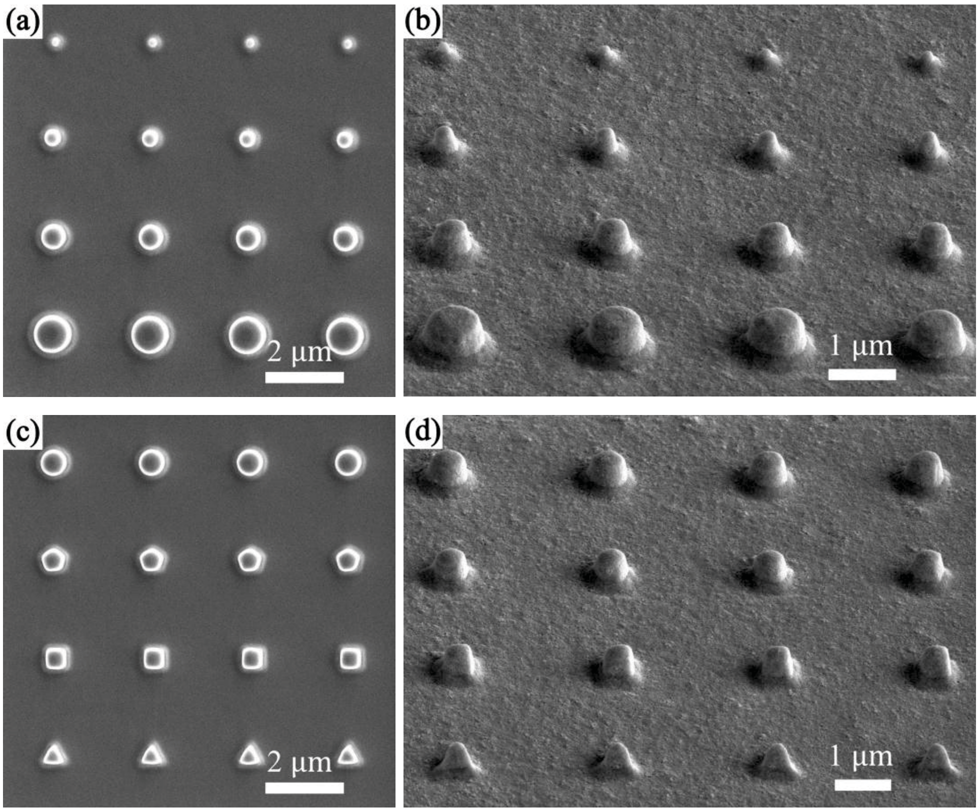

**Figure 4-7**. SEM images of FIB patterned silicon masters with (a) different sizes and (c) different shapes. (b) and (d) are 52° tilt SEM images of ZnO rods obtained from the hydrophilic PDMS molds fabricated from the silicon masters shown in (a) and (c), respectively.

The effect of the solids loading on the fidelity of soft lithographic micromolding is also examined. Figures 7a and 7b show ZnO rods obtained from 20 vol% and 30 vol% ZnO nanoparticle suspensions, respectively. Both sets of rods have the same height as ZnO rods fabricated from the 40 vol% suspension (750 nm), as shown in Figure 4-8e, and the shrinkage of the ZnO feature dimensions due to drying of the suspension can be ignored. However, there are many missing rods in the pattern obtained from the 20 vol% nanoparticle suspension, and the bottoms of the remaining ZnO rods also show evidence of fracture. During the drying process, water only evaporates at the suspension/atmosphere interface. There is no evaporation of water at the interface of the filled suspension and the mold pore wall. Thus, the dry ZnO rods should maintain the pore outline. When the solids loading is high (30 vol% and higher), the particle packing density is high enough to replicate the shapes of the mold features; however, low solids loading will lead to low packing density for the ZnO rods, which leads to fracture, missing features, and a loss of the fidelity of soft lithographic micromolding. Therefore, it is important to obtain high solids loading nanoparticle suspensions.

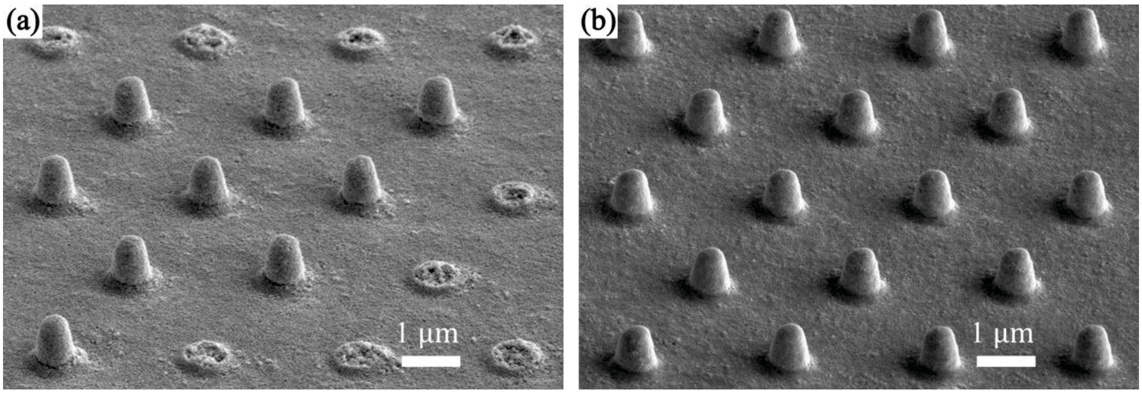

**Figure 4-8**. SEM images of ZnO rod arrays fabricated by ZnO nanoparticle suspensions with different solids loading: (a) 20 vol% and (b) 30 vol%.

ZnO has broad applications in the electrochemical, electronic, and optoelectronic fields, such as in dye sensitized solar cells and field emission devices. Therefore, I chose ZnO as a model material to fabricate sub-micrometer arrays by micromolding nanoparticle suspensions. Nevertheless, this soft lithography technique is a generic method that can be used to fabricate different sub-micrometer patterns, such as $TiO_2$, $Al_2O_3$, $ZrO_2$, and $SiO_2$, as long as high solids loading nanoparticle suspensions can be obtained.

### 4.2.4. Summary

ZnO sub-micrometer rod arrays with an aspect ratio around 1 have been successfully achieved by a soft lithographic micromolding approach. This generic method can create patterns with different feature arrangements, feature sizes, and feature shapes. The dimensions of the ZnO rods created range from 200 nm to 1 μm; circular, pentagonal, square, and triangular features have been obtained. The wetting property of the suspension on the PDMS molds significantly influences the aspect ratio of the ZnO rods. For the pristine PDMS and gold coated PDMS molds, large contact angles lead to small filling depths of the suspension into the pores. For the hydrophilic PDMS containing 3 wt% TX-100, the small contact angle and positive Laplace pressure cause the trapped air to be compressed, which further increases the dissolution and diffusion of trapped air through the ZnO nanoparticle suspension. After drying, ZnO rod patterns with dimension as same as the patterns on hydrophilic PDMS mold are achieved. Nanoparticle suspensions with high solids loading are required to maintain the fidelity of the features during soft lithographic micromolding; otherwise, missing sites and fractures occur and compromise the fidelity of the rod arrays.

# Chapter 5. Anodic $TiO_2$ Nanotubes and Their Applications

## Abstract:

In recent years, anodic $TiO_2$ nanotubes have attracted significant interest due to their great application potentials in energy conversion and storage, electrochromic devices, and sensors. However, the mechanism governing the formation of anodic $TiO_2$ nanotubes is still uncertain, which hinders the engineering of optimized $TiO_2$ nanotubular structures for specific applications. Moreover, the self-organized anodization alone can only produce randomly arranged nanotubes. In this study, dehydration of titanium hydroxide cell wall is proposed to understand the formation mechanism of anodic $TiO_2$ nanotubes. FIB guided anodization is used to create highly ordered $TiO_2$ nanotube arrays with different intertube distances and tube arrangements. Fundamentally different nanotube arrangements, such as square, oblique hexagonal, alternating-sized patterns, and asymmetrical patterns are created. Hierarchically branched $TiO_2$ nanotubes with tailored diameters and branch numbers are successfully achieved by adjusting the anodization voltage. Bamboo-type $TiO_2$ nanotubes with large surface area are achieved by cycling high and low applied potentials. After thermal treatment in $H_2$ atmosphere, the bamboo-type $TiO_2$ nanotubes show large specific capacitance and high water splitting efficiency.

## 5.1. Growth mechanism of anodic $TiO_2$ nanotubes

### 5.1.1. Introduction

Until now, the driving force for the formation of nanotubular but not nanoporous anodic $TiO_2$ arrays still remains an unanswered question. Four different models have been proposed to explain the nanotubular $TiO_2$ structures. First, Su et al. proposed that oxides at the junction areas suffer a high degree of localized dielectric breakdown, which produces a large number of voids at the inter-pore areas and separates the neighboring $TiO_2$ nanotubes.[89] Second, Grimes et al. claimed that the un-anodized metallic Ti between neighboring pores can undergo the same oxidation and field-assisted dissolution process, thus gaps develop between neighboring $TiO_2$ nanotubes.[67, 90] Third, Schmuki et al. attributed the nanotube separation to the dissolution of the fluoride-rich outer shell of nanotube walls due to the higher migration rate of $F^-$ ions than $O^{2-}$ ions during the anodization.[92, 98] Fourth, Su et al. proposed that the Ti substrate is anodized both by $O^{2-}$ ions to form the $TiO_2$ inner shell and by $OH^-$ ions to form a titanium hydroxide outer shell during the anodization; the volume shrinkage due to the dehydration of the titanium hydroxide outer shell leads to the formation of gaps between neighboring $TiO_2$ nanotubes.[6, 209] However, the mechanism for the formation of $TiO_2$ nanotubes is still uncertain, which results in difficulty when designing $TiO_2$ nanotube-related devices.

In this study, the effect of $OH^-$ concentration in the electrolyte on anodic $TiO_2$ nanostructures is explored. A new pore separation mechanism based on the dehydration of titanium hydroxide is proposed to explain the evolution of anodic $TiO_2$ nanostructures when $OH^-$ concentration is changed. The structural development of anodic $TiO_2$ nanotubes after the anodization is examined in order to evaluate different formation mechanisms. Electrochemical impedance spectroscopy is used to monitor the structure of as-grown $TiO_2$ nanotubes when submerged in electrolyte or dried in air.

### 5.1.2. Experimental procedure

High purity titanium foil (99.6+%, 0.2 mm thick, Goodfellow, Oakdale, PA) was sonicated in acetone, isopropanol, and methanol, and then electropolished in a freezing electrolyte (~1℃) composed of glacial acetic acid/perchloric acid (9/1 vol ratio) at 55 V with 800 rpm stirring speed for 2 min. The anodization was carried out in a two-electrode electrochemical cell in ethylene glycol electrolyte with 0.1 M $NH_4F$ and varying amounts of DI water or ammonium hydroxide with pH=11. The anodization in the electrolyte with 0.5 vol% DI water or ammonium hydroxide was carried out in a glovebox (OMNI-Lab system, Vacuum Atmospheres Company 101965, Hawthorne, CA). The glovebox contained an atmosphere of purified $N_2$, and the moisture and oxygen levels were maintained at less than 0.6 ppm. The anodization in the ethylene glycol electrolyte with 0.1 M $NH_4F$ and 10 vol% DI water was performed in ambient atmosphere at room temperature. The power supply for the anodization was Bertan 210-01R, and the applied potential during the anodization was controlled by LabView software.

Electrochemical impedance spectroscopy (EIS) measurements were carried out using an electrochemical workstation (1480 multistat, Solartron Analytical) in 1 M KCl. EIS measurements of different $TiO_2$ nanotubes (as-grown, submerged in the anodization electrolyte for different time, and dried in air for different time) were conducted in a frequency range of 100 mHz to 100 kHz at a constant potential of 0.1 V and an AC voltage amplitude of 10 mV. The structures of the anodized $TiO_2$ nanotube arrays were characterized by scanning electron microscopy (SEM, Quanta 600 FEG, FEI Company, Hillsboro, OR).

### 5.1.3. Results and discussion

Figure 5-1 shows that the $OH^-$ concentration in the electrolyte plays a crucial role in whether self-ordered $TiO_2$ nanotubes or nanopores are formed during the anodization. Anodization of titanium foil in anhydrous ethylene glycol electrolyte with 0.1 M $NH_4F$ and 0.5 vol% DI water leads to the formation of an anodic nanoporous $TiO_2$ structure (as shown in Figures 1a and 1b). However, when the DI water is replaced by ammonium hydroxide with pH=11 while maintaining 0.5 vol% concentration, nanotubular structures are produced instead of nanoporous structures, as shown in Figures 1c and 1d. The transition of $TiO_2$ nanopores into nanotubes by increasing the $OH^-$ concentration in the electrolyte is difficult to understand based on the mechanisms that have previously been proposed for the formation of $TiO_2$ nanotubes. The concentration of water in these two electrolytes is almost the same, while the main difference is the $OH^-$ concentration. If the formation of gaps between $TiO_2$ nanotubes is ascribed to the dissolution of the fluoride-rich boundary by water, as proposed by Schmuki et al,[92, 98] the dissolution rate of the boundary should not be different in those two electrolytes and both anodization processes should result in $TiO_2$ nanopores. The localized dielectric breakdown model suggests that the small localized dielectric breakdown in non-aqueous glycerol solution with very low water content should lead to the formation of anodic $TiO_2$ nanopores instead of nanotubes.[89] However, even if the $OH^-$ concentration is increased, as long as the water concentration remains very low, the localized dielectric breakdown should still be suppressed to a low degree such that only anodic $TiO_2$ nanopores form. The mechanism proposed by Grimes et al.[67, 90] that anodization and further dissolution of protruded metallic Ti between nanopores also cannot explain why $TiO_2$ nanopores are obtained in anhydrous ethylene glycol electrolyte with a low water content.

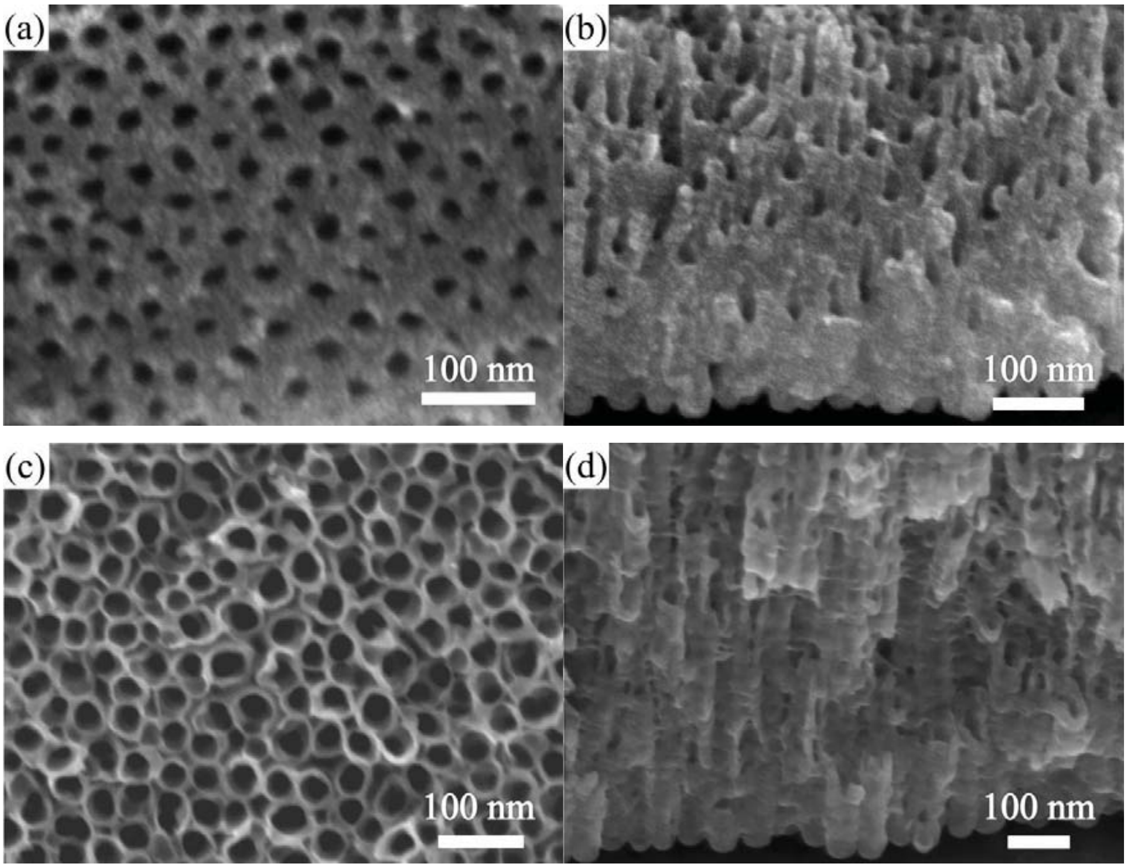

**Figure 5-1**. SEM images of anodic $TiO_2$ nanostructures after 15 min anodization at 20 V in ethylene glycol electrolyte with 0.1 M $NH_4F$ and 0.5 vol% liquid: (a, b) DI water, and (c, d) ammonium hydroxide with pH=11. (a) and (c) are surface SEM images, (b) and (d) are cross section images.

I propose that volume shrinkage during the dehydration of titanium hydroxide in the cell wall is the driving force for the separation of neighboring $TiO_2$ nanotubes. During the anodization, the metallic Ti at the oxide/metal interface is anodized by both $O^{2-}$ and $OH^-$ ions, and the balance of the $TiO_2$ dissolution and oxidation processes leads to the growth of nanoporous structures as shown in Figure 5-2a. The $TiO_2$ barrier layer dissolves under the reaction:

$$TiO_2 + 6F^- + 4H^+ \rightarrow TiF_6^{2-} + 2H_2O \qquad (5\text{-}1)$$

The cell wall and the bottom of the $TiO_2$ nanopores are composed of a mixture of $TiO_2$ and $Ti(OH)_4$ based on the following reactions:

$$H_2O \rightarrow H^+ + OH^- \qquad (5\text{-}2)$$

$$\mathrm{OH^{-}} \rightarrow \mathrm{H^{+}} + \mathrm{O^{2-}} \qquad (5\text{-}3)$$

$$\mathrm{Ti} + 4\mathrm{OH^{-}} \rightarrow \mathrm{Ti(OH)_4} + 4\mathrm{e^{-}} \qquad (5\text{-}4)$$

$$\mathrm{Ti} + \mathrm{O^{2-}} \rightarrow \mathrm{TiO_2} + 2\mathrm{e^{-}} \qquad (5\text{-}5)$$

Fourier transform infrared (FTIR) spectroscopy of anodized $TiO_2$ region shows a broad band between 3000 $cm^{-1}$ and 3700 $cm^{-1}$, which corresponds to structural $OH^{-}$, while the FTIR spectroscopy of the region with un-anodized metallic Ti does not show any obvious peak between 3000 $cm^{-1}$ and 3700 $cm^{-1}$ (Figure 5-3). Therefore, FTIR spectroscopy demonstrates the existence of $OH^{-}$ in anodic $TiO_2$ nanostructures. Subsequently, the titanium hydroxide can dehydrate into $TiO_2$:

$$\mathrm{Ti(OH)_4} \rightarrow \mathrm{TiO_2} + 2\mathrm{H_2O} \qquad (5\text{-}6)$$

which leads to the volume shrinkage. At the cell boundary where two neighboring cell walls encounter each other, the volume shrinkage from the dehydration of titanium hydroxide leads to the separation of neighboring nanotubes, as shown in Figure 5-2b. At the oxide/metal interface, the dehydration of titanium hydroxide also results in the formation of gaps between the nanotubes and the metallic substrate, which might be the reason why anodic $TiO_2$ nanotubes can easily be peeled off from the metallic Ti substrate by tape.

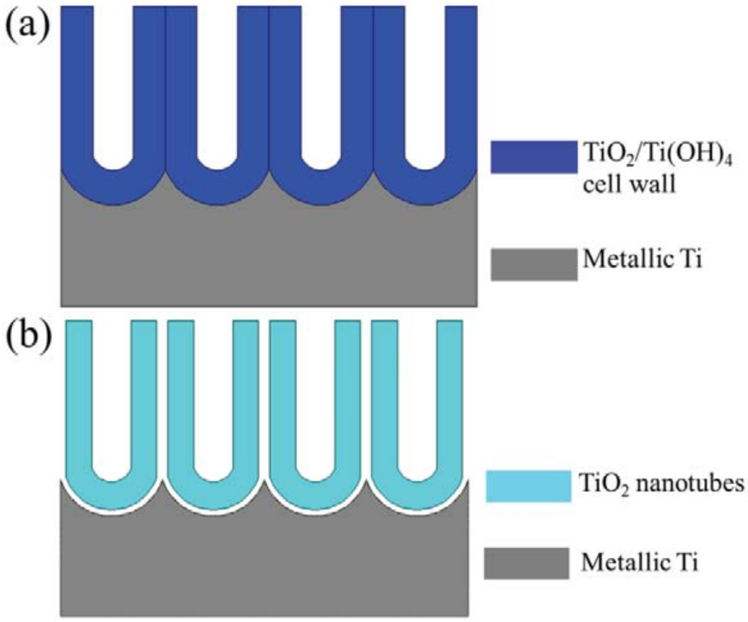

**Figure 5-2**: Illustration of the nanotubular $TiO_2$ formation process: (a) formation of $TiO_2/Ti(OH)_4$ cell walls; (b) dehydration of $Ti(OH)_4$ in the cell walls creates gaps between neighboring nanotubes and gaps between the nanotubes and the metallic substrate.

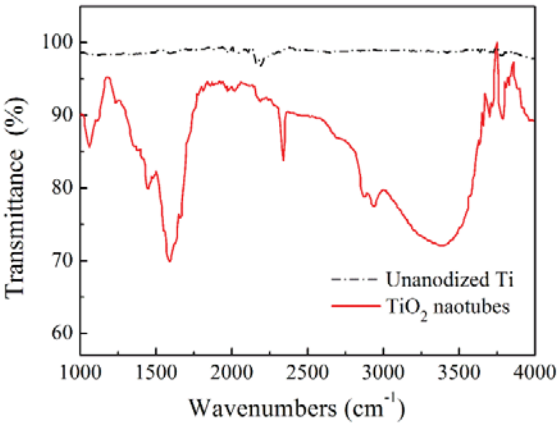

**Figure 5-3**. FTIR spectroscopy of Ti sample in different regions: un-anodized metallic Ti region and anodic $TiO_2$ nanotubular region.

Low content of water in an electrolyte limits the amounts of $OH^-$ ions and $O^{2-}$ ions and leads to a slow formation rate of the $TiO_2/Ti(OH)_4$ cell wall, which makes $Ti(OH)_4$ in the cell wall to dehydrate during the anodization. As a result, the volume shrinkage from the dehydration can be continually compensated by the volume expansion due to the anodization of Ti into $TiO_2$ and $Ti(OH)_4$. No gaps form between the neighboring cells, and anodic $TiO_2$ nanopore structure is obtained. However, increasing the $OH^-$ concentration in the electrolyte by ammonium hydroxide accelerates the formation rate of $Ti(OH)_4$ in the cell wall and enhances the rate of volume shrinkage during dehydration, which causes the transition of $TiO_2$ nanopores into nanotubes.

Based on the observation of double layer structure of $TiO_2$ nanotube walls and the existence of $OH^-$ ions in anodic $TiO_2$ nanotubes, Su and Zhou proposed that the $TiO_2$ nanotubes have a titanium hydroxide outer shell, and the volume shrinkage of this outer shell leads to the generation of gaps.[6, 209] However, they cannot explain why the titanium hydroxide layer can form at the nanotube outer wall. During the anodization, three anions migrate from the electrolyte to the oxide/metal interface: $F^-$, $O^{2-}$, and $OH^-$. Due to the small size of $F^-$ compared to $O^{2-}$, the migration rate of $F^-$ ions is almost twice that of $O^{2-}$ ions. This leads to the accumulation of fluoride at the boundary of the nanotubes. The outer shell of $TiO_2$ nanotube walls should be a fluoride-rich layer, not a titanium hydroxide layer. Moreover, because of the smaller size and higher charge of $O^{2-}$ ions compared to $OH^-$ ions, $O^{2-}$ ions migrate faster than $OH^-$ ions. As a result, titanium hydroxide should distribute throughout the whole cell wall, instead of accumulating at the tube outer shell. Therefore, in our model, I propose that the cell wall of the as-grown $TiO_2$ nanostructure is composed of a mixture of titanium hydroxide and titanium oxide.

The dehydration process of titanium hydroxide in the cell wall takes time to happen, thus examination of the structural evolution of anodic $TiO_2$ nanostructures after the anodization is a good way to verify our Ti anodization model. Here, I introduce the EIS technique to *in-situ* monitor the structure evolution of the as-grown anodic $TiO_2$ nanotubes after being submersed in the ethylene glycol electrolyte (with 10 vol% DI water and 0.1 M $NH_4F$) or dried in air. The Nyquist plots of the EIS diagram in Figure 5-4 can be deconvoluted by complex non-linear fitting based on the equivalent circuit shown in the inset. $R_S$ is the serial ohmic resistance, which includes bulk material resistance and interfacial contact resistance. Parallel connection of $R_b$ and $C_b$ indicates the interface resistance and capacitance related to the space charge layer within the bulk $TiO_2$, in which a constant phase element is used instead of the capacitance. The second loop consists of the interface resistance or charge transfer resistance $R_{ct}$ and double layer capacitance $Q_{ct}$, which indicates the process in the electrochemical double layer. $W$ is Warburg impedance and is correlated with the ion transport process.[210-211] From Figure 5-4, $R_{ct}$ decreases from 1200 $\Omega\cdot cm^2$ to 225 $\Omega\cdot cm^2$ after immersion in the electrolyte for 30 min. Once the $TiO_2$ nanotubes are dried in air, $R_{ct}$ becomes 69 $\Omega\cdot cm^2$ within 1 min. Further drying does not appear to be helpful because $R_{ct}$ is 46 $\Omega\cdot cm^2$ even after drying for 1 h.

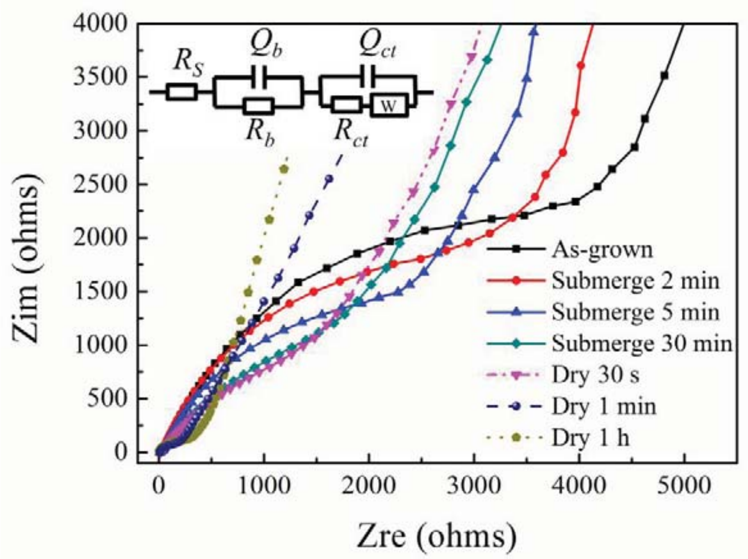

**Figure 5-4**. Nyquist plots of different $TiO_2$ nanotubes: as-grown, submersed in anodization electrolyte for different time, and dried in air for different time. The inset shows the equivalent circuit for the EIS diagram.

Physically, the formation of gaps and the separation of neighboring $TiO_2$ nanotubes may increase the electrochemical interface and relies on both the inner and outer surfaces of $TiO_2$ nanotubes for charge transfer, which causes the decrease of $R_{ct}$ in EIS. When submersion in the ethylene glycol electrolyte with 10 vol% DI water and 0.1 M $NH_4F$, the titanium hydroxide in the cell wall of nanoporous $TiO_2$ is slowly dehydrated to form the gap between $TiO_2$ nanotubes. When drying the as-grown anodic $TiO_2$ nanotubes in air, the titanium hydroxide can be rapidly dehydrated. Therefore, drying the as-grown anodic $TiO_2$ nanotubes in air for 30 s has a similar EIS result as the $TiO_2$ nanotubes submersed in electrolyte for 30 min. Moreover, the similar EIS features between the samples dried in air for 1 min and dried in air for 1 hour indicate the time scale for dehydration of titanium hydroxide is around 1 minute. As a result, when the as-grown anodic $TiO_2$ sample is transferred into the SEM chamber for characterization, the dehydration of titanium hydroxide has already occurred, which explains why the evolution of anodic $TiO_2$ nanotubes after anodization has seldom been detected before.

Moreover, the evolution of the EIS diagrams of the as-grown $TiO_2$ nanotubes by submersing them in an electrolyte or drying them in air challenges the validity of other formation mechanisms of $TiO_2$ nanotubes. Based on the localized dielectric breakdown model, as long as the anodization ceases, the localized dielectric breakdown should be suspended. As a result, there should be no variation in structure between the anodic $TiO_2$ nanotubes during the submersion in the electrolyte and drying in air. If the formation of the gaps between the $TiO_2$ nanotubes is ascribed to field assisted oxidation and dissolution of inter-tube metallic part as proposed by Grimes et al.,[67, 90] there should be no change in anodic $TiO_2$ nanotubes after the applied potential is turned off. The fluoride-rich wall splitting mechanism seems to be able to explain the changes observed in the EIS of $TiO_2$ nanotubes when being submerged in the electrolyte, because the fluoride-rich wall undergoes dissolution in the electrolyte. However, no dissolution can take place during drying, thus it is hard to understand why the EIS diagram of the $TiO_2$ nanotubes changes when being dried in air based on the fluoride-rich wall splitting mechanism.

Interestingly, if there are gaps present between the neighboring nanotubes during the anodization, the electrolyte can directly contact the metallic substrate at the gap locations, which results in a larger electrical field at the gap locations than that in the bottom regions, leading to preferential anodization and growth of nanotubes at the gap locations. However, during the anodization the nanotubes always keep growing in the bottom regions of the tubes. This question has never been addressed before by other anodization mechanisms. According to our titanium hydroxide dehydration mechanism, at the cell boundary of anodic $TiO_2$ nanostructures the two neighboring cell walls just encounter each other, as shown in Figure 5-2a, so the electrical resistance is very large, which greatly reduces the electrical field at cell boundaries. Therefore, the electrical field at the cell bottom is larger than that at the cell boundary, which leads to the continuous growth of $TiO_2$ nanostructures in the bottom regions. The gaps between the neighboring nanotubes are formed after the oxidation of metallic Ti due to the dehydration of the titanium hydroxide cell wall.

The existence of gaps between the anodic $TiO_2$ nanotubes and the metallic substrate after anodization is also examined in this study. After the anodization at 85 V in ethylene glycol with 0.1 M $NH_4F$ and 10 vol% water for 8 min and drying the as-grown $TiO_2$ nanotubes in air for 1 h, second-step anodization is carried out at 42.5 V for 3 h. As shown in Figures 5a-5c, the second-layer nanotubes all develop from the footprint of the first-layer nanotubes, and the first-layer nanotubes have closed tube bottoms. This indicates that during drying in air the dehydration of the $Ti(OH)_4$ cell wall leads to the formation of gaps between the $TiO_2$ nanotubes and the metallic substrate. Therefore, during the second-step anodization, the electrolyte can pass through the gaps and directly contact the metallic substrate underneath the first-layer $TiO_2$ nanotubes. As a result, the second-layer nanotubes preferentially develop in the footprint of the first-layer $TiO_2$ nanotubes, as illustrated in Figure 5-5d. However, if the second-step anodization at a low applied voltage is carried out directly without drying in air, the second-layer nanotubes all develop at the junctions of neighboring first-layer nanotubes, not in the footprints of the first-layer nanotubes (Figures 5-5e and 5-5f). The backside SEM image in Figure 5-5g clearly demonstrates the newly formed second-layer nanotubes originiating from the junction locations of the first-layer $TiO_2$ nanotubes. In this case, the continual anodization prohibits the formation of gaps between the $TiO_2$ nanotubes and the metallic substrate, and the barrier layer is thinner at the junctions of neighboring first-layer nanotubes than that at the tube bottom, which will be discussed in next paragraph. As a result, during the second-step anodization at low applied voltage, the $O^{2-}$ and $OH^-$ ions can only migrate across the junctions of neighboring nanotubes, and the second-layer nanotubes grow at junction locations.

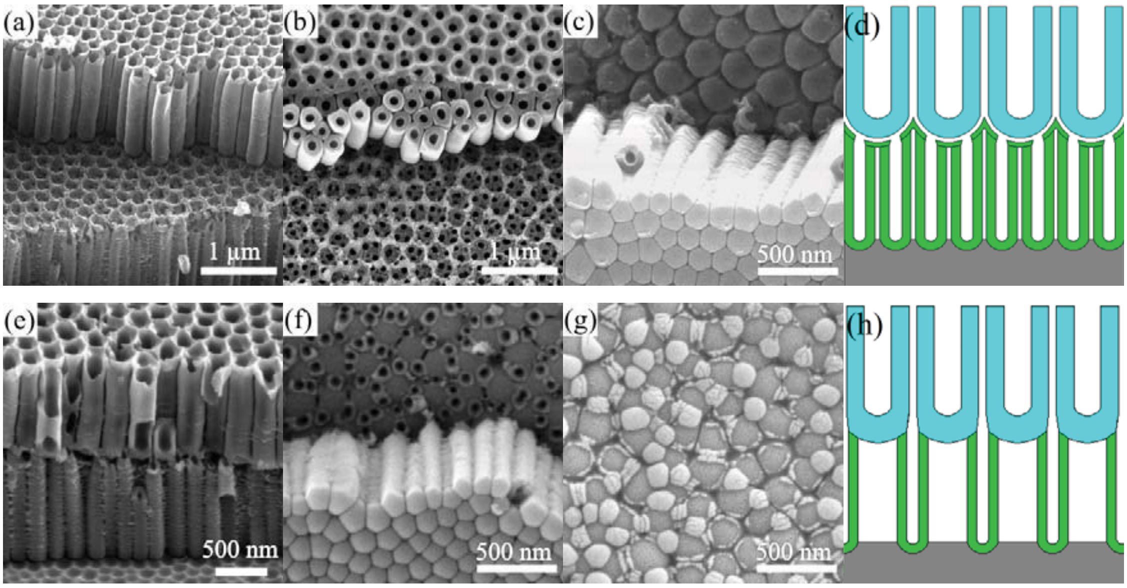

**Figure 5-5**. $TiO_2$ nanotubes obtained by anodization at 85 V for 8 min followed by drying in air for 1 h and then anodizing at 42.5 V for 3 h: (a) cross section image, (b) surface image, and (c) backside image of the double-layer $TiO_2$ nanotubes, (d) illustration of the double-layer $TiO_2$ nanotubes. (e) cross section image and (f) backside image of the $TiO_2$ nanotubes obtained by continual anodization at 85 V for 8 min and then at 42.5 V for 3 h; (g) backside image when the second-layer nanotubes initially develop; and (h) illustration of $TiO_2$ nanotubes in (e and f). In (d) and (h) the cyan color represents the first-layer $TiO_2$ nanotubes, and the green color represents the second-layer $TiO_2$ nanotubes.

### 5.1.4. Summary

A new $TiO_2$ nanotube formation mechanism based on volume shrinkage during the dehydration of titanium hydroxide cell wall is proposed. Increasing $OH^-$ concentration in the electrolyte leads to the transformation of nanoporous to nanotubular $TiO_2$ structure. Consistent with the model of dehydration of the titanium hydroxide cell wall, the as-grown $TiO_2$ nanotubes show structural evolution during submersing in an electrolyte or drying in air after the anodization, which is demonstrated by EIS measurement for the first time. The additional drying process between high potential anodization and low potential anodization demonstrates the existence of gaps between the anodic $TiO_2$ nanotubes and the metallic substrate.

## 5.2. $TiO_2$ nanotube arrays created by FIB pattern guided anodization

### 5.2.1. Introduction

Electrochemical anodization of titanium substrate is the most common method to generate $TiO_2$ nanotubes. So far, anodic $TiO_2$ nanotubes have been obtained from four different types of electrolytes: HF-based electrolyte,[67, 69] aqueous weak acids with buffered electrolytes (such as KF, $NH_4F$, or NaF),[70-72] polar organic solvents and fluoride electrolytes (such as ethylene glycol/$NH_4F$, dimethyl sulfoxide/HF),[76-77] and non-fluoride based electrolytes (such as HCl, HCl/$H_2O_2$).[82-83] Traditional one-step anodization can only create disordered $TiO_2$ nanotube arrays. Two-step anodization,[100-102] using better arranged concaves after the first-step anodization as guiding seeds, has been explored to achieve ordered $TiO_2$ nanotubes. Similar to anodic alumina nanopores, it is difficult to rely on two-step anodization to attain hexagonal close packing for $TiO_2$ nanotubes. Even in the best case scenario, the arrangement is only limited to hexagonal patterns, other important nanotube arrangement cannot be obtained.

FIB lithography and nanoimprint lithography are two widely used patterning techniques to fabricate highly ordered porous anodic alumina with both hexagonal and square arrangements.[23-32] Moreover, alumina nanopore arrays with variable pore densities,[212-213] such as Moiré patterns, have also been realized by FIB pattern guided anodization. It is of great interest if similar guided anodization strategies can be applied to titanium anodization. However, titanium has very high Young’s modulus (116 GPa) and no study has been reported in generating ordered nanotube arrays through patterning methods.

In this study, FIB patterning is used to guide the anodization of $TiO_2$ nanotubes. Highly ordered $TiO_2$ nanotubes in hexagonal arrangement are achieved. $TiO_2$ nanotubes in square and triangular shapes and arrangements are also made possible with the FIB guided anodization of square and graphite lattice concave arrays, respectively. Asymmetrical $TiO_2$ nanotube arrays in a sunflower pattern are realized by the FIB guided anodization.

### 5.2.2. Experimental procedure

Titanium substrate (99.6+%, 0.2 mm thick, Goodfellow, Oakdale, PA) was first washed by acetone, isopropanol, and methanol in ultrasound for 10 min each, and then electropolished in freezing electrolyte (~1℃) of glacial acetic acid/perchloric acid (9/1 vol %) at 55 V with 800 rpm stirring speed for 2 min. The guiding patterns for the anodization were created on the electropolished titanium surface by a FIB microscope (FEI Helios 600 NanoLab). The patterning ion beam current was 28 pA under 30 kV acceleration potential, and the ion exposure time at each patterned concave was 90 ms. The anodization was carried out in a two-electrode electrochemical cell in an electrolyte mixture of 0.1 M $NH_4F$ and 10 vol % $H_2O$ in ethylene glycol at room temperature with 2.7 mA constant current for 5 min. The voltage stabled at 88 V within 30 s. In order to separate the $TiO_2$ nanotube layer from the metallic Ti substrate for backside examination, the anodic $TiO_2$ foil was ultrasonically agitated in DI water/ethanol (1/9 vol %) for 1 min, then immersed in 0.1 M HCl for 1 h. After rinsing with DI water and drying in nitrogen stream, the anodic nanotube layer was easily peeled off from the substrate by a tape. For morphological characterization of the samples, scanning electron microscope (Quanta 600 FEG, FEI) and atomic force microscope (Digital Instruments MultiMode SPM, Veeco Instruments Inc.) were used.

### 5.2.3. Results and discussion

#### 5.2.3.1 Highly ordered $TiO_2$ nanotubes

For FIB patterning, ordered concave patterns with uniform diameter in hexagonal arrangement is created on the eletropolished titanium surface as shown in Figure 5-6a. The diameter of the concaves is 50 nm, and the depth of the concaves is 40 nm. The interpore distance is 250 nm. After the anodization, highly ordered $TiO_2$ nanotube arrays with hexagonal arrangement are obtained (Figure 5-6b). There is a layer of $TiO_2$ nanopores on the top surface, and all the nanopores grow at the sites of the FIB patterned concaves. The diameter of the nanopores is uniform, around 60 nm, and hexagonal pore outer walls are also seen on the surface. The tilted view of the backside of the $TiO_2$ nanotube array (insert of Figure 5-6b) indicates that all the nanopores have developed into nanotubes with the hexagonal arrangement unchanged, and the free-standing nanotube arrays have hexagonal tube outer shape with 250 nm uniform intertube distance. Therefore, with the guidance of FIB patterned concaves on the eletropolished titanium surface, highly ordered $TiO_2$ nanotube arrays with corresponding hexagonal arrangement are successfully fabricated.

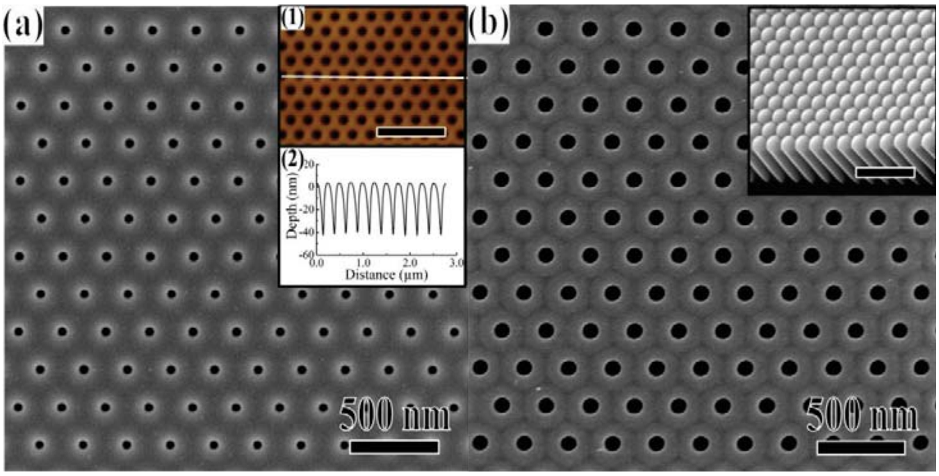

**Figure 5-6**. (a) SEM image of FIB guiding pattern in hexagonal arrangement with 250 nm interpore distance. The insert 1 is AFM image of (a), and insert 2 is the surface topology along the line in insert 1. (b) Anodic $TiO_2$ nanotube array after the FIB guided anodization, and the insert is the tilted view of the $TiO_2$ nanotube backside. The scale bars in all the inserts are 1 μm.

The FIB guidance capability for anodic $TiO_2$ nanotubes is also explored for square arrangement. An ordered concave guiding pattern, with square arrangement and 250 nm interpore distance, is created on the titanium surface by FIB (Figure 5-7a). During the anodization, the concaves serve as the seeds to grow ordered $TiO_2$ nanotubes with the same square arrangement (Figure 5-7b). The surface and backside SEM images show that the nanotubes have square outer walls with 250 nm edge length. There is a thin layer of nanopores on the top of $TiO_2$ nanotube arrays, and all the nanotubes develop from the nanopores. The cross section illustrates the effective guidance of the FIB patterned concaves and the vertical growth of the nanotubes. With the FIB guidance, $TiO_2$ nanotube arrays with the arrangement fundamentally different from self-organized hexagonal pattern are attained.

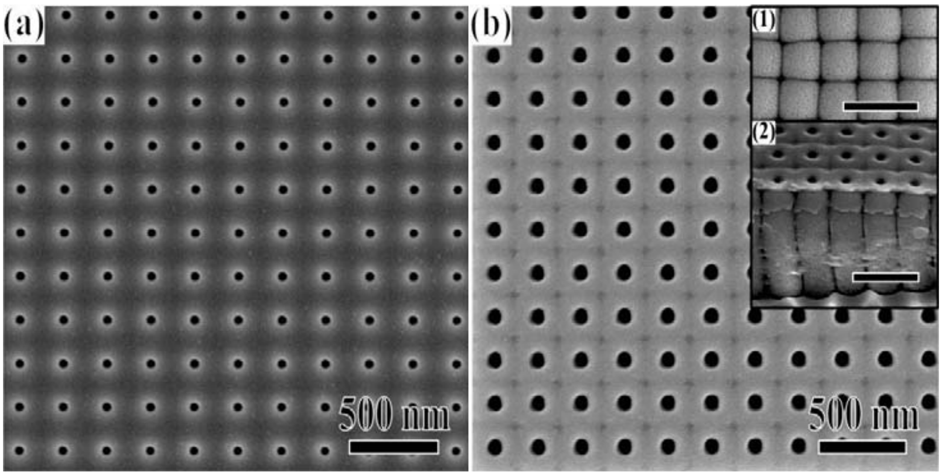

**Figure 5-7**. (a) SEM image of FIB guiding pattern in square arrangement with 250 nm interpore distance. (b) Anodic $TiO_2$ nanotube array after the FIB guided anodization. The insert 1 and insert 2 in (b) are the backside and cross section views of the $TiO_2$ nanotube arrays, respectively. All scale bars in the inserts are 500 nm.

Besides hexagonal and square outer tube shapes and arrangements, the fabrication of triangular $TiO_2$ nanotube shape is also studied here. The FIB patterned concaves with graphite lattice arrangement and 225 nm interpore distance are used to guide the anodization development (Figure 5-8a). After the anodization, all the $TiO_2$ nanotubes grow at the FIB patterned locations (Figure 5-8b). The backside and cross section views of the $TiO_2$ nanotube arrays demonstrate that no tubes form at the centers of the graphite lattice structure. The growth of each nanotube is confined by the three neighboring nanotubes, thus the nanotube outer wall can only expand to the three neighboring centers of the graphite lattice structure (as shown in the insert of Figure 5-8a). As a result, anodized $TiO_2$ nanotube array with triangular outer wall shapes in graphite lattice arrangement is obtained.

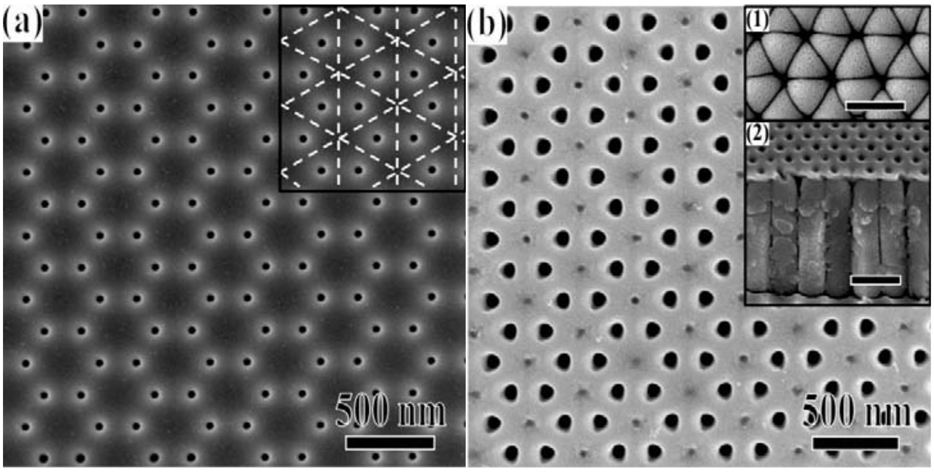

**Figure 5-8**. (a) SEM image of FIB guiding pattern in graphite lattice arrangement with 225 nm interpore distance. The insert in (a) is the schematic drawing of development of triangular nanotubes from graphite lattice structure. (b) Anodic $TiO_2$ nanotube array after the FIB guided anodization. The insert 1 and insert 2 in (b) are the backside and cross section views of the $TiO_2$ nanotube arrays, respectively. All scale bars in the inserts are 500 nm.

The mechanism of FIB pattern guided Ti anodization can be understood as follows. During the anodization, the local electrical field at the FIB patterned concave bottoms is large. The titanium oxidation and $TiO_2$ dissolution rate are accelerated at these FIB patterned locations. Moreover, $Ga^+$ implantation and titanium amorphization during the FIB bombardment also facilitate the development of the nanopores at the FIB patterned concaves. As a result, those concaves serve as seeds for the growth of the $TiO_2$ nanopores. Self-organized titanium anodization only forms hexagonal nanotube arrangement in order to minimize the volume expansion stress. For the FIB guided anodization, the intertube distance can be accurately varied and the tube arrangement can be designed into different patterns.

### 5.2.3.2 Effect of FIB pre-pattern interval distance

FIB patterned concave arrays in hexagonal arrangement with five different interpore distances ($d_{inter}$) are used to guide the anodization: 150 nm, 200 nm, 300 nm, 400 nm, and 500 nm. Figure 5-9a shows a typical FIB patterned hexagonal array on the Ti foil with 300 nm interpore distance. The diameters are 50 nm and the depths are 40 nm for all the FIB patterned concaves (Figure 5-9a insert). The periodicity of the pores is excellent. Figures 5-9b-f demonstrate the anodic $TiO_2$ nanotube arrays under the guidance of the hexagonal FIB patterns with different $d_{inter}$. After the anodization, a thin layer of ordered nanopore arrays develop at the FIB patterned positions. The backside and cross section views of the anodic $TiO_2$ in the inserts of Figure 5-9 show that the nanopores grow into separated $TiO_2$ nanotubes. The depths of the $TiO_2$ nanotube arrays are ~1.3 µm.

When $d_{inter}$ of the FIB guiding pattern is 150 nm, all the $TiO_2$ nanotubes grow at the FIB patterned concaves, thus the anodized $TiO_2$ surface has ordered nanotube arrays (Figure 5-9b). However, with further growth, some nanotubes have enlarged outer diameters while some nanotubes terminate as shown in the middle point of the cross section (insert 2 of Figure 5-9b). As a result, the anodized $TiO_2$ arrays have disordered arrangement at the tube bottoms with outer sizes ranging from 200-300 nm (insert 1 of Figure 5-9b). The tube outer wall shape is irregular polygon.

When $d_{inter}$ is 200 nm, the bottom view shows that all the tubes maintain the hexagonal arrangement with slight outer size variation (Figure 5-9c). The tube outer wall shows hexagonal shape and the sizes are 180-220 nm. When $d_{inter}$ is further increased to 300 nm and 400 nm, both the anodized surfaces and the tube bottoms show highly ordered $TiO_2$ nanotube arrays with uniform sizes and ordered hexagonal arrangement (Figure 5-9d and e). The tube outer wall shows ideally hexagonal shape. The top surface SEM images in Figure 5-9d and e also show hexagonal outer wall boundaries of the nanotubes. The tube bottom images in the inserts of Figure 5-9d and e show the outer sizes are around 300 nm and 400 nm, respectively, which are the same as the $d_{inter}$ of the FIB guiding patterns. The freestanding nanotubes are closely bound together, and the spaces between the tubes are very small. This demonstrates the exceptional capability of FIB patterning in guiding ordered $TiO_2$ nanotube growth. When $d_{inter}$ = 400 nm, some new concaves form at the tri-junctions of the FIB guided nanotubes on the top surface (Figure 5-9e). However, these concaves terminate at the very surface and do not develop into new tubes. This is because the outer walls of the neighboring FIB guided nanotubes are close to each other, and there is no extra space left to develop new tubes.

When $d_{inter}$ is increased to 500 nm, anodic $TiO_2$ nanotubes develop not only at the FIB patterned sites but also at the tri-junctions of the FIB patterned concaves (Figure 5-9f). The newly formed tubes distribute randomly at the tri-junctions. The large $d_{inter}$ allows the FIB guided $TiO_2$ nanotubes to fully expand the outer walls into circular shapes on the top surface. The nanotube bottoms in the insert of Figure 5-9f indicate that the shapes of these newly developed tube walls are triangular, and the sizes are smaller than that of the FIB guided tubes. Moreover, due to the growth of these new tubes, the outer wall shapes of the FIB guided tubes also change into rhombus or pentagon, and the sizes of the FIB guided tubes decrease from 440 nm to 350 nm.

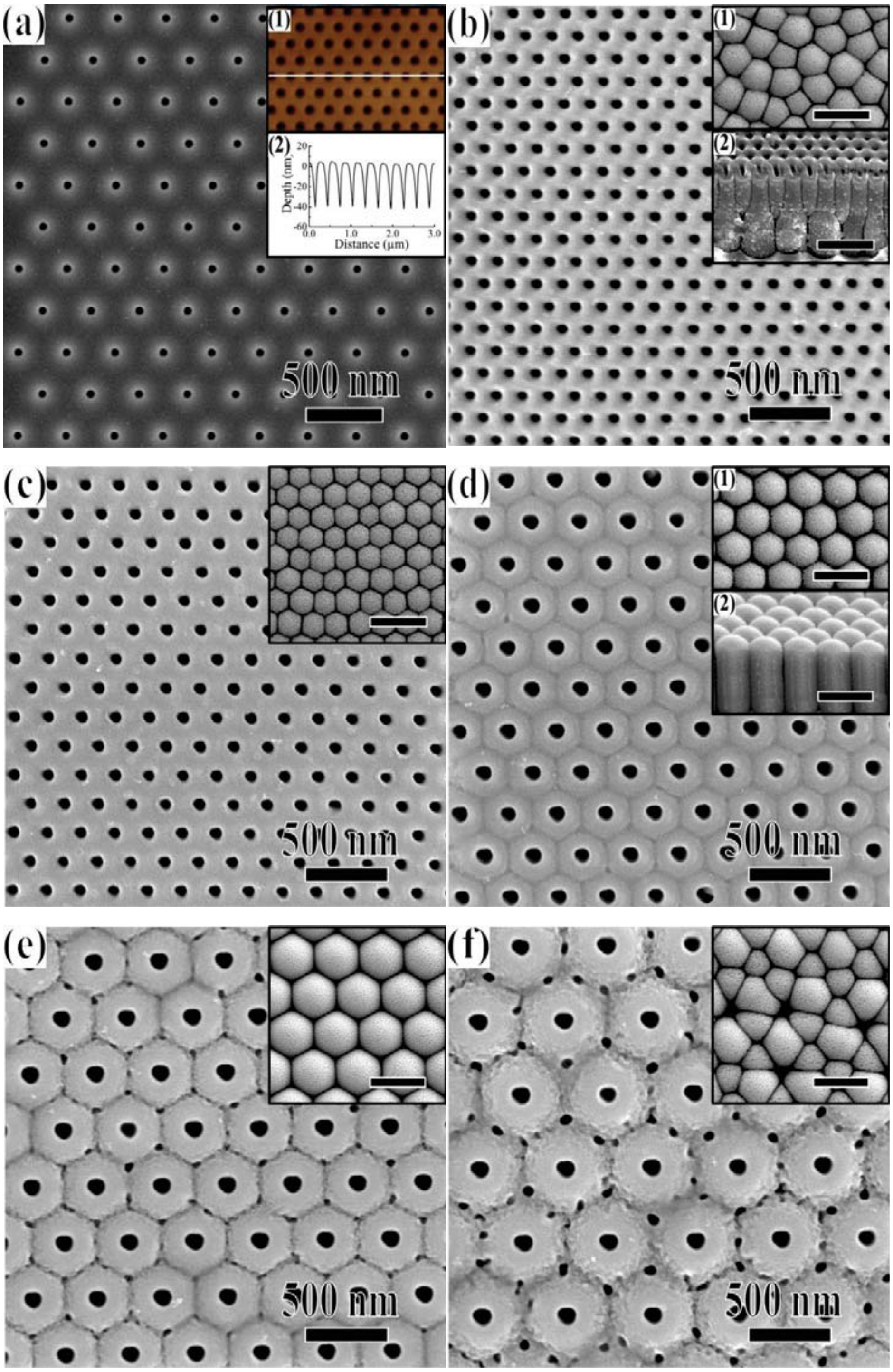

**Figure 5-9**. (a) FIB guiding pattern in hexagonal arrangement with 300 nm interpore distance. The insert 1 is the AFM image of (a), and the insert 2 is the surface topology along the line in insert 1. Anodized $TiO_2$ nanotube arrays under the guidance of hexagonal FIB pattern with different $d_{inter}$: (b) 150 nm, (c) 200 nm, (d) 300 nm, (e) 400 nm, and (f) 500 nm. The first inserts in b-f are the backside view of the anodic $TiO_2$ nanotube arrays. The insert 2 in (b) and (d) is the cross section of the anodized $TiO_2$ nanotubes. The scale bars in all the inserts are 500 nm.

Even though the FIB patterned concaves can effectively guide the growth of the $TiO_2$ nanotubes in the beginning of the anodization, whether the highly ordered hexagonal nanotube arrays can maintain the arrangement in the depth direction is related to the applied potential. In general, the outer diameter of self-organized $TiO_2$ nanotubes can be described by $D=2f_{growth}U$,[87-88] where $f_{growth}$ is the growth factor for anodic oxides, 2.5 $nm\cdot V^{-1}$ for $TiO_2$, and U is the applied potential. This is the case when the $TiO_2$ tubes are apart from each other, the growth of $TiO_2$ tubes does not influence the neighboring tubes, and the shape of the tubes is circular. For the anodization condition here, the applied potential is 88 V, thus $D = 2 \times 2.5\, nm\, V^{-1} \times 88\, V = 440\, nm$.

When the $d_{inter}$ of the FIB guiding pattern is 150 nm, much smaller than D of 440 nm, there is strong competition between the closely arranged nanotubes for outer wall growth, and the large volume expansion stress (volume expansion from Ti to $TiO_2$ is the Pilling Bedworth ratio of 1.95)[86, 214] enlarges the diameter of some tubes through terminating the neighboring tubes. As a result, the hexagonal nanotube arrangement cannot be maintained and changes into disordered tube arrays. When $d_{inter}$ is increased to 200 nm, the competition of the volume expansion of the $TiO_2$ tubes decreases but still influences the pattern development. The hexagonal arrangement is maintained but with slight difference in tube outer sizes. When $d_{inter}$ is further increased to 300 nm and 400 nm, the volume expansion stress between neighboring $TiO_2$ tubes is small. Consequently, the anodized $TiO_2$ nanotube arrays maintain the highly ordered hexagonal arrangement. Due to the confinement of the neighboring tubes, a tube stops expanding its outer diameter once meeting the neighboring tube walls, and the outer wall shape is hexagonal. In the case of $d_{inter}$ =500 nm (>D of 440 nm), even when the tubes fully expand into circular shapes, there is still enough space ($500/\sqrt{3} - 200 = 69\, nm$) left at the tri-junctions of the FIB patterned concaves to develop new tubes. Furthermore, the development of the new tubes changes the nanotube arrangement and $d_{inter}$ at the tube bottoms, which confines the diameter of the FIB guided tubes.

The interval distance of the FIB pre-patterned concaves also influences the anodic $TiO_2$ nanotube arrays with square arrangement. At the beginning of the anodization, ordered nanotubes with square arrangement form due to the square FIB pattern guidance. However, further development of the anodized tubes is related to the interpore distance. When $d_{inter}$ (150 nm) < D (440 nm), the tubes are close to each other, the large volume expansion stress from the neighboring tubes makes some tubes terminate and some tubes expand, thus the square arrangement changes into disordered arrangement with tube outer sizes ranging 180-280 nm. When $d_{inter}$ is 200 nm, the volume expansion stress from the neighboring tubes is reduced, and the square arrangement remains unchanged. However, the tube sizes are still not uniform because of the competition of the volume expansion from neighboring tubes (Figure 5-10c). When $d_{inter}$ is further increased to 300 nm and 400 nm, as discussed above, the volume expansion stress between neighboring tubes is small. The tubes expand equally and thus highly ordered $TiO_2$ nanotube arrays with square arrangement and square outer wall shape are obtained as shown in Figure 5-10d and e. At 400 nm intertube distance, some shallow pores form at the quadral-junctions of the patterned concaves. However, these new pores terminate and do not develop into new tubes (Figure 5-10e). When $d_{inter}$ (500 nm) > D (440 nm), the $TiO_2$ nanotubes expand into more circular shapes on the top surface, the un-anodized region at the quadral-junctions is approximately $500 \times \sqrt{2} - 440 = 122$ nm in size. New tubes form at the quadral-junctions with diameters smaller than the FIB guided tubes (210 nm vs. 340 nm). Also, the guided nanotubes evolve into more circular shapes while the new tubes have almost ideal rhombus shapes. As a result, $TiO_2$ nanotube arrays with square arrangement and alternating sizes are fabricated (Figure 5-10f).

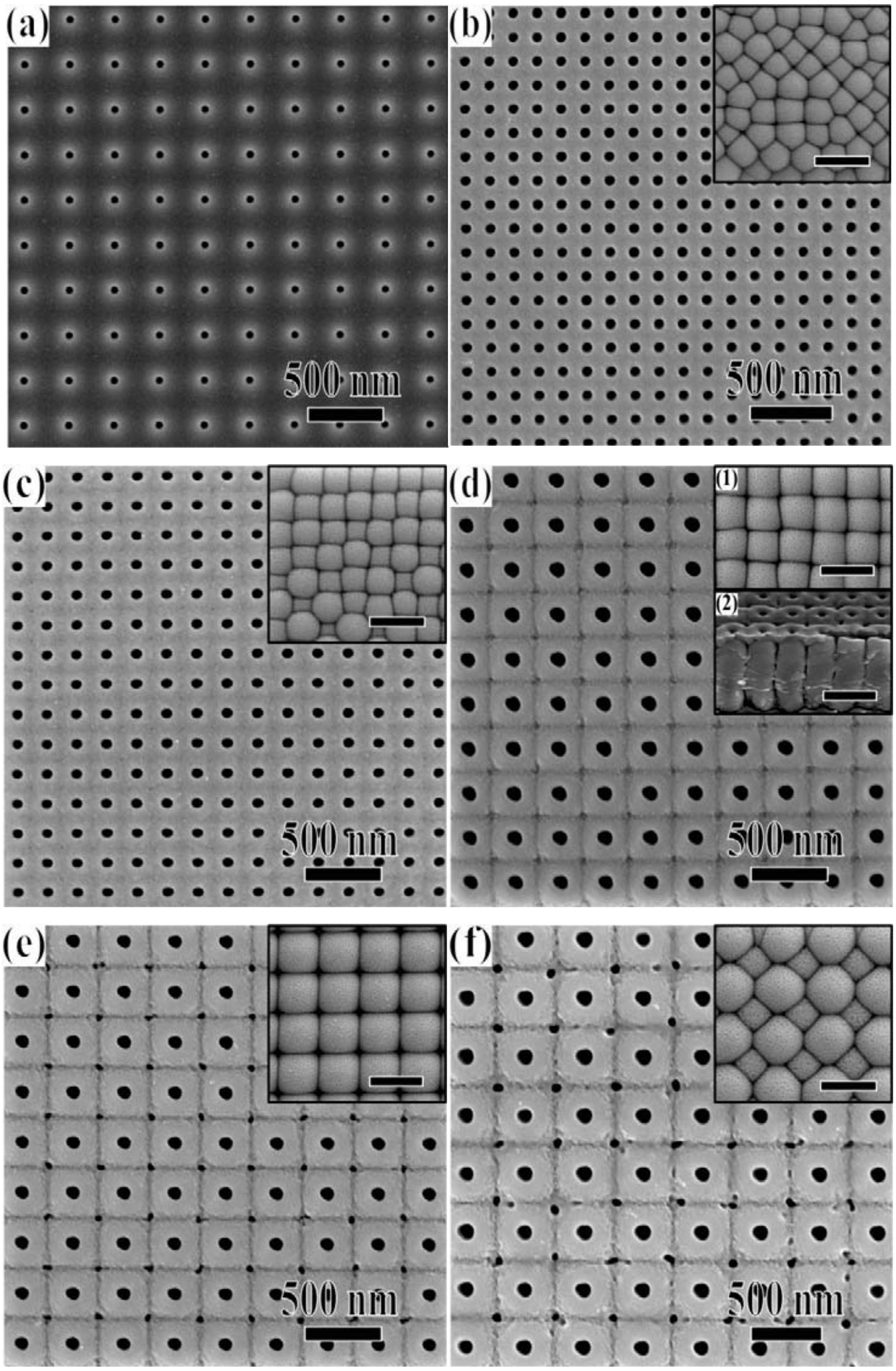

**Figure 5-10**. (a) FIB guiding pattern in square arrangement with 300 nm interpore distance. Anodic $TiO_2$ nanotube arrays with different intertube distance: (b) 150 nm, (c) 200 nm, (d) 300 nm, (e) 350 nm, and (f) 400 nm. The first inserts in all the images are the backside view of the anodic $TiO_2$ nanotube arrays. The insert 2 in (d) is the cross section of the tubes. The scale bars in all the inserts are 500 nm.

#### 5.2.3.3 $TiO_2$ nanotube arrays with more sophisticated arrangements

In this study, not only the guidance of symmetrical FIB patterns (such as hexagonal and square structures) on anodic $TiO_2$ nanotube formation is examined, but also the guidance of asymmetrical FIB patterns is explored.

Figure 5-11a shows FIB patterned concave arrays with oblique hexagonal arrangement. There are three different interpore distances for the neighboring concaves: 200 nm, 250 nm, and 300 nm as shown in the insert of Figure 5-11a. All the interpore distances are smaller than that of the free expanding $TiO_2$ nanotubes (440 nm). The diameters of all the FIB patterned concaves are 50 nm, and the corresponding depths are 40 nm. After the anodization, ordered nanopore arrays are developed on the top surface, and the arrangement stays unchanged (Figure 5-11b). The backside view of the anodic $TiO_2$ in the insert of Figure 5-11b shows that the freestanding $TiO_2$ nanotubes are closely bound with each other. The shape of the tube bottoms is parallelogram, and the arrangement of the tube array remains oblique hexagonal. The center distances of the three neighboring tube bottoms remain at 200 nm, 250 nm, and 300 nm, respectively. However, if the three interpore distances of the oblique hexagon are decreased to 150 nm, 200 nm, and 250 nm, respectively, the anodized $TiO_2$ nanotube array cannot maintain the oblique hexagonal arrangement but changes into disordered distribution. As discussed above for the hexagonal patterns, the intertube distance from 200 nm to 400 nm is suitable for maintaining regular arrangements during the anodization; for the square patterns, the intertube distance from 200 to 350 nm can be maintained the square arrangements. Figure 5-11 shows that even for asymmetrical nanopore arrangement, nanotube arrays with intertube distance ranging from 200 nm to 300 nm can be formed under the guidance of the FIB patterned concaves.

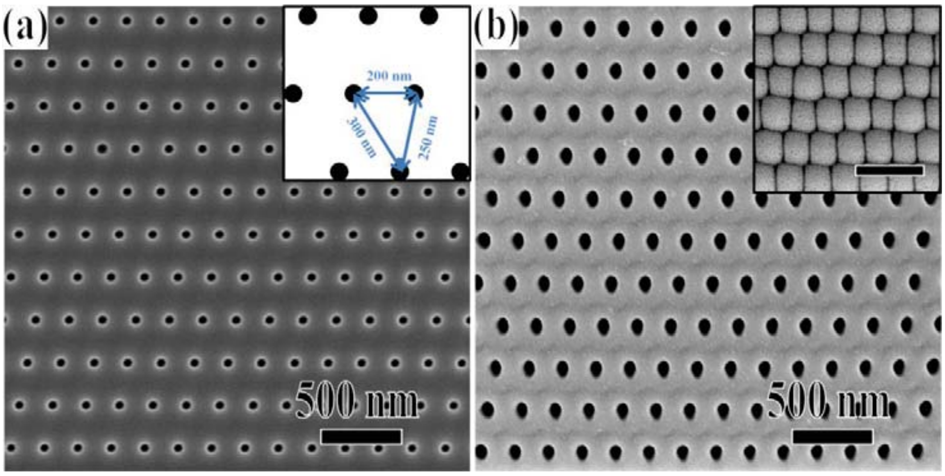

**Figure 5-11**. (a) FIB guiding pattern with asymmetrical arrangement and three different interpore distances: 200 nm, 250 nm, and 300 nm. The insert in (a) is the schematic of different interpore distances. (b) Anodic $TiO_2$ nanotube arrays after the anodization. The insert in (b) is the backside view of the anodic $TiO_2$ nanotube arrays, and the scale bar is 500 nm.

Figure 5-12b shows the FIB guiding concave pattern, and Figure 5-12c shows the corresponding anodized $TiO_2$ nanotube arrays with a sunflower pattern. Even though the $TiO_2$ nanotube arrays have asymmetrical nanotube arrangement, the backside view of the tube bottoms indicates that the FIB concave pattern can still effectively guide the growth of $TiO_2$ nanotubes. In this case, the intertube distances of the $TiO_2$ nanotube sunflower pattern range from 200 to 260 nm. Similar to a sunflower (Figure 5-12a), the $TiO_2$ nanotube sunflower is made up of nanotubes that are located at the pattern center, along with the nanotubes distributed outward in an optimal filling of the space. Each $TiO_2$ nanotube settles into a position that has a certain rotation angle relative to the previous nanotube. The pattern can be mathematically described with polar coordinates: [215]

$$r = d\sqrt{k},\ \theta = k\alpha \tag{5-7}$$

where r is the distance from the center of the sunflower to each nanotube, d is the distance of the nearest nanotube to the center nanotube (180 nm), k is the seed number, $\theta$ is the rotation angle of each nanotube, and $\alpha$ is 0.618 (decimal fraction of golden ratio) of a complete turn (222.5°). Two sets of spirals can be identified for the $TiO_2$ nanotube sunflower, one curving counterclockwise and the other clockwise. In Figure 5-12c, the $TiO_2$ nanotube arrays can be either grouped into 55 counterclockwise spirals (insert 1 of Figure 5-12d) or 34 clockwise spirals (insert 2 of Figure 5-12d), which are two nearby Fibonacci numbers (the numbers in the sequence: $a_n=a_{n-1}+a_{n-2}$, such as 0, 1, 1, 2, 3, 5, 8, 13, 21, 34, 55, 89, 144, …). The fabrication of the $TiO_2$ nanotube sunflower pattern demonstrates the significant potential of FIB guided anodization to design nano-devices in the future.

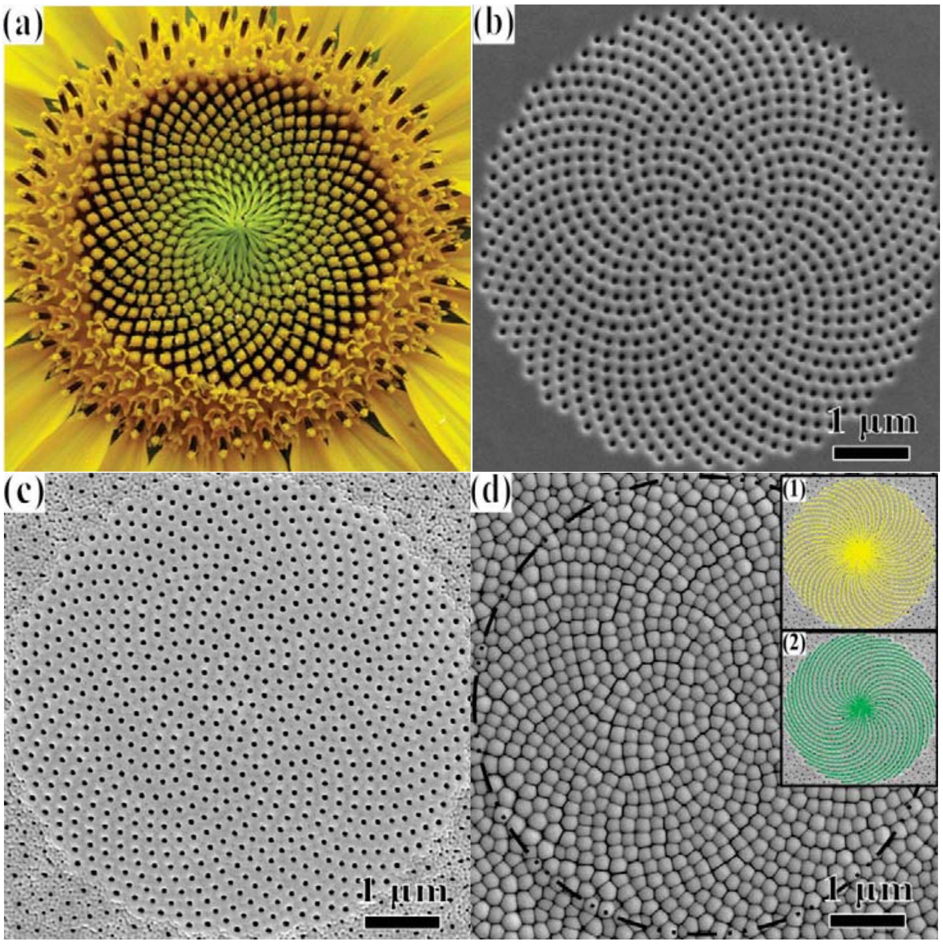

**Figure 5-12**. (a) Photograph of a sunflower head in nature, (b) SEM image of the FIB guiding pattern, (c) $TiO_2$ nanotube arrays after the FIB guided anodization, (d) The backside view of the anodic $TiO_2$ nanotube arrays. The insert 1 and insert 2 in (d) are the schematic of counterclockwise spirals and clockwise spirals in the $TiO_2$ nanotube sunflower, respectively. The circle with dashed line in (d) is schematic of the location of FIB guided $TiO_2$ nanotubes.

Another sophisticated pattern studied here is hexagonal arrangement with alternating-sized FIB concaves. The diameter of the small concaves is 50 nm, and the diameter of the large concaves is 100 nm (Figure 5-13a). The interpore distance is 250 nm. After the anodization, the top surface SEM image (Figure 5-13b) shows the anodic $TiO_2$ nanotubes have almost the same inner diameter at ~65 nm, with the larger tubes showing a crater around the tubes. The backside view of the $TiO_2$ nanotube arrays indicates that the tubes developed from the large FIB concaves have larger outer dimension (330 nm) and hexagonal shape; while the small tubes developed from the small FIB concaves have elongated hexagonal shape with the long axis at 265 nm and the short axis at 170 nm. The larger size and more regular hexagonal shape of the larger tubes are believed to result from the larger diameter, more $Ga^+$ implantation, and titanium amorphization of the larger FIB concaves, which makes the corresponding nanotubes grow faster and experience less constraint from the neighboring tube volume expansion, and thus have thicker oxide walls. The small concaves have four small concaves and two large concaves as neighbors to start with. The oxide layer growth in the direction connecting the large tubes is restricted, thus the oxide layer is thinner than that in the direction perpendicular to the connecting line of the large tubes. As a result, the small concaves grow into small tubes with elongated hexagonal shapes.

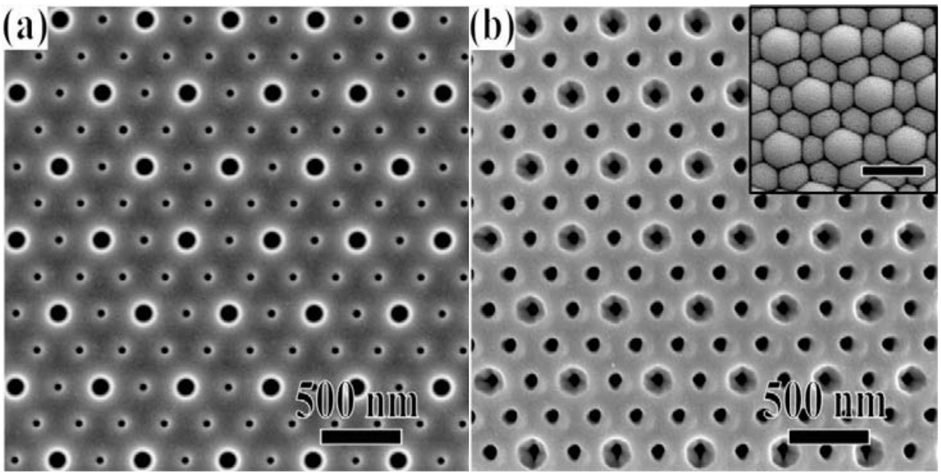

**Figure 5-13**. (a) FIB guiding pattern in hexagonal arrangement with alternating concave diameters, the interpore distance is 250 nm, and the diameters are 50 nm and 100 nm, respectively. (b) Anodic $TiO_2$ nanotube arrays after the anodization. The insert in (b) is the backside view of the anodic $TiO_2$ nanotube arrays, and the scale bar is 500 nm.

### 5.2.3.4 Self-compensating effect

The self-compensating effect of anodic $TiO_2$ nanotubes is another interesting finding for FIB guided anodization. A concave array with graphite lattice arrangement is created by the FIB patterning (Figure 5-14a). The interpore distance for neighboring concaves is 250 nm, with 50 nm concave diameter and 40 nm depth. After the anodization, the $TiO_2$ nanotubes not only grow at the FIB patterned concaves, but also at the centers of the graphite lattice structure due to the self-compensating effect. As a result, hexagonal arrangement of $TiO_2$ nanotubes with alternating sizes is obtained even though the FIB guiding concaves are purposely designed with missing sites in the hexagonal pattern center (Figure 5-14b). The cross section shows the development and vertical growth of the patterned and new tubes with alternating tube outer wall sizes (insert 2 in Figure 5b). The fundamental reason can still be traced back to the constraining effect of the oxide layers. For the current pattern design, the distance from each concave to the center of the graphite lattice structure is 250 nm, which is larger than $D/2=f_{growth}U=220$ nm. After the oxide layer fully expands in the direction of graphite lattice structure center, there is still enough space left for new tubes to develop at the centers of graphite lattice structure. However, other locations are effectively prevented from the anodization by the oxide layers. Moreover, due to the confinement of the FIB guided nanotubes, the size of the newly formed nanotubes is smaller than that of FIB guided nanotubes, while the hexagonal shape is maintained for both tube sizes. The self-compensation phenomenon, which tolerates the existence of missing concaves for the FIB patterning, is an important advancement in fabricating highly ordered and alternating-sized hexagonal $TiO_2$ nanotubes.

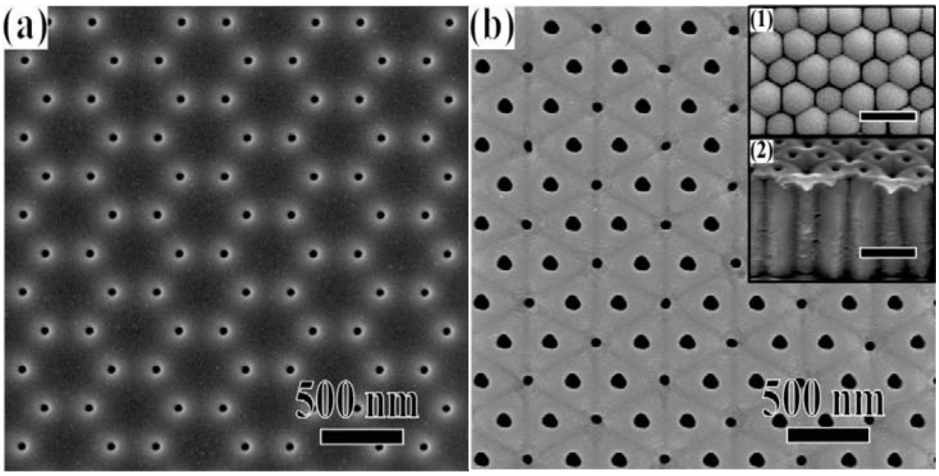

**Figure 5-14**. (a) FIB guiding pattern in graphite lattice arrangement with 250 nm interpore distance. (b) SEM image of $TiO_2$ nanotube arrays after the anodization. The insert 1 and insert 2 are the backside view and cross section of the $TiO_2$ nanotube arrays, respectively. The scale bars in all inserts are 500 nm.

### 5.2.4. Summary

Highly ordered hexagonal anodic $TiO_2$ nanotube arrays have been successfully obtained by the guidance of FIB patterned concaves. More importantly, under the FIB guided anodization, square nanotubes with square arrangement and triangular nanotubes with graphite lattice arrangement have also been obtained. The intertube distance for ordered hexagonal arrangement ranges from 200 nm to 400 nm, while for square arrangement it ranges from 200 nm to 350 nm.

When the intertube distance is below the guiding range, the anodized tubes initially grow at the locations of the FIB patterned concaves, however, some tubes terminate while other tubes grow larger, and the arrangement changes into disordered when the anodization continues. When the intertube distance is increased above the guiding range, new tubes develop at the junctions of the FIB patterned concaves. More sophisticated $TiO_2$ nanotube arrays, such as oblique, alternating-sized hexagonal patterns, and sunflower structure, have been successfully created by the FIB guided anodization. Missing sites from the graphite lattice structure guiding pattern can be self-compensated during the anodization to form ordered hexagonal $TiO_2$ nanotube arrays with alternating-sized diameters. FIB patterning is proved to be an effective method to fabricate highly ordered and novel $TiO_2$ nanotube arrays.

## 5.3. Fabricated different $TiO_2$ nanotube structures

### 5.3.1. Introduction

Two-step anodization method has been used to achieve highly ordered $TiO_2$ nanotubes.[100-102, 105] After peeling off the $TiO_2$ nanotubes generated in the first-step anodization, the well-ordered footprints of the initial nanotubes serve as the seeds to guide the growth of ordered $TiO_2$ nanotubes during the second-step anodization. A modified two-step anodization has also been exploited to obtain more complicated structures. When the applied voltage in the second-step anodization was lower than that in the first-step anodization, lotus-root-shaped nanotubes with several smaller nanotubes contained in each footprint were obtained.[95, 102]

Different types of multi-branched anodic aluminum oxide nanopores have been fabricated by adjusting the anodization voltage.[40-43] For anodic $TiO_2$ nanotubes, double-layer nanotube arrays with branched nanotubes growing underneath the truck nanotubes are obtained by anodization at the same applied voltage but in different electrolytes. For example, one double-layer array was created by first anodization in a HF aqueous electrolyte, followed by anodization in a glycerol/$NH_4F$ mixture.[105] However, the diameters of the branched nanotubes and the number of branches were hard to control. Alternating voltages in the same anodization electrolyte, with a sequence of high voltage (120 V for 1 min) and low voltage (40 V for 5 min), led to alternating growth of tubes and the formation of a compact layer.[103-104] As a result, $TiO_2$ nanotubes with bamboo-like features were achieved. When the anodization voltage was reduced from 120 V to 40 V and maintained at 40 V for a long period of time, the large truck nanotubes diverged into several small branched nanotubes.[103] However, the fabrication of hierarchically branched $TiO_2$ nanotubes with controlled branch numbers, nanotube diameters, and multiple layers have not been achieved. And the mechanism for the formation of bamboo-type $TiO_2$ nanotubes is unknown.

In this paper, a modified two-step anodization method is used to fabricate hierarchically $TiO_2$ nanotubes. The approach utilizes the well-ordered footprints of the nanotubes from the first-step anodization to create ordered truck $TiO_2$ nanotube arrays. During the second-step anodization, the applied voltage is systemically reduced by a factor of $1/\sqrt{n}$ to generate $n$-branched $TiO_2$ nanotubes. This method demonstrates to be a generic method to fabricate multiple layers of hierarchically branched nanotubes by varying the applied voltage in multiple steps with different $1/\sqrt{n}$ factors. The combination of reducing and increasing anodization voltages in sequence is further explored to fabricate sophisticated $TiO_2$ nanotube structures. The mechanism for fabrication of bamboo-type $TiO_2$ nanotubes is also explored.

### 5.3.2. Experimental procedure

$TiO_2$ nanotube arrays were prepared by using a modified two-step anodization process. The anodization was carried out in a two-electrode electrochemical cell in ethylene glycol electrolyte containing 0.1 M $NH_4F$ and 10 vol % DI water at room temperature. The first-step anodization was performed under either 85 V or 42.5 V applied voltage for 1 h; then, the formed anodic $TiO_2$ nanotube arrays were peeled off by a tape. The second-step anodization was performed under the same conditions as the first-step to form the truck nanotubes, and then the anodization voltage was decreased by a factor of $1/\sqrt{n}$ or increased by a factor of $\sqrt{n}$ to fabricate hierarchical $TiO_2$ nanotube arrays. For the bamboo-type $TiO_2$ nanotubes, the anodization was carried out at cycling the applied potential between 85 V for 3 min and 42.5 V for 20 min.

### 5.3.3. Results and discussion

#### 5.3.3.1 n-branched nanotubes

Figure 5-15a shows the voltage-time and current-time curves during the anodization in ethylene glycol electrolyte containing 0.1 M $NH_4F$ and 10 vol% DI water at room temperature. The applied voltage is first maintained at 85 V for 8 min, and the current density decreases from 14 mA/cm$^2$ to 6 mA/cm$^2$ in 50 s due to the formation of a $TiO_2$ barrier layer at the concave bottom. The increase in current density from 6 mA/cm$^2$ to 9 mA/cm$^2$ in the next 1 min indicates the development of $TiO_2$ nanotubes. Then, the applied voltage is slowly reduced by a factor of $1/\sqrt{3}$ from 84 V to 49 V with a decreasing rate of 15 V/min. At the same time, the current density also decreases to 0.2 mA/cm$^2$. Finally, the applied voltage is maintained at 49 V for 1 h; the current density first increases to 2 mA/cm$^2$ in 4 min and then is maintained at 2 mA/cm$^2$.

Figures 5-15b and c show that the anodized $TiO_2$ nanotubes have branched structures. The surface structures of the large truck $TiO_2$ nanotubes (top region) and small branched $TiO_2$ nanotubes (bottom region) in Figure 5-15c clearly reveals the corresponding trifurcation of a truck nanotube into three small branched nanotubes. The white line contours of branched junctions in Figure 5-15d show that a large truck nanotube diverges into three small branched nanotubes and demonstrate the development of branched nanotubes as $1 \prec 3$ structure ($1 \prec n$, "$\prec$" stands for the junction where the branching takes place, and $n$ stands for the number of branches produced). The diameter of the truck $TiO_2$ nanotubes is 260 nm, and the diameter of the branched nanotubes is 155 nm. The lengths of the truck and branched $TiO_2$ nanotubes are 2.3 μm and 2.1 μm, respectively. The increase in the current density from 0.2 mA/cm$^2$ to 2 mA/cm$^2$ when the applied voltage changes to 49 V implies the growth of small branched nanotubes.

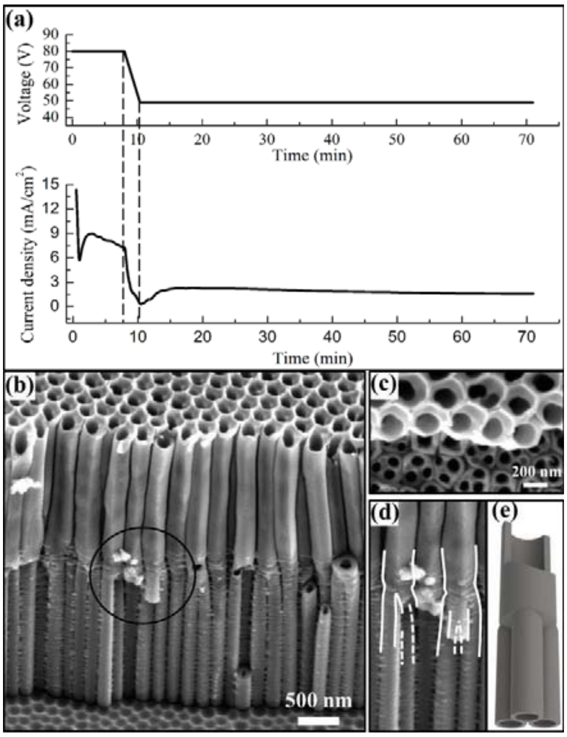

**Figure 5-15**. (a) Voltage-time and current-time curves during the second-step anodization. (b) SEM image of branched $TiO_2$ nanotubes after the anodization. (c) Surface image of the truck nanotubes (top region) and branched nanotubes (bottom region). (d) Highlight branching junctions in the circle of (b) by white line contours. (d) Schematic illustration of $1 \prec 3$ branched $TiO_2$ nanotubes.

The slow decreasing rate of the applied voltage from 85 V to 49 V is very important. If the applied voltage suddenly reduces from 85 V to 49 V, the current density will decrease to ~0 mA/cm$^2$ for the entire anodization time, and no branched nanotube structures can be formed. This can be understood as follows. When the Ti foil is anodized under a high applied voltage of 85 V, the oxide barrier layer at the nanotube bottom is thick, because the oxide barrier layer thickness at the bottom of the $TiO_2$ nanotubes is determined by the applied voltage: [87-88]

$$R = f_{growth} U \qquad (5\text{-}8)$$

where $f_{growth}$ is the growth factor for anodic oxides, and $U$ is the applied voltage. The inward oxygen ionic current $j$, which is related to the electric field $E$ across the barrier layer, determines the oxidation:[5]

$$j = j_0 \times e^{kE} \qquad (5\text{-}9)$$

where $j_0$ and $k$ are material dependent constants. When the applied voltage is decreased, the oxidation rate will decrease exponentially due to the reduced electric field across the barrier layer. At the same time, the local chemical micro-environments at the bottom of the nanotubes are unchanged. Therefore, the $TiO_2$ dissolution rate decreases slower than the $TiO_2$ formation rate.[93] As a result, the thickness of the oxide barrier layer decreases. When the applied voltage is reduced by a factor of $1/\sqrt{3}$ from 85 V to 49 V, the barrier layer thickness needs to reduce by a factor of $1/\sqrt{3}$ before the further growth of $TiO_2$ nanotubes. Otherwise, the thick barrier layer will lead to a small electric field, which is unable to drive the $O^{2-}$ anion migration for the $TiO_2$ nanotube growth.

The oxidation of Ti will generate $H^+$ ions:

$$Ti + 2H_2O \rightarrow TiO_2 + 4H^+ + 4e^- \qquad (5\text{-}10)$$

which affects the dissolution rate of the $TiO_2$ barrier layer under the reaction:

$$TiO_2 + 6F^- + 4H^+ \rightarrow TiF_6^{2-} + 2H_2O \qquad (5\text{-}11)$$

If the applied voltage is slowly reduced at the rate of 15 V/min, the oxidization will create enough $H^+$ ions to dissolve the barrier layer to the critical thickness. This ensures that the electric field is high enough to drive the anions to further nanotube growth. However, if the applied voltage suddenly reduces from 85 V to 49 V, the electric field will be too small and the oxidation will almost stop. As a result, there are not enough $H^+$ ions to reduce the barrier layer thickness and the nanotube growth terminates.

The influence of voltage drop on the electrolyte during the anodization should also be considered. Some studies show that the low conductivity non-aqueous electrolytes, such as ethylene glycol solvent, will lead to large voltage drop on the electrolyte during the anodization.[91] As a result, the actual voltage value on the Ti sample is much smaller than the applied voltage. However, during the anodization in this work, when the applied voltage is 85 V and 49 V, the voltage drop on the anodization electrolyte is 1.43 V and 0.74 V, respectively. In both cases, the voltage drop value is less than 2 % of the applied voltage. This can be ascribed to the addition of 10 vol% DI water in the ethylene glycol solvent, which increases the conductivity of the electrolyte. Therefore, voltage drop effect of the electrolyte is minor here, and can be neglected.

According to the literature, the outer diameter of the $TiO_2$ nanotubes is determined by the applied voltage: $D=2f_{growth}U$.[87-88] The growth factor for $TiO_2$ in the literature is 2.5 nm/V. However, this value only represents the situation that all nanotubes can fully expand the outer wall, and there is no restriction from the neighboring nanotubes. As a result, the nanotubes have perfect cylindrical outer shape. However, for the self-organized $TiO_2$ nanotubes here, the neighboring nanotubes limit the free expansion of the $TiO_2$ nanotube outer wall; the outer diameter is restricted by neighboring nanotubes, and the effective growth factor reduces from 2.5 nm/V to 1.5 nm/V. When the applied voltage is 85 V and 49 V, the outer diameter of the $TiO_2$ nanotubes is 260 nm and 155 nm, respectively. Since the outer diameter of the $TiO_2$ nanotubes is proportional to the applied voltage, when the applied voltage is reduced by a factor of $1/\sqrt{3}$ , the outer diameter is also reduced by a factor of $1/\sqrt{3}$ . As a result, the cross section area of the nanotubes is reduced by a factor of 1/3. Because the truck and branched nanotubes fully filled the top and bottom layers, a large truck nanotube diverges into three small branched nanotubes with the same size based on the equal-area model.[4-6]

Different types of branched ($1 \prec n$) $TiO_2$ nanotube structures can be obtained by reducing the applied voltage in a controlled manner. As shown in Figure 5-16a, when the applied voltage is first kept at 85 V for 8 min, then slowly decreased by a factor of $1/\sqrt{2}$ to 60 V with the reducing rate at 15 V/min, and finally maintained at 60 V for 1 h, the anodized $TiO_2$ nanotubes have $1 \prec 2$ (or Y-branching) structures (Figure 5-16a). The inset 2 of Figure 5-16a clearly shows the bifurcation of one large truck nanotube into two small branched nanotubes, and the reduction ratio of the diameter from 260 nm to 175 nm is $1/\sqrt{2}$ , which satisfies the reduction ratio of the applied voltage.

Similarly, when the applied voltage is slowly reduced by a factor of 1/2 from 85 V to 42.5 V with 15 V/min reducing rate, as shown in Figure 5-16b, the diameter of the branched nanotubes (125 nm) is reduced to half of the truck nanotube diameter (260 nm). As a result, the cross section area of the branched nanotubes is 1/4 of the truck nanotube, and the anodized $TiO_2$ nanotubes have $1 \prec 4$ structures (Figure 5-16b).

When the applied voltage is small, it takes a longer time to reduce the barrier layer to the critical thickness, thus the voltage reducing rate should be much slower. When the applied voltage is reduced by a factor of 1/3 from 85 V to 28 V, it should first be reduce from 85 V to 42.5 V at 15 V/min, then from 42.5 V to 28 V at 8 V/min. As a result, the diameter of the branched nanotubes is 90 nm, which is around 1/3 of the diameter of the truck nanotubes (265 nm). Thus, the cross section area of the branched nanotubes along the direction perpendicular to the depth direction is 1/9 of that of the truck nanotube. As shown in the schematic illustration in the insert 1 of Figure 5-16c, the anodized $TiO_2$ nanotubes have $1 \prec 9$ structures, and the nine branched nanotubes are closely packed with each other. However, from the cross section SEM image in Figure 5-16c, I can only see the three branched nanotubes, because these three branched nanotubes appear in the front of the other six branched nanotubes and block the observation of all nine branched nanotubes.

In general, as long as the applied voltage stays in the anodization window that forms $TiO_2$ nanotubes, slowly reducing the applied voltage by a factor of $1/\sqrt{n}$ will lead to $1 \prec n$ branched $TiO_2$ nanotubes, and the diameters of the branched nanotubes will be reduced to $1/\sqrt{n}$ of the truck nanotube diameter.

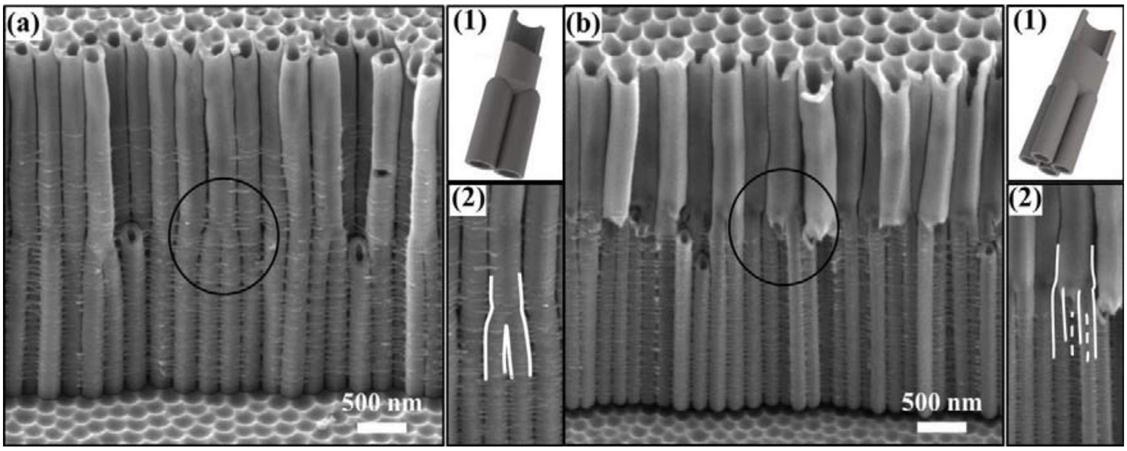

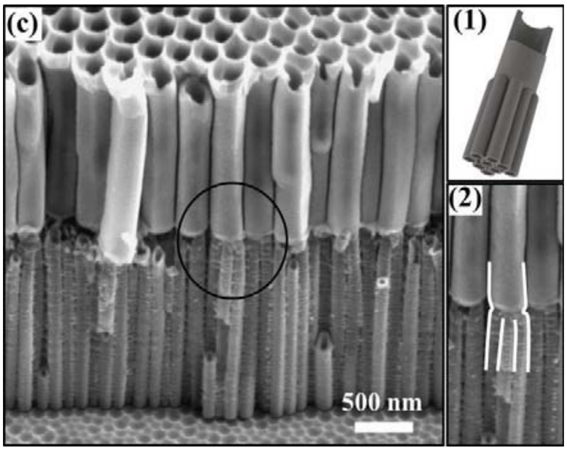

**Figure 5-16**. SEM images of anodized $1 \prec n$ branched TiO$_2$ nanotubes: (a) $1 \prec 2$ structure, (b) $1 \prec 4$ structure, and (c) $1 \prec 9$ structure. The inset 1 of all images is the corresponding schematic structure, and the white line contours in the inset 2 of all images highlight the branching junctions in the circle of the corresponding SEM image.

### 5.3.3.2 Hierarchically branched nanotubes with multi-layers

More interestingly, after the truck TiO$_2$ nanotubes diverge into multiple branches, further furcation of the branched nanotubes can lead to hierarchically branched nanotubes with sophisticated multi-layer structures ($1 \prec n \prec m$). This can be realized by reducing the applied voltage in multiple steps with factors of $1/\sqrt{n}$ and $1/\sqrt{m}$ consecutively. As shown in Figure 5-17a, when the applied voltage is first reduced by a factor of $1/\sqrt{3}$ from 85 V to 49 V for 1 h, and then further reduced by a factor of $1/\sqrt{2}$ from 49 V to 35 V for 1 h, the primary truck first diverges into three small branched nanotubes, and then each of the three branched nanotubes further subdivides into two even smaller nanotubes ( $1 \prec 3 \prec 2$ ). By the same token, a combination of two Y-branching layers results in $1 \prec 2 \prec 2$ branched TiO$_2$ nanotubes when the applied voltage is reduced by factors of $1/\sqrt{2}$ and $1/\sqrt{2}$ consecutively (Figure 5-17b). Continuing this approach, more sophisticated TiO$_2$ nanotube structures can be fabricated. Figure 5-17c shows hierarchically branched TiO$_2$ nanotubes with four layers ($1 \prec 2 \prec 2 \prec 2$) created by reducing the applied voltage by a factor of $1/\sqrt{2}$ three times, and the white arrows in Figure 5-17c and the insert 2 show the location of three branching layers. For $1 \prec 2 \prec 2 \prec 2$ branched TiO$_2$ nanotubes, the applied voltage is first maintained at 85 V for 8 min, then reduced to 60 V at 15 V/min for 30 min, further reduced to 42.5 V at 15 V/min for 1 h, and finally reduced to 30 V at 8

V/min for 1 h. The length of each branched $TiO_2$ nanotube layer is dependent on the anodization time and can be easily adjusted. As a result, by reducing the applied voltage in multiple steps with different $1/\sqrt{n}$ factors, different types of multi-layer branched $TiO_2$ nanotubes can be obtained.

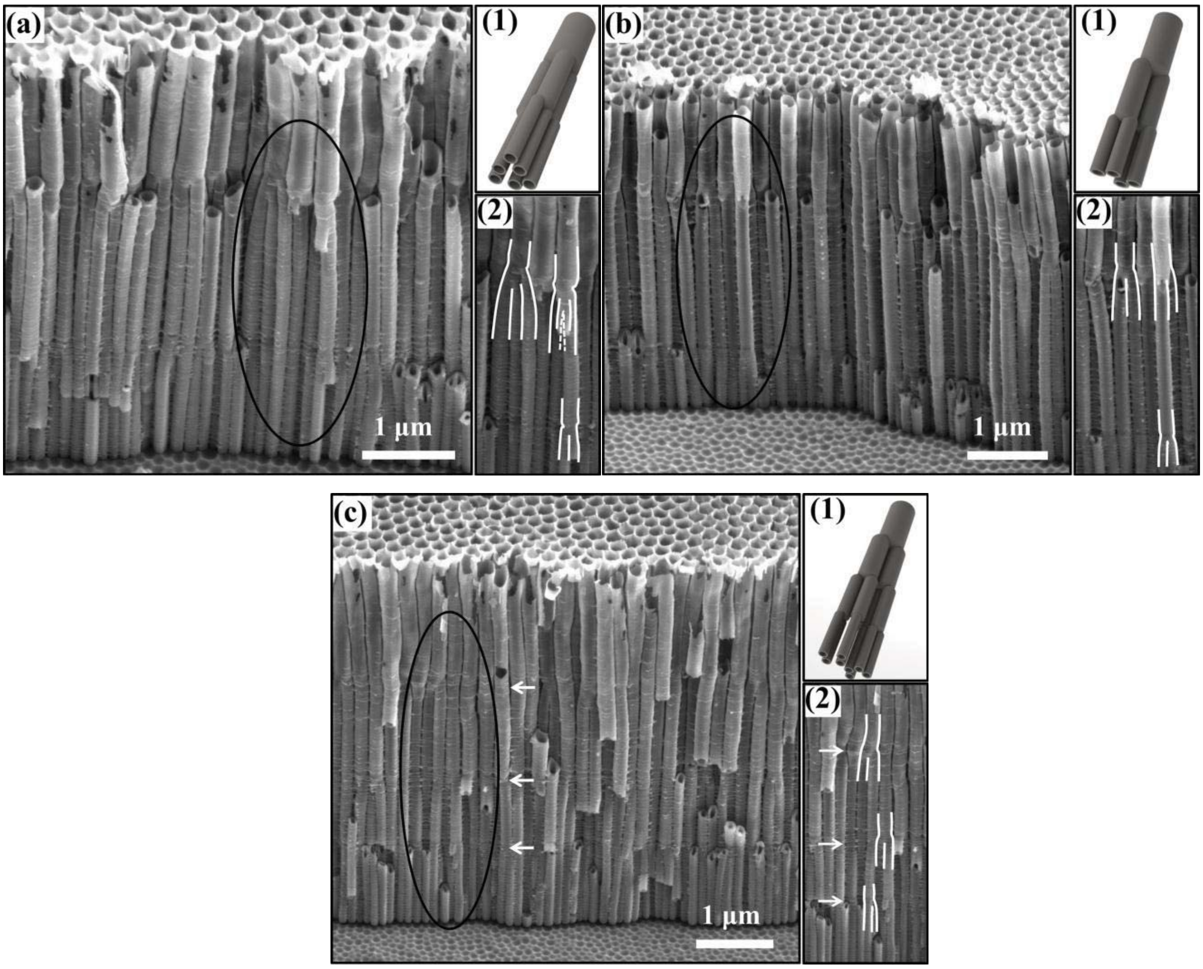

**Figure 5-17**. SEM images of multiple layers of branched $TiO_2$ nanotubes: (a) $1 \prec 3 \prec 2$ structure, (b) $1 \prec 2 \prec 2$ structure, and (c) $1 \prec 2 \prec 2 \prec 2$ structure. The inset 1 of all images is the corresponding schematic structure, and the white line contours in the inset 2 of all images highlight the branching junctions in the circle of the corresponding SEM image.

All the above discussed hierarchically branched $TiO_2$ nanotubes with multi-layer structures are fabricated through decreasing the applied voltage in steps. Differently, the structure of anodized $TiO_2$ nanotubes can be gradually changed when the applied voltage is continuously reduced. In Figure 5-18a, the Ti foil is first anodized at 85 V for 2.5 min to form truck $TiO_2$

nanotubes. When the applied voltage is gradually reduced from 85 V to 30 V as shown in Figure 5-18a, the outer diameter of the anodized $TiO_2$ nanotubes continually decreases from 260 nm to 95 nm. Unlike the branched $TiO_2$ nanotube structures shown in Figures 1-3, where furcation occurs at the same depth of the truck $TiO_2$ nanotubes, bifurcations in this case occur at different height of the truck $TiO_2$ nanotubes (Figure 5-18b). Moreover, the diameters of the nanotubes at the same depth are also different. Therefore, tree-like nanotube arrays are achieved with the branching junctions at different depths of the nanotubes, as highlighted by white line contours in Figure 5-18c; some nanotubes have $1 \prec 2 \prec 2$ structures while others have $1 \prec 2 \prec 2 \prec 2$ structures.

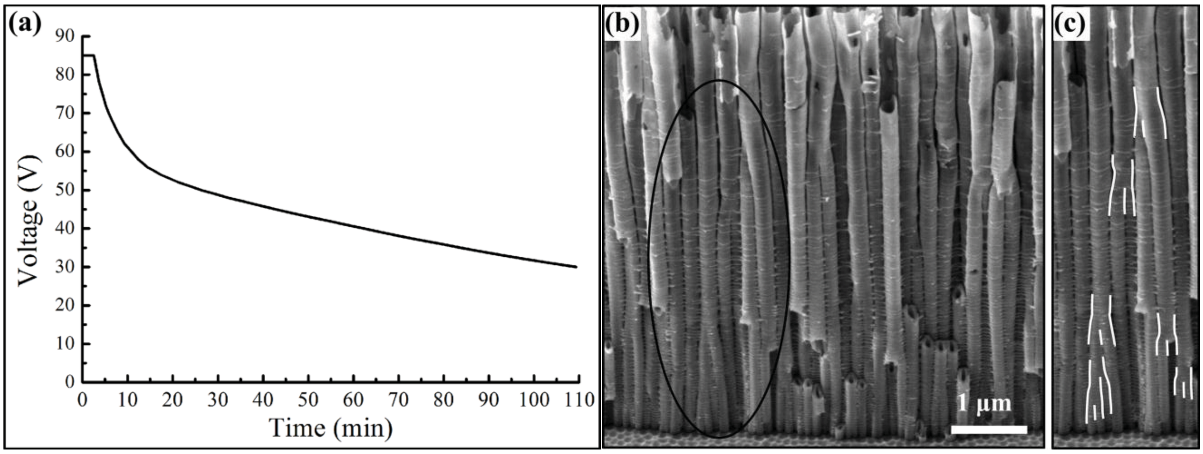

**Figure 5-18**. (a) Voltage-time curve when the applied voltage gradually decreases from 85 V to 30 V. (b) SEM image of the branched $TiO_2$ nanotubes. (c) Highlight branching junctions in the circle of (b) by white line contours.

The reason for the formation of these tree-like $TiO_2$ nanotubes can be understood as follows. In the situation that nanotube wall can fully expand, the growth factor $f_{growth}$ is 2.5 nm/V, and 52 V can maintain the 260 nm nanotube diameter. For the self-organized $TiO_2$ nanotube arrays is this study, the restriction from the neighboring nanotubes confines the free expansion of the nanotubes, which limits the growth factor $f_{growth}$ to 1.5 nm/V. When the applied voltage is decreased, all the nanotubes grow under the guidance of truck nanotubes, but the diameters do not immediately reduce with the decrease of the applied voltage. As the tubes grow deeper, the applied voltage decrease causes the restriction from the neighboring nanotubes to diminish, and the growth factor increases. At the same time, the thickness of the oxide barrier layer at the bottom of each nanotube reduces. When the applied voltage decreases to $85/\sqrt{2}$ =60 V, which is before the growth factor $f_{growth}$ increases to 2.5 nm/V at 52 V, the truck nanotubes split into small two nanotubes as discussed before. However, not all the nanotubes split, due to the slight variations in the local chemical micro-environment at each nanotube bottom, such as chemical concentration, temperature, or structural imperfections, the barrier layer thickness of the nanotubes are slightly different. The barrier layer thicknesses of some truck nanotubes reach the critical value first, and the branched nanotubes form and grow. The growth of these branched nanotubes causes their diameters to expand and occupy some space from their neighboring nanotubes. Therefore, the diameters of their neighboring nanotubes decrease. In order to decrease the diameter by a factor of $1/\sqrt{2}$ for bifurcation, the applied voltage and barrier layer thickness need to be further reduced before branching occurs for these nanotubes. As a result, the diameters of the nanotubes at the same depth are also different, as shown in Figure 5-18b. The combination of different diameters and different barrier layer thicknesses leads to competitive growth of the branched nanotubes. The splitting of the nanotubes at different height of the nanotubes results in tree-like $TiO_2$ nanotube arrays. Moreover, as soon as the applied voltage is reduced to a small enough value for bifurcation, branching will occur, while $1 \prec 3$ and $1 \prec 4$ branching need even smaller applied voltage and seldom occur in here.

#### 5.3.3.3 $TiO_2$ nanotube superstructures with branching and termination

While all the results so far are on different types of $1 \prec n$ branched nanotubes, $TiO_2$ nanotubes with $n \succ 1$ structures are also examined ("$\succ$"stands for the junction where the enlargement and termination occur). As shown in Figure 5-19a, double layer $TiO_2$ nanotubes are obtained through a modulated two-step anodization. The Ti foil is first anodized at 42.5 V for 1 h, and then the anodic $TiO_2$ nanotubes are peeled off by a tape. The second-step anodization is carried out at 42.5 V for 1 h, and then the applied voltage is increased to 85 V within 5 s and maintained at 85 V for 8 min. When the voltage is increased, merging of several small nanotubes into a large nanotube does not occur. Instead, some nanotubes enlarge their diameters by a factor of 2 from 130 nm to 255 nm, which the increase of applied voltage by a factor of 2; while the growth of some nanotubes terminates due to the restriction from the enlarged neighboring nanotubes. The increase of tube diameter by a factor of 2 leads to the increase of cross section area by a factor of 4. As a result, the enlargement and termination of the nanotubes lead to $TiO_2$ nanotubes with $4 \succ 1$ structure.

The increase of the applied voltage does not need to be kept at a slow rate as explained before for the applied voltage decrease. This is because as long as the applied voltage increases, the accelerated oxidation rate can increase the barrier layer thickness to the critical value, and the nanotube growth will not stop. However, when the applied voltage decreases, it needs to be slow enough to generate $H^+$ ions to decrease the barrier layer thickness, otherwise the nanotube growth will stop.

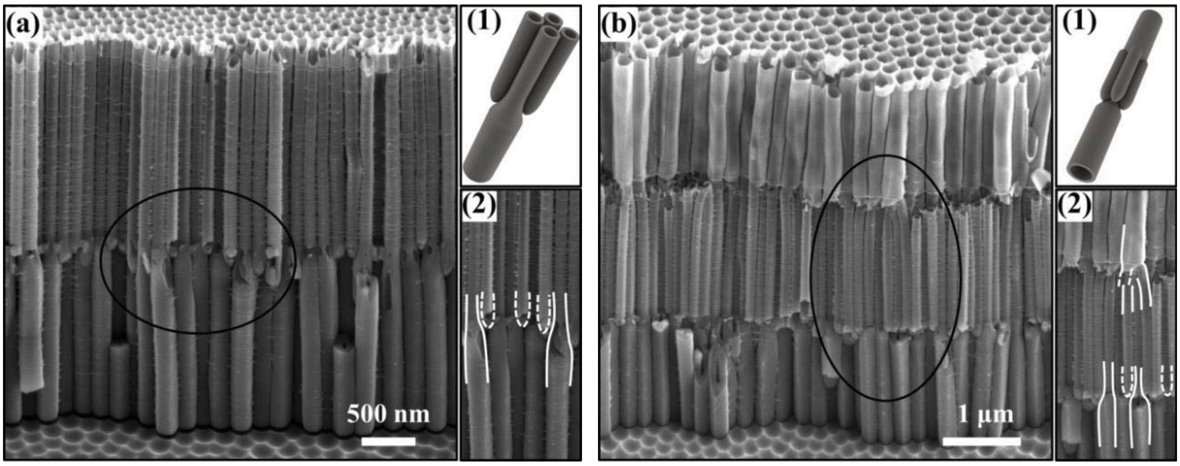

**Figure 5-19**. (a) SEM image of anodized $TiO_2$ nanotubes with $4 \succ 1$ structure when the applied voltage increases from 42.5 V to 85 V. (b) SEM image of anodized $TiO_2$ nanotubes with $1 \prec 4 \succ 1$ structure when the applied voltage decreases from 85 V to 42.5 V, and then increases to 85 V. The inset 1 of both images is the corresponding schematic structure, and the white line contours in the inset 2 of both images highlight the branching junctions in the circle of the corresponding SEM image.

The mechanism of the enlargement and termination of the nanotubes can be understood as follows. When the applied voltage is increased, the enlarged electric field leads to the oxidation rate to be faster than the dissolution rate. Therefore, the oxide barrier layer thickness of the $TiO_2$ nanotubes increases. Due to the competition of neighboring nanotubes, only the $TiO_2$ nanotubes that increase the barrier layer thickness quickly can grow and enlarge their diameters. The diameter increase of these nanotubes consumes the space underneath their neighbors. When the diameter is increased by a factor of $\sqrt{n}$ , the cross section area of the corresponding nanotube will increase by a factor of *n*. As a result, due to the limited space available, only 1/n of the nanotubes enlarges their diameters, while other nanotubes have to terminate, and $TiO_2$ nanotubes with $n \succ 1$ structure are created.

By combining the $1 \prec n$ branched nanotubes with the $n \succ 1$ $TiO_2$ nanotubes, anodized $TiO_2$ nanotubes with $1 \prec n \succ 1$ superstructures are also achieved. Figure 5-19b shows the anodized $TiO_2$ nanotubes with $1 \prec 4 \succ 1$ superstructure, which is obtained by anodization at 85 V for 8 min, followed by anodization at 42.5 V for 1 h, and finally at 85 V for 8 min. When the applied voltage is decreased, the large truck nanotubes with 255 nm diameter diverge into four small branched nanotubes with 130 nm diameter. When the applied voltage is increased, some nanotubes enlarge their diameters from 130 nm to 250 nm by a factor of 2, while other nanotubes terminate the growth. Therefore, the anodized $TiO_2$ nanotubes with $1 \prec 4 \succ 1$ supetstructure are successfully fabricated.

#### 5.3.3.4 Bamboo-type $TiO_2$ nanotubes

After anodization at 85 V in ethylene glycol with 0.1 M $NH_4F$ and 10 vol% water for 8 min, second-step anodization at 42.5 V for 30 min leads to the formation of thick hemispherical layers covering both the bottoms and junctions of $TiO_2$ nanotubes (Figure 5-20a). Reducing the applied potential decreases the electrical field across the tube bottom, which significantly suppresses $O^{2-}$ and $OH^-$ migration rate across the barrier layer at the tube bottom. The slow formation rate of $Ti(OH)_4$ at the bottom of the anodic $TiO_2$ layer allows dehydration to happen during the anodization, thus the volume shrinkage from the dehydration of $Ti(OH)_4$ can be compensated by the volume expansion from the anodization of Ti into $TiO_2$ and $Ti(OH)_4$. As illustrated in the inset of Figure 5-20a, a hemispherical barrier layer is formed at the bottom of each $TiO_2$ nanotube, which also covers the junctions of neighboring $TiO_2$ nanotubes. After the formation of the hemispherical barrier layer, if the applied voltage is recovered to 85 V, the $TiO_2$ nanotubes can continuouly grow along the stems of the nanotubes, which leaves the thick barrier layer at the junctions of the neighboring nanotubes as a ‘bamboo-ring’ after the anodization. As a result, cycling the applied potential between 85 V and 42.5 V leads to the formation of bamboo-type $TiO_2$ nanotubes, as shown in Figure 5-20b.

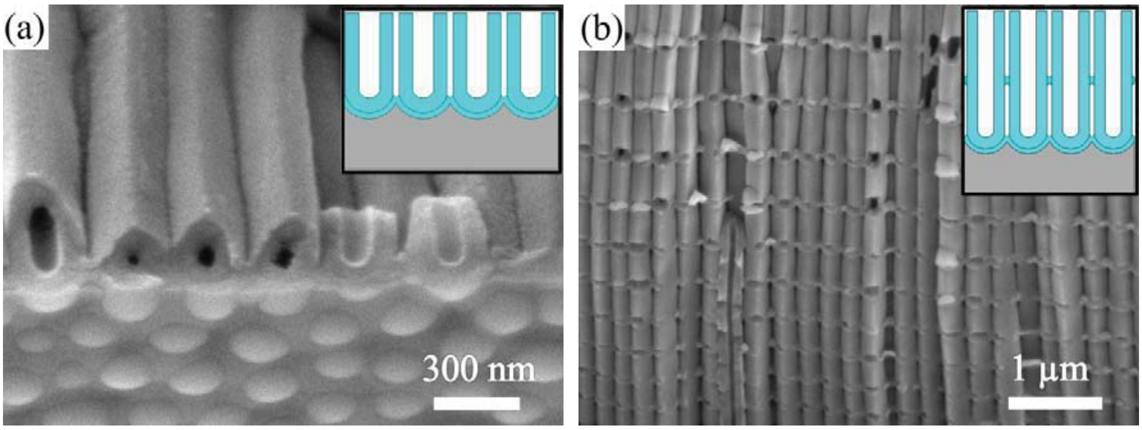

**Figure 5-20**. (a) SEM image of $TiO_2$ nanotubes obtained by anodization at 85 V for 8 min and then at 42.5 V for 30 min, and the inset is the illustration of the formation mechanism of the thick barrier layer. (b) SEM image of bamboo-type $TiO_2$ nanotubes obtained under cycling applied potential at 85 V for 3 min and at 42.5 V for 30 min. The inset is the illustration of the correponding $TiO_2$ nanostructures.

### 5.3.4. Summary

A generic method is demonstrated to fabricate hierarchically branched $TiO_2$ nanotubes by adjusting the anodization voltage. The number of branches and the diameter of branched nanotubes are determined by the applied voltage, which can be decreased by a factor of $1/\sqrt{n}$ to generate $1 \prec n$ branched nanotubes from a truck nanotube, resulting in the diameter of the branched nanotubes as $1/\sqrt{n}$ of the truck nanotube. If the applied voltage is further decreased by a factor of $1/\sqrt{m}$, each of the branched nanotubes further subdivides into multiple smaller nanotubes ($1 \prec n \prec m$). Continuing this approach, four layers of branched $TiO_2$ nanotubes with $1 \prec n \prec m \prec k$ structures are created. On the other hand, when the anodization voltage is increased by a factor of $\sqrt{n}$, some nanotubes enlarge the diameter to $\sqrt{n}$ times of the truck nanotubes, while other nanotubes terminate the growth. As a result, $TiO_2$ nanotubes with $n \succ 1$ structures are obtained. A combination of the $1 \prec n$ branched nanotubes with the $n \succ 1$ $TiO_2$ nanotubes leads to anodized $TiO_2$ nanotubes with $1 \prec n \succ 1$ structures. Cycling the applied potential between high value and low value leads to the formation of bamboo-type $TiO_2$ nanotubes.

## 5.4. Application of $TiO_2$ nanotubes in energy conversion and storage

### 5.4.1. Introduction

Supercapacitors have attracted a great deal of attention due to their potential for energy storage, which results in a higher power density than batteries and a higher energy density than conventional dielectric capacitors.[216] Based on charge storage mechanisms, supercapacitors can be classified into: (a) electrical double layer capacitors (EDLCs), which store charge by rapid adsorption/desorption at the electrode surfaces, and (b) pseudo-capacitors, in which charge is stored and released by Faradaic reactions on electrode materials. Pseudo-capacitors usually have a higher energy density than EDLCs, but they have relatively poor cycling stability because the electrodes undergo electrochemical reactions during the charge/discharge process.[217] EDLCs are based on reversible physical adsorption of ions without any chemical reactions, thus have long lifetimes but suffer from low capacitance.[218] Major strategies for enhancing the capacitance of EDLCs include increasing the surface area, electrical conductivity, and inter-connectivity of active materials.[219] Due to the large specific surface area and direct pathway for charge transport in $TiO_2$ nanotubes, making $TiO_2$ nanotubes into an electrode might offer an opportunity to improve the capacitance of EDLCs. However, the semiconducting nature of $TiO_2$ limits the electrical conductivity and impedes specific capacitance in the charge-discharge process.[220]

Suitable semiconductor to serve as photoanodes for photoelectrochemical water splitting should have the following characteristics: (a) chemical stability both under illumination and dark; (b) bandgap larger than 1.23 eV; (c) conduction band edge more negative than $H^+/H_2$ reduction potentials and valence band edge more positive than $O_2/OH^-$ oxidation potentials; (d) good conductivity for charge separation and migration.[221] Since the discovery of photocatalytic splitting of water on a $TiO_2$ electrode in 1972 by Fujishima and Honda,[138] due to excellent resistance to photocorrosion and suitable band edge position, enormous efforts have been devoted to varous types of $TiO_2$ photoanodes.[83, 94, 106, 141-144, 222-223] Because the conduction band edge potential of $TiO_2$ is insufficiently negative to activate hydrogen reduction, an externally applied bias voltage is required to decompose water. Anatase $TiO_2$ with a bandgap of 3.2 eV and rutile $TiO_2$ with a bandgap of 3.0 eV result in the $TiO_2$ only absorb UV light.[221] Many researches have demonstrated that doping $TiO_2$ with non-metal elements (such as N, B, F, S, C) or metal elements (such as Fe or Nb) or coupling with narrow band gap semiconductors (CdS, CdTe, CdSe, NiO, and $SrTiO_3$) can enhance its light absorption in visible light region.[83, 94, 106, 141-144, 222-223] Compared with $TiO_2$ nanoparticle film, $TiO_2$ nanotube arrays have larger specific surface area and fewer interfacial grain boundaries, which promote charge transport and water splitting efficiency. However, the low electrical conductivity of $TiO_2$ limits the charge separation and migration.

In this study, I focus on optimize the specific surface area and improve the inter-connectivity of $TiO_2$ nanotube arrays by creating bamboo structures, and improve the electric conductivity of $TiO_2$ nanotube arrays to facilitate the charge separation and migration for both supercapacitors and photoelectrochemical water splitting.

### 5.4.2. Experimental procedure

High purity titanium foil (99.6+%, 0.2 mm thick, Goodfellow, Oakdale, PA) was sonicated in acetone, isopropanol, and methanol, and then electropolished in a freezing electrolyte (~1℃) composed of glacial acetic acid/perchloric acid (9/1 vol ratio) at 55 V with 800 rpm stirring speed for 2 min. The anodization in the ethylene glycol electrolyte with 0.1 M $NH_4F$ and 10 vol% DI water was performed in ambient atmosphere at room temperature. The power supply for the anodization was Bertan 210-01R, and the applied potential during the anodization was controlled by LabView software. For the bamboo-type $TiO_2$ nanotubes, the anodization was carried out at cycling the applied potential between 85 V for 3 min and 42.5 V for 20 min, cycle number is 10 times. For smooth $TiO_2$ nanotubes, the anodization was carried out at 85 V for 30 min. After the anodization, the $TiO_2$ nanotubes were annealed in $H_2$ atmosphere at 400 ºC for 1 h with 5 ºC/min heating and cooling rates.

Cyclic voltammetry (CV) and galvanostatic charge-discharge (CD) measurements were carried out using an electrochemical workstation (1480 multistat, Solartron Analytical) in 1 M KCl. CV tests were carried out in a voltage range of 0 to 0.8 V at various scan rates (from 10 to 1000 mV/s). Galvanostatic charge-discharge (CD) measurement was performed under a constant current density of 100 $\mu A/cm^2$. Photoelectrochemical J-E measurement was performed in 1 M KOH by Solartron Analytical system. Typical three-electrode system was utilized for testing the photoelectrochemical anode, in which Pt served as counter electrode and Ag/AgCl as reference electrode. Illumination source was from a 150 W Xenon lamp (Oriel, 6256).

### 5.4.3. Results and discussion

Compared with the smooth $TiO_2$ nanotubes obtained by applying a constant voltage, the bamboo-type $TiO_2$ nanotubes created by cycling applied potential offer a large surface area and inter-connectivity between the nanotubes, which leads to the great promise as supercapacitor electrodes. In order to further improve the electrical conductivity of $TiO_2$ nanotubes to overcome the semiconducting nature of $TiO_2$, the as-grown $TiO_2$ nanotubes undergo thermal treatment in $H_2$ atmosphere at 400ºC for 1 h, which should introduce oxygen vacancies and greatly increase electrical conductivity. Figure 5-21 shows the supercapacitor performance of different types $TiO_2$ nanotubes: as-grown bamboo-type nanotubes, as-grown smooth nanotubes, $H_2$ treated bamboo-type and smooth nanotubes. The specific capacitance is proportional to the area under the CV curve, as shown in Figure 5-21a; the performance of as-grown bamboo-type nanotubes is twice that of as-grown smooth $TiO_2$ nanotubes, and the thermal treatment in $H_2$ atmosphere enhances the specific capacitance by around seven times. Figure 5-21b shows that $H_2$ treated bamboo-type $TiO_2$ nanotubes have large specific capacitance with 2.0-3.4 mF/cm$^2$ at scan rates between 10 and 1000 mV/s. Moreover, $H_2$ treated bamboo-type $TiO_2$ nanotubes have 6-14 times higher specific capacitance than as-grown bamboo-type $TiO_2$ nanotubes. Compared to smooth $TiO_2$ nanotubes, the performance of $H_2$ treated bamboo-type nanotubes increases by 60-80 % at different scan rates. Because a long cycle life is among the most important criteria for a supercapacitor, an endurance test for $H_2$-treated bamboo-type nanotubes has been conducted using galvanostatic charging-discharging cycles at 100 μA/cm$^2$. The first and last 10 charging-discharging cycles are shown in the inset of Figure 5-21c. During the 5000 cycles, the specific capacitance fluctuates slightly. After 5000 cycles, the capacitance retention is around 96%, which indicates that the $H_2$-treated bamboo-type $TiO_2$ nanotubes have high chemical stability.

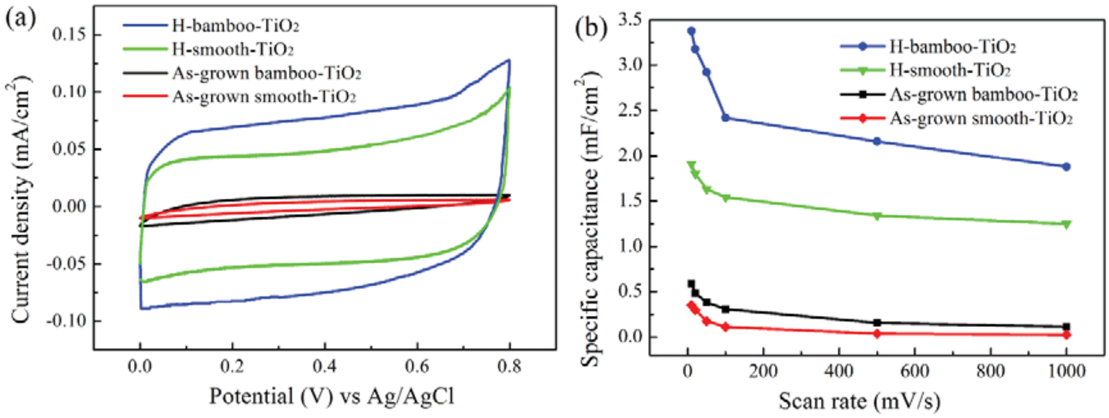

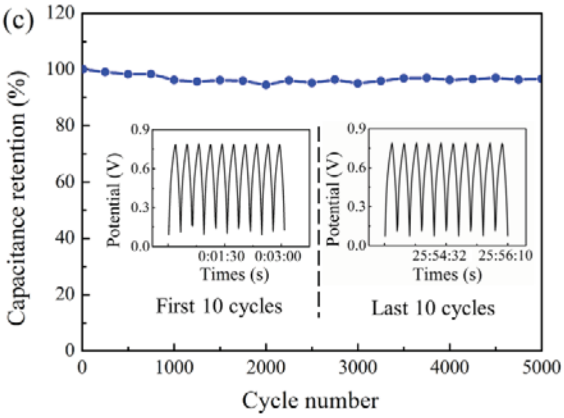

**Figure 5-21**: (a) CV curves of different types of $TiO_2$ nanotubes in 1 M KCl at a scan rate of 50 mV/s; (b) calculated specific capacitance at different scan rates; (c) cycle performance of $H_2$ treated bamboo-type nanotubes at current density of 100 $\mu A/cm^2$, and the inset is the first 10 and last 10 charge and discharge cycles.

Figure 5-22 shows the performance of photoelectrochemical water splitting for different types of $TiO_2$ nanotubes. Bamboo-type $TiO_2$ nanotubes display larger photocurrent density than smooth $TiO_2$ nanotubes, and $H_2$-treated $TiO_2$ nanotubes display larger photocurrent density than as-grown $TiO_2$ nanotubes. Photoelectrochemical efficiencies can be evaluated through the equation:

$$\eta\% = j_p(E^0_{rev} - |E_{bias} - E_{aoc}|)\frac{100}{I_0} \qquad (5\text{-}12)$$

where $j_p$ is the photocurrent density, $E^0_{rev} = 1.23\,\mathrm{V}$ is the standard state reversible potential for the water splitting reaction, $E_{bias}$ is the bias potential at which $j_p$ is measured, and $E_{aoc}$ is the bias potential at open circuit (-0.4 V). The maximum photoelectrochemical efficiencies of $H_2$-treated bamboo-type, $H_2$-treated smooth nanotubes, as-grown bamboo-type nanotubes, and as-grown smooth nanotubes are 2.96 %, 1.10 %, 0.38 %, and 0.11 %, respectively. Compare to smooth $TiO_2$ nanotubes, the bamboo structure leads to increase of photoelectrochemical efficiency by around 3 times for both $H_2$ treated and as-grown nanotubes. Compare to as-grown $TiO_2$ nanotubes, $H_2$ treated leads to increase of photoelectrochemical efficiency by 7.8 times and 10 times for bamboo-type and smooth nanotubes, respectively. As a result, due to the large specific surface area and enhanced electric conductivity, the $H_2$-treated bamboo-type $TiO_2$ nanotubes have high photoconversion efficiency.

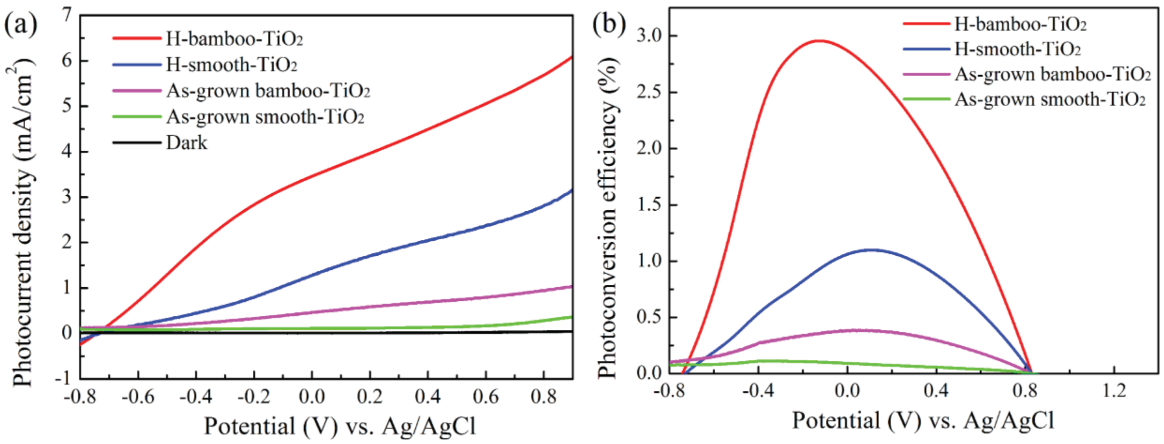

**Figure 5-22**: (a) J-E curves and dark currents and (b) photoconversion efficiency of different types of $TiO_2$ nanotubes.

### 5.4.4. Summary

In order to increase the performance of the anodic $TiO_2$ nanotubes in energy conversion and storage, I focused on increase the surface area, inter-connectivity, and electrical conductivity of $TiO_2$ nanotubes. The bamboo-type $TiO_2$ nanotubes produced by cycling applied voltage can increase the specific surface area and inter-connectivity of tubes, and the thermal treatment in $H_2$ atmosphere increase the electrical conductivity of $TiO_2$ nanotubes. As a result, the bamboo-type $TiO_2$ nanotubes shows higher supercapacitors and water splitting efficiency than smooth $TiO_2$ nanotubes, and the $H_2$ treated $TiO_2$ nanotubes shows higher supercapacitors and water splitting efficiency than as-grown $TiO_2$ nanotubes. The $H_2$ treated bamboo-type $TiO_2$ nanotubes are the excellent candidate for energy conversion and storage.

# Chapter 6. Influence of Concave Depth and Surface Curvature on $TiO_2$ Nanotubes and AAO

## Abstract:

Vertically aligned $TiO_2$ nanotubes and AAO have been obtained by pattern guided anodization with uniform concave depths. There are some studies about the effect of surface curvature on the growth of $Al_2O_3$ nanopores. However, the surface curvature influence on the development of $TiO_2$ nanotubes is seldom studied. Moreover, there is no research about the effect of heterogeneous concave depths of the guiding patterns on the anodized $TiO_2$ nanotubes and AAO characteristics. In this study, focused ion beam lithography is used to create concave patterns with heterogeneous depths on flat surfaces and with uniform depth on curved surfaces. For the former, bending and bifurcation of nanotubes/nanopores are observed after the anodization. For the latter, bifurcation of a large tube into two smaller tubes occurs on concave surfaces, while termination of existing tubes occurs on convex surfaces. For curved surface, the growth direction of all $TiO_2$ nanotubes is perpendicular to the local surface. At the edge of the Ti foil where two facets meet, the nanotube growth direction is bent, resulting in a large stress release that causes the formation of cracks.

## 6.1. Effect of FIB patterned concave depths

### 6.1.1. Introduction

In recently years, several patterning techniques have been utilized to fabricate highly ordered $TiO_2$ nanotubes and $Al_2O_3$ nanopores.[23-33] Besides the hexagonal arrangement of the self-organized alumina nanopore arrays, square arrangement, gradient and alternating diameter arrangements, as well as asymmetrical Moiré patterns have been obtained through pre-pattern guided anodization. Ordered concave arrays are first created on the electropolished aluminum surface. Due to the high electrical field at the concave bottoms, the anodized nanopores preferentially develop at the pre-patterned locations, even when the arrangement of the nanopores deviates from the self-organized hexagonal pattern. Up to now, all the pre-patterned concaves have the same depth, and the depth ranges from 5 nm to 50 nm.[23-33]

However, the effect of heterogeneous concave depths of the guiding patterns on the growth of $TiO_2$ nanotubes and $Al_2O_3$ nanopores has not been studied. Moreover, the development of $Al_2O_3$ nanopores at the boundary of pre-patterned region and none patterned region has also not investigated before. In this section, the formation mechanisms of $TiO_2$ nanotube and $Al_2O_3$ nanopores under heterogeneous concave depths are investigated.

### 6.1.2. Experimental procedure

The guiding patterns for the anodization were created on the electropolished Ti and Al surfaces using a FIB microscope (FEI Helios 600 NanoLab). The patterning ion beam current was 28 pA under 30 kV acceleration potential. In order to create concave arrays with heterogeneous depths, the FIB bitmap was overlapped by a serial of bitmaps. The depth of concave was determined by how many bitmaps overlapped at that point. More bitmaps overlapped at that point, longer FIB milling time, and deeper of the concave depth. The cross sections of the anodized nanopores were obtained in the FIB microscope using 0.28 nA current to cut the anodized porous structures. Before cutting the $TiO_2$ nanotubes or $Al_2O_3$ nanopores, the surfaces were coated with a layer of Pt to protect the anodized structures. For morphological characterization of the samples, scanning electron microscope (Quanta 600 FEG, FEI) and atomic force microscope (Digital Instruments MultiMode SPM, Veeco Instruments Inc.) were used.

### 6.1.3. Results and discussion

#### 6.1.3.1 Effect of heterogeneous FIB patterned concave depths

Figure 6-1a shows the FIB patterned concave arrays with different depths on the electropolished flat titanium surface. The concaves are arranged in a hexagonal pattern with 350 nm interpore distance. The depth of the concaves is shown in the inset AFM image of Figure 6-1a. The depths of concaves on the left and right sides are uniform, around 8 nm, while the depths of concaves in the center gradually change from 15 nm to 36 nm.

Figure 6-1b shows the anodized $TiO_2$ nanotube arrays after the anodization in the electrolyte mixture of 0.1 M $NH_4F$ and 10 vol% $H_2O$ in ethylene glycol at 85 V with 15 $mA/cm^2$ constant current for 12 min. The $TiO_2$ nanotubes only develop at the FIB patterned locations and the hexagonal arrangement is maintained. The cross section of the $TiO_2$ membrane in Figure 6-1c indicates that the nanotubes are covered by a thin layer of $TiO_2$ nanopores, and all the nanotubes initiate perpendicularly to the surface (region I). With further anodization, the cross section shows that the $TiO_2$ nanotubes developed from the FIB patterned gradient concave depth region curve outwards, labeled as 1, 2, 3, 4 in Figure 6-1c. Moreover, the outer diameters of the tubes 1 and 2 increase from 350 nm to 430 nm when the $TiO_2$ nanotubes grow deeper (region Ⅱ). With the further development of the nanotubes, the large nanotube 1 branches into two small tubes (region Ⅲ). The two branched nanotubes also increase in diameter, and then further diverge into four even smaller tubes (region Ⅳ). Therefore, tree-like nanotubes form. On the other hand, the $TiO_2$ nanotubes developed from uniform concave depth in the left and right regions grow perpendicularly to the surface (only the left region is shown in Figure 6-1c). For nanotube 4, which is located at the boundary between the uniform and gradient FIB concave depth regions, the outward bending is obvious with a decreasing diameter. The tube growth finally terminates when tube 4 encounters neighboring vertical nanotube 5.

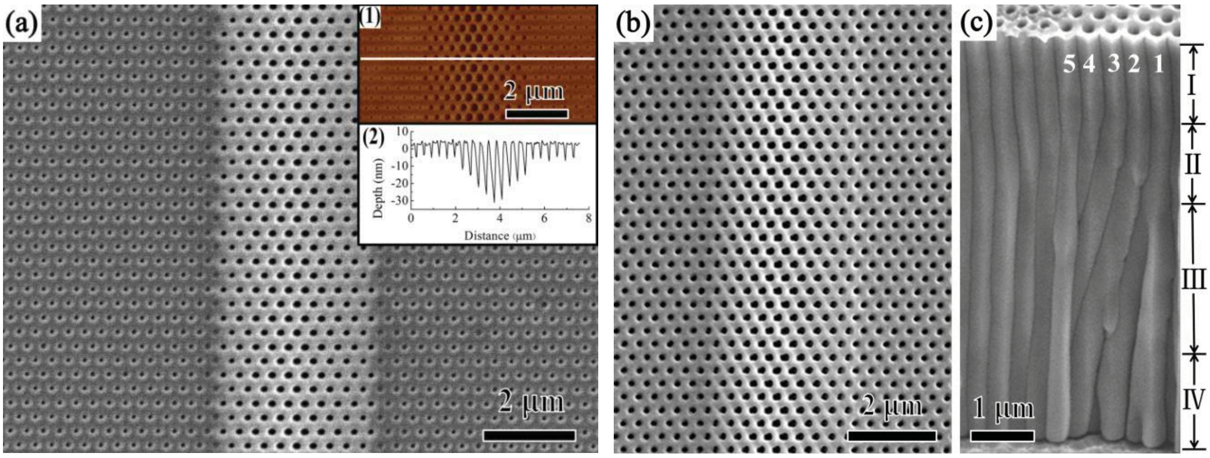

**Figure 6-1**. (a) SEM image of FIB patterned concaves with different pore depths on electropolished titanium surface. The inset 1 is AFM image of (a), and inset 2 is the surface topology along the line in inset 1. (b) Surface SEM image of the corresponding anodized $TiO_2$ nanotube arrays. (c) Cross section of the anodized $TiO_2$ nanotubes.

The above nanotube curving and terminating phenomena can be explained by equifield strength theory. Electric field is the driving force for the growth of the nanotubes in the anodic $TiO_2$ membrane, and the direction of the electric field significantly influences the growth direction of the nanotubes. At the initial stage of the anodization, the electric field is perpendicular to the Ti surface; the enhanced oxidation and dissolution rates along the electric field direction cause the nanotubes to grow perpendicularly to the surface. Due to the large electric field at the FIB patterned concaves, the nanotubes preferentially grow there. Therefore, the arrangement of the nanotubes at the beginning is still hexagonal. The anodized $TiO_2$ nanotubes have a double-layer wall; the inner layer is $TiO_2$ and the outer layer is lower density $Ti(OH)_4$.[93] During the anodization, the decomposition of $Ti(OH)_4$ leads to separated $TiO_2$ nanotubes.

When the FIB patterned concaves have different depths, the $TiO_2$ nanotube growth has a different scenario. As illustrated in Figure 6-2a, tube α, which is located at the center, is deeper than tube β, so the electric field at the joint position A is the combination of the electric field from tube α ($E_{BA}$) and tube β ($E_{CA}$). The combined electric field direction at A is shown in Figure 6-2a by an arrow. Therefore, the oxidation rate at A is much faster than at any other position on the bottom of tube β due to $O^{2-}$ migration from both sides at location A. As a result, the joint position A moves downwards and outwards in the direction of the electric field. This leads to the growth direction of tube β to bend. Similarly, due to the depth difference between tube β and tube γ, the grow direction of tube γ is bent (Figure 6-2b).

As the thickness of the oxide layer at position A increases, the electric field decreases. Although both the oxidation and dissolution rates are reduced as the electric field is decreased, the former is expected to reduce faster than the latter.[5] This can be understood as follows. The inward oxygen ionic current $j$, which is related to the electric field $E$ across the barrier layer, determines the oxidation rate: [5]

$$j = j_0 \times e^{kE} \qquad (6\text{-}1)$$

where $j_0$ and $k$ are material dependent constants. Therefore, the oxidation rate decreases exponentially with the electric field. However, the dissolution rate of $TiO_2$, which is affected by the electric field through polarization and impairment of the Ti-O bond, decreases slowly as the electric field decreases. As a result, the dissolution rate of the oxide layer at positions B and C is faster than the oxidation rate at position A, which leads to a reduction of the wall thickness at position C and an increase in the inner diameter of tube α (Figure 6-2b). In region I of Figure 6-2a tube α is deeper than tube β, and there is no confinement from neighboring tubes, the electric field cross the tube wall also drives the migration of $O^{2-}$ ions to oxidize the tube wall, enabling tube α to expand its outer diameter. Due to the outward bending of nanotube β, more space is available for tube α to further increase its diameter, and the intertube distance also increases.

Similarly, due to the depth difference of tube β and tube γ, tube β also increases its diameter during the anodization. However, the diameter can only increase to a critical value:[87, 224]

$$D_{\max} = 2 f_{growth} \times U \tag{6-2}$$

where $f_{growth}$ is the growth factor for anodic oxides, 2.5 nm/V for $TiO_2$, and $U$ is the applied potential. Since the applied potential in this study is 85 V, the critical diameter value is $D_{max}$= 2×2.5×85= 425 nm, which agrees with the experimental value of 430 nm in Figure 6-1c. When the diameter of tube α reaches this critical value (Figure 6-2c), the oxidization rate balances the dissolution rate at the wall and bottom of tube α, and the tube outer diameter should remain unchanged. However, due to the large combined electric field from two neighboring tubes at the junction position A′, the nanotube growth rate is faster than at the center of the tube center E′. As a result, tube α diverges into two small tubes $\alpha_1$ and $\alpha_2$ as shown in Figure 6-2d. Since the diameters of both tube $\alpha_1$ and $\alpha_2$ are smaller than the critical value, they increase accordingly until the same critical value is reached again during the anodization.

The situation at the boundary between the uniform and gradient depth FIB concave regions is a little different. The volume expansion during the $TiO_2$ anodization generates large compressive stresses in the film (volume expansion from Ti to $TiO_2$ follows the Pilling Bedworth ratio of 1.95).[86, 214] In the uniform FIB concave depth region (as shown in Figure 6-1c), the large compressive stress restricts the bending of nanotube 5 at the boundary, and causes it to grow vertically to the surface throughout the anodization. As a result, nanotube 5 decreases in diameter so that nanotube 4 can bend. Nonetheless, the available spatial volume for $TiO_2$ nanotube growth is limited; finally, nanotube 4 ceases to grow. At the same time, nanotube 5 continues to grow in the depth direction, even when it encounters nanotube 3. Further growth of nanotube 3 is also restricted by nanotube 5 and eventually terminates.

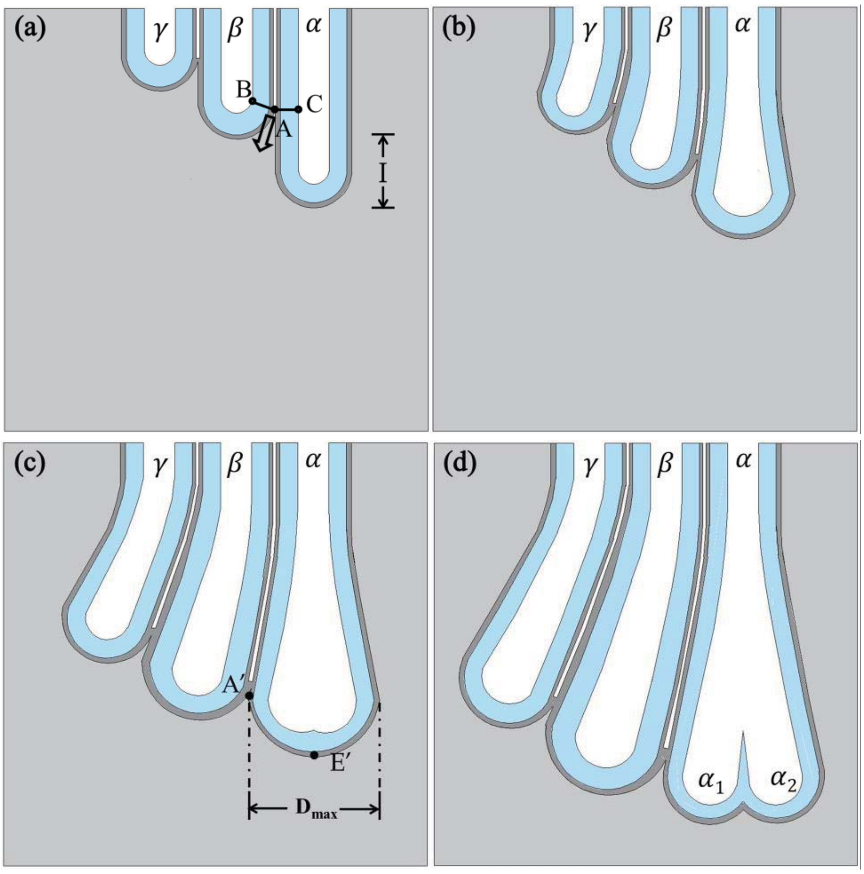

**Figure 6-2**. The schematic of bending and branching of anodized nanotubes developed from FIB concaves with different depths.

The influence of different FIB guided concave depths on the development of anodized $Al_2O_3$ nanopores is also explored. Similarly, the electropolished and flat Al surface is patterned with FIB concave arrays. The arrangement of the concaves is hexagonal and the interpore distance is 350 nm. The depth of the concaves is shown in the insert of Figure 6-3a. There are three regions in which the concave depths gradually change from 8 nm to 53 nm, and the concave depths in the regions between them are uniform (~8 nm).

After the anodization in 0.3 M phosphoric acid at 20 mA/cm$^2$ constant current for 5 min, the anodized pores grow at the FIB patterned locations and remain in the hexagonal arrangement (Figure 6-3b). The cross section in Figure 6-3c is obtained by FIB cutting. Prior to the cutting, the surface is covered by a layer of Pt to protect the $Al_2O_3$ nanopores; this is why the top surface has a metal layer covered on the $Al_2O_3$ nanopores. Similar to the anodic $TiO_2$ nanotubes, the cross section image indicates that the nanopores bend and some nanopores also diverge into two nanopores in the region with gradient FIB concave depths.

However, there are three differences between the anodized $Al_2O_3$ nanopores (Figure 6-3) and $TiO_2$ nanotubes (Figure 6-1). First, the $TiO_2$ nanotube growth direction in the uniform FIB concave depth region is perpendicular to the surface, while the $Al_2O_3$ nanopore growth direction in the uniform FIB concave depth region also bends. Second, unlike the vertical $TiO_2$ nanotube growth direction at the beginning stage as shown in Figure 6-1c region I, the growth direction of the $Al_2O_3$ nanopores bends at the beginning of the anodization (Figure 6-3c). Third, after the anodization, the $Al_2O_3$ surface is uneven, and protrudes in the regions with gradient FIB concave depths (Figure 6-3c). These differences can be understood by the difference in the Young's moduli between anodic $TiO_2$ nanotubes and $Al_2O_3$ nanopores. The Young's modulus of porous materials can be estimated by: [12]

$$E = E_{bulk}(1-p^2) \qquad (6\text{-}3)$$

where $E_{bulk}$ is the Young's modulus of bulk oxide material, and $p$ is the porosity of the anodized structure. The porosities of anodic $TiO_2$ nanotube film and $Al_2O_3$ nanopore film can be calculated from the diameter (120 nm for $TiO_2$ nanotubes and 80 nm for $Al_2O_3$ nanopores) and interval distance (350 nm) of the features; the result is 14.2% and 6.3% porosity, respectively. $E_{bulk}$ for bulk $TiO_2$ and $Al_2O_3$ is 283 GPa and 41 GPa, respectively.[12, 225] As a result, the Young's moduli are calculated to be 208 GPa and 36 GPa for $TiO_2$ nanotubes and $Al_2O_3$ nanopores, respectively. However, since both anodized $TiO_2$ nanotubes and $Al_2O_3$ nanopores are amorphous, the Young's moduli are actually much smaller than the calculated values. Direct compression measurement of an individual as-anodized amorphous $TiO_2$ nanotube shows that the Young's modulus is 23-34 GPa.[226-227] Although there has been no direct experimental result of Young's modulus for amorphous $Al_2O_3$ nanopores, it is expected to be much smaller than that of the $TiO_2$ nanotubes. The large Young's modulus of anodic $TiO_2$ causes the nanotubes in the region with uniform FIB concave depth to resist the bending effect from the gradient FIB concave depth region, and thus maintain the vertical tube growth direction. However, the anodic $Al_2O_3$ nanopores bend in the region with uniform FIB concave depth because of the smaller Young's modulus. The bent nanopores increase the growth rate of their neighbors, which causes the pores near the gradient FIB concave depth region to grow faster than those located further away from it. Moreover, the difference in the growth rate leads to different volume expansion, and eventually causes the anodized $Al_2O_3$ to have a convex surface in the deeper nanopore region.

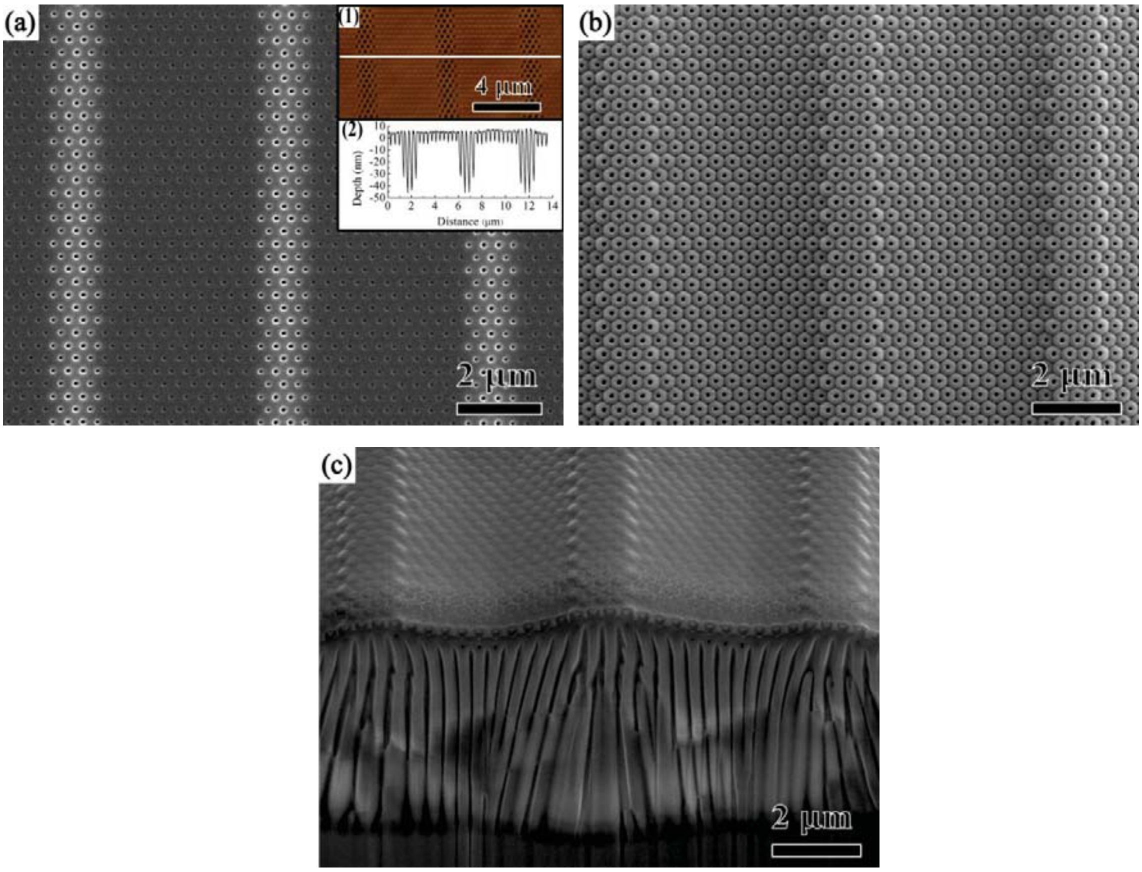

**Figure 6-3**. (a) SEM image of FIB patterned Al concaves with different pore depths. The inset 1 is AFM image of (a), and inset 2 is the surface topology along the line in inset 1. (b) Surface SEM image of the anodized $Al_2O_3$ nanopore developed from different pore depths. (c) Cross section of the anodized $Al_2O_3$ nanopores.

### 6.1.3.2 Edge effect of FIB pattern during the anodization

Figure 6-4 shows the cross section of the anodized nanopores at the boundary with and without FIB patterning guidance after the anodization in 0.3 M oxalic acid at 50 V for 5 min. The FIB pattern was generated at 9.7 pA for 6 s of ion beam exposure time. Some interesting phenomena can be discussed as follows.

First of all, the growth rate of the anodized nanopores with the FIB patterning is much faster than that of the nanopores without the FIB patterning. The depth of the nanopores with the FIB patterning is 2.2 μm while that without the FIB patterning is only 500 nm; the latter is less than a quarter of the former. This is because the $Ga^+$ implantation at the FIB patterned region creates more active surface and accelerates the anodization rate. Additionally, at the beginning of the anodization the FIB patterned region already has nano-concaves, the nanopores grow immediately at the bottom of the concaves because of the electrical field assisted anodization. For the un-patterned region, a smooth and uniform alumina layer forms first, the electrical field and the anodization rate are low, and pores need to stabilize before a self-organized pattern can be developed. These two factors cause the anodization rate at the FIB patterned sites four times faster than that at the un-patterned sites.

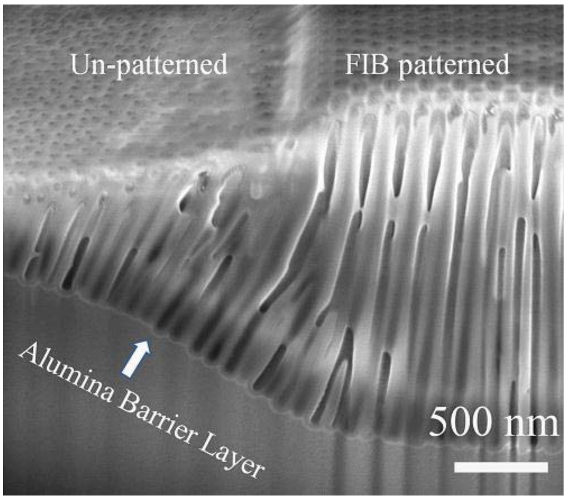

**Figure 6-4**. SEM image of AAO regions with and without FIB patterning guidance.

Another observation is that the growth direction of the anodized nanopores in both FIB patterned and un-patterned regions is vertical; however, the growth direction of the nanopores at the boundary bends to the un-patterned region. This phenomenon is observed most clearly at the bottom of the alumina barrier layer. The maximum nanopore bending angle, which is about 35°, happens at the boundary center of the FIB patterned and un-patterned regions. In the FIB patterned region, the nanopore bending angle decreases to 20° at locations 500 nm away from the boundary, and decreases to 5° at locations 1 μm away from the boundary. In the un-patterned region, the bending angle remains at 35° at locations 1 μm away from the boundary, and decreases to 10° at locations 5 μm away from the boundary. This can be understood by equifield strength model, which uses the balance between the electric field enhanced oxide dissolution rate and oxygen anion migration rate to explain the self-adjustment of pore diameter and arrangement. As discussed above, the patterned and un-patterned nanopores have different depths at the beginning of the anodization (Figure 6-5a). The nanopore $\beta_I$ induced by the FIB patterning is deeper than the un-patterned nanopore $\alpha_I$, the oxidation rate at the joint position B of the nanopores is much higher than at any other position because oxygen anions migrate from both sides. The joint position B moves down to the lower position D more quickly. As a result, the thickness of the oxide layer at position D increases, the dissolution rate of the oxide layer at positions A and C is faster than the oxidation rate at position D, leading to a reduction of the oxide layer thickness and a faster growth rate for nanopore $\alpha_I$ This explains why the nanopore $\alpha_I$ is deeper than the nanopore $\alpha_{II}$, and the depth of the nanopores from the boundary to the un-patterned region decreases. Due to the marked difference in depth for nanopores $\alpha_I$ and $\beta_I$, the oxidation rate at B of nanopore $\beta_I$ is faster than that in other directions, and the nanopore $\beta_I$ bends to the position of D. During the anodization, each pore experiences diameter increase and thus restricts the growth of the neighboring pores. The repulsive force from the bending of nanopore $\beta_I$ restricts the growth direction of nanopore $\alpha_I$, making it bend to the position of D′. The depth difference between nanopores $\alpha_I$ and $\beta_I$ is the largest among all the pores, therefore nanopore $\alpha_I$ has the largest bending angle. Since the nanopores $\alpha_I$ and $\alpha_{II}$ have the same depth in Figure 6-5a, they have intermediate depth difference after the anodization (Figure 6-5b), the nanopore $\alpha_{II}$ has a medium bending angle. For the nanopores $\beta_I$ and $\beta_{II}$, the depth difference is small, therefore the nanopore $\beta_I$ only bends a small angle. The nanopore bending effect weakens fast in the FIB patterned region. This edge effect from the FIB pattern guidance has not been reported before.

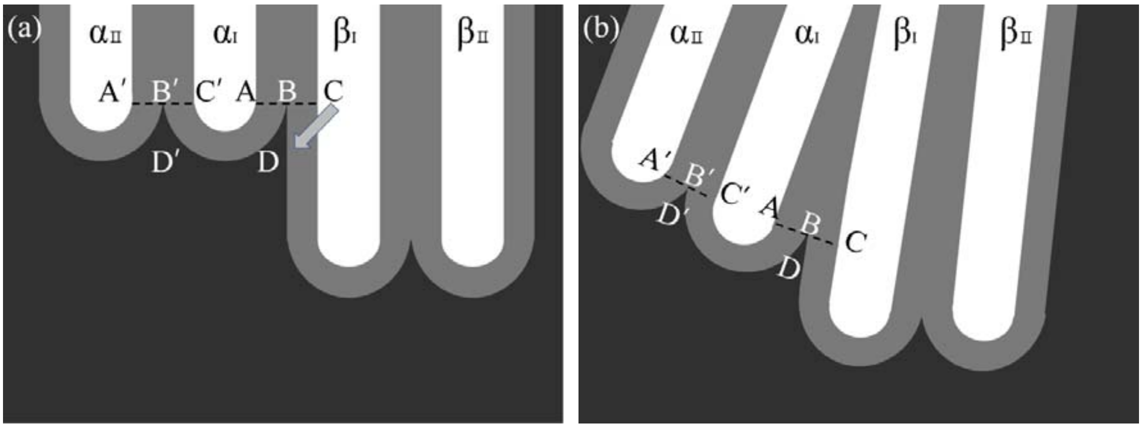

**Figure 6-5**. (a) Schematic drawing of two deep FIB patterned nanopores and two shallow un-patterned nanopores; (b) schematic drawing showing the bending of the nanopores during the anodization.

Moreover, the height of the nanopore arrays in the FIB patterned region is ~300 nm higher than that of the un-patterned region. In our study, it has been observed that this height difference increases with the FIB exposure time. The reason for this might be the volume expansion from aluminum oxidation to alumina during the anodization. The nanopores with the FIB patterning guidance grow faster and experience more volume expansion and repulsive forces. Subsequently, the surface in the FIB patterned region is higher. The longer the FIB exposure time, the larger the anodization rate difference. This leads to more difference in the volume expansion and height between the FIB patterned and un-patterned regions. When the interpore distance is increased, the oxide wall of the nanopores can fully expand before meeting that of the neighboring pores. As a result, the oxide walls of the anodized alumina nanopores bulge out like a volcano.

### 6.1.4. Summary

The growth of anodized $TiO_2$ nanotubes and $Al_2O_3$ nanopores has been investigated with FIB patterned heterogeneous concave depths on a flat surface. The growth direction of the nanotubes/nanopores is not perpendicular to the flat surface but bends due to the heterogeneous concave depths. The change in the growth direction increases the diameter and interval distance of the nanotubes/nanopores, and leads to bifurcation and termination of the nanotubes/nanopores during the anodization. The equifield strength theory is used to explain the mechanism of the above phenomena. For the FIB concave guided pattern development, there exists an edge effect. The nanopores developed from the FIB patterned concaves grow faster than those without the guidance of the FIB patterning. The nanopore growth direction bends away from the FIB pattern at the boundary of patterned and un-patterned regions. Therefore, in order to create highly ordered $TiO_2$ nanotubes and $Al_2O_3$ nanopores, the depth of pre-patterned concaves must have the uniform depth.

## 6.2. Influence of the surface curvature on the anodization

### 6.2.1. Introduction

For the effect of surface curvature, there are some studies on the growth of anodic $Al_2O_3$ nanopores, and the mechanism of the $Al_2O_3$ nanopore formation on non-planar surface are proposed in these publications.[45-47, 228] However, the effect of a curved surface on the growth direction, diameter, and intertube distance of $TiO_2$ nanotubes has not yet been investigated. Most studies of $TiO_2$ nanotubes up to now are focused on flat Ti foils. The growth direction of the $TiO_2$ nanotubes is parallel to each other and perpendicular to the flat surface. The diameter and the intertube distance of the nanotubes are the same throughout the anodic $TiO_2$ membrane and are only varied by the anodization conditions, such as electrolytes and applied voltages. For some applications of $TiO_2$ nanotubes, the non-planar substrate is demanded, it is important to understand the mechanism of $TiO_2$ nanotubes development on curved surface.

In this section, the growth of $TiO_2$ nanotubes on curved Ti surfaces (concave and convex surfaces) and Ti surfaces with different shapes (such as Ti foils with rectangular and triangular cross sections) is also studied.

### 6.2.2. Experimental procedure

For the feature creation using the FIB microscope, Serif Drawplus 4.0 software was used to design the features first. The patterns were designed with varying contrast. During the feature creation, the feature shapes were produced on the Ti surfaces after the FIB microscope imported the feature designs and directed the ion beam movement accordingly. In order to create different surface curvature, the patterning ion beam current was 0.28 nA under 30 kV acceleration potential. The image contrast difference dictates the material removal amount on the Ti surfaces. The Ti material in the bright area was removed. The material in the dark area was left intact. The material in the gray area had partial material removal in-between. This created different features with varying curvature on the Ti surfaces. Subsequently, concave arrays with uniform depth and hexagonal arrangement were created by FIB microscope with 28 pA beam current and 30 kV acceleration potential. The anodization was carried out in a two-electrode electrochemical cell at 85 V in ethylene glycol electrolyte containing 0.1 M $NH_4F$ and 10 vol% DI water at room temperature for 12 min. The cross sections of the anodized nanotubes were obtained in the FIB microscope using 0.28 nA current to cut the anodized porous structures. Before cutting the $TiO_2$

nanotubes, the surfaces were coated with a layer of Pt to protect the anodized structures.

### 6.2.3. Results and discussion

FIB patterned concave arrays with different concave depths lead to different depths of anodized nanotubes/nanopores, which changes the electric field direction at the tube/pore bottom and the tube/pore growth direction. Based on this understanding, another method to change the electric field distribution is to develop nanotubes/nanopores directly on a curved surface. The electric field should be perpendicular to the tangential line of each individual point along the curved surface, and lead to the anodized nanotubes/nanopores to bend accordingly instead of growing in parallel.

Figure 6-6a shows FIB patterned concaves with uniform 8 nm depth on a grooved Ti surface. The arrangement of the concaves is hexagonal, and the interpore distance is 350 nm. The width of the groove is 6.75 µm, the length is 8 µm, and the depth gradually changes from 0 to 1 µm.

After the anodization, all the anodized $TiO_2$ nanotubes grow at the locations of the FIB patterned concaves and retain the hexagonal arrangement. The cross section image in Figure 6-6c shows that the tube growth direction in the grooved region is bent and perpendicular to the curved surface. The reason for this is that the growth direction of the nanotubes is determined by the electric field, which is perpendicular to the curved surface. The $TiO_2$ nanotubes underneath the concave surface bend outwards and lead to an increase in the intertube distance with the growth of the tubes. With further increase in the intertube distance, some nanotubes branch into two tubes, as shown in circle 1 of Figure 6-6c. The nanotubes underneath the convex surface bend inwards, which leads to a reduction in the intertube distance with the growth of the tubes. As a result, some tubes terminate growth in order to compensate for the reduced spatial volume (as shown in circle 2 of Figure 6-6c). Consequently, the anodized tubes are not parallel to each other, but are perpendicular to the surface. Depending on the curvature, branched nanotubes are obtained at the concave surface, and nanotube termination is observed at the convex surface.

The development of the $Al_2O_3$ nanopores on a curved surface is also studied. Figure 6-6d shows anodized $Al_2O_3$ nanopores on a grooved Al surface with the guidance of FIB patterned concaves. The FIB patterned concaves have 8 nm uniform depth and 350 nm interpore distance. After the anodization, the anodized nanopores remain in the hexagonal arrangement. The cross section in Figure 6-6e shows that all the nanopores grow perpendicularly to the Al surface.

Therefore, the nanopores under the concave surface bend outwards, and the interpore distance increases with the growth of the nanopores. Some nanopores diverge into two pores, as discussed in Figure 6-2, when the interpore distance is large enough.

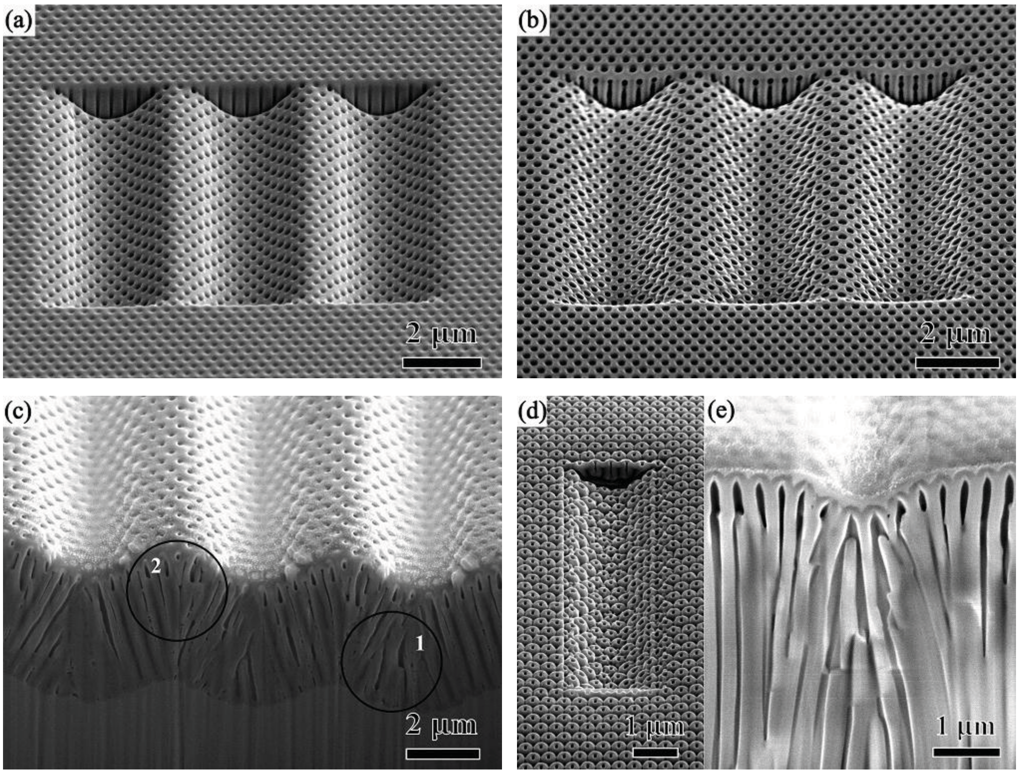

**Figure 6-6**. (a) Ti grooved surface with FIB patterned concaves in hexagonal arrangement, viewed at a 52° tilt angle. The FIB patterned concaves have uniform depth. (b) Surface and (c) cross section SEM images of the corresponding anodized $TiO_2$ nanotubes. Circle 1 shows the bifurcation of the nanotubes under the concave surface. Circle 2 shows the termination of the nanotubes under the convex surface. (d) Surface and (e) cross section SEM images of the anodized $Al_2O_3$ nanopores on grooved Al surface with uniform FIB patterned concave depth.

In order to illustrate more clearly about the growth of the nanotubes and nanopores on a curved surface, the development of $TiO_2$ nanotubes on electropolished Ti foils with rectangular and triangular cross sections is examined. The rectangular Ti foil, shown in Figure 6-7a, has a 190 µm×70 µm cross section. After the anodization, the anodic $TiO_2$ nanotubes grow perpendicularly to the Ti surface on all of the facets as shown in the enlarged images in Figure 6-7a. The diameter of the $TiO_2$ nanotubes is 250 nm, and the length is 2.6 µm. Due to the 90° rotation of the neighboring Ti foil facets, the growth direction of the nanotubes also rotates 90°

from the nanotubes grown on the neighboring facet. Moreover, cracks appear at the edge of two neighboring facets, as shown in the four corner inserts of Figure 6-7a and in Figure 6-7b.

The fundamental process for the crack formation can be understood as follows. During the anodization, the large volume expansion from Ti to $TiO_2$ leads to a large compressive stress on the anodic $TiO_2$ film. The linear elastic strain at the Ti/$TiO_2$ interface is given by: [12]

$$\varepsilon = \sqrt[3]{V_{\exp}} - 1 \qquad (6\text{-}4)$$

where $V_{exp}$ is the volume expansion factor 1.95, so the elastic strain is around 0.25. Due to the large Young's modulus of the anodized $TiO_2$ nanotubes mentioned above (23-34 GPa), the compressive stress at the anodic $TiO_2$ film is around 5.75-11.0 GPa. Therefore, the volume expansion during the anodization leads to large compressive stresses in the $TiO_2$ nanotube layer. If the compressive stress exceeds the critical stress that the $TiO_2$ nanotube layer can sustain, cracks will form. For the four planar facets of the Ti substrate, the $TiO_2$ nanotubes can expand the volume vertically and laterally, the compressive stress can be dissipated effectively. Therefore, no cracks are generated on the planar facets. However, for the nanotubes growing along the edge, the volume expansion is spatially restricted because of the nanotube convergence. As a result, a large compressive stress is created along the edges and leads to the formation of cracks.

The curvature of the surface strongly influences the compressive stress at the edges. A larger change in the nanotube growth direction between two neighboring facets will result in a larger compressive stress along the edges, and thus lead to more severe cracking. Figure 6-7c shows the anodic $TiO_2$ nanotubes developed on a Ti foil with a triangular cross section. All the nanotubes grow perpendicularly to the surface. The large curvature at the edge of the triangular Ti foil generates a large compressive stress. As a result, a large crack forms along the edge, which has a nearly 90° inclined angle from the two sides of the crack.

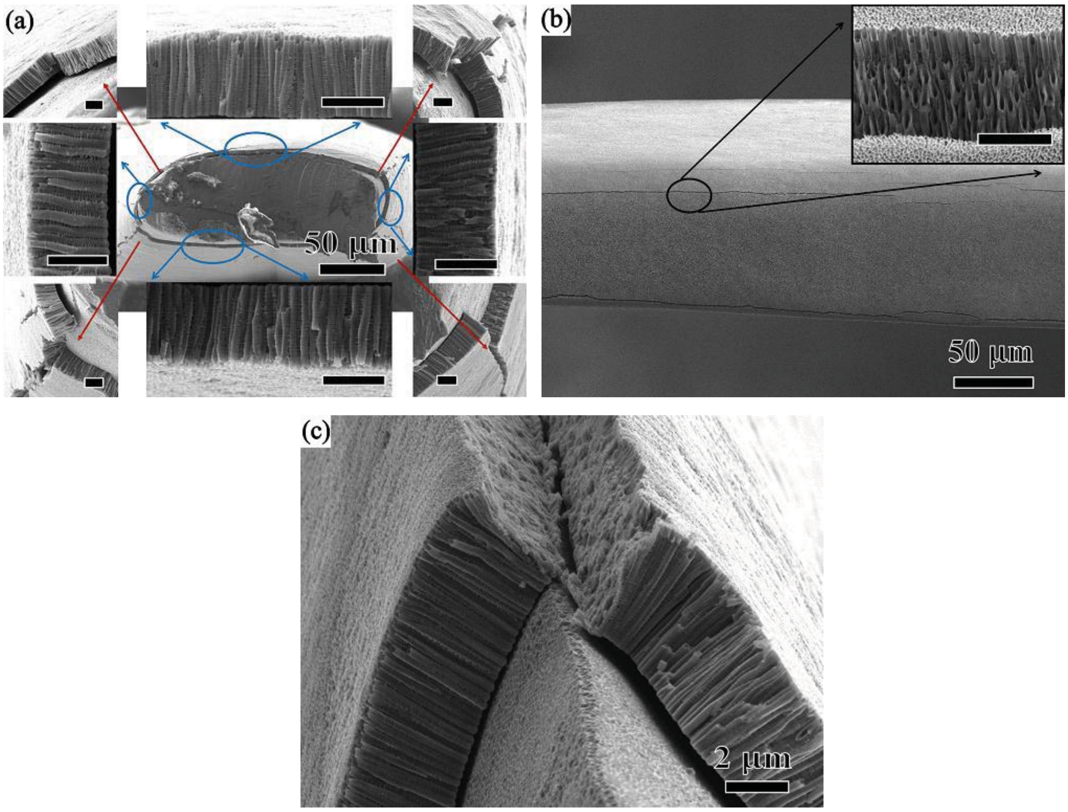

**Figure 6-7**. (a) Cross section SEM images of anodic $TiO_2$ nanotubes grown on an electropolished rectangular Ti foil after being cut along its cross section. The eight inserts are the enlarged images of the $TiO_2$ nanotubes at different facets and edges, and they show that all $TiO_2$ nanotubes grow perpendicularly to the surface. (b) SEM image of a crack at the edge of anodized Ti foil, and the insert is the enlarged image of the crack. (c) SEM image of anodic $TiO_2$ nanotubes grown on a Ti foil with triangular cross section. The scale bars in all inserts are 2 μm.

### 6.2.4. Summary

The surface curvature and geometric shape of the anodization surface also affect the development of the $TiO_2$ nanotubes. The $TiO_2$ nanotubes grow perpendicularly to the local surface. Bifurcation and termination of the nanotubes occur on concave and convex surfaces, respectively. The growth directions of the $TiO_2$ nanotubes at neighboring facets change and lead to cracks along the edge due to large compressive stress release. This study not only understand the development of $TiO_2$ nanotubes on the curved surface and under the guidance of heterogeneous concave pattern, but will also open opportunity in the applications where the substrates are demanded to be curved, such as sensor, catalysis, optic fiber, and so on.

# Chapter 7. Application of FIB on Nanoscale sculpting and Three-dimensional Analysis

## Abstract:

FIB sculpting can selectively close and re-open the anodic $TiO_2$ nanotubes. Under a 30 kV $Ga^+$ beam, $TiO_2$ nanotubes are closed with a 65 nm shield layer covering the top entrance when the ion dose is larger than $1.2\times10^{17}$ ion/cm$^2$; under a 5 kV $Ga^+$ beam, the shield layer is removed and the closed tubes are re-opened. An ion-induced viscous flow model has been proposed to explain the influence of $Ga^+$ ion beam flux, substrate temperature, initial tube diameter, ion beam dwell time, and the incidence angle of the ion beam. Three-dimensional (3D) reconstruction by FIB cutting and SEM imaging offers an opportunity to directly and quantitatively observe the pore evolution to understand the sintering process. Utilize the 3D reconstruction, the evolution of pore volume, pore-solid interfacial area, pore shape, pore connectivity, and pore number during the two-step sintering of ZnO nanoparticles are investigated.

## 7.1. Selective FIB sculpting of and mechanism understanding

### 7.1.1. Introduction

Ion beam sculpting can induce mass transport along the bombarded surface and result in the closing of nanopores or the formation of self-organized nanostructures (such as ripples and nanodots), which may allow the modification of the top surfaces of $TiO_2$ nanotubes.[229-230] Several models, such as adatom diffusion model and viscous flow model, have been proposed to understand the ion beam sculpting process. According to the adatom diffusion model,[231-234] the ion beam mobilizes the adatoms on the bombarded surface so that they can independently diffuse along the surface until they are annihilated at the edge of the pores, which leads to shrinkage of the pore area. This model provides a good quantitative prediction of the relationship between nanopore closing rate and ion beam flux, flux pulsing, and substrate temperature. At the same time, the viscous flow model is based on ion-stimulated anisotropic deformation and explains the dependence of closing rate on initial nanopore diameter, which is difficult to be understood by adatom diffusion.[235] However, the viscous flow model is challenged by the effect of ion beam flux and substrate temperature on ion beam sculpting. So far, the mechanism of ion beam sculpting remains unclear. Even with such uncertainty at the fundamental level, the focused ion beam (FIB) has been explored as a method of sculpting the surface of nanostructures.[31-32, 236-237] The most important advantage of FIB sculpting is the precise control of exposure locations. Modification of the top surface of $TiO_2$ nanotubes may present the opportunity to load multiple dyes into dye sensitized $TiO_2$ nanotube solar cells and to fabricate flow through $TiO_2$ nanotubes for solar fuel. However, whether or not FIB sculpting can be used to selectively modify $TiO_2$ nanotube surfaces is unknown.

In this study, highly ordered $TiO_2$ nanotube arrays with a uniform diameter are first created by FIB patterning guided anodization, they are then sculpted with a focused $Ga^+$ beam with energy ranging from 2 kV to 30 kV. The effects of the $Ga^+$ ion beam flux, substrate temperature, initial tube diameter, dwell time, and incidence angle on the FIB sculpting process are explored. Also, different mass transport mechanisms, such as sputter erosion, ion-enhanced viscous flow, surface adatom diffusion, swelling, and redeposition are examined. Finally, the mechanism of the FIB sculpting is proposed.

### 7.1.2. Experimental procedure

In order to obtain highly ordered $TiO_2$ nanotube arrays, pre-patterned concave arrays with 180 nm interpore distance were created under the radiation of a 30 kV $Ga^+$ beam by the dual beam FIB (FEI Helios 600 NanoLab, Hillsboro, OR). The anodization was carried out in a two-electrode electrochemical cell in an ethylene glycol electrolyte containing 0.1 M $NH_4F$ and 10 vol % DI water at room temperature. After the 20 minute anodization under a constant 60 V applied potential, the foils were rinsed with DI water several times and dried in a nitrogen stream. The anodized $TiO_2$ nanotube arrays were bombarded by different $Ga^+$ beam energies ranging from 2 kV to 30 kV. The ion beam flux was changed from 0.61 to 18.82 $\text{ions}\cdot\text{cm}^{-2}\cdot\text{s}^{-1}$; the substrate temperature was changed from 93 K to 300 K; the initial diameter of the $TiO_2$ nanotubes ranged from 70 nm to 115 nm; the dwell time of the ion beam at each spot ranged from 1 μs to 60 μs; the ion beam incidence angle was changed from 0° to 52°. The substrate temperature effect was carried out by Quanta 200 3D dual beam FIB (FEI Company, Hillsboro, OR).

### 7.1.3. Results and discussion

### 7.1.3.1 Effect of ion beam energy during FIB sculpting

Highly ordered $TiO_2$ nanotube arrays with a uniform diameter of 80 nm and hexagonal arrangement are obtained by FIB patterning guided anodization. A thin layer of ordered nanopores covers the top of the $TiO_2$ nanotube arrays,[238-239] thus in this study I use the pore area to monitor the FIB sculpting of the $TiO_2$ nanotube arrays. After the anodization, these highly ordered $TiO_2$ nanotube arrays are sculpted by FIB with 30 kV $Ga^+$ ions. During this process, the area and diameter of the $TiO_2$ nanotubes decrease with an increase in the ion dose, as shown in Figure 7-1a. The $TiO_2$ nanotubes are eventually closed when the ion dose is larger than $0.9\times10^{17}$ ion/cm$^2$. Figure 7-1b shows the changes in the thickness of the shield layer, which covers the entrance of the $TiO_2$ nanotubes after the tubes are closed. The shield layer thickness increases from 0 nm to 42 nm under $0.9\times10^{17}$ ion/cm$^2$ exposure, and stabilizes at a thickness of 65 nm and an ion dose larger than $1.2\times10^{17}$ ion/cm$^2$. When the energy of the $Ga^+$ ion beam is decreased, the cross section area shrinkage rate for the $TiO_2$ nanotubes also slows: under the sculpting at the same ion dose of $6.0\times10^{17}$ ion/cm$^2$, the $TiO_2$ nanotube area shrinks to 0, 2800 nm$^2$, 4400 nm$^2$, and 4900 nm$^2$ for 30 kV, 16 kV, 8 kV, and 5 kV, respectively (Figure 7-1c). However, the $TiO_2$ nanotubes with initial diameters of 80 nm cannot be completely closed under the $Ga^+$ ion sculpting beam with an energy ranging from 5 kV to 16 kV. The eventual diameter of the bombarded $TiO_2$ nanotubes increases with a reduction of $Ga^+$ beam energy from 60 nm to 75 nm when the acceleration voltage decreases from 16 kV to 8 kV.

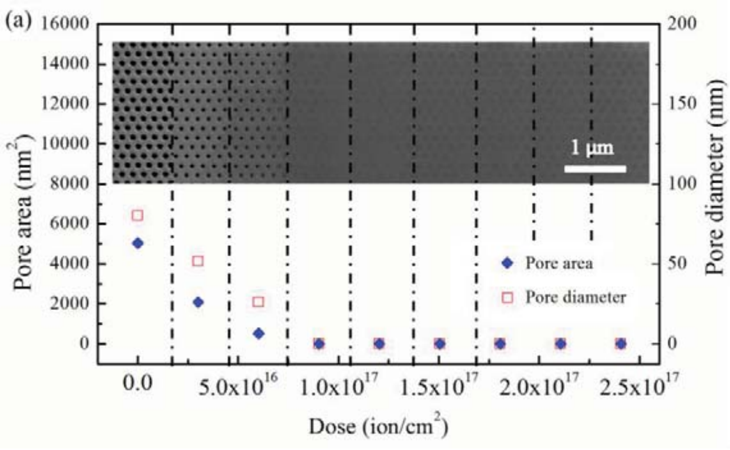

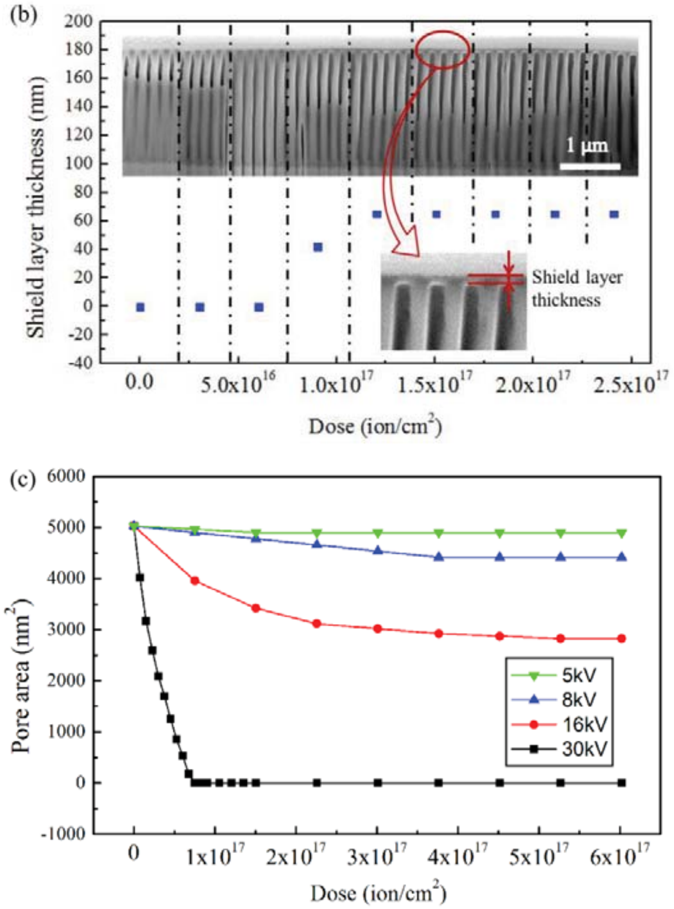

**Figure 7-1**. (a) Shrinkage of pore area and (b) change in the shield layer thickness with an ion dose under 30 kV $Ga^+$ ion beam sculpting at 1.75 ions·$cm^{-2}$·$s^{-1}$ beam flux; the insets in (a) and (b) are the corresponding SEM images of the surface and cross section of the bombarded $TiO_2$ nanotubes at different ion dose; (c) shrinkage of pore area under different $Ga^+$ ion beam energies.

FIB sculpting causes not only sputter erosion of surface material but also lateral mass transport along the bombarded surface. For high energy ion beam sculpting, the lateral mass transport dominates the sculpting process and leads to closing of $TiO_2$ nanotubes; while sputter erosion plays a dominant role in the low energy ion beam sculpting. Therefore, the $TiO_2$ nanotubes cannot be completely closed as shown in Figure 7-1c. In this study, once the $TiO_2$ nanotube surfaces are closed by the bombardment of 30 kV $Ga^+$ ion beam, further ion beam exposure with low kinetic energy $Ga^+$ ion is explored to open the shield layer. As illustrated in Figure 7-2a, when the closed $TiO_2$ nanotubes are exposed to16 kV and 8 kV $Ga^+$ ion beams, the thickness of the shield layer decreases rapidly and eventually stabilizes at 33 nm and 27 nm, respectively. However, sculpting at16 kV and 8 kV $Ga^+$ ion beams cannot open the closed $TiO_2$ nanotubes. Under the exposure of 5 kV and 2 kV $Ga^+$ ion beams, even though the reduction rate of the shield layer thickness slows down, the shield layer can be completely removed to finally re-open the closed $TiO_2$ nanotubes. The SEM image in the inset of Figure 7-2b shows the re-opening process of the closed $TiO_2$ nanotubes and the reduction of the shield layer thickness under 5 kV $Ga^+$ ion sculpting. The nanotubes are re-opened to a diameter similar to the initial tube diameter of 80 nm when the ion dose is larger than $4.5\times10^{17}$ ion/$cm^2$.

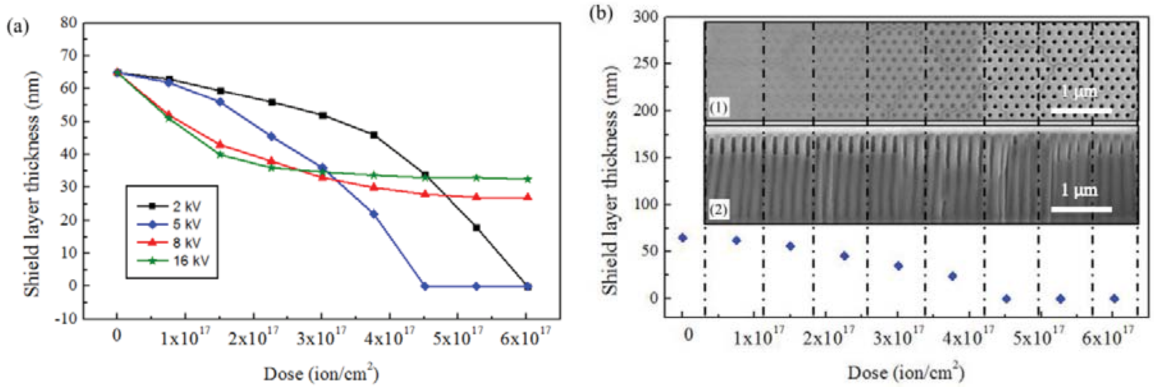

**Figure 7-2**. (a) Change in shield layer thickness under different $Ga^+$ beam energies; (b) shield layer thickness of $TiO_2$ nanotubes at different ion dose under 5 kV $Ga^+$ beam sculpting, and the insets 1 and 2 are the surface and cross section SEM images of bombarded $TiO_2$ nanotubes at different ion doses, respectively.

### 7.1.3.2 Selective closing and re-opening of TiO2 nanotubes

Selective closing and re-opening of $TiO_2$ nanotubes can be achieved through the combination of FIB patterning and ion beam sculpting. The advantage of FIB patterning is that the exposure can be controlled at selective regions by importing designed patterns. Figure 7-3a shows highly ordered $TiO_2$ nanotubes in a hexagonal arrangement, with an intertube distance of 180 nm and an internal tube diameter of 80 nm. After selective exposure to a 30 kV $Ga^+$ ion beam with $1.2\times10^{17}$ ion/$cm^2$ ion dose at alternating strip locations, Figure 7-3b demonstrates the sculpted $TiO_2$ nanotube arrays with alternating closed and open $TiO_2$ nanotubes. If selectively sculpted $TiO_2$ nanotube sample is further uniformly bombarded by 30 kV $Ga^+$ ion beam with another $1.2\times10^{17}$ ion/$cm^2$ dose, all the $TiO_2$ nanotubes can be closed (Figure 7-3c). Based on Figure 7-1b, the shield layer thickness is 65 nm. Subsequently, selective exposure of the closed $TiO_2$ nanotubes under 5 kV $Ga^+$ ion beam with $5.0\times10^{17}$ ion/$cm^2$ dose at specific locations can re-open $TiO_2$ nanotubes at any desired patterns through the control of the ion beam sculpting locations in the FIB patterning. For instance, one line and two lines of $TiO_2$ nanotubes are successfully re-opened by ion beam line scan with 180 nm and 360 nm widths, respectively (Figure 7-3d). Selectively opening one, two, and three neighboring $TiO_2$ nanotubes is also accomplished by controlling the diameter of the ion beam spot (Figure 7-3d). Similarly, opening the $TiO_2$ nanotubes in a 5 μm × 3 μm rectangular area can be easily achieved by selective ion exposure (Figure 7-3e). Moreover, the opened $TiO_2$ nanotubes can be selectively closed again by 30 kV $Ga^+$ beam sculpting, as shown in Figure 7-3f. Therefore, FIB patterning with alternating ion beam energy has the capability to selectively close and open the anodized $TiO_2$ nanotubes.

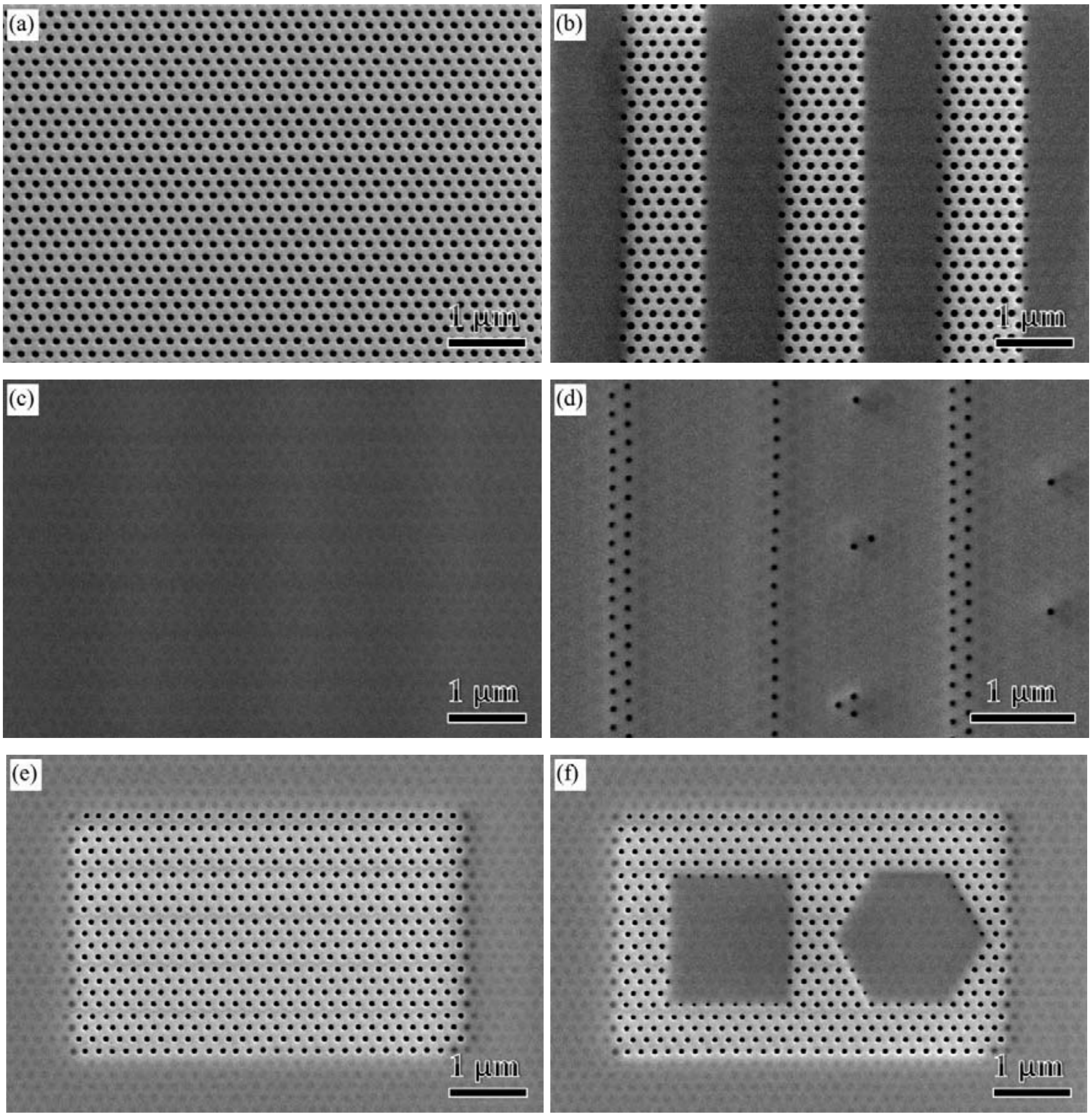

**Figure 7-3**. (a) Anodized $TiO_2$ nanotubes; (b) selectively closed $TiO_2$ nanotubes under 30 kV $Ga^+$ ion beam sculpting with a $1.2\times10^{17}$ ion/cm$^2$ exposure dose; (c) further uniform exposure of the entire sample with another $1.2\times10^{17}$ ion/cm$^2$ dose to close all of the nanotubes; (d) and (e) selective opening of the closed $TiO_2$ nanotubes by a 5 kV $Ga^+$ beam with a $5.0\times10^{17}$ ion/cm$^2$ dose; (f) selective re-closing of the opened $TiO_2$ nanotubes under a 30 kV $Ga^+$ beam sculpting with a $1.2\times10^{17}$ ion/cm$^2$ exposure dose.

### 7.1.3.3 Mechanism of FIB sculpting

The fundamental mechanism for the closing and re-opening of the $TiO_2$ nanotubes during FIB sculpting has been studied. I propose that the FIB sculpting is ascribed to the balance between ion-induced viscous flow and ion sputter erosion, while surface adatom diffusion, anisotropic deformation, atomic displacement, and redeposition have negligible effects on the closing and re-opening of the $TiO_2$ nanotubes.

The ion-induced viscous flow model can be understood through stress relaxation during local thermal spikes induced by a collision cascade at ion beam bombarded regions. During FIB sculpting, ions transfer energy from the projected particles to the target by nuclear collision and electronic excitation, which leads to increased local temperatures and a corresponding decrease in viscosity. According to the thermal spike theory, the relationship between the temperature distribution in cylindrical coordinates and the bombarded spot is: [240-241]

$$T(F_d, r, t, T_S) = \frac{F_d}{4\pi\kappa t}\exp(-\rho C r^2 / 4\kappa t) + Ts \qquad (7\text{-}1)$$

where $F_d$ is the energy deposited into the track per unit length, $\kappa$ is the thermal conductivity of $TiO_2$ (11.7 W/m/k), $\rho$ is the density of $TiO_2$ (3.8 g/cm$^3$), $C$ is the heat capacity of $TiO_2$ (57.12 J/mol/K), $t$ is the relaxation time, $r$ is the related distance to bombarded spot, and $T_S$ is the substrate temperature.[225] When the temperature under the beam spot reaches the critical flow temperature (equal to the melting temperature of $TiO_2$, $T_m$= 2113 K),[225] the stress can be completely relaxed by viscous flow. Ion radiation enhances fluidity and leads to the flux-dependent viscosity, $\eta$: [240-241]

$$\eta = \frac{\eta_{rad}}{f} \qquad (7\text{-}2)$$

where $f$ is ion beam flux, and $\eta_{rad}$ is dependent on $F_d$ and $T_S$ but independent of $f$ (see supporting information). The ion-induced diffusion coefficient, based on viscous flow, can be obtained by the Stokes-Einstein relationship:

$$D_{viscous} = \frac{k_B T}{6\pi\eta R_0} \tag{7-3}$$

where $k_B$ is the Boltzmann's constant, $T$ is the local temperature for viscous flow, and $R_0$ is the radius of one $TiO_2$ molecule (0.25 nm).

The evolution of cross-sectional profile of $TiO_2$ nanotube entrance under FIB sculpting is shown in Figure 7-4. When the FIB bombards the tube edge, local thermal spike at $A_0$ results in formation of viscous flow along the tube internal wall. Due to temperature gradient from hot spike $A_0$ and cold substrate $B_1$, more materials accumulate near the local spike, which leads to the growth of extruded tip $A_1$ with $h_1$ width. With further sculpting, viscous flow moves along the instantaneous substrate $A_1B_1$. Similarly, the temperature gradient from $A_1$ to $B_1$ causes faster the mass growth rate at $A_1$ than $B_1$, which leads to more pronounced tip $A_2$ and more curved surface $A_2B_2$. Under the same amount of viscous flow, the volume of the extruded tip formed each time is the same, which means the area profile $B_0A_1B_1$, $A_1A_2B_2B_1$, $A_2A_3B_3B_2$, and $A_3A_4B_4B_3$ is the same as shown in Figure 7-4. However, more curved surface $A_2B_2$ (compared to $A_1B_1$) leads to smaller width for the extruded tip ($h_2$ is less than $h_1$). This means the extruded tips both grow inwards and rotate downwards during the FIB sculpting. When the extruded tips developed from the edges of a tube encounter with each other at the tube center, the $TiO_2$ nanotube can be completely closed. Further ion-induced viscous flow and sputter erosion smooth the shield layer and make its thickness uniform.

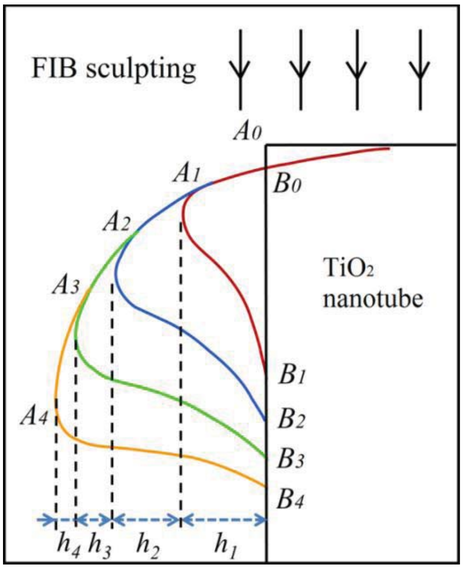

**Figure 7-4**. Illustration of the evolution of $TiO_2$ nanotube profile under FIB sculpting.

For high ion beam energy sculpting, such as at 30 kV, the ion-induced viscous flow overcomes the sputter erosion, thus the $TiO_2$ nanotubes can be closed. When the $Ga^+$ beam energy is decreased, based on Monte Carlo simulation by SRIM,[242] the energy deposited into the track per unit length $F_d$ is reduced. $F_d$ is 1.89 kV/nm, 1.6 kV/nm, 1.27 kV/nm, 1.06 kV/nm, and 0.71 kV/nm for 30 kV, 16 kV, 8 kV, 5 kV, and 2 kV $Ga^+$ beam sculpting, respectively. According to Equation (7-1), the temperature for local thermal spikes will significantly decrease when the $Ga^+$ beam energy is reduced, as shown in Figure 7-5. However, the temperatures at local thermal spikes under 16 kV and 8 kV $Ga^+$ beam sculpting are still slightly higher than the critical flow temperature ($T_m$= 2116 K), thus the ion-induced viscous flow still plays an important role and results in the failure of opening the closed $TiO_2$ nanotubes, as shown in Figure 7-2a. For 5 kV and 2 kV $Ga^+$ beam sculpting, the temperatures at local thermal spikes are much lower than the critical flow temperature. Therefore, the ion-induced viscous flow is suspended, and the sputter erosion dominates the low energy FIB sculpting process, which re-opens the closed $TiO_2$ nanotubes under 5 kV and 2 kV $Ga^+$ beam sculpting (as shown in Figure 7-2b).

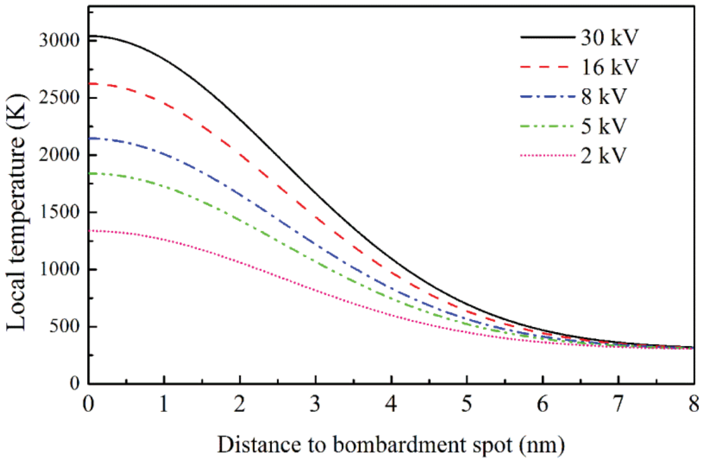

**Figure 7-5**. Temperature distribution in cylindrical coordinates related to bombardment spot for 30 kV, 16 kV, 8 kV, 5 kV, and 2 kV FIB sculpting.

Different parameters (such as ion beam flux *f*, substrate temperature $T_S$, initial tube diameter $d_0$, ion beam dwell time *DT*, and ion beam incidence angle $\theta$) can affect the closing rate of $TiO_2$ nanotubes under 30 kV FIB sculpting. The ion-induced viscous flow mechanism agrees with the influences of these parameters on FIB sculpting.

As shown in Figure 7-6a, it takes $8.3\times10^{16}$ ion/cm$^2$ dose to close 80 nm $TiO_2$ nanotubes under 0.61 ions·cm$^{-2}$·s$^{-1}$ flux, while it only takes 4.5×10$^{16}$ ion/cm$^2$ dose to close the same $TiO_2$ nanotubes under 18.82 ions·cm$^{-2}$·s$^{-1}$ flux. When the ion beam flux is increased, the ion-induced viscosity $\eta$ decreases based on Equation (7-2), which enhances both viscous flow and mass transport rates based on Equation (7-3). Therefore, the closing rate of the $TiO_2$ nanotubes should accelerate under a large $f$, agreeing with the experimental results about the flux effect in Figure 7-6a.

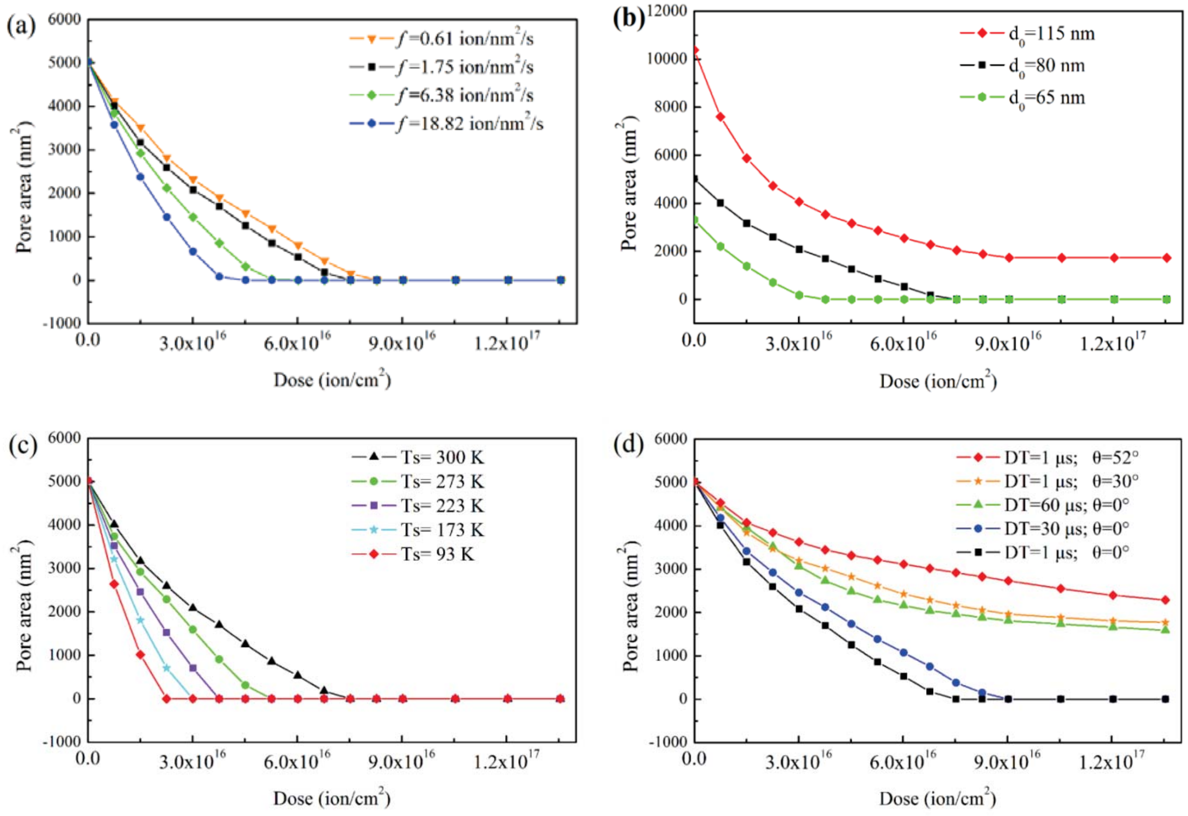

**Figure 7-6**. Influence of (a) ion beam flux $f$, (b) initial tube diameter $d_0$, (c) substrate temperature $T_S$, (d) dwell time $DT$ and incidence angle $\theta$ of ion beam on the closing rate during 30 kV FIB sculpting.

Interestingly, as shown in Figure 7-6b, the closing rates of $TiO_2$ nanotubes are sensitive to the initial tube diameter $d_0$. At the same instantaneous diameter, the nanotubes that start with a larger $d_0$ close more slowly. For the nanotube with $d_0$=80 nm, after the diameter shrinks to 65 nm under a 1.5×10$^{16}$ ion/cm$^2$ dose, it needs another 6.0×10$^{16}$ ion/cm$^2$ dose to close the tube. However, for the nanotube with $d_0$=65 nm, it only needs 3.7×10$^{16}$ ion/cm$^2$ dose to close the tube. Moreover, when $d_0$ is 115 nm, the $TiO_2$ nanotubes cannot be closed even with a prolonged ion dose. This phenomenon can be explained by the reduction in the inwards mass transport rate due to the rotation of an extruded tip. As shown in Figure 7-4, the bottom of the extruded tip becomes more curved during the FIB sculpting, thus the incremental width of the extruded tip under the same amount of viscous flow is decreased: $h_4<h_3<h_2<h_1$. For the nanotube with $d_0$=65 nm, it just experiences FIB sculpting, the initial incremental width ($h_1$) of the extruded tip under viscous flow is large (Figure 7-7a); for the nanotube with 65 nm instantaneous diameter and 80 nm initial diameter, the instantaneous tube edge has a curved profile due to the development of the tip, thus the mass transport occurs both inwards and downwards, which reduces the initial incremental width ($h_1'$) of the extruded tip: $h_1' <h_1$ (Figure 7-7b). Therefore, the closing rate of a nanotube with $d_0$=65 nm is faster. If $d_0$ is increased to 115 nm, more extruded tip rotation leads to the incremental width of the extruded tip further decreases to 0, which suspends the inwards mass transport and the viscous flow only moves in the downwards direction. In this case, the nanotubes stops shrinking and cannot be closed by the FIB sculpting (Figure 7-7c).

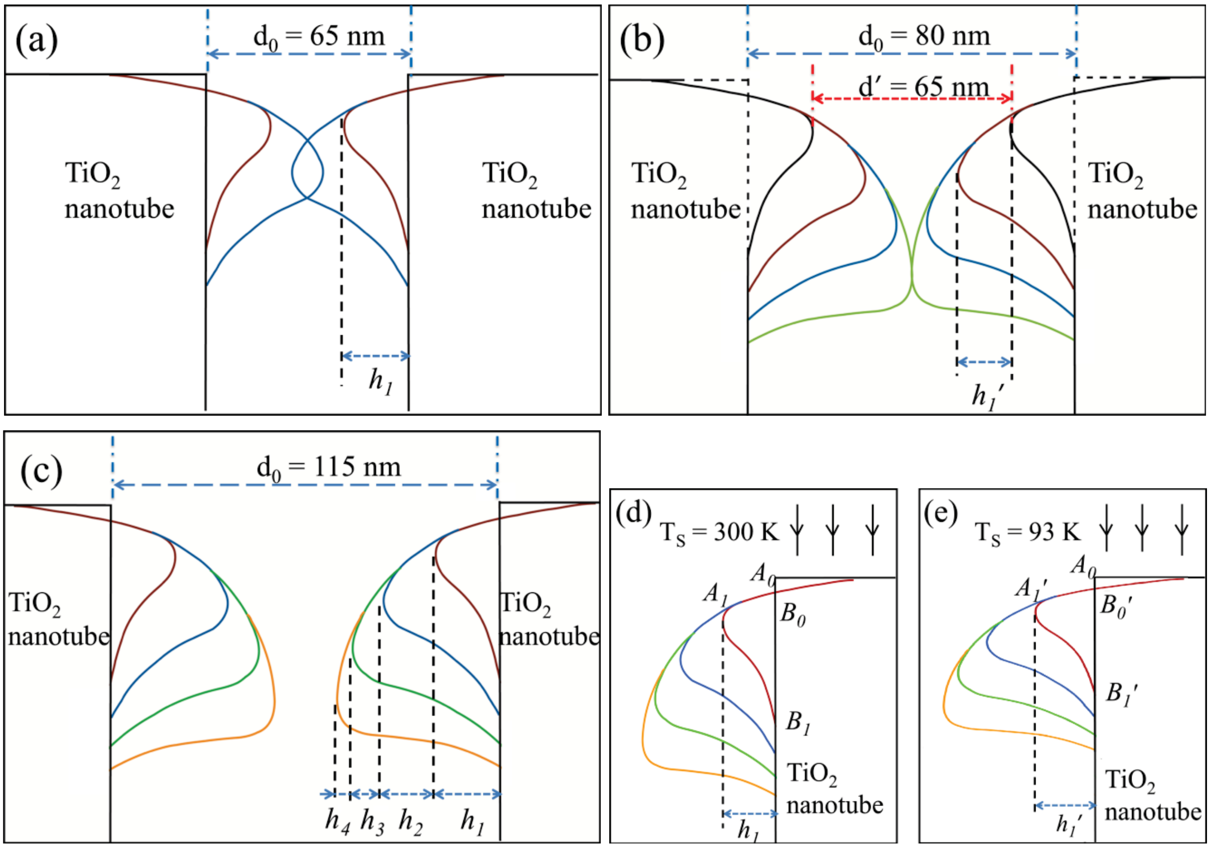

**Figure 7-7**. Illustration of the evolution of $TiO_2$ nanotube profile under FIB sculpting with different initial diameter $d_0$ and substrate temperature $T_S$: (a) $d_0$=65 nm, (b) $d_0$=80 nm and instantaneous diameter $d'$= 65 nm, (c) $d_0$=115 nm, (d) $T_S$=300 K, and (e) $T_S$=93 K.

When $T_S$ is cooled from 300 K to 93 K, the minimum ion dose to close 80 nm $TiO_2$ nanotubes decreases from $7.5\times10^{16}$ ion/cm$^2$ to $2.2\times10^{16}$ ion/cm$^2$, thus the closing rate increases (Figure 7-6c). The low $T_S$ enlarges the temperature gradient from the thermal spikes to the substrate, thus accelerates the freezing rate of viscous flow when it moves along the instantaneous surface. Under the same amount of viscous flow, more mass accumulates at the extruded tip $A_1'$ and the distance from $B_0'$ to $B_1'$ is decreased: $B_0'B_1'<B_0B_1$ (Figure 7-7d and 7-7e). For the areas $B_0'A_1'B_1'$ and $B_0A_1B_1$ to be equal, the width of the extruded tip $h_1'$ should be larger than $h_1$. As a result, low substrate temperature increases the inward mass transport rate and the closing rate of the $TiO_2$ nanotubes. On the other hand, due to the high temperatures at the local thermal spikes under the FIB sculpting, the decrease in $T_S$ only slightly influences the ion-induced diffusion coefficient $D_{vicous}$ (Figure 7-8), which means the effect of $T_S$ can be neglected.

Figure 7-6d shows that a longer dwell time of FIB sculpting at each pixel (which means a slower scan rate) leads to a slower closing rate of the $TiO_2$ nanotubes. The explanation is that the longer dwell time at each spot could increase the substrate temperature underneath the local thermal spikes and decrease the temperature gradient from the local spikes to the substrate; therefore, as discussed above, a smaller temperature gradient leads to a slower closing rate. However, short dwell time enables the substrate underneath the local thermal spikes to recover the low temperature more quickly and thus facilitates an increase in the freezing rate of the viscous flow and accelerates the closing rate of the $TiO_2$ nanotubes.

The incidence angle, $\theta$, of the ion beam also affects the FIB sculpting process. For normal incidence angle ($\theta$=0°), the ion-induced viscous flow can close the $TiO_2$ nanotubes as discussed above. However, when $\theta$ is increased to 30°, the $TiO_2$ nanotubes cannot be closed and the diameters remain at 48 nm under $1.35\times10^{17}$ ion/cm$^2$ dose (Figure 7-6d). When $\theta$ is increased to 52°, the $TiO_2$ nanotubes still cannot be closed, remaining at a diameter of 55 nm. This effect can be understood through the balance between the ion-induced viscous flow and the ion sputter erosion. Experimental results and SRIM simulation reveal that the ion sputter yield rate increases with an increasing $\theta$.[242-244] Meanwhile, the tilted incidence angle enlarges the projected beam spot at the sample surface, which decreases the beam flux and leads to the reduction of the ion-induced viscous flow. As a result, sputter erosion dominates over the ion-induced viscous flow at a large $\theta$, and the $TiO_2$ nanotubes cannot be closed. This is similar to the tube opening process at low ion beam energies, where the sputter erosion dominates the ion beam sculpting, and the shield layer on the closed $TiO_2$ nanotube surface is removed to open the tube.

The viscous flow model proposed by Aziz et al. is based on anisotropic deformation[235]. However, anisotropic deformation only occurs when electronic stopping (the energy transferred by the ion to the target electrons) dominates over nuclear stopping (the energy transferred by the ion to the target nuclei) at mega-electron-volt ion energies.[245-247] Because the focused $Ga^+$ beam energies in this study ranges from 2 kV to 30 kV, electronic stopping only accounts for a small ratio of the total collision cascades. Therefore, the anisotropic deformation is negligible, and I propose that the ion-enhanced fluidity is the driving force for viscous flow.

Adatom diffusion model was established by Golovchenko et al. to explain noble gas ion sculpting.[231-234] The annihilation of mobile adatoms at the edges of the pores leads to the closing of the nanopores. The characteristic distance of adatom diffusion before annihilation, $X_m$, depends on the ion flux $f$ and surface diffusivity $D$: [231-234]

$$\frac{1}{X_m^2} = \frac{1}{\ell_{trap}^2} + \frac{\sigma}{D} f \tag{7-4}$$

$$D = D_0 \exp(-E_a / kT_S) \tag{7-5}$$

where $\sigma$ is the cross section for adatom annihilation by an impinging ion, $\ell_{trap}$ is the average distance between surface defects that might trap an adatom, $D_0$ is a material dependent prefactor, and $E_a$ is the activation energy for surface diffusion (0.8 eV).[248] A typical value for the prefactor $D_0$, $10^{-3}$ $cm^2/s$, is used to estimate the surface diffusivity.[233] According to the adatom diffusion model, the influences of different parameters on the FIB sculpting are as follows. First, adatom diffusion length $X_m$ should decrease with an increase in $f$, which indicates that the closing rate decreases when $f$ increases. Second, the thermally activated surface diffusivity $D$ decreases exponentially with $T_S$ as shown in Figure 7-8, and low $T_S$ is expected to freeze the adatom diffusion and reduce the closing rate. Third, the closing rate should be independent of the initial diameter of the nanotube. However, all these expectations based on the adatom diffusion model contradict the experimental results in Figure 7-6, which demonstrates the negligible effect of adatom diffusion on the FIB sculpting.

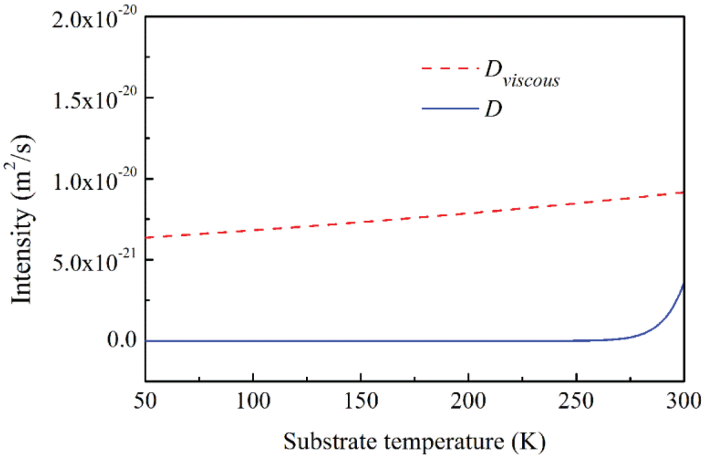

**Figure 7-8**. The relation of ion-induced diffusion coefficient ($D_{viscous}$) and thermal activated surface diffusivity ($D$) with substrate temperature, which is calculated based on Equation 3 and 5, respectively.

The atomic displacement or amorphization due to ion beam induced damage and the additional volume increase by $Ga^+$ ion implantation lead to swelling of the bombarded surface. Normally, the surface expansion due to swelling is less than the ion penetration depth.[249-250] For the exposure of the $TiO_2$ surfaces by 30 kV $Ga^+$ ion, the Monte Carlo simulation by SRIM shows that the ion penetration depth is 15.9 nm;[242] thus, swelling will be limited to 16 nm, which is too small to close the 80 nm $TiO_2$ nanotubes. Moreover, the swelling effect should be independent of the ion flux, substrate temperature, and dwell time of the ion beam, which contradicts the experimental results shown in Figure 7-6. Therefore, the swelling effect can be neglected during the FIB sculpting.

Redeposition during ion beam bombardment is a result of reduced collisional mean free path between collisions of sputtered particles because of the intensified local pressure by introduction of sputtered target materials.[251-252] Under the same instantaneous ion dose, a single slow scan leads to a larger localized pressure than a repeated fast scan. Therefore, a slower scan (or longer dwell time) should cause more redeposition and accelerate the closing rate. However, the $Ga^+$ ion beam sculpting in this study shows a reduced closing rate corresponding to an increase in the dwell time. Hence, redeposition is not the mechanism for mass transport during the FIB sculpting.

The selective closing and re-opening of the $TiO_2$ nanotubes can be utilized to modify the surface of the $TiO_2$ nanotubes. The combination of this technique with electrodeposition can allow for the selective growth of different conductive materials into different regions of the $TiO_2$ nanotubes. Moreover, selectively closing and re-opening $TiO_2$ nanotubes presents an opportunity to load multiple dyes into dye sensitized $TiO_2$ nanotube solar cells to increase the light absorption window and the solar cell efficiency. The opening process under low energy ion beam sculpting provides an approach to remove the barrier layer of freestanding $TiO_2$ nanotubes to obtain $TiO_2$ nanotubes with two open ends.

### 7.1.4. Summary

Highly ordered $TiO_2$ nanotube arrays have been selectively closed under the sculpting of a 30 kV focused $Ga^+$ beam; meanwhile, the closed $TiO_2$ nanotubes can be re-opened by reducing the energy of the $Ga^+$ beam to 5 kV. The closing rate of the $TiO_2$ nanotubes increases with a larger ion beam flux. Reducing the substrate temperature to as low as 93 K does not freeze the lateral mass transport; on the contrary, the closing rate of $TiO_2$ nanotubes is increased when the substrate cools down. The FIB sculpting efficiency is sensitive to the initial diameter of the $TiO_2$ nanotubes: smaller initial tube diameters can be closed more quickly, but the tube cannot be closed if the initial diameter is too large. Long dwell time and large incidence angle of the ion beam decrease the closing rate. I propose that the balance between ion-induced viscous flow and sputter erosion is the mechanism for closing and re-opening of the $TiO_2$ nanotubes under the FIB sculpting. This model is consistent with all of the experimental observations.

## 7.2. Understanding sintering characteristics by FIB-SEM 3D analysis

### 7.2.1. Introduction

It is believed the pore shrinkage is accompanied with density increase during sintering, which leads to the formation of closed pores and eventual pore removal. However, quantitatively analysis of the evolution of pore network is difficult. Traditional methods, such as BET and mercury porosimetry techniques, analyze the size, distribution and surface area of pores relying on gas or liquid to penetrate into the pores, which are only suitable for open pores.[253-256] The failure of gas or liquid penetration into close pores means that these methods cannot monitor the pore evolution during the sintering process. Moreover, these methods cannot evaluate the pore shape and connectivity.

3D reconstruction by focused ion beam cutting/scanning electron imaging (FIB-SEM) has recently been developed to analyze various electrodes of solid oxide fuel cells.[257-260] SEM cross section image created by FIB cutting can effectively differentiate different materials and pores in the electrodes. Utilizing the 3D FIB-SEM reconstruction, a variety of solid oxide fuel cell microstructural parameters have been quantified, such as triple-phase boundary (TPB) density, TPB length, volume porosity, particle size, phase connectivity, phase tortuosity, and surface area. FIB-SEM tomography offers an opportunity to directly analyze the microstructural evolution during sintering.

In this paper, I describe the 3D microstructure reconstruction by FIB-SEM tomography to understand pore evolution during the two-step sintering of ZnO nanoparticles. Sample linear shrinkage and weight loss at different temperature are examined by dilatometry and thermogravimetric analysis (TGA) to identify suitable temperatures for first and second step sintering. Key microstructural parameters including the relative density, surface area of ZnO matrix, pore shape, pore connectivity, and pore number are measured by 3D reconstruction.

### 7.2.2. Experimental procedure

ZnO green samples were prepared as discussed in 4.2.2. Subsequently, ZnO green samples were sintered at different conditions. The linear shrinkage of the ZnO samples at different temperatures with 5ºC/min heating rate was measured by a dilatometer (Model 1600D, The Edward Orton JR. Ceramic Foundation, Westerville, OH). Weight loss of ZnO samples was carried out by a simultaneous TGA/DSC unit (449 C Jupiter, Netzsch Instruments N.A. LLC., Burlington, MA). Two-step sintering was carried out by first heating the sample to 1000ºC with 5ºC/min heating rate and maintaining at 1000ºC for 1 min, and then decreasing the temperature to 850ºC with 100ºC/min cooling rate and keeping at 850ºC for different time.

The microstructures of the sintered ZnO samples were characterized by FIB-SEM three-dimensional analysis. First, the sintered ZnO sample was mounted on a FIB sample holder by graphite conductive adhesive and then sputter coated with a 10 nm gold layer to increase the conductivity. Second, a platinum protective layer with 1 μm thickness and 10 μm×10 μm size was deposited on the ZnO surface at 0° tilt angle in order to avoid the milling of ZnO surface structure and waterfall artifact during the FIB cutting. Third, three regular cross sections on different sides of the sample were obtained in order to create a ZnO protruding tip with 5 μm×5 μm size. Fourth, platinum protective layers with 1 μm thickness were further deposited on the left and right sides of the ZnO protruding tip at 52° tilt angle, which significantly increased the conductivity of the ZnO sample during the FIB milling. Fifth, a nanopore array with 200 nm interpore distance and ~500 nm depth was created on the platinum protective layer at the top surface of the protruding tip, which was used as markers for three-dimensional analysis. Sixth, as the FIB milled away the material at the front of the ZnO protruding tip, a series of 2D cross section SEM images were continuously acquired. The slice to slice distance was 10 nm, and the milling current was 93 pA. Finally, the 2D cross section SEM images were aligned and stacked to form the 3D microstructure of the sintered ZnO samples by Amara software.

### 7.2.3. Results and discussion

#### 7.2.3.1 Densification and 2D microstructure observation

In order to identify proper temperatures for the first-step and second-step sintering, dilatometry and TGA were carried out to analyze the shrinkage and weight loss during sintering. The relative density of the green samples is 44%. As shown in Figures 7-9a and b, there are ~1.4% shrinkage and 5.4% weight loss at 450ºC, and these changes are due to the decomposition of PAA and evaporation of water. Rapid linear shrinkage occurs when the temperature is increased to >850ºC, reaches 16% at 1000ºC, and stabilizes at ~24.5% at 1100ºC. Based on the linear shrinkage curve, the lowest temperature to activate densification should be around 850ºC. Thus 850ºC is chosen as the second-step sintering temperature, which should allow densification through grain boundary diffusion while still being not high enough to activate grain growth. Assuming that the shrinkage is isotropic during sintering, we can calculate the relative density of the ZnO samples at different temperatures based on the dilatometry and TGA data, as shown in Figure 7-9c. The relative density is 44% before 850ºC, and increases rapidly after 850ºC. The relative densities at 1000ºC, 1100ºC, and 1200ºC are 69.9%, 96.0%, and 98.1%, respectively. The density measured after 1000ºC sintering is 66%, which is very close to the calculated value in Figure 7-9c. In order to achieve a critical density value of 75% before the second-step sintering, the ZnO green sample is heated to 1000ºC and maintained at 1000ºC for 1 min during the first-step sintering. The density at this state is measured to be 75%.

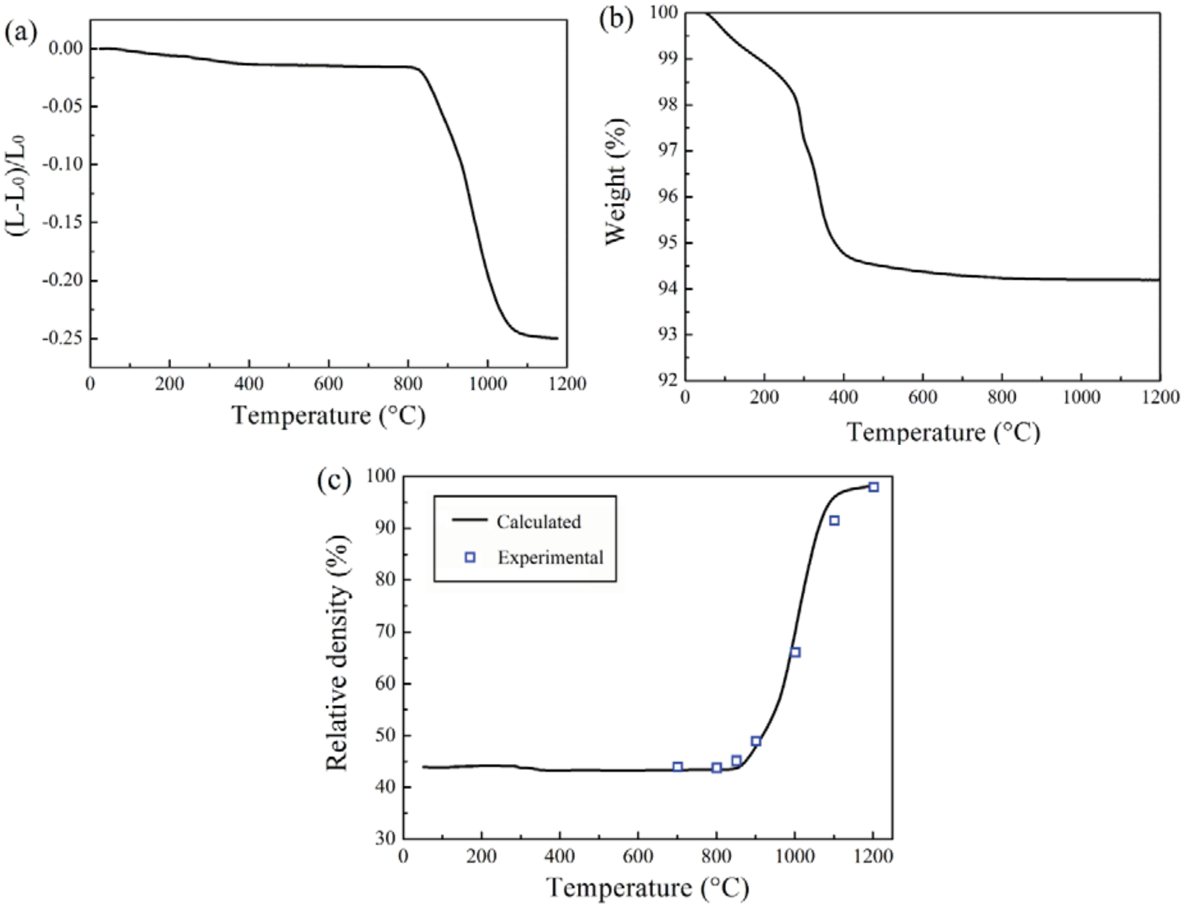

**Figure 7-9**. (a) Dilatometry curve of the ZnO sample, (b) TGA curve of the ZnO sample, (c) calculated relative density of the ZnO sample based on the dilatometry and TGA data.

As shown in Figure 7-10a, the grain size for the green sample is almost the same as the ZnO nanoparticle size, which is around 20-30 nm. After the first step sintering at 1000ºC for 1 min, the grain size increases to 90-400 nm while the relative density increases to 75%. The rapid increases in ZnO density and grain size at 1000ºC demonstrate that both grain boundary migration and grain boundary diffusion are active at 1000ºC. When the second step sintering at 850ºC is carried out for 2 h, 5 h, 20 h, and 50 h, the relative density increases to 83%, 91%, 96%, and 97%, respectively. At the same time, the SEM image in Figure 7-10e shows that the grain size is only slightly enlarged to 150-580 nm after 50 h of sintering at 850ºC. This means during these periods grain boundary migration is minimal. If the temperature for the second step sintering is increased to 900ºC, after 5 h of sintering some grain sizes increase to as large as 1.1 µm, as shown in Figure 7-10f. Therefore, the second step sintering at 850ºC effectively avoids the grain growth and while still keeping the grain boundary diffusion active to densify the ZnO samples.

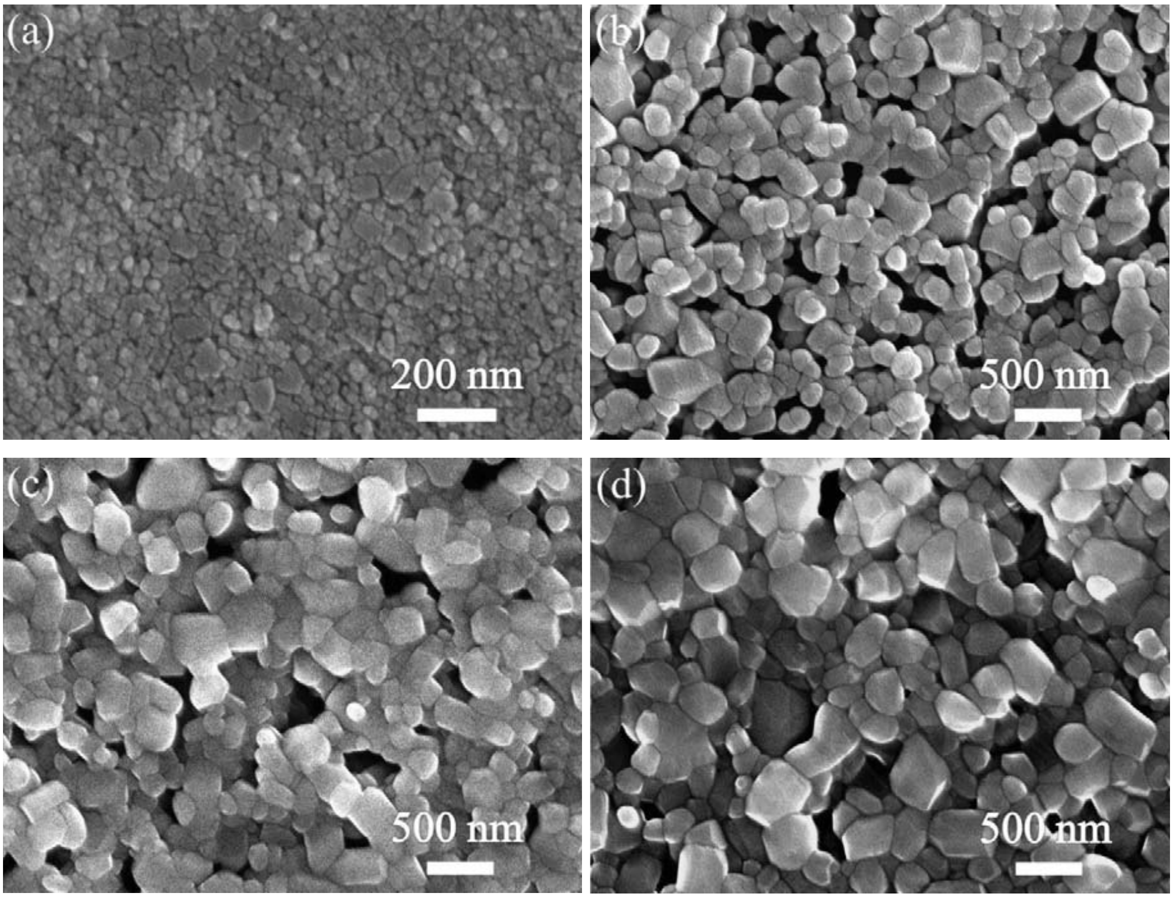

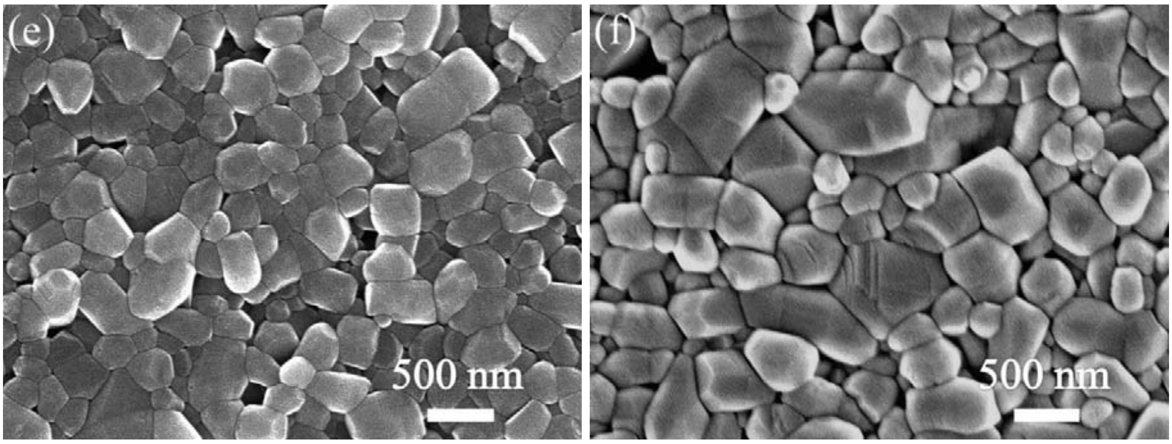

**Figure 7-10**. SEM images of ZnO samples at different sintering stages: (a) green sample; (b) after first-step sintering at 1000ºC; (c-e) after second-step sintering at 850ºC for 2 h, 5 h, and 50 h, respectively; (f) after second-step sintering at 900ºC for 5 h.

### 7.2.3.2 3D microstructure reconstruction

The 2D SEM images are difficult to show the evolution of pores during the sintering process. Therefore, here I introduce a 3D microstructure reconstruction method to analyze the evolution of pore connectivity, pore size, pore number, and pore shape. The SEM-FIB duel beam system is used to collect a series of 2D cross section SEM images with 10 nm interval distance. The electrical conductivity of the sample surface plays a crucial role in determining whether high quality 2D images can be obtained or not. As shown in Figure 7-11a, FIB cutting can be used to create a cross section surface in the region of interest, and then a corresponding SEM image can be obtained at the backside wall of the cut. Even though the top surface is coated with a platinum layer, the electrical conductivity is low. Positively charged $Ga^+$ ions mill the sample during the FIB cutting, and negatively charged electrons sculpt the sample during the SEM imaging. If the electrical conductivity of the sample surface is low, serious charging will occur at the milled region, which leads to sample drifting under ion beam and electron beam, as shown in Figure 7-11b. In this case, it is hard to maintain the same distance between the slices during the FIB cutting. Here, I first create a protruding tip by FIB, and then coat a thick platinum protective layer to cover both the top and side surfaces of the protruding tip. As a result, during the FIB cutting, the side and top surfaces of the examined region are always covered by a conductive platinum layer to maintain good electrical conductivity and overcome the charging issue. Thus, I can greatly decrease the interval distance between the slices of FIB cutting to 10 nm. Moreover, a nanopore array with 200 nm interpore distance is introduced on the top surface of the protruding tip to monitor the distance between each cutting. It takes 20 cuts to go from one row of nanopores to the next row of nanopores, which confirms that the distance between each cutting is 10 nm. Because the focused ion beam has a Gauss distribution and the minimum ion beam spot is 30 nm for 30 kV and 93 pA condition, it is difficult to obtain slice interval distance less than 10 nm.

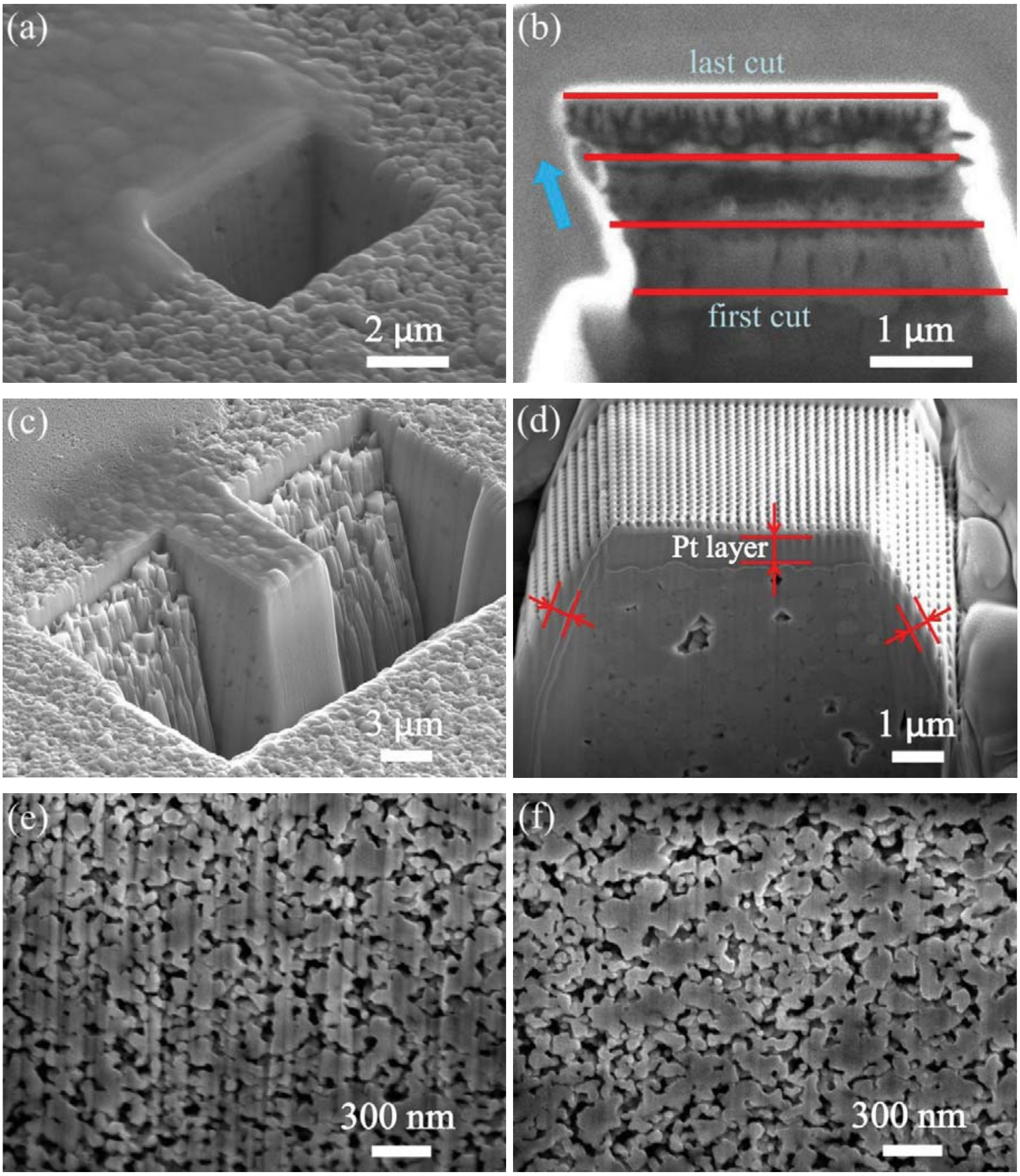

**Figure 7-11**. (a) FIB cutting with a dent in the region of interest; (b) drifting of FIB cutting locations; (c) new sample preparation method by creating a protruding tip; (d) coating the side and top surfaces by a thick platinum protective layer and creating a nanopore array on the top surface of the protruding tip to monitor the FIB cutting quality; (e) cross section image with waterfall artifact when a platinum layer on the top surface is thin; (f) cross section image with a thick platinum protective layer on the side and top surfaces of the protruding tip.

If the thickness of the platinum protective layer is less than 300 nm, then some vertical artifact lines are developed at the cross section (Figure 7-11e), this waterfall artifact is one of the main issues affecting the quality of cross section SEM images. I find that a platinum protective layer with a thickness larger than 1 μm is necessary in order to effectively avoid the waterfall artifact. For the protruding tip with a thick platinum layer on the side and top surfaces, good quality SEM cross section images can be achieved, as shown in Figure 7-11f.

After obtaining 150 slices of 2D cross section SEM images, the Amira software is used to align the slices and crop the interested region into 3 μm × 3 μm areas. Subsequently, 3D microstructure reconstruction of the ZnO samples is achieved by stacking all the slices together with 10 nm interval distance, as illustrated in Figure 7-12a. Figure 7-12b shows the 3D reconstruction result of the ZnO sample after the first step sintering, the blue (darker in print) color represents the pores inside the sample, and the red color (light in print) represents the ZnO matrix. The ZnO matrix blocks the observation of pore structures inside the sample. In order to distinguish all the pores, each pore can be labeled by a different color and extracted from the ZnO matrix, as shown in Figure 7-12c. The pore volume is very high and the pores are interconnected with each other. Except for several isolated pores at the edge, a large open pore dominates. The reason for the isolated pores at edge locations is due to the spatial limitation of 3D reconstruction in 3 μm × 3 μm × 1.5 μm volume, which artificially cuts out their connection with other open pores. This indicates that after the first-step sintering the ZnO sample has high pore volume and the pores are interconnected with each other to form a large open pore.

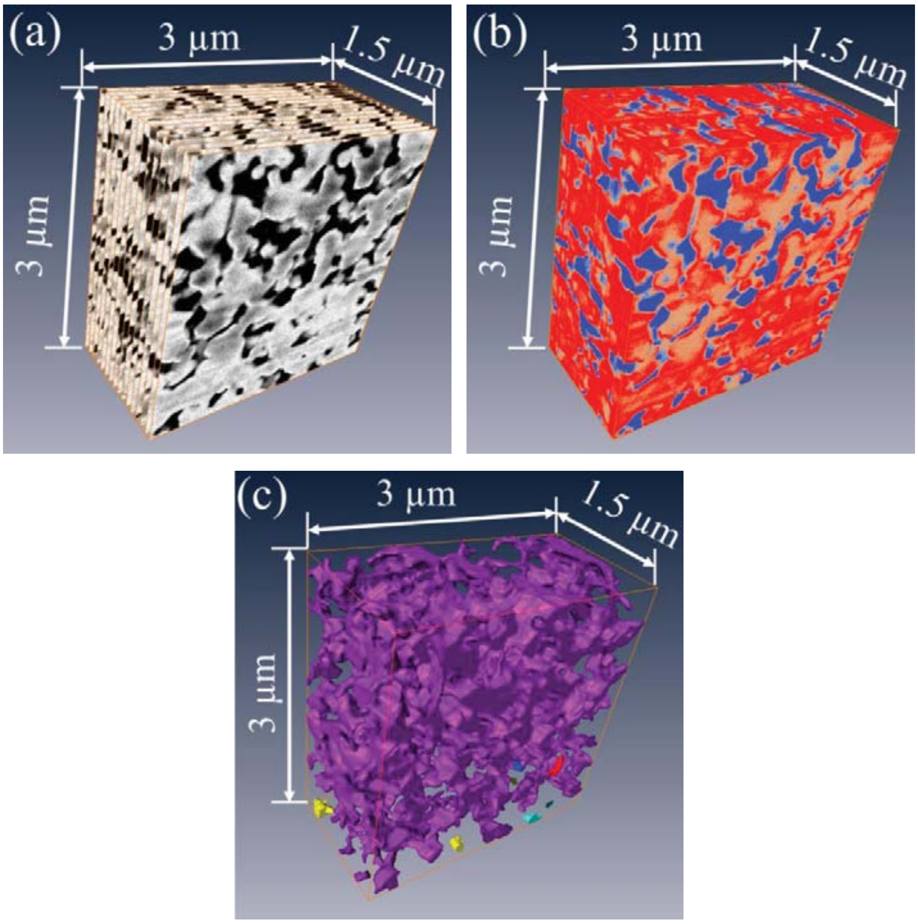

**Figure 7-12**: (a) Illustration of 3D microstructure reconstruction by stacking slices together, in order to clearly demonstrate the illustration, we show the SEM images every 10 slices; (b) 3D mcirostructure of ZnO sample after the first step sintering; (c) 3D structure of pores for the ZnO sample after the first step sintering.

### 7.2.3.3 3D microstructure understanding

Figure 7-13 shows the 3D reconstruction result of pore evolution in the ZnO samples after different times of second step sintering. Both size and shape of the pores present change during sintering process. With the increase of second-step sintering time, pore shrinkage causes large interconnected open pores (as shown in Figure 7-12c) to break into many small pores. After 2 h of second-step sintering, the pore number increases to 49, but some of the pores are still interconnected and open (Figure 7-13a). When the sintering time is increased to 5 h and 20 h, the pore number further increases to 66 and 96, respectively, while more and more closed pores forms. Figure 7-13c shows many small isolated pores for the ZnO sample after 20 h of second-step sintering. Moreover, the pore size has a large range. Even though the ball milling sample preparation greatly break up the agglomerates, any minor variations in the original particle packing or particle-size are exaggerated during the pore growth process, which leads to a range of pore sizes present during intermediate stages of sintering; at the same time, spaces between agglomerates and occasional larger voids further enlarge the pore size distribution.

Prolonging the sintering time to 50 h leads to the disappearance of some small isolated pores, thus the pore number decreases to 33. At the same time, it is hard to remove large isolated pores even with very long sintering time. According to the sintering theory, the pore stability is related to the number of surrounding grains and ratio of pore size to grain size. For the large pores, due to high number of surrounding grains and large ratio of pore size to grain size, the pores not only remains stable but grow. Most of the sintering theory assume the isolated pores have spherical shape, however, the 3D reconstruction result clearly shows that the pore shape is irregular even after sintering at 850°C for 50 h.

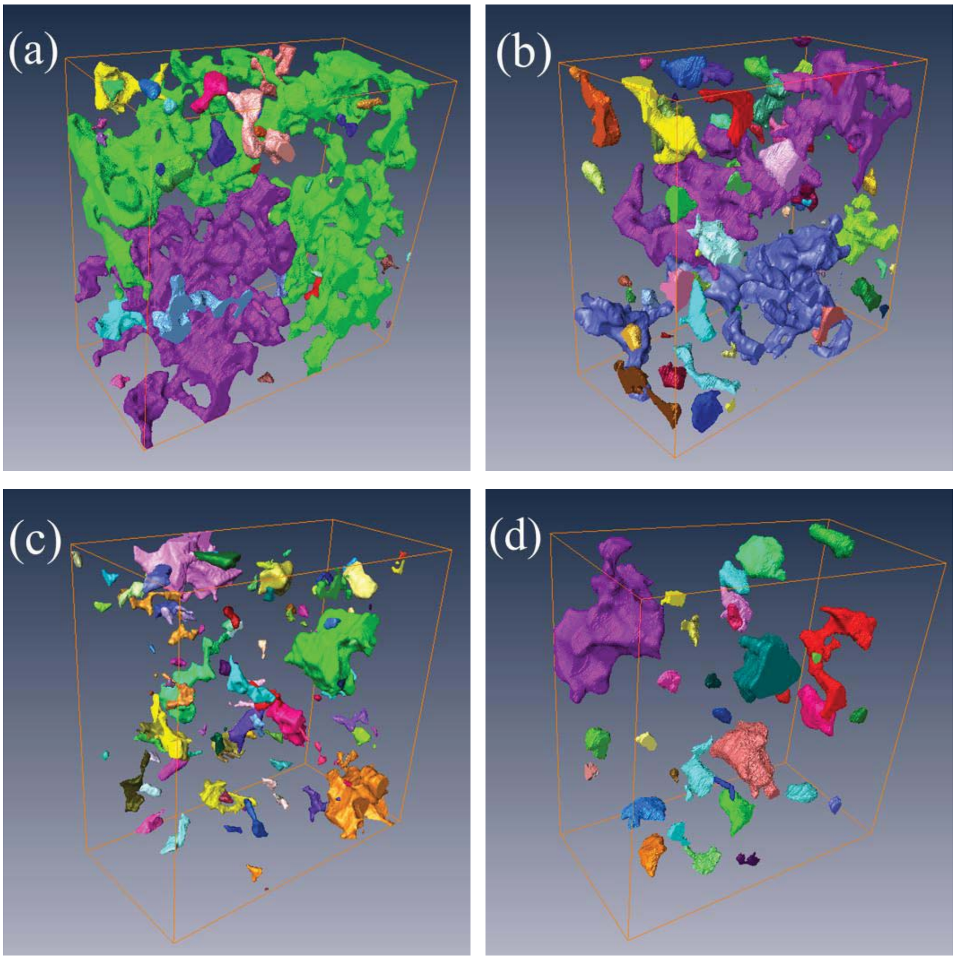

**Figure 7-13**. 3D structure of pores for the ZnO samples after second step sintering for different times: (a) 2 h, (b) 5 h, (c) 20 h, and (d) 50 h. The volume of the reconstruction region is 3 μm × 3 μm × 1.5 μm, the same as in Figure 7-12.

Based on the 3D reconstruction data, relative density, pore volume, pore-ZnO matrix interfacial area, and pore number can be quantitatively obtained and are summarized in Figure 7-14. With the increase of the second step sintering time from 0 h, to 2 h, 5 h, 20 h, and 50 h, the total pore volume in the 3 μm × 3 μm × 1.5 μm reconstruction space decreases from 3.65 $\mu m^3$ to 2.39 $\mu m^3$, 1.34 $\mu m^3$, 0.60 $\mu m^3$, and 0.57 $\mu m^3$, respectively, which indicates that the relative density of the ZnO samples increases from 72.9% to 82.3%, 90.0%, 95.6%, and 95.8%, respectively. The relative density from 3D reconstruction is consistent with the experimental results, as shown in Figure 7-14a, which indicates the reliability of this 3D reconstruction method.

The traditional methods to measure pore volume, such as BET and mercury porosimetry techniques, can only detect open pores because gas or liquid cannot penetrate into isolated pores. Here, the FIB-SEM 3D reconstruction method enables evaluation of pore structures for both open pores and isolated pores. Therefore, it is an excellent tool to measure the changes of pore-grain interfacial area during sintering. As shown in Figure 7-14b, the total interfacial area in the reconstructed region dramatically decreases from 85.7 $\mu m^2$ to 48.8 $\mu m^2$, 34.2 $\mu m^2$, 14.3 $\mu m^2$, and 11.5 $\mu m^2$ after 2 h, 5 h, 20 h, and 50 h of second-step sintering, respectively. At the early stage of second-step sintering, the ZnO sample has a higher porosity, the mean diffusion distance is small. This leads to significant shrinkage and segmentation of pores, which is accompanied with rapid increase of relative density and decrease of pore-solid interfacial area. When densification occurs, many pores become isolated from grain boundaries, and the diffusion distance between pores and a grain boundary becomes large, thus the rate of sintering decreases, which decelerates the increasing rate of relative density and decreasing rate of pore-solid interfacial area.

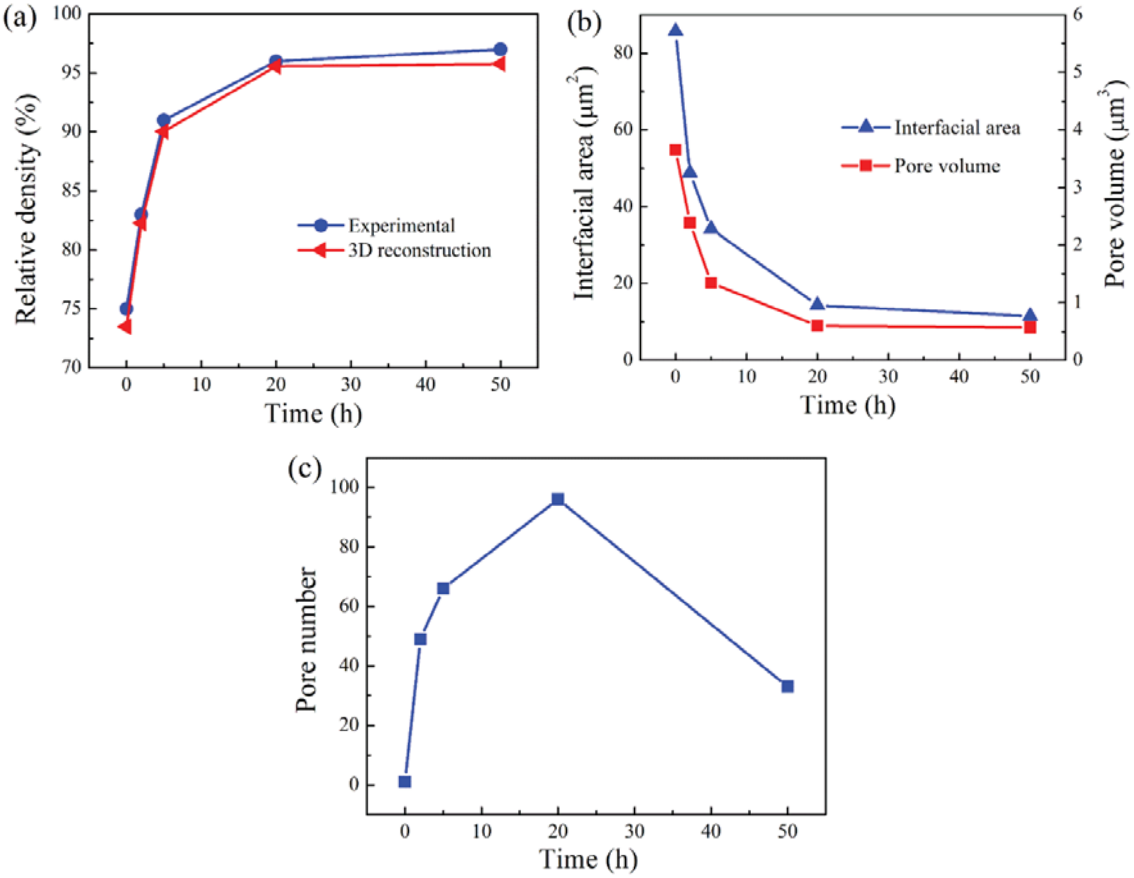

**Figure 7-14**. (a) Experimental and 3D reconstruction density results for the ZnO samples at different time of second step sintering; (b) 3D reconstruction results for interfacial area and pore volume and (c) pore number at different time of second step sintering in 3 μm × 3 μm × 1.5 μm sample volume.

### 7.2.4. Summary

In this study, I utilize FIB-SEM 3D reconstruction to understand the microstructure evolution of sintered ZnO samples, especially during the two-step sintering. The linear shrinkage measurement by dilatometry shows a rapid shrinkage starting from 850ºC. New FIB cutting method, which introduces a protruding tip with thick platinum protective layer covering both the top and side surfaces, overcomes the drifting issue and waterfall artifact for the FIB cutting, and improves the FIB cutting resolution to 10 nm. Based on the 3D reconstruction, the relative density, pore volume, pore-ZnO matrix interfacial area, pore shape, pore connectivity, and pore number have been achieved. With increase in second-step sintering time, the relative density of the ZnO samples increases. During the sintering, the pore volume decreases changes the interconnected open pores to isolated-closed pores; at the same time, the pore number first increases due to the formation of closed pores, and then decreases due to the disappearance of the small closed pores. Due to densification and the formation of isolated pores, the diffusion distance between pores and grain boundaries increase, which slow down the shrinkage rate of pore volume and decreasing rate of pore-solid interfacial area.

# Chapter 8. Conclusion

## 8.1. Conclusion

In this dissertation, I focus on the growth of anodic alumina nanopores and $TiO_2$ nanotubes and their applications. First, highly ordered AAO arrays with different structures are achieved by FIB pre-pattern guided anodization. During the anodization, the electric field at the FIB patterned concaves is large, thus facilitate the development of nanopores at the FIB patterned locations. The FIB patterned concave with only 1.5 nm depth can efficiently guide the growth of nanopores. FIB lithography has the advantage to create concave arrays with various arrangements, interpore distances, and diameters, which enables AAO arrays with corresponding structures. With the guidance of the FIB patterned concaves, the anodization windows are increased, and this offers more capability to design the AAO template with different interval distance and arrangement. Hexagonal AAO arrays with interpore distances ranging from 200 nm to 350 nm can be fabricated at 140 V in 0.3 M phosphoric acid; hexagonal AAO arrays with 150 nm interpore distances can be obtained under the applied potential ranging from 50 V to 80 V in oxalic acid. As a result, AAO with Moiré pattern, which has various interpore distances and alternating high and low nanopore area specific densities, is successfully fabricated by FIB guided anodization. However, when the interpore distance of FIB patterned concave increases to a large value, new nanopores start to develop at the tri-junction centers of the FIB pattern.

Vertically aligned and high aspect ratio h-PDMS nanorod arrays with Moiré pattern arrangements have been synthesized by nanoimprinting a prepolymer with the AAO template. The key to release the h-PDMS nanorods without bending and ground collapse is to introduce a low surface energy AAO template through a polymer monolayer. For the ceramic micro-fabrication by soft lithography, there are two important steps. First, a high solids loading nanoparticle suspension is prepared through both electrostatic stabilization and steric stabilization. Second, a hydrophilic PDMS mold surface is created by adding 3 wt% TX-100. The large capillary force between the suspension and the PDMS mold surface enables the suspension to fully fill the features on the mold, and the high solids loading is required to maintain the fidelity of the features during soft lithographic micromolding.

In this dissertation, I discovered two important phenomena, which challenge the validity of existing formation mechanisms of anodic $TiO_2$ nanotubes. First, increasing $OH^-$ concentration in the electrolyte leads to the transformation of nanoporous to nanotubular $TiO_2$ structure. Second, the as-grown $TiO_2$ nanotubes show structural evolution during the submersion in an electrolyte or drying in air after the anodization, which is demonstrated by EIS measurement for the first time. Based on this, dehydration of titanium hydroxide cell wall is proposed to understand the formation mechanism of anodic $TiO_2$ nanotubes. Combining the FIB lithography with electrochemical anodizationcan create not only highly ordered $TiO_2$ nanotube arrays but also $TiO_2$ nanotube arrays with different arrangements, interpore distances, and diameters. $TiO_2$ nanotube arrays with branched structure and bamboo-type structure have been fabricated by adjusting the anodization voltage.

Bamboo-type $TiO_2$ nanotubes produced by cycling applied voltage show large specific surface area and inter-connectivity, and thermal treatment in $H_2$ atmosphere increases the electrical conductivity of the $TiO_2$ nanotubes. As a result, the bamboo-type $TiO_2$ nanotubes demonstrate larger supercapacitors and higher water splitting efficiency than smooth $TiO_2$ nanotubes, and the $H_2$ treated $TiO_2$ nanotubes demonstrate larger supercapacitors and higher water splitting efficiency than as-grown $TiO_2$ nanotubes. $H_2$ treated bamboo-type $TiO_2$ nanotubes are an excellent candidate for energy conversion and storage.

The surface curvature and heterogeneous concave depths influence the growth direction of $TiO_2$ nanotubes and alumina nanopores. In order to investigate these effects, I used FIB lithography to create nanopores with heterogeneous depths on flat surfaces and with uniform depth on curved surfaces. Bending and bifurcations of nanotubes/nanopores are observed under the pattern guidance with heterogeneous depths. For the curved surface, the growth direction of all $TiO_2$ nanotubes is perpendicular to the local surface; bifurcation of a large tube into two smaller tubes occurs on concave surfaces, while termination of existing tubes occurs on convex surfaces. This study also opens an opportunity in the applications of AAO and $TiO_2$ nanotubes where curved substrates are needed.

The mechanism of focused ion beam sculpting on anodic $TiO_2$ nanotube surface is studied, and an ion-induced viscous flow model has been proposed to explain the influence of $Ga^+$ ion beam flux, substrate temperature, initial tube diameter, ion beam dwell time, and the incidence angle of the ion beam. The anodic $TiO_2$ nanotubes can be selectively closed by 30 kV $Ga^+$ beam, and be re-opened by 5 kV $Ga^+$ beam.

Pore evolution (such as the change of pore volume, pore-solid interfacial area, pore shape, pore connectivity, and pore number) during the two-step sintering of ZnO nanoparticles is investigated by a 3D reconstruction method. During the process, FIB cutting and SEM imaging produce a series of cross section images with constant interval distance; these images are stacked together to provide a direct and quantitative observation of pore evolution during sintering. In order to overcome the drifting issue and waterfall artifact during the FIB cutting, a protruding tip with a thick platinum protective layer covering both the top and side surfaces is used in this study. This decreases the interval distance between FIB cuts to 10 nm and improves the z-direction resolution for 3D reconstruction to 10 nm.

## 8.2. Future work

Further research can focus on the following topics:

1, Fabricate ordered AAO directly on Si substrates with no barrier layer between the AAO with Si substrate. One possible method is to use the highly conductive Si wafer as a substrate, and deposit Al onto the Si wafer by electron deposition or thermal deposition. Because the Si substrate has high electrical conductivity, the anode can directly contact with the backside of the Si substrate during the anodization. Subsequently, two-step anodization can be carried out to form ordered AAO on the Si substrate. After the entire Al has been anodized, the electric field at the pore bottom is large; this will facilitate the dissolution of the barrier layer and form AAO structure on the Si substrate with two open ends. Then, electrodeposition, chemical vapor deposition, pulsed laser deposition, sol-gel, or other techniques can be applied to grow nanowires inside the AAO template. After dissolving the AAO template with NaOH, free standing nanowires can be formed on the Si substrate. During drying the large capillary force might lead to collapse and agglomeration of the nanowires, in this case supercritical drying or freeze drying should be introduced to avoid this issue.

2, Further increase the supercapacitors and photochemical water splitting efficiency of devices using $TiO_2$ nanotube arrays. The first approach would be to modify the bamboo-type $TiO_2$ nanotubes with $Fe_2O_3$ nanoparticles by dip coating in a $Fe(NO_3)_3$ solution, or $MnO_2$ nanoparticles by dip coating in a $Mn(NO_3)_2$ solution. The second approach would be to introduce an N-dope the bamboo-type $TiO_2$ nanotubes through thermal treatment under $NH_3$ atmosphere. The third approach would be to electrodeposit the bamboo-type $TiO_2$ nanotubes with Fe, Ni, or Nb to increase the performance in energy related applications.

3, Explore focused ion beam sculpting technique on different substrates, such as semiconductor and metal, oxide materials. This method is to use the influence of $Ga^+$ ion beam flux, substrate temperature, initial pore diameter, ion beam dwell time, and the incidence angle of the ion beam to investigate the focused ion beam sculpting mechanism. Moreover, the mechanism of electron beam sculpting and ion beam sculpting should be studied in future.

4, Improve the quality of cross section SEM image for 3D reconstruction to not only clearly differentiate pore and grains but also identify the grain boundaries. In this case, the 3D FIB-SEM reconstruction can simultaneously demonstrate the grain evolution and pore evolution during sintering, which will enable the investigation of the mechanism of sintering process.

# Chapeter 9. Publications

## Journal papers

1. *Bo Chen*; Junbo Hou; Kathy Lu. Formation mechanism of $TiO_2$ nanotubes and their application in supercapacitors. 2012, Submitted.
2. *Bo Chen*; Kathy Lu; Kelly Ramsburg. ZnO sub-micrometer rod array by soft lithographic micromolding with high solid loading nanoparticle suspension. ***J. Am. Ceram. Soc.*** 2012, Accepted.
3. *Bo Chen*; Kathy Lu. Selective focused-ion-beam sculpting of $TiO_2$ nanotubes and mechanism understanding. ***Phys. Chem. Chem. Phys.*** 2012, Accepted.
4. *Bo Chen*; Zhenbo Xia; Kathy Lu. Understanding sintering characteristics of ZnO nanoparticles by FIB-SEM three-dimensional analysis. 2012, Submitted.
5. Zhenbo Xia; *Bo Chen*; Kathy Lu. 3D microstructure construction of sintered ZrO2 under different sintering conditions. 2012, Submitted.
6. *Bo Chen*; Kathy Lu. Hierarchically branched titania nanotubes with tailored diameters and branch numbers. ***Langmuir***, 2012, 28, 2937–2943.
7. Zhiguang Wang; Yanxi Li; *Bo Chen*; R. Viswan; J. F. Li; D. Viehland. Self-assembled $NaNbO_3$-$Nb_2O_5$ (ferroelectric-semiconductor) heterostructures grown on $LaAlO_3$ substrates. ***Appl. Phys. Lett.*** 2012, 101, 132902.
8. *Bo Chen*; Kathy Lu; J. A. Geldmeier. Highly ordered titania nanotube arrays with square, triangular, and sunflower structures. ***Chem. Commun.*** 2011, *47*, 10085–10087.
9. *Bo Chen*; Kathy Lu; Zhipeng Tian. Effects of titania nanotube distance and arrangement during focused ion beam guided anodization. ***J. Mater. Chem.*** 2011, *21*, 8835–8840.
10. *Bo Chen*; Kathy Lu. Influence of patterned concave depth and surface curvature on the anodization of titania nanotubes and alumina nanopores. ***Langmuir*** 2011, 27, 12179–12185.
11. *Bo Chen*; Kathy Lu; Zhipeng Tian. Novel patterns by focused ion beam guided anodization. ***Langmuir*** 2011, *27*, 800–808.
12. *Bo Chen*; Kathy Lu. Moire pattern nanopore and nanorod arrays by focused ion beam guided anodization and nanoimprint molding. ***Langmuir*** 2011, 27, 4117– 4125.

13. *Bo Chen*; Kathy Lu. Understanding focused ion beam guided anodic alumina nanopore development. ***Electrochim. Acta*** 2011, *56*, 9802–9807.
14. Zhipeng Tian; Kathy Lu; *Bo Chen*. Unique nanopore pattern formation by focused ion beam guided anodization. ***Nanotechnology*** 2010, *21*, 405301.
15. Zhipeng Tian; Kathy Lu; *Bo Chen*. Fundamental mechanisms of focused ion beam guided anodization. ***J. Appl. Phys.*** 2010, *108*, 094306.
16. *Bo Chen*; Kathy Lu; Zhipeng Tian. Gradient and alternating diameter nanopore templates by focused ion beam guided anodization. ***Electrochim. Acta*** 2010, *56*, 435–440.

## Proceeding papers

1. *Bo Chen*; Lu, Kathy; Tian, Z. P. Effect Of Focused Ion Beam Patterning On Enlarging Anodization Window And Interpore Distance For Ordered Porous Anodic Alumina, Ceramic Transactions, Proceeding of Materials Science & Technology 2010 Conference and Exhibit (MS&T '10), John Wiley & Sons: Houston, TX, October 17-21, 2010.
2. Lu, Kathy; *Bo Chen*; Titania Nanoparticle Synthesis and Soft Lithographic Molding, Proceedings of 2011 NSF Engineering Research and Innovation Conference, Atlanta, GA, January 4-7, 2011.
3. Lu, Kathy; *Bo Chen*. Single Nanometer $TiO_2$ Particle Synthesis and Soft Lithographic Molding, Proceedings of 2011 NSF Engineering Research and Innovation Conference, Atlanta, GA, January 4-7, 2011.
4. Lu, Kathy; *Bo Chen*; Tian, Z. P. Directed Patterning: Focused Ion Beam Guided Anodization, Proceedings of 2011 NSF Engineering Research and Innovation Conference, Atlanta, GA, January 4-7, 2011.

## Book Chapter

1. Kathy Lu; Wenle Li; *Bo Chen*. “Sintering of Nanoparticle-based Porous Materials,” Assisted Sintering, Nanosintering and Grain Growth, Editors: Ricardo H. R. Castro, Klaus van Benthem, Springer, 2011.

# References

1. Keller, F.; Hunter, M. S. A.; Robinson, D. L. *J. Electrochem. Soc.* **1953,** *100*, 411-419.
2. Jessensky, O.; Muller, F.; Gosele, U. *Applied Physics Letters* **1998,** *72*, 1173-1175.
3. Singh, G. K.; Golovin, A. A.; Aranson, I. S. *Physical Review B* **2006,** *73*, 205422.
4. Su, Z. X.; Zhou, W. Z. *Advanced Materials* **2008,** *20*, 3663-3667.
5. Su, Z. X.; Hahner, G.; Zhou, W. Z. *J. Mater. Chem.* **2008,** *18*, 5787-5795.
6. Su, Z. X.; Zhou, W. Z. *Adv. Mater.* **2008,** *20*, 3663-3667.
7. Su, Z. X.; Hahner, G.; Zhou, W. Z. *Journal of Materials Chemistry* **2008,** *18*, 5787-5795.
8. Asoh, H.; Nishio, K.; Nakao, M.; Yokoo, A.; Tamamura, T.; Masuda, H. *J. Vac. Sci. Technol. B* **2001,** *19*, 569-572.
9. Masuda, H.; Hasegwa, F.; Ono, S. *Journal of the Electrochemical Society* **1997,** *144*, L127-L130.
10. Masuda, H.; Fukuda, K. *Science* **1995,** *268*, 1466-1468.
11. Li, F. Y.; Zhang, L.; Metzger, R. M. *Chemistry of Materials* **1998,** *10*, 2470-2480.
12. Li, A. P.; Muller, F.; Birner, A.; Nielsch, K.; Gosele, U. *J. Appl. Phys.* **1998,** *84*, 6023-6026.
13. Masuda, H.; Yada, K.; Osaka, A. *Jpn. J. Appl. Phys. Part 2 - Lett.* **1998,** *37*, L1340-L1342.
14. Nielsch, K.; Choi, J.; Schwirn, K.; Wehrspohn, R. B.; Gosele, U. *Nano Lett.* **2002,** *2*, 677-680.
15. Lee, W.; Ji, R.; Gosele, U.; Nielsch, K. *Nature Materials* **2006,** *5*, 741-747.
16. Lee, W.; Schwirn, K.; Steinhart, M.; Pippel, E.; Scholz, R.; Gosele, U. *Nature Nanotechnology* **2008,** *3*, 234-239.
17. Lee, W.; Kim, J. C.; Gosele, U. *Advanced Functional Materials* **2010,** *20*, 21-27.
18. Losic, D.; Lillo, M. *Small* **2009,** *5*, 1392-1397.
19. Li, Y.; Ling, Z. Y.; Chen, S. S.; Cwang, J. *Nanotechnology* **2008,** *19*, 225604.
20. Schwirn, K.; Lee, W.; Hillebrand, R.; Steinhart, M.; Nielsch, K.; Gosele, U. *Acs Nano* **2008,** *2*, 302-310.
21. Lee, W.; Scholz, R.; Gosele, U. *Nano Lett.* **2008,** *8*, 2155-2160.
22. Kashi, M. A.; Ramazani, A.; Noormohammadi, M.; Zarei, M.; Marashi, P. *Journal of Physics D-Applied Physics* **2007,** *40*, 7032-7040.
23. Yasui, K.; Nishio, K.; Nunokawa, H.; Masuda, H. *J. Vac. Sci. Technol. B* **2005,** *23*, L9-L12.
24. Masuda, H.; Yamada, H.; Satoh, M.; Asoh, H.; Nakao, M.; Tamamura, T. *Applied Physics Letters* **1997,** *71*, 2770-2772.
25. Masuda, H.; Yotsuya, M.; Asano, M.; Nishio, K.; Nakao, M.; Yokoo, A.; Tamamura, T. *Applied Physics Letters* **2001,** *78*, 826-828.
26. Lee, W.; Ji, R.; Ross, C. A.; Gosele, U.; Nielsch, K. *Small* **2006,** *2*, 978-982.
27. Choi, J.; Luo, Y.; Wehrspohn, R. B.; Hillebrand, R.; Schilling, J.; Gosele, U. *Journal of Applied Physics* **2003,** *94*, 4757-4762.
28. Liu, C. Y.; Datta, A.; Liu, N. W.; Peng, C. Y.; Wang, Y. L. *Applied Physics Letters* **2004,** *84*, 2509-2511.
29. Liu, C. Y.; Datta, A.; Wang, Y. L. *Applied Physics Letters* **2001,** *78*, 120-122.
30. Liu, N. W.; Datta, A.; Liu, C. Y.; Wang, Y. L. *Applied Physics Letters* **2003,** *82*, 1281-1283.

31. Liu, N. W.; Liu, C. Y.; Wang, H. H.; Hsu, C. F.; Lai, M. Y.; Chuang, T. H.; Wang, Y. L. *Adv. Mater.* **2008,** *20*, 2547-2551.
32. Liu, N. W.; Datta, A.; Liu, C. Y.; Peng, C. Y.; Wang, H. H.; Wang, Y. L. *Adv. Mater.* **2005,** *17*, 222-225.
33. Sun, Z. J.; Kim, H. K. *Applied Physics Letters* **2002,** *81*, 3458-3460.
34. Asoh, H.; Ono, S.; Hirose, T.; Nakao, M.; Masuda, H. *Electrochimica Acta* **2003,** *48*, 3171-3174.
35. Kwon, N.; Kim, K.; Heo, J.; Chung, I. *J. Vac. Sci. Technol. A* **2009,** *27*, 803-807.
36. Masuda, H.; Asoh, H.; Watanabe, M.; Nishio, K.; Nakao, M.; Tamamura, T. *Advanced Materials* **2001,** *13*, 189-192.
37. Choi, J.; Wehrspohn, R. B.; Gosele, U. *Electrochimica Acta* **2005,** *50*, 2591-2595.
38. Shingubara, S.; Maruo, S.; Yamashita, T.; Nakao, M.; Shimizu, T. *Microelectronic Engineering* **2010,** *87*, 1451-1454.
39. Choi, J.; Nielsch, K.; Reiche, M.; Wehrspohn, R. B.; Gosele, U. *J. Vac. Sci. Technol. B* **2003,** *21*, 763-766.
40. Li, J.; Papadopoulos, C.; Xu, J. *Nature* **1999,** *402*, 253-254.
41. Meng, G. W.; Jung, Y. J.; Cao, A. Y.; Vajtai, R.; Ajayan, P. M. *Proceedings of the National Academy of Sciences of the United States of America* **2005,** *102*, 7074-7078.
42. Chen, S. S.; Ling, Z. Y.; Hu, X.; Li, Y. *Journal of Materials Chemistry* **2009,** *19*, 5717-5719.
43. Zhang, J. P.; Day, C. S.; Carroll, D. L. *Chemical Communications* **2009**, 6937-6939.
44. Kopp, O.; Lelonek, M.; Knoll, M. *J. Phys. Chem. C* **2011,** *115*, 7993-7996.
45. Lelonek, M.; Kopp, O.; Knoll, M. *Electrochimica Acta* **2009,** *54*, 2805-2809.
46. Yin, A. J.; Guico, R. S.; Xu, J. *Nanotechnology* **2007,** *18*.
47. Zakeri, R.; Watts, C.; Wang, H. B.; Kohli, P. *Chemistry of Materials* **2007,** *19*, 1954-1963.
48. Liu, K.; Nogues, J.; Leighton, C.; Masuda, H.; Nishio, K.; Roshchin, I. V.; Schuller, I. K. *Applied Physics Letters* **2002,** *81*, 4434-4436.
49. Lee, W.; Alexe, M.; Nielsch, K.; Gosele, U. *Chemistry of Materials* **2005,** *17*, 3325-3327.
50. Thongmee, S.; Ma, Y. W.; Ding, J.; Yi, J. B.; Sharma, G. *Surf. Rev. Lett.* **2008,** *15*, 91-96.
51. Yi, J. B.; Pan, H.; Lin, J. Y.; Ding, J.; Feng, Y. P.; Thongmee, S.; Liu, T.; Gong, H.; Wang, L. *Advanced Materials* **2008,** *20*, 1170-1174.
52. Chen, B. S.; Xu, Q. L.; Zhao, X. L.; Zhu, X. G.; Kong, M. G.; Meng, G. W. *Advanced Functional Materials* **2010,** *20*, 3791-3796.
53. Su, Z. X.; Sha, J.; Niu, J. J.; Liu, J. X.; Yang, D. R. *Physica Status Solidi a-Applications and Materials Science* **2006,** *203*, 792-801.
54. Li, X. D.; Meng, G. W.; Xu, Q. L.; Kong, M. G.; Zhu, X. G.; Chu, Z. Q.; Li, A. P. *Nano Lett.* **2011,** *11*, 1704-1709.
55. Kang, D. W.; Suh, J. S. *Journal of Applied Physics* **2004,** *96*, 5234-5238.
56. Yuan, Z. H.; Huang, H.; Dang, H. Y.; Cao, J. E.; Hu, B. H.; Fan, S. S. *Applied Physics Letters* **2001,** *78*, 3127-3129.
57. Gao, H.; Mu, C.; Wang, F.; Xu, D. S.; Wu, K.; Xie, Y. C.; Liu, S.; Wang, E. G.; Xu, J.; Yu, D. P. *Journal of Applied Physics* **2003,** *93*, 5602-5605.
58. Jung, H. Y.; Jung, S. M.; Gu, G. H.; Suh, J. S. *Applied Physics Letters* **2006,** *89*.
59. Kang, T. S.; Smith, A. P.; Taylor, B. E.; Durstock, M. F. *Nano Lett.* **2009,** *9*, 601-606.
60. Hoyer, P. *Langmuir* **1996,** *12*, 1411-1413.

61. Lakshmi, B. B.; Dorhout, P. K.; Martin, C. R. *Chemistry of Materials* **1997,** *9*, 857-862.

62. Shin, H. J.; Jeong, D. K.; Lee, J. G.; Sung, M. M.; Kim, J. Y. *Advanced Materials* **2004,** *16*, 1197-1200.

63. Sander, M. S.; Cote, M. J.; Gu, W.; Kile, B. M.; Tripp, C. P. *Advanced Materials* **2004,** *16*, 2052-2057.

64. Wang, W. Z.; Varghese, O. K.; Paulose, M.; Grimes, C. A.; Wang, Q. L.; Dickey, E. C. *Journal of Materials Research* **2004,** *19*, 417-422.

65. Kasuga, T.; Hiramatsu, M.; Hoson, A.; Sekino, T.; Niihara, K. *Langmuir* **1998,** *14*, 3160-3163.

66. Du, G. H.; Chen, Q.; Che, R. C.; Yuan, Z. Y.; Peng, L. M. *Applied Physics Letters* **2001,** *79*, 3702-3704.

67. Rani, S.; Roy, S. C.; Paulose, M.; Varghese, O. K.; Mor, G. K.; Kim, S.; Yoriya, S.; LaTempa, T. J.; Grimes, C. A. *Phys. Chem. Chem. Phys.* **2010,** *12*, 2780-2800.

68. Varghese, O. K.; Gong, D. W.; Paulose, M.; Ong, K. G.; Dickey, E. C.; Grimes, C. A. *Advanced Materials* **2003,** *15*, 624-627.

69. Ghicov, A.; Macak, J. M.; Tsuchiya, H.; Kunze, J.; Haeublein, V.; Frey, L.; Schmuki, P. *Nano Lett.* **2006,** *6*, 1080-1082.

70. Liu, D. W.; Xiao, P.; Zhang, Y. H.; Garcia, B. B.; Zhang, Q. F.; Guo, Q.; Champion, R.; Cao, G. Z. *J. Phys. Chem. C* **2008,** *112*, 11175-11180.

71. Macak, J. M.; Tsuchiya, H.; Schmuki, P. *Angewandte Chemie-International Edition* **2005,** *44*, 2100-2102.

72. Macak, J. M.; Zlamal, M.; Krysa, J.; Schmuki, P. *Small* **2007,** *3*, 300-304.

73. Cai, Q. Y.; Paulose, M.; Varghese, O. K.; Grimes, C. A. *Journal of Materials Research* **2005,** *20*, 230-236.

74. Shankar, K.; Mor, G. K.; Fitzgerald, A.; Grimes, C. A. *J. Phys. Chem. C* **2007,** *111*, 21-26.

75. Paulose, M.; Shankar, K.; Yoriya, S.; Prakasam, H. E.; Varghese, O. K.; Mor, G. K.; Latempa, T. A.; Fitzgerald, A.; Grimes, C. A. *J. Phys. Chem. C* **2006,** *110*, 16179-16184.

76. Ruan, C. M.; Paulose, M.; Varghese, O. K.; Mor, G. K.; Grimes, C. A. *Journal of Physical Chemistry B* **2005,** *109*, 15754-15759.

77. Kuang, D.; Brillet, J.; Chen, P.; Takata, M.; Uchida, S.; Miura, H.; Sumioka, K.; Zakeeruddin, S. M.; Gratzel, M. *Acs Nano* **2008,** *2*, 1113-1116.

78. Shankar, K.; Mor, G. K.; Prakasam, H. E.; Yoriya, S.; Paulose, M.; Varghese, O. K.; Grimes, C. A. *Nanotechnology* **2007,** *18*, 065707.

79. Wang, J.; Lin, Z. Q. *Chemistry of Materials* **2008,** *20*, 1257-1261.

80. Prakasam, H. E.; Shankar, K.; Paulose, M.; Varghese, O. K.; Grimes, C. A. *J. Phys. Chem. C* **2007,** *111*, 7235-7241.

81. Paulose, M.; Prakasam, H. E.; Varghese, O. K.; Peng, L.; Popat, K. C.; Mor, G. K.; Desai, T. A.; Grimes, C. A. *J. Phys. Chem. C* **2007,** *111*, 14992-14997.

82. Allam, N. K.; Grimes, C. A. *J. Phys. Chem. C* **2007,** *111*, 13028-13032.

83. Allam, N. K.; Shankar, K.; Grimes, C. A. *J. Mater. Chem.* **2008,** *18*, 2341-2348.

84. Yasuda, K.; Macak, J. M.; Berger, S.; Ghicov, A.; Schmuki, P. *Journal of the Electrochemical Society* **2007,** *154*, C472-C478.

85. Yoriya, S.; Grimes, C. A. *Journal of Materials Chemistry* **2011,** *21*, 102-108.

86. Wang, J.; Lin, Z. Q. *J. Phys. Chem. C* **2009,** *113*, 4026-4030.

87. Ghicov, A.; Schmuki, P. *Chem. Commun.* **2009**, 2791-2808.

88. Berger, S.; Kunze, J.; Schmuki, P.; Valota, A. T.; LeClere, D. J.; Skeldon, P.; Thompson,

G. E. *J. Electrochem. Soc.* **2010,** *157*, C18-C23.
89. Su, Z. X.; Zhou, W. Z.; Jiang, F. L.; Hong, M. C. *J. Mater. Chem.* **2012,** *22*, 535-544.
90. Mor, G. K.; Varghese, O. K.; Paulose, M.; Shankar, K.; Grimes, C. A. *Sol. Energ. Mat. Sol. Cells* **2006,** *90*, 2011-2075.
91. Roy, P.; Berger, S.; Schmuki, P. *Angew. Chem. Int. Ed.* **2011** *50*, 2904-2939.
92. Albu, S. P.; Ghicov, A.; Aldabergenova, S.; Drechsel, P.; LeClere, D.; Thompson, G. E.; Macak, J. M.; Schmuki, P. *Adv. Mater.* **2008,** *20*, 4135-4139.
93. Su, Z. X.; Zhou, W. Z. *J. Mater. Chem.* **2009,** *19*, 2301-2309.
94. Su, Z. X.; Zhou, W. Z. *Journal of Materials Chemistry* **2011,** *21*, 8955-8970.
95. Wang, D. A.; Liu, Y.; Yu, B.; Zhou, F.; Liu, W. M. *Chemistry of Materials* **2009,** *21*, 1198-1206.
96. Lee, K.; Kim, J.; Kim, H.; Lee, Y.; Tak, Y.; Kim, D.; Schmuki, P. *Journal of the Korean Physical Society* **2009,** *54*, 1027-1031.
97. Raja, K. S.; Gandhi, T.; Misra, M. *Electrochemistry Communications* **2007,** *9*, 1069-1076.
98. Wei, W.; Berger, S.; Hauser, C.; Meyer, K.; Yang, M.; Schmuki, P. *Electrochem. Commun.* **2010,** *12*, 1184-1186.
99. Macak, J. M.; Albu, S. P.; Schmuki, P. *Physica Status Solidi-Rapid Research Letters* **2007,** *1*, 181-183.
100. Shin, Y.; Lee, S. *Nano Lett.* **2008,** *8*, 3171-3173.
101. Wang, D. A.; Yu, B.; Wang, C. W.; Zhou, F.; Liu, W. M. *Advanced Materials* **2009,** *21*, 1964-1967.
102. Li, S. Q.; Zhang, G. M.; Guo, D. Z.; Yu, L. G.; Zhang, W. *J. Phys. Chem. C* **2009,** *113*, 12759-12765.
103. Kim, D.; Ghicov, A.; Albu, S. P.; Schmuki, P. *J. Am. Chem. Soc.* **2008,** *130*, 16454-16455.
104. Albu, S. R.; Kim, D.; Schmuki, P. *Angew. Chem. Int. Ed.* **2008,** *47*, 1916-1919.
105. Macak, J. M.; Albu, S.; Kim, D. H.; Paramasivam, I.; Aldabergerova, S.; Schmuki, P. *Electrochemical and Solid State Letters* **2007,** *10*, K28-K31.
106. Chen, Q. Q.; Xu, D. S.; Wu, Z. Y.; Liu, Z. F. *Nanotechnology* **2008,** *19*.
107. Tighineanu, A.; Ruff, T.; Albu, S.; Hahn, R.; Schmuki, P. *Chemical Physics Letters* **2010,** *494*, 260-263.
108. Ghicov, A.; Albu, S. P.; Hahn, R.; Kim, D.; Stergiopoulos, T.; Kunze, J.; Schiller, C. A.; Falaras, P.; Schmuki, P. *Chemistry-an Asian Journal* **2009,** *4*, 520-525.
109. Macak, J. M.; Gong, B. G.; Hueppe, M.; Schmuki, P. *Advanced Materials* **2007,** *19*, 3027-3031.
110. Macak, J. M.; Zollfrank, C.; Rodriguez, B. J.; Tsuchiya, H.; Alexe, M.; Creil, P.; Schmuki, P. *Adv. Mater.* **2009,** *21*, 3121-3125.
111. Seabold, J. A.; Shankar, K.; Wilke, R. H. T.; Paulose, M.; Varghese, O. K.; Grimes, C. A.; Choi, K. S. *Chemistry of Materials* **2008,** *20*, 5266-5273.
112. Mohapatra, S. K.; Banerjee, S.; Misra, M. *Nanotechnology* **2008,** *19*, 315601.
113. Lorenz, K.; Bauer, S.; Gutbrod, K.; Guggenbichler, J. P.; Schmuki, P.; Zollfrank, C. *Biointerphases* **2011,** *6*, 16-21.
114. Fang, D.; Huang, K. L.; Liu, S. Q.; Luo, Z. P.; Qing, X. X.; Zhang, Q. G. *Journal of Alloys and Compounds* **2010,** *498*, 37-41.
115. Fang, D.; Huang, K. L.; Liu, S. Q.; Qin, D. Y. *Electrochemistry Communications* **2009,** *11*, 901-904.

116. Albu, S. P.; Ghicov, A.; Macak, J. M.; Hahn, R.; Schmuki, P. *Nano Lett.* **2007,** *7*, 1286-1289.
117. Lin, C. J.; Yu, W. Y.; Chien, S. H. *Journal of Materials Chemistry* **2010,** *20*, 1073-1077.
118. Xie, Y.; Zhou, L.; Huang, C.; Huang, H.; Lu, J. *Electrochimica Acta* **2008,** *53*, 3643-3649.
119. Pan, X. A.; Chen, C. H.; Zhu, K.; Fan, Z. Y. *Nanotechnology* **2011,** *22*, 235402.
120. Gao, X. F.; Sun, W. T.; Hu, Z. D.; Ai, G.; Zhang, Y. L.; Feng, S.; Li, F.; Peng, L. M. *J. Phys. Chem. C* **2009,** *113*, 20481-20485.
121. Padture, N. P.; Wei, X. Z. *J. Am. Ceram. Soc.* **2003,** *86*, 2215-2217.
122. Xin, Y. C.; Jiang, J.; Huo, K. F.; Hu, T.; Chu, P. K. *ACS Nano* **2009,** *3*, 3228-3234.
123. Yang, Y.; Wang, X. H.; Sun, C. K.; Li, L. T. *Nanotechnology* **2009,** *20*, 055709.
124. Yang, Y.; Wang, X. H.; Zhong, C. F.; Sun, C. K.; Li, L. T. *Appl. Phys. Lett.* **2008,** *92*, 122907.
125. Zhang, J.; Bang, J. H.; Tang, C. C.; Kamat, P. V. *ACS Nano* **2010,** *4*, 387-395.
126. Mao, Y. B.; Banerjee, S.; Wong, S. S. *Chemical Communications* **2003**, 408-409.
127. Zhu, K.; Neale, N. R.; Miedaner, A.; Frank, A. J. *Nano Lett.* **2007,** *7*, 69-74.
128. Shankar, K.; Bandara, J.; Paulose, M.; Wietasch, H.; Varghese, O. K.; Mor, G. K.; LaTempa, T. J.; Thelakkat, M.; Grimes, C. A. *Nano Lett.* **2008,** *8*, 1654-1659.
129. Sodergren, S.; Hagfeldt, A.; Olsson, J.; Lindquist, S. E. *J. Phys. Chem.* **1994,** *98*, 5552-5556.
130. Jennings, J. R.; Ghicov, A.; Peter, L. M.; Schmuki, P.; Walker, A. B. *J. Am. Chem. Soc.* **2008,** *130*, 13364-13372.
131. Basham, J. I.; Mor, G. K.; Grimes, C. A. *Acs Nano* **2010,** *4*, 1253-1258.
132. Mor, G. K.; Basham, J.; Paulose, M.; Kim, S.; Varghese, O. K.; Vaish, A.; Yoriya, S.; Grimes, C. A. *Nano Lett.* **2010,** *10*, 2387-2394.
133. Shankar, K.; Feng, X.; Grimes, C. A. *Acs Nano* **2009,** *3*, 788-794.
134. Roy, S. C.; Varghese, O. K.; Paulose, M.; Grimes, C. A. *Acs Nano* **2010,** *4*, 1259-1278.
135. Varghese, O. K.; Paulose, M.; LaTempa, T. J.; Grimes, C. A. *Nano Lett.* **2009,** *9*, 731-737.
136. Adachi, K.; Ohta, K.; Mizuno, T. *Sol. Energy* **1994,** *53*, 187-190.
137. Tan, S. S.; Zou, L.; Hu, E. *Catal. Today* **2006,** *115*, 269-273.
138. Fujishima, A.; Honda, M. *Nature* **1972,** *238*, 37-38.
139. Gratzel, M. *Nature* **2001,** *414*, 338-344.
140. Shankar, K.; Basham, J. I.; Allam, N. K.; Varghese, O. K.; Mor, G. K.; Feng, X. J.; Paulose, M.; Seabold, J. A.; Choi, K. S.; Grimes, C. A. *J. Phys. Chem. C* **2009,** *113*, 6327-6359.
141. Das, C.; Roy, P.; Yang, M.; Jha, H.; Schmuki, P. *Nanoscale* **2011,** *3*, 3094-3096.
142. Mohapatra, S. K.; Misra, M.; Mahajan, V. K.; Raja, K. S. *J. Phys. Chem. C* **2007,** *111*, 8677-8685.
143. Park, J. H.; Kim, S.; Bard, A. J. *Nano Lett.* **2006,** *6*, 24-28.
144. Yin, Y. X.; Jin, Z. G.; Hou, F. *Nanotechnology* **2007,** *18*.
145. Allam, N. K.; Grimes, C. A. *Langmuir* **2009,** *25*, 7234-7240.
146. Chen, X. B.; Shen, S. H.; Guo, L. J.; Mao, S. S. *Chemical Reviews* **2010,** *110*, 6503-6570.
147. Liu, C. Y.; Datta, A.; Liu, N. W.; Wu, Y. R.; Wang, H. H.; Chuang, T. H.; Wang, Y. L. *J. Vac. Sci. Technol. B* **2008,** *26*, 651-654.
148. Giannuzzi, A.; Stevie, F. A. *Springer, NY* **2005**.
149. Wu, M. T.; Leu, I. C.; Hon, M. H. *J. Vac. Sci. Technol. B* **2002,** *20*, 776-782.
150. Peng, C. Y.; Liu, C. Y.; Liu, N. W.; Wang, H. H.; Datta, A.; Wang, Y. L. *J. Vac. Sci.*

*Technol. B* **2005,** *23*, 559-562.
151. Choi, J. S.; Wehrspohn, R. B.; Gosele, U. *Advanced Materials* **2003,** *15*, 1531-1534.
152. Nishijima, Y.; Oster, G. *J. Opt. Soc. Am.* **1964,** *54*, 1-5.
153. Oster, G.; Wasserman, M.; Zwerling, C. *J. Opt. Soc. Am.* **1964,** *54*, 169-175.
154. Harthong, J. *Adv. Appl. Math.* **1981,** *2*, 24-75.
155. Amidror, I. *J. Opt. Soc. Am. A* **2003,** *10*, 1900-1919.
156. Amidror, I., *Thetheory of the Moiré phenomenon*. Kluwer Academic Publisher:Norwell: MA, 2000.
157. Chen, J.-T.; Chen, D.; Russell, T. P. *Langmuir* **2009,** *25*, 4331-4335.
158. Lee, H.; Lee, B. P.; Messersmith, P. B. *Nature* **2007,** *448*, 338-U4.
159. Grimm, S.; Giesa, R.; Sklarek, K.; Langner, A.; Goesele, U.; Schmidt, H.-W.; Steinhart, M. *Nano Lett.* **2008,** *8*, 1954-1959.
160. Steinhart, M.; Wehrspohn, R. B.; Gosele, U.; Wendorff, J. H. *Angewandte Chemie-International Edition* **2004,** *43*, 1334-1344.
161. Zhang, M. F.; Dobriyal, P.; Chen, J. T.; Russell, T. P.; Olmo, J.; Merry, A. *Nano Lett.* **2006,** *6*, 1075-1079.
162. Grimm, S.; Martin, J.; Rodriguez, G.; Fernandez-Gutierrez, M.; Mathwig, K.; Wehrspohn, R. B.; Goesele, U.; San Roman, J.; Mijangos, C.; Steinhart, M. *Journal of Materials Chemistry* **2010,** *20*, 3171-3177.
163. Wu, S., *Polymer Interfaces and Adhesion*. Marcel Dekker: New York, 1982.
164. Grimm, S.; Schwirn, K.; Goering, P.; Knoll, H.; Miclea, P. T.; Greiner, A.; Wendorff, J. H.; Wehrspohn, R. B.; Goesele, U.; Steinhart, M. *Small* **2007,** *3*, 993-1000.
165. Lee, D. Y.; Lee, D. H.; Lim, H. S.; Han, J. T.; Cho, K. *Langmuir* **2010,** *26*, 3252-3256.
166. Li, Z.; Gu, Y.; Wang, L.; Ge, H.; Wu, W.; Xia, Q.; Yuan, C.; Chen, Y.; Cui, B.; Williams, R. S. *Nano Lett.* **2009,** *9*, 2306-2310.
167. Bietsch, A.; Michel, B. *Journal of Applied Physics* **2000,** *88*, 4310-4318.
168. Huang, Y. G. Y.; Zhou, W. X.; Hsia, K. J.; Menard, E.; Park, J. U.; Rogers, J. A.; Alleyne, A. G. *Langmuir* **2005,** *21*, 8058-8068.
169. Zhang, Y.; Lo, C. W.; Taylor, J. A.; Yang, S. *Langmuir* **2006,** *22*, 8595-8601.
170. Greiner, C.; del Campo, A.; Arzt, E. *Langmuir* **2007,** *23*, 3495-3502.
171. Schmid, H.; Michel, B. *Macromolecules* **2000,** *33*, 3042-3049.
172. Odom, T. W.; Love, J. C.; Wolfe, D. B.; Paul, K. E.; Whitesides, G. M. *Langmuir* **2002,** *18*, 5314-5320.
173. Odom, T. W.; Thalladi, V. R.; Love, J. C.; Whitesides, G. M. *J. Am. Chem. Soc.* **2002,** *124*, 12112-12113.
174. Goh, C.; Coakley, K. M.; McGehee, M. D. *Nano Lett.* **2005,** *5*, 1545-1549.
175. Cho, W. K.; Choi, I. S. *Advanced Functional Materials* **2008,** *18*, 1089-1096.
176. Lee, Y.; Park, S.-H.; Kim, K.-B.; Lee, J.-K. *Advanced Materials* **2007,** *19*, 2330-+.
177. Lee, T. W.; Mitrofanov, O.; Hsu, J. W. R. *Advanced Functional Materials* **2005,** *15*, 1683-1688.
178. Suh, K. Y.; Kim, Y. S.; Lee, H. H. *Advanced Materials* **2001,** *13*, 1386-1389.
179. Kim, E.; Xia, Y. N.; Whitesides, G. M. *Nature* **1995,** *376*, 581-584.
180. Hua, F.; Sun, Y. G.; Gaur, A.; Meitl, M. A.; Bilhaut, L.; Rotkina, L.; Wang, J. F.; Geil, P.; Shim, M.; Rogers, J. A.; Shim, A. *Nano Lett.* **2004,** *4*, 2467-2471.
181. Williams, S. S.; Retterer, S.; Lopez, R.; Ruiz, R.; Samulski, E. T.; DeSimone, J. M. *Nano Lett.* **2010,** *10*, 1421-1428.

182. Chandra, D.; Yang, S. *Accounts Chem. Res.* **2010,** *43*, 1080-1091.

183. Hui, C. Y.; Jagota, A.; Lin, Y. Y.; Kramer, E. J. *Langmuir* **2002,** *18*, 1394-1407.

184. Roca-Cusachs, P.; Rico, F.; Martinez, E.; Toset, J.; Farre, R.; Navajas, D. *Langmuir* **2005,** *21*, 5542-5548.

185. Glassmaker, N. J.; Jagota, A.; Hui, C. Y.; Kim, J. *J. R. Soc. Interface* **2004,** *1*, 23-33.

186. Armani, D.; Liu, C.; Aluru, N., *In Twelfth IEEE International Conference on Micro Electro Mechanical Systems*. IEEE: Orlando, FL, 1999.

187. Lee, Y. W.; Park, S. H.; Kim, K. B.; Lee, J. K. *Advanced Materials* **2007,** *19*, 2330-2335.

188. Liu, X.; Li, Y. L.; Hou, F. *J. Am. Ceram. Soc.* **2009,** *92*, 49-53.

189. Holthaus, M. G.; Kropp, M.; Treccani, L.; Lang, W.; Rezwan, K. *J. Am. Ceram. Soc.* **2010,** *93*, 2574-2578.

190. Ahn, S. J.; Min, J. H.; Kim, J.; Moon, J. *J. Am. Ceram. Soc.* **2008,** *91*, 2143-2149.

191. Ahn, S. J.; Moon, J. *J. Am. Ceram. Soc.* **2005,** *88*, 1171-1174.

192. Yang, H.; Deschatelets, P.; Brittain, S. T.; Whitesides, G. M. *Adv. Mater.* **2001,** *13*, 54-58.

193. Zhang, D.; Su, B.; Button, T. W. *J. Eur. Ceram. Soc.* **2007,** *27*, 645-650.

194. Heule, M.; Schell, J.; Gauckler, L. J. *J. Am. Ceram. Soc.* **2003,** *86*, 407-412.

195. Lee, D.-H.; Park, K.-H.; Hong, L.-Y.; Kim, D.-P. *Sens Actuators A Phys* **2007,** *135*, 895-901.

196. Kim, H. D.; Nakayama, T.; Hong, B. J.; Imaki, K.; Yoshimura, T.; Suzuki, T.; Suematsu, H.; Niihara, K. *J. Eur. Ceram. Soc.* **2010,** *30*, 2735-2739.

197. Gobel, O. F.; Nedelcu, M.; Steiner, U. *Adv. Funct. Mater.* **2007,** *17*, 1131-1136.

198. Khan, S. U.; Gobel, O. F.; Blank, D. H. A.; ten Elshof, J. E. *ACS Appl. Mater. Interfaces* **2009,** *1*, 2250-2255.

199. Jim, K. L.; Lee, F. K.; Xin, J. Z.; Leung, C. W.; Chan, H. L. W.; Chen, Y. *Microelectron. Eng.* **2010,** *87*, 959-962.

200. Tredici, I. G.; Yaghmaie, F.; Irving, M.; Wijesundara, M. B. J.; Maglia, F.; Quartarone, E.; Anselmi-Tamburini, U. *J. Am. Ceram. Soc.* **2011,** *94*, 3171-3174.

201. Lu, K.; Hammond, C. *Int. J. Appl. Ceram. Technol.* **2011,** *8*, 965-976.

202. Lu, K.; Kessler, C. S.; Davis, R. M. *J. Am. Ceram. Soc.* **2006,** *89*, 2459-2465.

203. Liang, Y. X.; Lu, K. *Int. J. Appl. Ceram. Technol.* **2011,** *9*, 911-919.

204. Lu, K.; Zhu, X. J. *Int. J. Appl. Ceram. Technol.* **2008,** *5*, 219-227.

205. Lu, K. *J. Am. Ceram. Soc.* **2007,** *90*, 3753-3758.

206. Lu, K. *Ceram. Int.* **2008,** *34*, 1353-1360.

207. Ran, C. B.; Ding, G. Q.; Liu, W. C.; Deng, Y.; Hou, W. T. *Langmuir* **2008,** *24*, 9952-9955.

208. Li, Z. R.; Wang, J. X.; Zhang, Y. Z.; Wang, J. J.; Jiang, L.; Song, Y. L. *Appl. Phys. Lett.* **2010,** *97*, 233107.

209. Su, Z. X.; Zhou, W. Z. *J. Mater. Chem.* **2011,** *21*, 8955-8970.

210. Baram, N.; Ein-Eli, Y. *J. Phys. Chem. C* **2010,** *114*, 9781-9790.

211. Yahia, S. A. A.; Hamadou, L.; Kadri, A.; Benbrahim, N.; Sutter, E. M. M. *J. Electrochem. Soc.* **2012,** *159*, K83-K92.

212. Choi, J. S.; Wehrspohn, R. B.; Gosele, U. *Advanced Materials* **2003,** *15*, 1531-+.

213. Chen, B.; Lu, K. *Langmuir* **2011,** *27*, 4117-4125.

214. Berger, S.; Macak, J. M.; Kunze, J.; Schmuki, P. *Electrochem. Solid State Lett.* **2008,** *11*, C37-C40.

215. Naylor, M. *Math. Mag.* **2002,** *75*, 163-172.

216. Zhao, X.; Sanchez, B. M.; Dobson, P. J.; Grant, P. S. *Nanoscale* **2011,** *3*, 839-855.

217. Kim, J.-H.; Zhu, K.; Yan, Y.; Perkins, C. L.; Frank, A. J. *Nano Lett.* **2010,** *10*, 4099-4104.
218. Zhang, G. G.; Huang, C. J.; Zhou, L. M.; Ye, L.; Li, W. F.; Huang, H. T. *Nanoscale* **2011,** *3*, 4174-4181.
219. Salari, M.; Konstantinov, K.; Liu, H. K. *J. Mater. Chem.* **2011,** *21*, 5128-5133.
220. Salari, M.; Aboutalebi, S. H.; Konstantinov, K.; Liu, H. K. *Phys. Chem. Chem. Phys.* **2011,** *13*, 5038-5041.
221. Grimes, C. A.; Varghese, O. K.; Ranjan, S., *Light, water, Hydrogen*. Springer: 2008.
222. Mor, G. K.; Shankar, K.; Paulose, M.; Varghese, O. K.; Grimes, C. A. *Nano Lett.* **2005,** *5*, 191-195.
223. Wang, G.; Wang, H.; Ling, Y.; Tang, Y.; Yang, X.; Fitzmorris, R. C.; Wang, C.; Zhang, J. Z.; Li, Y. *Nano Lett.* **2011,** *11*, 3026-3033.
224. Macak, J. M.; Hildebrand, H.; Marten-Jahns, U.; Schmuki, P. *J. Electroanal. Chem.* **2008,** *621*, 254-266.
225. Shackelford, J. F.; Alexander, W., *CRC Materials Science and Engineering Handbook, 3rd ed.* 2001.
226. Shokuhfar, T.; Arumugam, G. K.; Heiden, P. A.; Yassar, R. S.; Friedrich, C. *ACS Nano* **2009,** *3*, 3098-3102.
227. Crawford, G. A.; Chawla, A. N.; Das, K.; Bose, S.; Bandyopadhyay, A., , *Acta Biomater.* **2007,** *3*, 359–367.
228. Kopp, O.; Lelonek, M.; Knoll, M. *Electrochimica Acta* **2009,** *54*, 6594-6597.
229. Chan, W. L.; Chason, E. *J. Appl. Phys.* **2007,** *101*, 121301.
230. Chason, E.; Aziz, M. J. *Scr. Mater.* **2003,** *49*, 953-959.
231. Li, J.; Stein, D.; McMullan, C.; Branton, D.; Aziz, M. J.; Golovchenko, J. A. *Nature* **2001,** *412*, 166-169.
232. Stein, D.; Li, J. L.; Golovchenko, J. A. *Phys. Rev. Lett.* **2002,** *89, 276106.*
233. Hoogerheide, D. P.; George, B.; Golovchenko, J. A.; Aziz, M. J. *J. Appl. Phys.* **2011,** *109, 074312.*
234. Cai, Q.; Ledden, B.; Krueger, E.; Golovchenko, J. A.; Li, J. L. *J. Appl. Phys.* **2006,** *100, 024914.*
235. George, H. B.; Tang, Y. Y.; Chen, X.; Li, J. L.; Hutchinson, J. W.; Golovchenko, J. A.; Aziz, M. J. *J. Appl. Phys.* **2010,** *108*, 014310.
236. Schenkel, T.; Radmilovic, V.; Stach, E. A.; Park, S. J.; Persaud, A. *J. Vac. Sci. Technol. B* **2003,** *21*, 2720-2723.
237. Kim, Y. R.; Chen, P.; Aziz, M. J.; Branton, D.; Vlassak, J. J. *J. Appl. Phys.* **2006,** *100*, 104322.
238. Chen, B.; Lu, K.; Geldmeier, J. A. *Chem. Commun.* **2011,** *47*, 10085-10087.
239. Chen, B.; Lu, K.; Tian, Z. P. *J. Mater. Chem.* **2011,** *21*, 8835-8840.
240. Brongersma, M. L.; Snoeks, E.; Polman, A. *Appl. Phys. Lett.* **1997,** *71*, 1628-1630.
241. Trinkaus, H. *J. Nuclear Mater.* **1995,** *223*, 196-201.
242. Ziegler, J. F.; Biersack, J. P.; Littmark, U., *The Stopping and Range of Ions in Solids*. Pergamon: New York, 2008.
243. Kim, H. B.; Hobler, G.; Steiger, A.; Lugstein, A.; Bertagnolli, E. *Nanotechnology* **2007,** *18*, 245303.
244. Bischoff, L.; Teichert, J.; Heera, V. *Appl. Surf. Sci.* **2001,** *184*, 372-376.
245. van Dillen, T.; Polman, A.; van Kats, C. M.; van Blaaderen, A. *Appl. Phys. Lett.* **2003,** *83*, 4315-4317.

246. Brongersma, M. L.; Snoeks, E.; van Dillen, T.; Polman, A. *J. Appl. Phys.* **2000,** *88*, 59-64.

247. Otani, K.; Chen, X.; Hutchinson, J. W.; Chervinsky, J. F.; Aziz, M. J. *J. Appl. Phys.* **2006,** *100*, 023535.

248. Dittrich, T.; Weidmann, J.; Timoshenko, V. Y.; Petrov, A. A.; Koch, F.; Lisachenko, M. G.; Lebedev, E. *Mater. Sci. Eng. B* **2000,** *69*, 489-493.

249. Nipoti, R.; Albertazzi, E.; Bianconi, M.; Lotti, R.; Lulli, G.; Cervera, M.; Carnera, A. *Appl. Phys. Lett.* **1997,** *70*, 3425-3427.

250. Lehrer, C.; Frey, L.; Petersen, S.; Ryssel, H. *J. Vac. Sci. Technol. B* **2001,** *19*, 2533-2538.

251. Han, J.; Lee, H.; Min, B.-K.; Lee, S. J. *Microelectron. Eng.* **2010,** *87*, 1-9.

252. Santamore, D.; Edinger, K.; Orloff, J.; Melngailis, J. *J. Vac. Sci. Technol. B* **1997,** *15*, 2346-2349.

253. deWith, G.; Glass, H. J. *J. Eur. Ceram. Soc.* **1997,** *17*, 753-757.

254. Egger, C. C.; du Fresne, C.; Raman, V. I.; Schadler, V.; Frechen, T.; Roth, S. V.; Muller-Buschbaum, P. *Langmuir* **2008,** *24*, 5877-5887.

255. Walton, K. S.; Snurr, R. Q. *J. Am. Chem. Soc.* **2007,** *129*, 8552-8556.

256. Koh, K.; Wong-Foy, A. G.; Matzger, A. J. *J. Am. Chem. Soc.* **2009,** *131*, 4184-4185.

257. Gostovic, D.; Vito, N. J.; O'Hara, K. A.; Jones, K. S.; Wachsmanw, E. D. *Journal of the American Ceramic Society* **2011,** *94*, 620-627.

258. Gunda, N. S. K.; Choi, H. W.; Berson, A.; Kenney, B.; Karan, K.; Pharoah, J. G.; Mitra, S. K. *Journal of Power Sources* **2011,** *196*, 3592-3603.

259. Wilson, J. R.; Duong, A. T.; Gameiro, M.; Chen, H. Y.; Thornton, K.; Mumm, D. R.; Barnett, S. A. *Electrochemistry Communications* **2009,** *11*, 1052-1056.

260. Wilson, J. R.; Kobsiriphat, W.; Mendoza, R.; Chen, H. Y.; Hiller, J. M.; Miller, D. J.; Thornton, K.; Voorhees, P. W.; Adler, S. B.; Barnett, S. A. *Nature Materials* **2006,** *5*, 541-544.